In compliance with the
Canadian Privacy Legislation
some supporting forms
may have been removed from
this dissertation.

While these forms may be included
in the document page count,
their removal does not represent
any loss of content from the dissertation.

University of Alberta

Electrospray Ionization for Applications in Ion Mobility Spectrometry

by

Eric Ching Sung Cheong

A thesis submitted to the Faculty of Graduate Studies and Research in partial fulfillment of the requirement for the degree of Master of Science

Department of Electrical and Computer Engineering

Edmonton, Alberta

Fall 2003

National Library
of Canada

Acquisitions and
Bibliographic Services

395 Wellington Street
Ottawa ON K1A 0N4
Canada

Bibliothèque nationale
du Canada

Acquisisitons et
services bibliographiques

395, rue Wellington
Ottawa ON K1A 0N4
Canada

Your file Votre référence
ISBN: 0-612-87737-X
Our file Notre référence
ISBN: 0-612-87737-X

The author has granted a non-exclusive licence allowing the National Library of Canada to reproduce, loan, distribute or sell copies of this thesis in microform, paper or electronic formats.

The author retains ownership of the copyright in this thesis. Neither the thesis nor substantial extracts from it may be printed or otherwise reproduced without the author's permission.

L'auteur a accordé úne licence non exclusive permettant à la Bibliothèque nationale du Canada de reproduire, prêter, distribuer ou vendre des copies de cette thèse sous la forme de microfiche/film, de reproduction sur papier ou sur format électronique.

L'auteur conserve la propriété du droit d'auteur qui protège cette thèse. Ni la thèse ni des extraits substantiels de celle-ci ne doivent être imprimés ou aturement reproduits sans son autorisation.

Canadä

University of Alberta

Library Release Form

Name of Author: Eric Ching Sung Cheong

Title of Thesis: Electrospray ionization for applications in ion mobility spectrometry

Degree: Master of Science

Year this Degree Granted: 2003

Permission is hereby granted to the University of Alberta Library to reproduce single copies of this thesis and to lend or sell such copies for private, scholarly or scientific research purposes only.

The author reserves all other publication and other rights in association with the copyright in the thesis, and except as herein before provided, neither the thesis nor any substantial portion thereof may be printed or otherwise reproduced in any material form whatever without the author's prior written permission.

Date submitted: Aug. 8/03

University of Alberta

Faculty of Graduate Studies and Research

The undersigned certify that they have read, and recommend to the Faculty of Graduate Studies and Research for acceptance, a thesis entitled "Electrospray Ionization for Applications in Ion Mobility Spectrometry" submitted by Eric Ching Sung Cheong in partial fulfillment of the requirements for the degree of Master of Science.

Aug 7/03

Abstract

In this work, Electrospray Ionization (ESI) was studied for applications in Ion Mobility Spectrometry (IMS). As such, a simple ion mobility spectrometer was constructed that was based upon the use of printed circuit boards (PCBs), and that did not require the specialized (drift and sheath) gases, heater assemblies, or high voltage pulsers that are typical of such instruments described in the literature. Despite its simplicity, our IMS system performed well, with capabilities comparable to those reported in the field. The sample used was the protein Cytochrome c in concentrations of 1 – 5 mg/mL in the solvent (50:50 Methanol/Water per volume). The resultant signal limit of detection (LOD_{signal}) was ~2 pA, with a concentration limit of detection (LOD_{conc}) of ~111 ppm for the cytochrome c, and peak resolutions (R_p) of ~20. Integration of microfluidic ES chips, coupled with the microcontroller system, could potentially lead to a handheld ES-IMS device.

To my parents, my brother, and my friends, who have supported and encouraged me throughout my University career

Acknowledgements

I would first like to thank my supervisor, Dr. Chris Backhouse, for his support, his guidance, and his encouragement during this project. I appreciate having been introduced to the fascinating fields of Electrospray Ionization and Ion Mobility Spectrometry (IMS). I feel I have learned much during my time in the Backhouse Lab, and that the process of learning these lessons has enabled me to grow professionally and personally, thus enabling me to develop confidence and skill in laboratory and research work in general.

Next, I wish to thank Ben Bathgate, an ECE (Department of Electrical and Computer Engineering) technician partially associated with the Backhouse Lab. Without his design ideas, his vast knowledge of practical electronics, and his willingness to aid this utter novice, the IMS systems used in this project would not have turned out as elegantly as they have. Thank you Ben for designing, milling out, and assembling all three IMS Columns (I, II, and III), including the Detectors (or Pico) I – IV, and for providing advice on all things electrical and for holding my hand while I first learned how to put together and test the electrical components.

I would also like to thank the following technicians for their help throughout this project. To Loi Hua, thanks for helping with the technical and practical aspects of operating the ES-IMS Device II. To Ed Tiong, thanks for helping with the construction and testing of the preliminary Electrospray Ionization Devices, and for obtaining the electrical components that I needed. To Albert Huizinga, thanks for helping with the woodwork for the baseboard for the preliminary Plastic Box.

I wish to extend my appreciation to those of you, too numerous to name, who have given me support and have shared/exchanged ideas that have benefited my project, basically everyone with whom I have spoken in the past several years. Particularly, I would extend my thanks to Patrick Pilarski for help with drawing up the designs for the Control Box, the Clear Box, and various other components. I would also like to thank Tim Footz for help with things biological.

To the members of my committee, Dr. Ying Y. Tsui and Dr. Fred E. Vermeulen, I wish to sincerely thank you for your help and understanding during the course of my Masters Program. To Dr. David Wishart, thank you for all your suggestions and new ideas related to this Project.

Finally, I wish to thank Herbert Dexel and his group in the ECE Machine Shop, especially Barry Arnold for the timely construction of the Clear Box and Mike Boissonneault for help with machining the various holes and grooves in the Control Box. I would extend my thanks to the Machine Shop for also constructing the pre-"Column" ES-IMS component grids and the preliminary Plastic Box.

Table of Contents

Page

Chapter 1. Introduction

1.1. Introduction 2
1.2. Electrospray Ionization 3
1.2.1. Taylor Cone Formation 9
1.2.1.1. Corona Discharge 11
1.2.2. Electrospray Mechanism 12
1.2.2.1. Electrophoretic Charging Mechanism 12
1.2.2.2. Ion Droplet Evolution: Charge Residue Model vs. Ion Desorption Model 13
1.3. Applications in Ion Mobility Spectrometry 16
1.3.1. Comparisons with Electrophoresis and Electro-osmotic flow 16
1.3.2. History of IMS 18
1.3.3. Types of Ion Sources for IMS 21
1.3.4. Types of Ion Mobility Spectrometry Drift Columns 22
1.3.5. Radioactive ^{63}Ni Ionization – Ion Mobility Spectrometry 24
1.3.6. Electrospray Ionization – Ion Mobility Spectrometry 26
1.4. Applications in Mass Spectrometry 30
1.5. Outline of this thesis 31
1.6. References 32

Chapter 2. Design and Testing of the Prototype Electrospray – Ion Mobility Spectrometry System

2.1. Introduction 41
2.2. Experimental Design and Testing of Various ES Source Types 42
2.2.1. Plastic Chip Electrospray Source 42
2.2.1.1. Fabrication of the Plastic Chip Electrospray Source 43
2.2.1.2. Evaluation of the Plastic Chip Electrospray Source 45
2.2.2. Microfluidic Glass Chip Electrospray Source 48
2.2.2.1. Fabrication of the Glass Chip Electrospray Source 48
2.2.2.2. Evaluation of the Glass Chip Electrospray Source 50
2.2.3. Capillary Electrospray Source 53
2.2.3.1. Fabrication of the Capillary Electrospray Source 53
2.2.3.2. Evaluation of the Capillary Electrospray Source 53
2.2.4. Preliminary ES Source Results 56
2.3. Experimental Design of the Preliminary ES-IMS System 57
2.3.1. Design and Fabrication of ES-IMS Device I 57
2.3.1.1. Electrospray Ion Source I (ESIS I) 57
2.3.1.2. IMS Drift Column I 60
2.3.1.3. Collector-Detector (C-D) Assembly I 69
2.3.1.4. External Equipment 73

2.4. Results and Discussion of the Preliminary ES-IMS System 74
2.4.1. Evaluation of the Fast Detection Circuit 74
2.4.2. Evaluation of ESIS I 80
2.4.3. Evaluation of Drift Column I 83
2.5. Conclusions 87
2.6. References 89

Chapter 3. Follow-up Design of a PCB-based Electrospray – Ion Mobility Spectrometer
3.1. Introduction 93
3.2. Follow-up Design and Testing of a Novel ES-IMS System 93
3.2.1. Description of ES-IMS Device II 95
3.2.1.1. Description of ESIS II 95
3.2.1.2. Description of IMS Drift Column II 96
3.2.1.3. Description of C-D Assembly II 105
3.2.1.4. Description of the Control Box 109
3.2.1.5. Description of (ES-IMS) Clear Box 111
3.2.1.6. Description of the External Equipment 113
3.3. Results and Discussion 114
3.3.1. Cytochrome c 125
3.4. Conclusions 136
3.5. References 138

Chapter 4. Future Work
4.1. ES-IMS Device III 141
4.1.1. Collector-Detector Assembly III 146
4.2. Microfluidic Electrospray Chip Applications 150
4.3. Ion Thruster Applications 151
4.3.1. Theoretical Analysis and Estimates of Thrust 152
4.3.2. Low Vacuum Design and Testing of an Ion Thruster – Propelled Craft 155
4.3.2.1. Design of IT Pendulum I 158
4.3.2.2. Design of the Control Tube for IT Pendulum I 160
4.3.2.3. Experimental Setup for Testing IT Craft III: "Vac I" 162
4.3.3. Ion Thruster Arrays 163
4.4. References 164

Appendices

A1.0. Chapter Appendices 167
A2.0. Chapter 2 Appendices 167
A2.0.1. IMS Column I Design Considerations 167
A2.0.1.1. IMS Column I Capacitance Considerations 167
A2.0.1.2. Circuit Analysis of the Keithley High Speed Picoammeter 170
A3.0. Chapter 3 Appendices 174
A3.0.1. More Images of the ES-IMS System 174
A3.0.2. Details of the Control Box 176
A3.0.2.1. Schematic (Block) Diagrams of Control Box Components 176
A3.0.2.2. Description of Control Box Components 178
A3.0.2.2. C-Program for ES – IMS Controller (or Control Box) 182
A3.0.3. More on the Ripple/Ringing Phenomenon 193
A3.0.4. Comparison Between the Averaged and Un-averaged Control Signals 198
A3.0.5. More on the unstable, polydisperse spray modes (SM-1 and SM-3) 199
A4.0. References 200

List of Tables

Page

Chapter 1

Table 1-1. **Various Radioactive ^{63}Ni type IMS Column Designs** 26

Table 1-2. **Various ES type IMS Column Designs** 29

Chapter 3

Table 3-1. **Comparison of the Reduced Mobilities (K_o) of Cytochrome c Peaks** 133

Chapter 4

Table 4-1. **Comparison of the Noise Pickup of the Various Detector Circuits** 150

Appendices

Table A2-1. Calculation of the Estimated Capacitance of the Aperture Grid - Collector Plate 169

List of Figures

Page

Chapter 1

Figure 1-1(a, b). Various CE-ES interfaces or ES tips. 6
Figure 1-1(c, d). Various CE-ES interfaces or ES tips. 7
Figure 1-2. 3D plot of Equation (1.1) for a potential of 5 kV. 8
Figure 1-3. Charge Residue Model (A) versus Ion Desorption Model (B). 15
Figure 1-4. Flowchart illustrating the operation of an IMS. 16
Figure 1-5. Schematic diagrams of two types of ion shutter gates. 23
Figure 1-6. Schematic diagram of the ^{63}Ni type IMS column. 26
Figure 1-7. Schematic diagram of the ES type IMS column. 28

Chapter 2

Figure 2-1. A transparent rendered model of a chip-based electrospray ionization source. 43
Figure 2-2. Photographs of the nozzle (left) and the electrode opening (right) of a plastic μchip ESIS. 44
Figure 2-3. Designs of a modified ("slim") plastic μchip ESIS. 45
Figure 2-4. Schematic of the setup for observing the formation of a Taylor cone and electrospray during HV operation. 46
Figure 2-5. Photographs of the "slim" plastic μchip ESIS during loading. 47
Figure 2-6. A schematic diagram of a Micralyne "simple cross" microfluidic chip. 49
Figure 2-7. A diagram of a microfluidic chip that was cut for the purpose of implementing ES. 49
Figure 2-8. A schematic diagram of the preliminary IMS arrangement. 51
Figure 2-9. A circuit diagram of the detection circuit used in conjunction with the preliminary IMS arrangement. 51
Figure 2-10. Transient signal obtained during μchip ES - IMS experiments. 52
Figure 2-11. Schematic of the setup for electrically evaluating the (CE) tube-type ESIS. 54
Figure 2-12. Still-photo-captures of electrospray (top), corona discharge (middle), and aftereffects of corona discharge (bottom) that were observed with the use of the (CE) tube-type ESIS emitter. 56
Figure 2-13. Photographs of (a) a 27-gauge SS hypodermic needle and (b) the flat-ground hypodermic needle tip of the (sheathless) electrospray ion source. 58
Figure 2-14. Schematic diagram of the electrospray ion source set in the ES-IMS system. 59
Figure 2-15. Schematic diagrams of the PCB (a) guard ring, (b) grid, and (c) shutter gate. 62

Figure 2-16. Electrical schematic diagram of the PCB IMS column including the ES source and the C-D. 63
Figure 2-17. Photograph of the Column I desolvation and drift regions (without the grids or shutter gate. 65
Figure 2-18. Schematic diagram of the ES-IMS Device I system setup. 66
Figure 2-19. Electrical schematic of the Bradbury-Nielsen type ion shutter gate controller. 67
Figure 2-20. Schematic diagram of the operation of the shutter gate. 68
Figure 2-21. Circuit diagram of the Keithley high speed picoammeter. 70
Figure 2-22. Schematic diagram of the picoammeter circuit that is the 1st detector. 71
Figure 2-23. Photographs of Collector-Detector Assembly I. 72
Figure 2-24. Schematic diagram for the testing of the precursor picoammeter circuit that was shown in Fig. 2-22. 75
Figure 2-25. A plot of the gain of the picoammeter. 75
Figure 2-26. Schematic diagram for the testing of the modified picoammeter circuit that was shown in Fig. 2-22. 77
Figure 2-27. Frequency versus gain of the detector circuit shown in Fig. 2-22. 78
Figure 2-28. Observation of the ripple (or ringing) effect in the detector output for a square-wave burst input of 1 nA (20 Hz frequency). 80
Figure 2-29. Ion spectra for the steady-state OPEN (top) and CLOSED (bottom) states of the shutter gate. 81
Figure 2-30. Indications of blockages in the ES needle that cause disruptions in the detected ion current. 82
Figure 2-31. Circuit schematic for the testing of the Bradbury-Nielsen type ion shutter gate controller (shown in Figs. 2-19 and 2-21). 84
Figure 2-32. Shutter response for 1 kHz square burst shutter inputs. 84

Chapter 3

Figure 3-1. A schematic illustration of the various modules of ES-IMS Device II. 94
Figure 3-2. Schematic diagram of IMS Column II. 99
Figure 3-3(a). Electrical schematic of the segregated (shutter) HV column configuration. 102
Figure 3-3(b). Comparison between the shutter gate responses before (with) and after (without) the removal of the shutter gate capacitors (C_{SG}). 102
Figure 3-4(a-c). The schematic (A), trigger signals (B), and response (C) of the shutter gate controller with R_{BE1} = 1 MΩ, R_g = 1 MΩ. 104
Figure 3-5. Schematic diagram of the picoammeter circuit that is the 2nd detector. 106

Figure 3-6. Photographs of Collector-Detector Assembly II. 107
Figure 3-7. An example of the feedback noise signal observed with the inclusion of the second and third stages of Detector II. 108
Figure 3-8. Schematic diagram of Detector II. 108
Figure 3-9. Photograph of the control box. 110
Figure 3-10. Schematic diagram of ES-IMS Device II. 112
Figure 3-11. Typical "control" spectrum detected by ES-IMS Device II. 114
Figure 3-12. Spectra representing (a) the "ink-jetting" and (b) the "over-spray" modes. 116
Figure 3-13. Ion mobility spectra of 50:50 (v/v) methanol/water. 118
Figure 3-14. Ion mobility spectrum of 50:50 (v/v) methanol/water obtained by Hill and co-workers. 119
Figure 3-15. Plot of the reduced mobility (K_o) values for 50:50 methanol/water for various temperatures, comparing among literature results. 120
Figure 3-16. A comparison of the ion mobility spectra of the solvent only and the methanol only runs. 122
Figure 3-17(a). Time resolved spectra of 50:50 (v/v) methanol/water for varying drift electric fields. 123
Figure 3-17(b). Time resolved spectra of 50:50 (v/v) methanol/water for a drift electric field of ~100 V cm^{-1}. 124
Figure 3-18. A comparison of the ion mobility spectra of cytochrome c (C3131; 1 and 5 mg/mL in 50:50 (v/v) methanol/water) with the solvent only and "control" runs. 127
Figure 3-19. A comparison of the ion mobility spectra of 1 mg/mL cytochrome c with solvent only (inset). 127
Figure 3-20. Time resolved spectra of cytochrome c (C3131; 5 mg/mL in 50:50 (v/v) methanol/water). 129
Figure 3-21. Overlapping spectra of cytochrome c (C3131; 5 mg/mL in 50:50 (v/v) methanol/water; from Fig. 3-20). 130
Figure 3-22. Ion mobility spectra of cytochrome c (C7752; ~3 mg/mL in 50:50 (v/v) methanol/water). 131
Figure 3-23. Calibration curve obtained for the ES-IMS Device II, for the protein cytochrome c (C3131). 135

Chapter 4

Figure 4-1. Photographs of the various components for IMS Column III. 142
Figure 4-2. Photographs of the assembled IMS Column III. 143
Figure 4-3. Photograph of the ion shutter gate and controller for IMS Column III. 144
Figure 4-4. Ion mobility spectrum of PEG-600 obtained by Chen and co-workers. 145
Figure 4-5. Individual circuit schematics of the Detector III stages. 147
Figure 4-6. Photographs of the various components for C-D Assembly III. 148
Figure 4-7. Photographs of the fully-assembled C-D Assembly III. 149
Figure 4-8. Schematic diagrams of the peristaltic pump-driven PDMS ES chip. 151
Figure 4-9. Plot of the velocity of a craft of varying mass over time. 155
Figure 4-10. Schematic diagrams of the torsion pendulum vacuum setup. 158
Figure 4-11. Schematic diagrams of the battery array within the control tube of the torsion pendulum setup. 161
Figure 4-12. (Top view) Schematic diagram of the control tube. 162
Figure 4-13. Schematic diagram of the Spindt field emitter array (FEA). 163

Appendices

Figure A2-1. Calculation of the estimated capacitance of the column grids. 168
Figure A2-2. Simplified circuit diagram of the Keithley high speed picoammeter. 170
Figure A2-3. Simplified circuit diagram of the modified high speed picoammeter. 172
Figure A2-4. (Top) Magnitude and (bottom) phase response of the modified high speed picoammeter for the case of noise pick-up. 173

Figure A3-1. Photographs of the ES-IMS Device II. 174
Figure A3-2. Schematic diagram showing the components for ES-IMS Device II. 175
Figure A3-3. Microboard component schematic. 176
Figure A3-4. Schematic of the high voltage (HV) input/output connections. 177
Figure A3-5. More photographs of the control box for the ES-IMS Device II (in its various stages of disassembly/reassembly). 181
Figure A3-6. Response with (a) and without (b, inset) all sixty-one 100 nF (50 V) capacitors in place for a system without the segregated (seg) array. 193
Figure A3-7. Response of the system with the segregated array with all sixty-one 100 nF (50 V) capacitors in place (a) compared with the same system with a few missing capacitors (b, inset). 194
Figure A3-8. Test conditions for obtaining the responses in Figs. A3-6, A3-7. 194
Figure A3-9(a). (A) Experimental setup for simulating the ripple effect. 195
Figure A3-9(b-d). (Simulated) Ripple signals detected by the antenna-like collector for varying distances and voltages. 196
Figure A3-10. Ripple signals detected by the antenna-like collector for varying distances with a 20 V_{pp} square-wave pulse/burst. 197
Figure A3-11. (a) Averaged and (b) un-averaged control signals obtained for a drift electric field of ~310 V cm^{-1}. 198
Figure A3-12. (a) Averaged and (b) un-averaged control signals obtained for varying drift electric fields. 198
Figure A3-13. ES-IMS spectra of the un-averaged control or zero-signal containing the pulsating effect. 199

List of Nomenclature

AC, ac, DC, dc	alternating current, direct current
ADC, DAC	analog-to-digital converter, digital-to-analog converter
AG, FG, SG	aperture grid, focus grid, (ion) shutter gate (refers to IMS)
B-N	Bradbury-Nielsen (type ion shutter gate)
BNC, RCA, RS-232	refer to wire connectors or interfaces (plug or jack)
BR, BW	buffer reservoir or waste well (of the microfluidic chip)
BSA	bovine serum albumin, a protein (MW ~ 66 kDa)
C-D	collector-detector (assembly)
CAD	collisionally-activated dissociation; computer aided design
CE	capillary electrophoresis
CE-ES	capillary electrophoresis – electrospray ionization
CI	chemical ionization
CID, CAD	collisionally-induced/activated dissociation
Cytochrome c, Cyt-c	a protein found in plants and animals (MW ~ 12.3 kDa)
D	diameter
DIP	dual in-line package (refers to electronics)
Difet	dielectrically-isolated field effect transistor
DMM	digital multimeter
DNA	deoxyribonucleic acid
Dp	Depth/Deep
D-Sub	(9-pin) D-Sub connector (used with RS-232)
dd H_2O	de-ionized and distilled water.
ECE	Department of Electrical and Computer Engineering, University of Alberta
EI	electron ionization
EM, IR, UV	electromagnetic, infra-red, ultra-violet (radiation or spectrum)
EMCO	EMCO C60 6 kV power supplies (EMCO High Voltage Corporation, Sutter Creek, CA)
EOF	electro-osmotic flow

EP	electrophoresis
ES(I)	electrospray (ionization)
ES-IMS (-MS)	electrospray – ion mobility spectrometry (– mass spectrometry)
ESIS	electrospray ion source / electrospray ionization source
ES-MS, ESMS	electrospray – mass spectrometry
ESD	electrostatic discharge
FG	focus grid
FAB	fast-atom bombardment
FEA	field emitter array (also the Spindt cathode; refers to ion thrusters)
FR-4	insulator layer (material) of the PCB
FT(MS)	Fourier transform (mass spectrometry)
FWHM	Full Width at Half Maximum (refers to spectral peak width)
GND	ground (potential)
GPE	gas phase electrophoresis (also known as IMS)
g-μchip, p-μchip	glass microfluidic chip (ESIS), plastic microfluidic chip (ESIS)
H	height
HF, LF	high frequency (e.g., kHz), low frequency (low Hz)
HV	high voltage
ICP	inductively coupled plasma
ID, i.d.	inner diameter
IEF, IEF-ES	isoelectric focusing, isoelectric focusing – electrospray ionization
IMS	ion mobility spectrometry
ITMS	ion trap mass spectrometry
JFET	junction field effect transistor
L	length
LCD	liquid crystal display (screen/interface)
LED	light emitting diode
LED-Hi, *LED-Low*	light emitting diode high (input for *OK1*), low (input for *OK2*)
LIF	laser-induced fluorescence (spectroscopy)
LOD	limit of detection (see LOD in *Variables and Constants*)
m/z	mass-to-charge ratio

MACI	Multimedia Advanced Computational Infrastructure Research Group
MALDI	matrix-assisted laser desorption ionization
MDL	minimum detectable levels (see LOD)
MS	mass spectrometry
MS/MS, MS^n	tandem mass spectrometry (to the n^{th} degree)
MW	molecular weight [measured in Daltons (Da) = g/mol]
μTK	microfluidic tool kit (Micralyne Inc., Edmonton, AB, Canada)
^{63}Ni	radioactive nickel (ionization source)
^{63}Ni-IMS	radioactive nickel – based ion mobility spectrometry/spectrometer
nano-ES	nanospray or nano-electrospray (refers to nL/min flow rates)
NiMH	nickel metal hydride (refers to rechargeable batteries)
NURBS	non-uniform b-splines (related to computer aided design)
OD, o.d.	outer diameter
OPEN, CLOSED	OPEN or CLOSED state of the SG (synonymous with ON / OFF)
op-amp	operational amplifier
OK1, OK2	high voltage phototransistor optocoupler 1,2 of the SG controller
osc.	oscilloscope; TDS 30320 (Tektronix, Inc., Beaverton, OR).
P1500	proprietary polyester compound (related to p-μchip)
PC	personal computer
PCB	printed circuit board
PCR	polymerase chain reaction (genetic amplification technique)
PDMS	polydimethylsiloxane, an elastomer
PEEK	polyetheretherketone, a polymer
PEG600	polyethylene glycol, an oligomer (MW ~ 600 Da)
PET	polyethylene terephthalate
PIC	PIC microprocessor (Microchip Technology Inc., Chandler, AZ)
Pico I,II,III,IV	refers to detector circuits (see *Chapter 4* for comparisons/details)
PMMA	polymethylmethacrylate (also Plexiglas), an acrylic or plastic
PMT	photomultiplier tube
POP4, POP6	Performance Optimized Polymers (Perkin-Elmer, Inc., Wellesley, MA)

ppb, ppm, pp_	parts per billion, parts per million, parts per _
RAM	random access memory (refers to temporary memory chips)
RC	resistor-capacitor (generally refers to the transient effect)
RF, rf	radio frequency
.STL	stereolithographic file format (related to computer aided design)
SG	(ion) shutter gate
SM-1,2,3	electrospray modes (1 = "pulsating," 2 = "stable," 3 = "overspray")
SNIS	solid needle ion(ization) source (refers to an ion thruster)
SR, SW	sample reservoir or waste well (of the microfluidic chip)
SS	stainless steel
S/N	signal-to-noise ratio
TAMRA	tetramethylrhodamine, a dye
Th	thickness
TIC, TIE	total ion current, total ion electropherogram
TNT	trinitrotoluene, an explosive
TOF(MS)	time-of-flight (mass spectrometry)
Triton X-100	a non-ionic protein solvent
tip	tip of ESIS or tip of Taylor cone
USB	univeral serial bus (connection used for data transfer)
V/A	current to voltage (gain)
V/V	voltage to voltage (gain)
v/v	(solvent) volume ratio
V_p, V_{pp}	peak voltage, peak-to-peak voltage
Vectorbord®	perforated electronics boards (Vector Electronics & Technologies Inc., North Hollywood, CA)
W	width
α, β	alpha-radiation, beta-radiation

Variables and Constants

A	area
A_{PCB}	surface area of the metal film layer of each PCB square
A_{wires}	surface area of the (rectangular) "wires" of each PCB grid

C	capacitance (of/between)
C_{Column}	capacitance of the (IMS) column
C_F, C_1	feedback/shunting capacitance, additional feedback capacitance
C_{FR-4}	capacitance between PCB pieces
C_{IN}	input capacitance
C_{SG},	shutter gate capacitors connected from the positive/negative reference points to GND
C_{wires}	capacitance between grid/shutter gate wires
conc	concentration (of sample)
d	distance or thickness [refer to *Notation* below]
d_{ES}	(point-to-plane) distance of the ESIS
d_{FR-4}	thickness of the FR-4 layer of the PCB
$d_{nozzle-apex}$	distance between the nozzle and apex (refers to a Taylor cone)
d_{wires}	distance between two grid/shutter gate wires
E	electric field
E_d	drift electric field
E_{ES}	electric field at the tip of an ESIS
G	gain
h	Planck constant, 6.63×10^{-34} J s
I, i	current / intensity
I_{array}	(resistor) array current
I_{ion}, I_p, I_{dom_peak}	ion current, peak intensity, intensity of dominant peak (see LOD)
I_{IN}	input current
K	(ion) mobility
K_o	reduced (ion) mobility
k_B	Boltzmann constant, 1.38×10^{-23} J K^{-1}
k_I	rate constant for emission of ions from droplets
L	length
L_d	length of drift
LOD	limit of detection
LOD	concentration (or sample) limit of detection (in g/mL or pp_)
sLOD	signal limit of detection (in pA)
N, n	number (of)
N_R	(specifically) number of resistors between the positive and negative reference points of the SG controller (see also, R_g)
N_{Res}	number of column resistors
n	number of data points (related to standard deviation calculation)
P	pressure
P_d	pressure in the drift region/tube

Q	(liquid) flow rate (in the ESIS)
Q_E, Q_S	electric field quality, shielding quality (in a drift tube or column)
q	ion (droplet) charge
R	resistance
R_{BE}, R_{BE1}	base-to-emitter resistor (of optocoupler 1)
R_d, R_g, R_D	resistance across the desolvation region, the gate reference points, or the (remainder of the) drift region
R_{Div1}, R_{Div2}	voltage divider resistors $[(R_{Div2} \times V) / (R_{Div1} + R_{Div2})]$
R_{eff}, R_{EFF}	effective resistance
R_F, R_1	feedback resistance, additional feedback resistance
R_{IN}	input resistance
R_{Min}	minimum (array/column) resistance
R^2	R-squared (statistical correlation) value of a linear regression
R_p, R_{pp}	Resolution (or Resolving Power) of single or double peaks
r	radius (e.g., ion droplet radius)
r_{C1}, r_{C2}	principal radii of curvature of a liquid cone
r_{ES}	radius of the tip of the ESIS
T	temperature
T_d	temperature in the drift region/tube
t	time
t_d, $t_{d1,2}$	time of drift (of an ion), drift times of peaks 1,2
V	voltage
V_{cc}, V_p, V_s, V_n	test voltage (same point as V_{FG}), voltage at the positive, shutter, and negative points of the SG controller
V_{Column}, V_{Col}	column voltage (voltage output of corresponding EMCO)
V_d	drift voltage or voltage of/across the drift region
V_{ES}	(point-to-plane) voltage of the ESIS
$V_{focus\ grid}$, V_{FG}	voltage at the focus grid of the IMS column
V_{gate}, V_g	voltage across the SG reference resistors (R_g)
V_{IN}, V_o, $V_{o\ mean}$	input voltage, output voltage, output mean voltage
v	velocity
v_d	drift velocity (of an ion)
$w_{½}$	temporal width (FWHM, Full Width at Half Maximum) of a single peak of a spectrum
$w_{1,2}$	(base-line) temporal widths of peaks 1,2
Z, $Z(s)$	complex impedance
ΔG	energy of activation

ε_o	permittivity of free space, 8.85×10^{-12} C V^{-1} m^{-1}
γ	surface tension
$\theta_{½}$	half angle (of the Taylor cone)
κ	dielectric constant
κ_{FR-4}	dielectric constant of the FR-4 layer of the PCB, ~ 4.75
σ	standard deviation
τ	time constant (defined as R x C)
$\left\lvert\frac{V_o}{V_{IN}}\right\rvert, \phi$	magnitude, phase of the ratio $\frac{V_o}{V_{IN}}$

Chemistry Symbols

(aq), (g), (s)	aqueous, gas(eous), solid
Am	americium
Ar	argon (gas)
Cl, Cl^-	chlorine, chlorine ion
CO_2	carbon dioxide (gas)
e^-	electron
Fe, Fe^{2+}	iron, iron ion
He	helium (gas)
H_2O, H_3O^+, OH^-	water, protonated water (ion), hydroxide ion
HNO_3, Nitric	nitric acid
M, M^{2+}	metal, metal ion
MeOH, CH_3OH	methanol (liquid, solvent)
N_2	nitrogen (gas)
Na, Na^+	sodium, sodium ion
NaCl	sodium chloride (commonly, salt)
NH_4^+	ammonium ion
O_2	oxygen (gas)
SF_6	sulphur hexafluoride (gas)
Zn, Zn^{2+}	zinc, zinc ion

Notations

A_	[subscript] – characteristic of an object (symbolized by "_"); example, area of an object; also, capacitance ("C_"), electric field ("E_"), current ("I_"), length ("L_"), mass ("m_"), number ("N_"), radius ("r_"), resistance ("R_"), voltage ("V_"), velocity ("v_"). This notation is not to be confused with the established nomenclature (such as in the literature or the conventions of a particular field of study) that are noted in the above lists.
d_ , d_-_	[subscript, special case] – "d_" refers to the thickness of an object; "d_-_" refers to the distance between the first point to the second; example, "d_{FG}" refers to the thickness of the focus grid, while "d_{tip-FG}" refers to the distance between the tip (of the ESIS or of the Taylor cone) and the focus grid.
-	[format] – "-" between two techniques/objects links them in series. Example, ES-IMS-MS describes an electrospray source interfaced to an ion mobility spectrometer that is in turn interfaced to a mass spectrometer.
/	[format] – "/" acts as an "OR" function. Example, "collisionally-induced/activated dissociation" can refer to either "collisionally-induced dissociation" or "collisionally-activated dissociation"; note that these two techniques are synonymous.
( ), [ ], { }	[format] – additional notes or information (or acronyms). Compounded brackets are given in the following order: "{ [(…)] }".
italics	[format] – italicized words represent references to a chapter (in general) or a section (in particular). The format for Tables and Figures (or Figs.) are reversed; that is, the caption headings for tables and figures are italicized while the references to them in the paragraphs are non-italicized. References to Equations (or Eqns.) are also non-italicized. Italicized words can also refer to components or connections (eg., "*OK1*"), please see the above list.
Appendices	[format] – The tables, figures, and equations found in the appendices are labeled with an "A" prior to normal labeling. Example, the second equation, third table, and first figure found in the appendix of Chapter 3 would be labeled "(A3.2)", "*Table A3-3*", and "*Figure A3-1*", respectively.
Citations	[format] – Citations are superscripted where relevant, typically after punctuation. Citations given before the punctuation refer to only a segment of the sentence.

Chapter 1

Introduction

Page

Table of Contents

1.1. Introduction 2
1.2. Electrospray Ionization 3
1.2.1. Taylor Cone Formation 9
1.2.1.1. Corona Discharge 11
1.2.2. Electrospray Mechanism 12
1.2.2.1. Electrophoretic Charging Mechanism 12
1.2.2.2. Ion Droplet Evolution: Charge Residue Model vs. Ion Desorption Model 13
1.3. Applications in Ion Mobility Spectrometry 16
1.3.1. Comparisons with Electrophoresis and Electro-osmotic flow 16
1.3.2. History of IMS 18
1.3.3. Types of Ion Sources for IMS 21
1.3.4. Types of Ion Mobility Spectrometry Drift Columns 22
1.3.5. Radioactive ^{63}Ni Ionization – Ion Mobility Spectrometry 24
1.3.6. Electrospray Ionization – Ion Mobility Spectrometry 26
1.4. Applications in Mass Spectrometry 30
1.5. Outline of this thesis 31
1.6. References 32

1.1. Introduction

In this work, we have developed a system to produce gas-phase ions from a liquid sample that we separate in air so that time-of-flight information about the ions (i.e., their relative charge, mass, and size) can be obtained. This involved interfacing an electrospray (ES) ion source (which emits ions from a liquid reservoir) with an in-house-built ion mobility spectrometer (IMS), which analyzes the ion drift in air. The eventual goal is to interface a microchip-based ES with a miniaturized IMS. This would couple the power of the microfluidic chip device (e.g., the highly parallel implementation, on-chip sample pre-separation, on-chip PCR, and on-chip protein digestion) with our compact, portable, and highly modular IMS.

For the analysis of ions, ES is often interfaced with one of the following ion separation/detection techniques: (1) mass spectrometry (MS) [1-19] or (2) ion mobility spectrometry (IMS) [20-25]. The former technique (MS) allows for the separation of ions in vacuum with respect to their mass-to-charge (m/z) ratios, while the latter technique with respect to their charge, mass, and cross-sectional area (or size) in air. In fact, due to its robustness, ES(I) can be interfaced with both IMS and MS in tandem, whereby an ES-IMS-MS [26-36] setup would first monitor the mobility of the ion(s) in atmospheric pressure then analyze the charge-to-mass characteristics of the same ion(s) in a vacuum.

There are various types of mass spectrometers, such as the tandem MS (MS/MS or MS^n),[11,12,37,38] the time-of-flight MS (TOFMS),[18,27,30,35,37-42] the quadrupole MS,[18,37,38,42] the ion trap MS (ITMS),[30-34,37,38,42,43] and the Fourier transform MS (FTMS) [37,38]. These MS types will be described further in *Section 1.4*, however, they represent bulky, complex systems that are not portable (portability is the goal of this project).

For ion mobility spectrometers, there are several types of ionization sources that can be implemented, besides the ESI source. The most common type is the radioactive (^{63}Ni) ionization source, since the first modern systems were of this type. A third source type is matrix assisted laser desorption ionization (MALDI), which is more common with MS. These and other ionization source types will be described more in *Section 1.3*. The applications for ES-IMS actually overlap with that for the more established ES-MS, where highly sensitive analysis of minute amounts of proteins,[22,30,44-46]

peptides,[26,29,44,47,48] drugs,[49-53] and explosives [54,55] can be made, perhaps even with space applications [56,57] in mind.

Currently, the only compact, hand-held, field portable IMS are based on the gas-phase ion source types (i.e., ^{63}Ni [58,59] and pulsed corona discharge ionization [60]), although various groups [57,61] (including our own) are developing a field portable ES-based (liquid phase) system, which would allow for the study of most biological materials (e.g., proteins, peptides, amino acids, DNA, etc.) that would be unsuitable for ^{63}Ni or the corona discharge ionization methods. These field portable ES-based systems [57,61] incorporate custom-made ES sources. The compact, microfluidic ES chip-based IMS (mentioned above) would represent a field portable system suitable for proteomic as well as genomic research.

As an overview, this introductory chapter will detail the concepts, the history, and the applications for (1) electrospray ionization (ES) [*Section 1.2*], (2) ion mobility spectrometry (IMS) [*Section 1.3*], and (3) mass spectrometry (MS) [*Section 1.4*].

1.2. Electrospray Ionization

As mentioned above, electrospray ionization is a method whereby a liquid phase substance (such as a liquid metal or a polar molecular mixture) is ionized. The main use of this property has been, and still is, to aid in the nebulization of solvents (i.e., the conversion from liquid sample to gas-phase ions) so that one can perform mass spectrometry (MS) or ion mobility spectrometry (IMS) analyses on the molecules or atoms within the solvents. This could lead (and to a certain extent has led) to better drug, explosives, or hazardous materials detection in such locations as airports, hospitals, battlefields, etc.

The study of electrically charged liquid jets began with Lord Rayleigh and others in the 1800s, when they applied mathematics to the calculation of jet properties.[62] Since then, the study of the spray modes for ES have been extensively researched, particularly in the past century.[63-68]

The following sections highlight some of the theory behind the formation of the Taylor cone (*Section 1.2.1.*), including descriptions of what it is, and some of the mechanisms that have been proposed to explain how electrospray works (*Section 1.2.2.*).

To achieve electrospray, there are various types of ES tips that can be utilized. These are most often used as capillary electrophoresis – electrospray (CE-ES) interfaces, which can take various forms: (a) a sheath flow configuration,[5,69,70] (b) a sheathless configuration,[1,2,5,70] (c) a liquid-junction configuration,[1,5,70] and (d) a direct electrode configuration [1,5].

In a sheath flow approach [shown in Fig. 1-1(a)], a fused silica CE tube that is used as the ES source is surrounded by a metal tube that is used to deliver a sheath liquid – such as methanol, acetonitrile, ethanol, isopropanol, or 2-methoxyethanol, whose properties are chosen to provide electrospray characteristics that perhaps cannot be controlled in conventional CE buffer solutions.[5,69] This rather common approach can be implemented with a tapered or pulled CE tip so as to obtain a high local electric field strength; this tip arrangement also serves to allow for the mixing of the sample and the sheath solutions, as well as to offer stability of the spray itself. To further assist in spray formation, a third tube is often included that would deliver a high velocity concentric gas flow to aid in the nebulization of the liquid and perhaps also to prevent corona discharge by sweeping or scavenging the region of/for stray electrons. Small droplets – created by the pneumatic evaporation of the liquid droplets by this sheath gas – allow for a low surface tension and low conductivity buffer/solvent liquid to be used (where previously, one was limited to high surface tension and high conductivity sheath liquids due to the less efficient spray).[5]

The major advantage of this technique, however, is that standard CE capillaries can be used without much modification, if at all, as the charging of the liquid is achieved by electrically connecting via the sheath liquid itself the metal sheath tube with the sample in the CE-ES tip.[5,69] A major disadvantage of the sheath flow technique is an increase in the background noise of the total ion electropherogram (TIE) that can result due to the addition of volatile salts, acids or bases in the sheath liquid. Because an additional liquid (i.e., the sheath liquid) is added to the spray liquid (i.e., the initial CE buffer), irreproducible mixing of the vastly different buffers can occur, which in the

worst case can change the mobility of the sample, thus seriously affecting time-of-flight measurements.[5] In fact, dilution of the sample by the sheath liquid has been observed.[70] Operating conditions of the CE-ES technique in terms of relative dimensions of the CE tube, the sheath liquid and the sheath gas tubes have also been studied for optimization.[5]

In a sheathless approach [shown in Fig. 1-1(b)], the ES tip is similar to that in the sheath flow except that (1) the sheath liquid tube is not implemented and (2) the CE tip (usually carefully sharpened or pulled [5,70]) is coated with a metal film (such as gold [5,70] or conducting silver epoxy [1]) that one would set to a high voltage potential. Because deterioration of the metal (typically gold) layer of the tip can occur,[1,70] disposable, interchangeable metal-coated CE tips can be made to interface with the CE system.[5] To help prevent corona discharge due to the higher electric field strengths that are typical of such an approach, a sheath gas (e.g., SF_6) is often used that (unlike the sheath flow approach) would take no part in the nebulization process. The advantage of this approach is that dilution of the sample does not occur, therefore a higher sensitivity than that of the sheath approach can be achieved. The disadvantages include the limitation of studies to low surface tension and low conductivity CE buffers – though this can be countered with the use of a sharp tip to increase the local electric field strength and with the addition of certain modifiers (e.g., volatile salts, acids and bases, or organic solvents like methanol).[5] Another disadvantage is that this method requires the use of specialized CE capillaries, which sometimes requires the application of the metal film on the tips of the capillaries (which represents the major time-consuming aspect of this technique [1]).[5]

In a liquid-junction approach, a low-dead-volume, metal block interface is used to connect the CE tube with the ES tip, with the high voltage being applied to the liquid in this junction via the metal interface itself.[1,5,70] An alternative to a simple metal block, low-dead-volume junction is a tee junction [shown in Fig.1-1(c)] that also serves to introduce a "make-up" liquid.[5] The advantages of a high velocity gas flow in the sheath flow approach can be duplicated here with the liquid junction.[5] One possible disadvantage of this approach is that hydrogen bubbles may form (via electrolysis) in the liquid junction that would disrupt the electrospray, and would require purging with a buffer solution.[1]

In a direct electrode approach [shown in Fig. 1-1(d)], a metal wire (either gold [5] or palladium [1]) is inserted into the blunt/unsharpened tip of the CE tube. Because in practice this approach resembles the sheathless technique, it offers the same advantages without the need for the metal film layer. However, the time saved with the (re)application of the metal film may be lost with the time and care required to position the wire such as to avoid corona discharge.[5] Herring and Qin (1999) [1] note a few other disadvantages with the direct electrode, namely (1) the turbulence caused by the wire would result in a drop in resolution and (2) the wire electrode (palladium, in their case) may be a source of multiple oxidations of peptide samples.

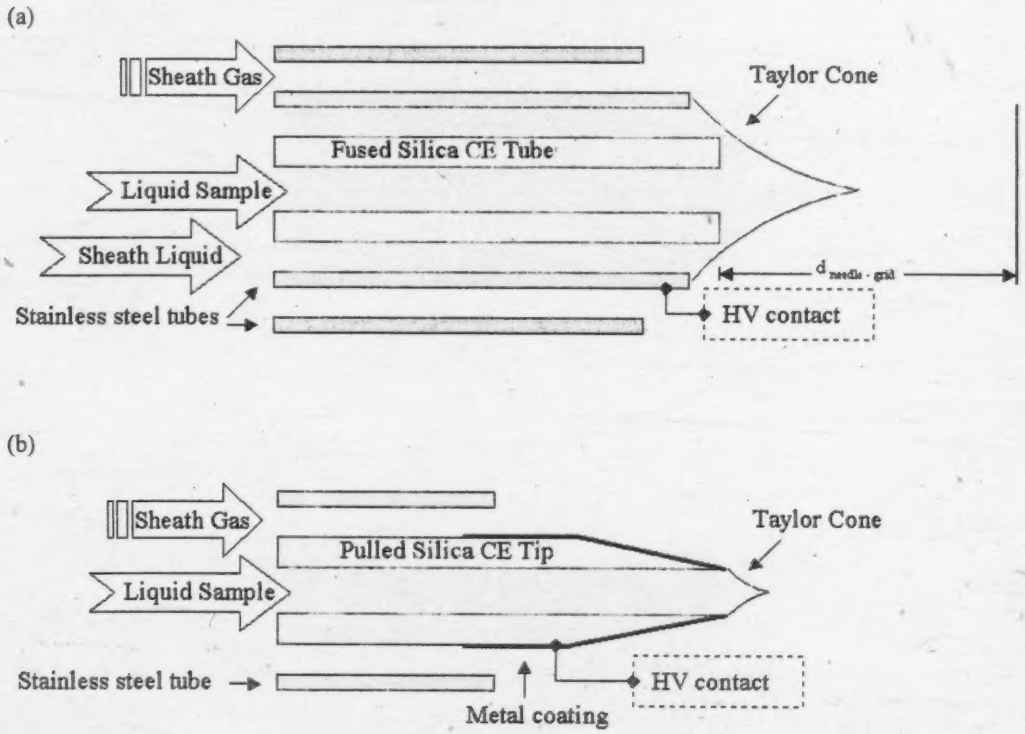

Figure 1-1(a, b). Various CE-ES interfaces or ES tips. Depicted are (a) the sheath flow and (b) the sheathless interfaces. Modified from Ref. 5.

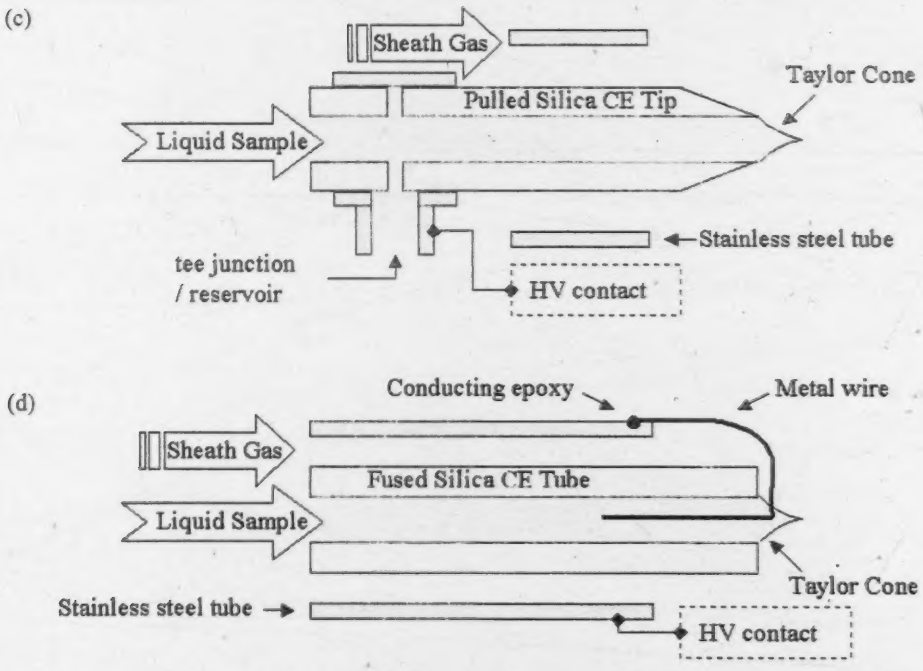

Figure 1-1(c, d). Various CE-ES interfaces or ES tips. Depicted are (c) the liquid-junction and (d) the direct electrode interfaces. Modified from Ref. 5.

For the case of CE-ES sources, it is sometimes important to know or even control the electric field at the tip, to optimize the spray without the occurrence of a corona discharge, for example. A commonly used relation for approximating this local electric field is given by Eqn. (1.1),[3,4,69,71] where E_{ES}, V_{ES}, r_{ES}, d_{ES} are the electric field at the CE tip, the voltage of the CE tip (relative to the cathode grid or plane, also known as the counter electrode), the (outer) radius of the CE tube, and the distance between the CE tip and the cathode grid/plane, respectively. As an example, Tang and Kebarle (1991) [4] listed values of 1.1×10^7 V m^{-1} (E_{ES}), 5 kV (V_{ES}), 127 μm (r_{ES}), and 4 cm (d_{ES}), respectively. (However, one must be cautious in the use of the resultant value because this equation was meant for vacuum at the tip; that is, this equation does not take into account any effects with the atmospheric pressure gases at the region near the CE tip, not to mention any sheath gas that may be used.) A plot of this electric field with respect to the point-to-plane distance [i.e., the needle to focus grid distance, see Fig. 1-1(a)] and the CE outer radius for a 5 kV potential is shown in Fig. 1-2. (Note that a change in the

voltages would result in a linear shift of the electric field strength, without changing the shape of the plot.)

$$E_{ES} = \frac{2\,V_{ES}}{r_{ES}\,\ln\left(\frac{4\,d_{ES}}{r_{ES}}\right)} \qquad (1.1)$$

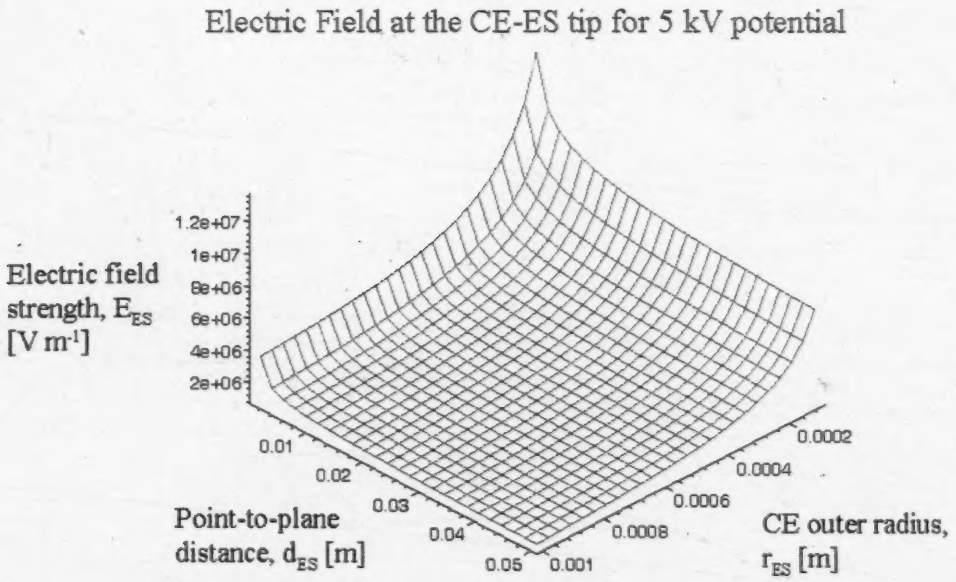

Figure 1-2. 3D plot of Equation (1.1) for a potential of 5 kV.

Besides the CE-ES systems described above, there exist microfluidic chip-based ES sources, an example of which is an isoelectric focusing (IEF) – ES tip developed by Wen *et al.*,[10] which is a microfabricated device constructed by sandwiching a piece of polyethylene terephthalate (PET) polymer film, with a heat-activated adhesive (25 μm thick silicone) on one-side, between two pieces of 100 (L) x 30 (W) x 6 mm (H) polycarbonate. Besides this IEF–ES based system, the literature describes various different types of microfluidic chip-based ES sources - some interfaced to a transfer capillary,[11,12,19,43,72] others affixed with customized tips,[39,72,73] while yet others with built-in nozzles [15,74] whose edge is sometimes coated with a hydrophobic reagent [13,14] – almost all of which are commonly interfaced with mass spectrometers. A more recent report (2002) by Chiou *et al.*[75] describes a PDMS-ES chip used for MS applications, which was

constructed by taking a tube with an inserted, thin metal wire and inserting the end of the metal wire to a silica capillary. A platinum wire (to be the electrode) was then glued to metal wire via silver conductive glue. This assembly was placed in a PMMA (poly-methyl-methacrylate) mold into which is injected the PDMS (poly-dimethyl-siloxane) that was cured for 15 minutes at 120 °C. Mechanically pulling out the metal wire exposed the microchannel, with the tube acting as the sample well. To prepare the ES tip, the end of the silica capillary was pulled then painted with silver conductive glue.[75] This technique represents a very easy means of producing a cheap, disposable ES microchip device. With a microfluidic ES chip, one could pre-separate the sample, implement protein digestion, or utilize polymerase chain reaction (PCR) on DNA samples on-chip prior to electrospray of the ions in the sample, whose drift in air can then be analyzed using an ion mobility spectrometer or a mass spectrometer (in vacuum).

1.2.1. Taylor Cone Formation

When a high electric field is applied to the tip of the electrospray (ES) source, the liquid in the source will form a cone – called a Taylor cone after Sir Geoffrey Ingram Taylor who first studied such charged liquids or electrically driven jets.[64] This Taylor cone is stable insofar as the force of attraction of the ions toward the cathode (i.e., grid or collector plate) perfectly balances the force of cohesion of the liquid at the surface of the cone (i.e., where the minimization of surface energies of the liquid is maintained). The process of nebulization occurs when the ions in the liquid escape the apex of this extended cone of liquid, partly because the force of attraction of these ions (located at the tip) toward the cathode overwhelms the surface forces that maintain the shape of the cone; additionally, repulsion of the positive ions at the tip may play a role in the ion expulsion. An alternative mechanism describes the breakdown of the tip of the Taylor cone due to the convergence of the electric field lines (i.e., via field ionization), however, this has been dismissed as an unlikely occurrence by at least one prominent group, who note that the separation of the charges in solution would suppress the external electric field, which would eliminate any field ionization effects.[3]

As for the actual mechanism behind the ionization and ion droplet evolution inherent during ES, there seem to be some debate among the researchers in this field. The differing points of view will be addressed in *Section 1.2.2* below. For now, the focus shall be to look at the mathematics that describe the formation of the Taylor cone, and also to note the experimental observations of the Taylor cone reported by various workers.

When one electrically charges a liquid in a microchannel ending in a nozzle – that is, in a capillary tube covered by a metal sheath [20,22,23,69,76] or in the main channel of a cut microfluidic chip – a (mathematically infinite) cone of liquid with a theoretical half-angle of 49.3° will form from the nozzle when the force (or stress) due to the surface tension of a liquid is balanced by the electrostatic force (or stress) due to the high voltage applied to the liquid.[62,77] This balance of forces (or equivalently pressures) can be represented by the following equation [62,77]:

$$\gamma\left(\frac{1}{r_{C1}}+\frac{1}{r_{C2}}\right)=\frac{1}{2}\varepsilon_o E^2 \qquad (1.2)$$

where γ is the surface tension of the liquid, r_{C1} and r_{C2} are the principal radii of curvature of the liquid cone, ε_o is the permittivity of free space, and E is the applied electric field. (The curved surfaces of the Taylor cone are depicted in Fig. 1-1 for each of the ES tips.) For a cone,[77] r_{C1} and r_{C2} can be characterized as follows, where $d_{nozzle\text{-}apex}$ represents the distance from the nozzle to the cone apex and $\theta_{½}$ the cone half angle in degrees:

$$r_{C1}=\infty\,;\, r_{C2}=\frac{/\cot\theta_{½}}{d_{nozzle\text{-}apex}} \qquad (1.3)$$

Experimental observations by Hayati and coworkers (1987) and de la Mora (1992) prove that the cone half-angles are not always the 49.3° as required by Taylor's models.[76] In fact, according to de la Mora and Loscertales,[76] one would observe a concave-convex surface [64] with a point of inflection on the surface of the cone for a moderately conducting liquid, while a more precise cone shape would be observed for a much more highly conducting liquid. Here, the conductivity (i.e., one of the properties of the liquid) was shown to affect the stability and shape of the Taylor cone. Various groups, including Cloupeau and co-workers as well as Taylor himself, point out that the

different cone shapes correspond to varying spray modes (e.g., the "pulsating" or "spitting" mode, the "stable" mode, etc.).[63-68]

However, it was noted by de la Mora [76] that so long as the cone is stable and the flow rate of the liquid is constant, the expected spray current is in essence independent of the electric field or the geometry of the electrodes. It was found that the spray current would depend more on such liquid properties as the flow rate,[69] the electrical conductivity,[69] the dielectric constant, the density, the viscosity, and the surface tension.[76]

1.2.1.1. Corona Discharge

A corona discharge is a visible electric arc that occurs when the electric field used exceeds the dielectric strength of the medium (e.g., air). In other words, exceeding a certain potential (or voltage) over a certain length or separation distance in air causes the phenomenon of air breakdown. (Note that air has a dielectric strength of ~3 kV/mm.)

Where electrospray ionization (ESI) is characterized by the evaporation and separation of a solvent into ionized liquid droplets, corona ionization is characterized by the ionization of primary ions (from the gas molecules surrounding the needle tip), which may react with any evaporated neutral molecules (from the liquid tip), thus resulting in varying product ions.[20] This reaction with neutral molecules results in different mass (and ion mobility) spectral data, which is usually undesirable. Although corona(spray) ionization is able to provide good sensitivity for a variety of compounds in solution,[22] as well as assisting in the electrospray of certain high surface tension liquids,[78,79] one would generally wish to avoid any sort of corona discharge during ES. This can be accomplished by using a sheath gas (e.g., SF_6), which scavenges the electrospray region of free electrons but is not involved in the electrospray process.[5]

1.2.2. Electrospray Mechanism

Though Electrospray is used quite frequently in research endeavors to study biomolecules, among other materials, the mechanism behind ES operation is incompletely understood. Various researchers have put forth differing mechanisms behind ES. The following sections will highlight the key points of these varying points of view on the workings of ES – mainly centering on the questions of the inherent nature of ion formation and of droplet evolution during ES.

1.2.2.1. Electrophoretic Charging Mechanism

The electrophoretic charging mechanism, also called the ion separation mechanism, was proposed by Kebarle and coworkers [3,4,80,81] – based on MS data involving 10^{-5}-10^{-3} M electrolytes such as NaCl in a methanol solvent – to explain the formation of ions in a (metal) CE capillary prior to ES, where the electrolytes would dissociate in the solvent to produce the positive and negative ions. In this mechanism, the positive and negative ions in solution (e.g., Na^+ and Cl^-) would separate in the presence of an electric field, with the positive being drawn toward the cathode of the ES device (i.e., either a grid or metal plate collector), while the negative (electrons) migrate to the anode (i.e., the metal cathode or metal capillary). The build-up of excess positive charge at the liquid-air interface would promote the formation of a Taylor cone (in the continued presence of the electric field). During steady state conditions, the positive charges would continually be removed by the electrospray of charged droplets, while the electrons would flow through the metal capillary of the ES device toward the source of the high voltage potential. [This group points out that the separation of the charges in solution would suppress the external electric field, thus negating such effects as field ionization (i.e., where electrons are stripped due to electrical breakdown).] At the metal-liquid interface, an electrolytic reaction [3,69,82] would occur, whereby the metallic interface would provide both the positive ions and the electrons. Any negative ions in solution would be converted into neutral molecules plus an electron. These oxidation reactions

can be expressed as follows for the electrospray of aqueous solutions (i.e., analytes dissolved in solvent water).

$$M_{(s)} \rightarrow M^{2+}_{(aq)} + 2e^- \qquad (1.4a)$$

$$4\,OH^-_{(aq)} \rightarrow O_{2(g)} + 2H_2O_{(l)} + 4e^- \qquad (1.4b)$$

It has been found that Zn^{2+} and Fe^{2+} signals were obtained with ESMS with the use of zinc and stainless steel capillaries, respectively.[3,4,80] Also reported was the formation of molecular radical cations (such as from neutral, nonpolar compounds) that result from electrochemical interactions at the liquid-metal interface.[82]

To prove that electrophoretic charging – which is based on interactions in solution of the electrolyte impurities – indeed leads to ES, Kebarle and coworkers [3] used a de-ionized solvent, with their results for distilled methanol showing a decrease in ES current, as well as an increased fluctuation in signal. Noted too was a decreased intensity of observed NH_4^+ and Na^+ impurity ions [3] (that were perhaps attributed to the solvent distillation process?). Also reported was a correlation between the positive/negative ions of the electrolytes in solution with the positive/negative ions detected, with extraneous ions occurring only with the onset of corona discharges.[3] Kebarle *et al.*[3] observed that the solvent and the solution composition would play a dominant role in terms of the onset potential for ES, and as such listed the various onset potentials for various ES solvents (e.g., methanol and water), calculated using Eqn. (1.1) combined with a relation for the onset of ES [83].

A more in-depth discussion of the various spray modes for ES can be found in the literature.[63-68] As for the formation of gas-phase ions that result from ES, these will be discussed in the following section.

1.2.2.2. Ion Droplet Evolution: Charge Residue Model vs. Ion Desorption Model

It has been observed that when one applies a sufficiently high electric field to an ES device, instability occurs at the cone tip, which leads to positively charged, micron-sized (i.e., micron-diameter) liquid filaments from which the droplets are emitted.[3,64,83,84]

According to the model proposed by Dole *et al.*,[9] known as the charge residue model [shown in Fig. 1-3(A)], the liquid filament at some point down-field would break off into a primary droplet that undergoes solvent evaporation to become the positively-charged "parent" droplet, which contains a large number of elementary surface charges.[3,83] When the charge per volume (or charge capacity) of the droplet approaches a certain point (known as the Rayleigh limit [3,9,85]) instability occurs, whereby this "parent" droplet will break down into "offspring" droplets (also positively charged), that would continue the process of evaporation and fission (which can be "even" or "uneven" in terms of the relative size and charge of the daughter droplets) until singly charged ion droplets are produced.[3,4,9,85] The Rayleigh limit is expressed in Eqn. (1.5), where q is the charge of the droplet, ε_o the permittivity free space (or vacuum), γ the surface tension of the droplet, and r the radius of the droplet.

$$q^2 = 64\,\pi^2 \varepsilon_o \gamma\, r^3 \qquad (1.5)$$

At low electric fields, a pulsating mode occurs.[63,65,67] With an increase in electric fields, the liquid filament length shortens, with a multispray phenomenon occurring at the higher fields.[3,84]

The other model, proposed by Iribarne and Thomson (1976) [86] and sometimes known as the ion desorption/evaporation model [shown in Fig. 1-3(B)], holds several similarities to the charge residue model, for example, ion formation results at least in part by evaporation of the droplet. The difference lies with the ion emission (or evaporation), and not fission, that occurs from very small droplets containing multiple elementary charges that are still larger than the Rayleigh limit of instability and also larger than any solid residue in the droplet.[3,86] In other words, instead of an unstable "parent" droplet that undergoes a series of evaporation/fission cycles, this method suggests that gas-phase ions are emitted from an initial small and highly charged ("parent") droplet, whereby evaporation occurs before the droplet approaches the Rayleigh limit (thus by-passing the fission steps).[3,86]

The equation for the rate of ion emission from charged droplets, on which the ion evaporation model is based, is given by Eqn. (1.6) where k_I is the rate constant for ion emission from droplets, k_B the Boltzmann constant, T the droplet temperature, h the Planck constant, and ΔG the transition state energy of activation.[3,86] Here, ΔG would

depend on the number of charges on the droplet (N_e) and the radius of the droplet (r), such that the rate constant (k_I) would increase with the former and decrease with the latter.[3]

$$k_I = \frac{k_B T}{h} \exp\left(\frac{-\Delta G}{k_B T}\right) \qquad (1.6)$$

In summary, there exist two main competing models for the evolution or the formation of an ion droplet that results from ES, followed by solvent evaporation. One, the charge residue model, describes a breakdown at (or near) the Rayleigh limit of "parent" droplets to smaller and smaller "daughter" droplets until ideally a single charge is left on the droplet (essentially a gas-phase ion). The other, the ion evaporation model, describes an evaporation of small ion droplets (that allow for multiple charges) that form from the initial ion ("parent" ion from the charge residue model), thus bypassing the fission process.

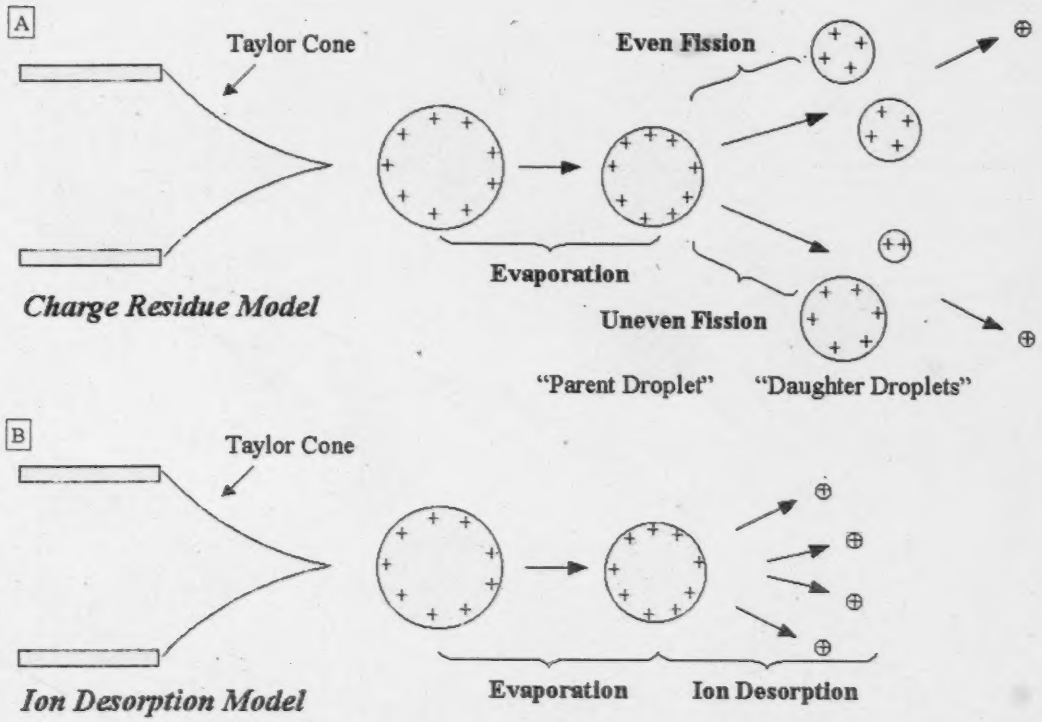

Figure 1-3. Charge Residue Model (A) versus Ion Desorption Model (B).

1.3. Applications in Ion Mobility Spectrometry

Ion mobility spectrometry (IMS), formerly known as plasma chromatography, is sometimes called the poor man's mass spectrometry (MS) due to the fact that mobility experiments in atmosphere eliminate the need for expensive vacuum systems (e.g., chambers, seals, pumps, etc.). The flowchart illustrated in Fig. 1-4 shows the general components of an IMS, where a continuous stream of ions produced at the ion source undergoes solvent evaporation in the desolvation region (for ES-based systems) or ion-molecule interactions in the reaction region (for ^{63}Ni-based systems). A pulse of these ions, created at the shutter gate by gating the continuous stream of ions from the desolvation/reaction region, undergoes ion separation in air in the drift region (according to relative charge, mass, and size), and is subsequently observed at the collector plate, where the signal is first amplified then recorded. The resultant ion mobility spectra can be analyzed to obtain time-of-flight data.

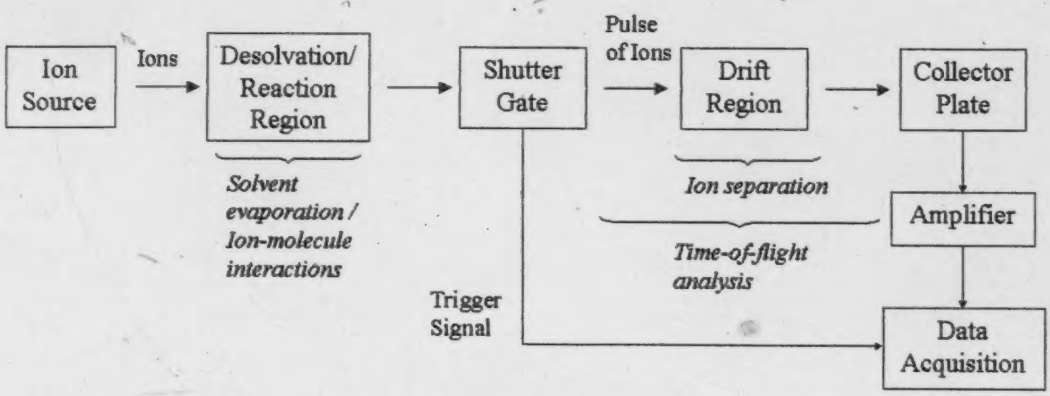

Figure 1-4. Flowchart illustrating the operation of an IMS.

1.3.1. Comparisons with Electrophoresis and Electro-osmotic flow

One can argue also that IMS is a form of electrophoretic (EP) separation in air, or gas phase electrophoresis (GPE) as Collins [87] puts it. In general, when one thinks of electrophoretic separations, one envisions the use of capillary tubes or more recently the

use of etched microfluidic glass chips with microchannels. In such cases, a sieving matrix (e.g., a polyacrylamide) in conjunction with the infusion of a buffer solution would be the medium through which an analyte (ion) would separate due to the influence of an electric field. In the case of both IMS and EP, the ions would separate according to three factors – (1) the charge, (2) the mass, and (3) the cross-sectional area (or size) of the ions – such that the ions with the highest charge, the lowest mass, and the smallest cross sectional area would generally drift the fastest along the direction of the electric field. For the case of MS, separations would be done in vacuum, where the cross-sectional area information of the ions would be lost; in vacuum (as in MS), only the charge and the mass of an ion can be inferred.

Now that the analogy between IMS and EP has been drawn, one can more closely focus on the differences. Firstly, the immediately obvious difference would be the medium through which the ions drift (highlighted above) whether it is air (for IMS) or a liquid (either a buffer solution alone or a buffer solution with a polymer sieving matrix, for EP). Secondly, IMS involves the formation of an electric field using a series of equally spaced metal guard rings that drop in voltage potential via the use of equal resistances connecting these guard rings. [Here the term guard ring is used to refer to the ability of these annuli to prevent widely divergent ions from drifting toward the detector, so that only those ions that drift along/near the center (or axis) of the drift tube are detected.] On the other hand, EP involves the use of two electrodes, one at a higher voltage potential than the other, where the resulting current would flow through the conducting liquid medium to transport the ions (or analytes) from the higher potential electrode to the lower one. Thirdly, because a sieving matrix is used for EP long molecular ions such as long-chain polymers or proteins that cluster together to form structures with cross-sectional areas larger than the interstitial spaces provided by the sieving matrix would be in essence strained or sieved from the smaller molecular ions that pass on toward the attracting electrode. In addition, where EP would have limits in the types of samples that can be analyzed – that is, non-neutral atoms, molecules, or polymers that can be tagged with a fluorophore (i.e., a dye) or that can be stained with dye to allow for light absorption (e.g., using silver stain or coomassie stain) [88] – IMS is more robust as conditions for light detection or light absorbance would not be necessary,

and a sample need not be ionic prior to solvation in a polar molecular solvent, due to the electrolytic reaction [3,69,82] that is thought to occur at the metal-liquid interface of the ES capillary (mentioned in *Section 1.2.2.1*).

A similar process to EP is electro-osmotic flow (EOF), which utilizes the same microfluidic microchannels as EP, only without the sieving matrix (e.g., POP6 or POP4 available from Perkin Elmer). EOF separations only require a buffer solution. However, the microchannels must be prepared with an acid-base protocol prior to experimentation, [89] so as to encourage the formation of an electrical double layer at the silica/solution interface [90]. The solvated positive ions in the outer layer of the double layer will be attracted to the lower potential electrode, thus dragging the solution along.[90] The velocity contribution of EOF may be greater than that of EP, so that the ions would drift along the electric field, regardless of whether they are positive or negative in charge, with the positive ones having the highest velocity and the negative ones the lowest velocity (due to the partial cancellation of the EOF and EP contributions).[90] So in another sense, EOF (without EP) is a better microfluidic analogy to IMS, except that no electrical double layer is needed, and the ions drag with them the neutral solvents that cluster about them.

1.3.2. History of IMS

The study of electrically charged liquid jets had begun in the 1800s, and as early as 1903, Paul Langevin, a French scientist who is known more for his work on piezoelectronics and ultrasonics, had already investigated the fundamentals of IMS – including the "placement of gas-phase ions in a weak electric field and the determination of the velocity of individual ions."[91] In fact, he had apparently already constructed a functional instrument similar to the drift tube of modern ion mobility spectrometers, and had collected elementary measurements, as well as having developed some theory for ion mobility.[91] In 1937, Chapman was noted to have measured the mobility of ions, which had been electrified in the liquid phase, using an Erikson mobility tube to guide the ions in the gas phase.[20] These atmospheric pressure methods in the early 1900s gave way to high vacuum ion analysis, namely mass spectrometry (MS).

The first modern ion mobility spectrometer (introduced as a plasma chromatograph) was actually constructed in 1970 by Franklin W. Karasek (of the University of Waterloo) and Martin J. Cohen (of Franklin GNO Corporation, later PCP, Inc.), who inserted a polished β-emitting radioactive ^{63}Ni source into the first guard ring of the reaction region of their device.[91] A 100 to 200 mL/min flow of carrier gas was used to transport the sample, entering the device from the front of the reaction region, and encountering the radioactive source that would ionize the gas and sample, which then became susceptible to the uniform electric field (of about 200 to 300 V/cm). The ions next encountered a Bradbury-Nielsen type shutter gate (set in the slightly larger drift tube) that allowed a small pulse of ions through into the drift region to produce the time-of-flight data at a collector plate (a Faraday cup). (Please see the next section for descriptions of the Bradbury-Nielsen type shutter gate.) In addition, a counter-flow of purified non-reactive (N_2) drift gas, with a flow rate between 400 and 700 mL/min, was introduced from the end of the drift tube (with a diameter of a few centimeters) and flowed through the axis of the drift tube and out the front end of the shutter gate (which was also where the carrier gas would exit). [Note that the reaction region would empty out into the larger diameter drift tube, with exhaust ports set in the front of drift tube to allow both the carrier and drift gases to exit.] The purpose of the drift gas was to inhibit further ion-molecule reactions in the drift region, that if allowed would produce a difficult-to-interpret spectrum representing a composite between the original ion and the final product ion. The entire drift tube was then sealed in an oven that could be heated to temperatures greater than 200°C.[91] (Please see *Section 1.3.5* for more on the ^{63}Ni-IMS.)

Eiceman [91] describes a "general disenchantment with IMS" by 1975 when users, seeking small, simple alternatives to mass spectrometers, found that the response of IMS to mixtures was confusing and inadequate. Interestingly, the fundamentally attractive principles of IMS – namely, the low detection limits, the reasonable selectivity, and the potential for miniaturization – were sufficient for the military establishments in the United States, the United Kingdom, and Canada to continue the research, especially with their realization that the main failings of IMS were related to the technology or engineering. It was also fortunate that the substances for which the military establishments were interested in detecting – nerve agents, particularly – matched well

with the ionization chemistry.[91] As military field analyzers, these hand-held ion mobility spectrometers proved that a practical, sensitive, selective miniature instrument could indeed be achieved, which led to a general resurgence of this technique.[91] Since the 1970's, IMS has served other, non-military functions, including such analytical applications as a stand-alone vapor monitor, an on-line liquid-stream process sensor, and a gas detector.[22,23,27] Today, commercial (^{63}Ni-based) IMS systems [58,59] can be found in airports, hospitals, and other places requiring quick detection of illicit and/or dangerous materials (e.g., drugs, explosives, etc.).

However, the first group to apply electrospray ionization (ESI) to ion mobility spectrometry (IMS) was Gieniec *et al.*, who in 1972 analyzed organic compounds using a modified plasma chromatograph.[20,22,24] Dole and co-workers followed in 1984 with their IMS system for the detection of electrospray-generated ions. Next came Smith *et al.*,[92] who in the early 1990s reported ion mobility spectra of cytochrome c and lysozyme ions in support of their mass spectrometric research. Then in 1994, Hill and co-workers [22] carried out the first full-scale investigation of IMS detection for electrospray. These researchers reported partially resolved peaks in the ion mobility spectra of cytochrome c (a protein) and Triton X-100 (a non-ionic protein solvent). This was the first documented observation of multiply charged peaks in IMS.[27] Since then, researchers have undertaken the task of developing novel approaches to ESI-IMS and ESI-MS.

In terms of sensitivity (or limits of detection), the ^{63}Ni-based IMS is capable of minimum detectable levels (MDL) of 10's and 100's of picograms for certain samples, detection limits ranging from <1 part per billion (ppb) to several parts per million (ppm), as well as a signal-to-noise (S/N) ratio of 1000 for 10 ng of the explosive 2,4,6-trinitrotoluene (TNT).[91] For ES-based IMS, ppb limits for ethylamphetamine (a drug) [93] and ppm for Terbutryn (a herbicide) [61] have been reported. It should be noted that the ES-based systems for which these limits of detection were reported, although ideal for analyzing biological material, are generally complex, bulky systems, unlike ^{63}Ni-based [58,59] systems. However, radioactive ionization systems are gas-phase devices that are unsuitable for the analyses of biological materials (especially those in solution – that is liquid-based samples).

1.3.3. Types of Ion Sources for IMS

IMS is extremely versatile in that it can be interfaced with a number of different types of ion sources. Already mentioned are the radioactive ionization sources [91,94-101] (most commonly employing ^{63}Ni) and the electrospray ionization sources [20,22,23,26-28,91]. The radioactive source type, which is used to ionize gas samples, has the major advantages that it can easily be miniaturized and that it requires no external power supply; its major disadvantages are that (a) licences and permits are required for handling the radioactive material of appropriate activity (~15 mCi) and that (b) the radioactive material must be prevented from migrating [91] during operating conditions of the IMS device. The ES type, due to its relatively gentle means of ionization, allows for the direct analysis of large and complex molecules in solution. Because it is a liquid phase analysis technique, it can be interfaced with microfluidic (chip) systems, and this makes it ideal for complex drug, biochemical, and proteomic research (as noted previously).

Other ion source types include the photoionization sources [91,102-104] (using photoionizing lamps [103] or lasers [104] or MALDI [40]), the flame ionization sources [91] (employing a hydrogen or hydrocarbon flame), and the corona(spray) discharge ionization [71,91] (which uses the electric field breakdown of air to ionize the air surrounding a liquid-sample-filled needle to promote ion-molecule reactions). The photoionization method, which operates in the ultraviolet (UV) portion of the electromagnetic (EM) spectrum, has the major advantage that the source can be chosen with an appropriate wavelength to selectively ionize the sample, which simplifies data analysis; its disadvantages include the complexity in the construction of the IMS device, the need for an external power supply, and its proneness to malfunctions.[91] The flame ionization method, usually implemented with a pulsed flame using a special technique so as to conserve fuel, is capable of increasing sensitivity to certain types of compounds such as hydrides and fluorides. Its major advantage is that higher ion currents may be obtained; its major disadvantages are the addition to the complexity of the device and the loss in the specificity of the detector.[91] This flame ionization method would also be unsuitable for studying biological material (at least without destroying the sample of interest). The corona(spray) discharge ionization method, which typically operates at

higher voltages than ES, allows for the direct analysis of the liquid sample. The disadvantage of this system is that it typically leads to undesired contaminants (i.e., ionized gases, etc.)

1.3.4. Types of Ion Mobility Spectrometry Drift Columns

There are two main designs of IMS drift columns: (1) the stacked ring type [20-22,25,94,95,100,101,105] and (2) the ceramic in-laid tube type [94-96,105]. The first, as the name suggests, consists of a number of guard rings – made of aluminum [101] or stainless steel [20-22,25,105] – that are stacked one on top of the other, separated by insulating materials – such as Teflon,[21,22,101] PEEK,[101] Macor,[25,105] glass,[20] or sapphire balls [94]. These equally-spaced guard/drift rings are then connected together via high impedance resistors, typically 1 MΩ [22,26,98] or 10 MΩ [25]. For the stacked ring type, Spangler [94] describes a spring-loaded compression clamp to maintain the mechanical integrity of the column. The other type consists of a coating of a resistive ink (DuPont composition 9519 [94,95]) on the inner surface of the ceramic material (macor or alumina [94,95]) of the drift tube.[94] In both cases, high voltage is applied to one end of the stack or tube, while a lower potential (ground potential, for instance) at the other end to form a uniform electric field that will guide the ions toward an ion detector, typically a Faraday cup/plate. The IMS may also be interfaced with an MS, where the m/z data can be obtained for the drift ions.

For obtaining ion mobility information, an ion shutter gate is employed, generally either of the Bradbury-Nielsen type [91,95,106] (i.e., a coplanar set of alternating wires that can be set to different voltage potentials) or the parallel plane type [i.e., two parallel planes of wires with one plane (or set of wires) offset horizontally by half the spacing of the wires, in a sort of "zig-zag" pattern if looking down on it], as illustrated in Fig. 1-5 below.

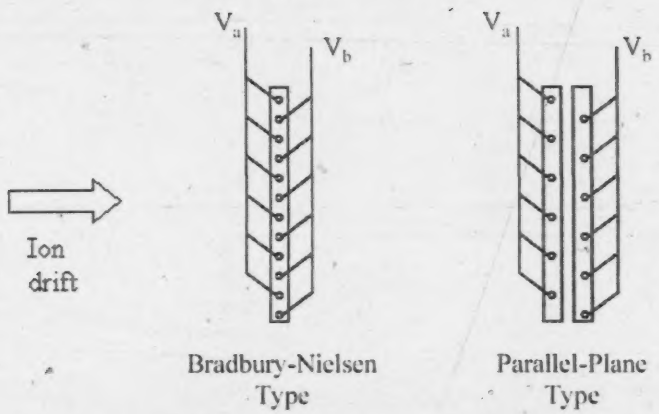

Figure 1-5. Schematic diagrams of two types of ion shutter gates. (left) A Bradbury-Nielsen type with alternating sets of parallel wires (represented by the circles) are set at different voltage potentials; (right) a parallel-plane type with two parallel planes of parallel wires offset horizontally by half the spacing of the wires and set at different voltage potentials.

For these ion shutter gates, one would create an orthogonal electric field (or approximately orthogonal field for the case of the parallel plane shutter) by setting the alternating wires of the shutter to different (or opposing) voltage potentials, thereby forcing/deflecting the ions from entering the drift region by sweeping them into the grid wires (thus annihilating them). Another type of ion gate, called the Tyndall gate,[91] has two parallel grids used such that the closing (OFF) state is achieved by setting the downfield grid to a much higher voltage potential than the up-field grid so as to develop a large enough reverse-electric field to repel the ions from the drift region; care must be taken, however, to set the grids to appropriate potentials to eliminate leakage. In any case, a time-of-flight (TOF) measurement can then be made by analyzing the spectrum obtained at the detector, located at the end of the drift tube. That is, the drift time (t_d) of the ions observed at the detector, in addition to the known length of the drift tube (L_d), allows one to infer the velocity of the ions (v_d), thus allowing for mobility (K) and reduced mobility (K_o) information to be gathered for the ions, as defined by Eqns. (1.7)-(1.9). Here the mobility (K) of an ion is a value that is indicative of an ion's relative charge, mass, and size as compared with other ions; that is, an ion with a mobility larger than a second ion would indicate that this ion possesses either a much larger charge, a much smaller mass, or a much smaller cross-sectional area, and that these characteristics

of the first ion enable it to drift toward the detector faster than the second. [It should also be noted here that it is possible for an ion with a mass larger than a second ion (and assuming the same cross sectional area) may have a mobility value larger than the second so long as the first ion possesses a sufficiently large charge to allow for a faster drift.] Since the various research groups in the field of IMS may employ varying drift temperatures and pressures for obtaining their mobility values, a normalized value – called the reduced mobility (K_o) of an ion – must be used in order for any meaningful comparisons to be made.

$$v_d = \frac{L_d}{t_d} \tag{1.7}$$

$$K = \frac{v_d}{E_d} = \frac{L_d}{t_d}\frac{L_d}{V_d} = \frac{L_d^2}{t_d \cdot V_d} \tag{1.8}$$

$$K_o = K\left(\frac{P_d}{760\,\text{Torr}}\right)\left(\frac{273\,K}{T_d}\right) \tag{1.9}$$

Here, E_d, V_d, P_d, and T_d represent the drift electric field, the drift voltage potential, the drift tube pressure, and the drift tube temperature, respectively.

The means of ionization have been previously covered, where the radioactive source (typically ^{63}Ni) and the Electrospray method – due to their effectiveness in ionizing samples for the analysis from the gas-phase and liquid-phase, respectively – are two of the most common ion sources for interfacing with an IMS device, therefore these two will be described in more detail in the following two sections.

1.3.5. Radioactive ^{63}Ni Ionization – Ion Mobility Spectrometry

The radioactive ionization method uses α- or β-radiation to remove an electron from each atom or molecule in the gas sample to create ions and secondary ions that in turn interact with neutral molecules to create more ions and more secondary electrons. Besides the above-stated advantages (e.g., miniaturization) and disadvantages (e.g., radiation permits), a particular disadvantage is that because this is a gas phase method this type of ionization source cannot be interfaced with microfluidic (chip) systems.

Also, this method is only suitable for volatile materials (thus excluding biological materials). Two radioactive materials used are the more common β-emitting ^{63}Ni and the α-emitting ^{241}Am (which can be found in most commercial household smoke detectors).

A ^{63}Ni-IMS device is typically composed of four stages: (1) the gas sample inlet (with filter); (2) the reaction region; (3) the drift region; and, (4) the detector. At the inlet (1), a carrier gas (which can be filtered by a semi-permeable membrane such as Dimethylsilicone [95] if the input is interfaced with atmospheric air, for example) is allowed to enter the reaction region [(2); generally smaller in diameter than the drift region] where beta particles (from ^{63}Ni -coated nickel or gold foil) would produce the reactant ions, which in-turn interact with sample molecules (in ion-molecule reactions) to produce product ions that drift along the applied electric field toward the normally closed shutter gate (i.e., with an orthogonal electric field several times that of the axial drift electric field), generally of the Bradbury-Nielsen type [20,26,28,95,106]. When pulsed open for a short duration, typically 0.1 – 1 ms,[95,98-100] the gate allows a small packet of ions through, to separate in the 1.5 – 4.25 cm inner diameter [95,99,101] drift region (3) according to their relative charge, mass, and size – so that the ions with the greatest charge, the smallest mass, and the smallest cross-sectional area would typically arrive at the collector plate (4) first, to be amplified/ analyzed by a picoammeter, a signal averager, or other suitable instruments. A pure, neutral drift gas – typically N_2 [91] – would be set to flow (at 400 to 700 mL/min) in the direction counter to the ion drift to inhibit any additional ion-molecule interactions that would result in spectra that are difficult to interpret (due to the addition of extraneous peaks caused by these interactions). The various configurations for the ^{63}Ni type IMS column are listed in Table 1-1, while the general schematic is depicted in Fig. 1-6.

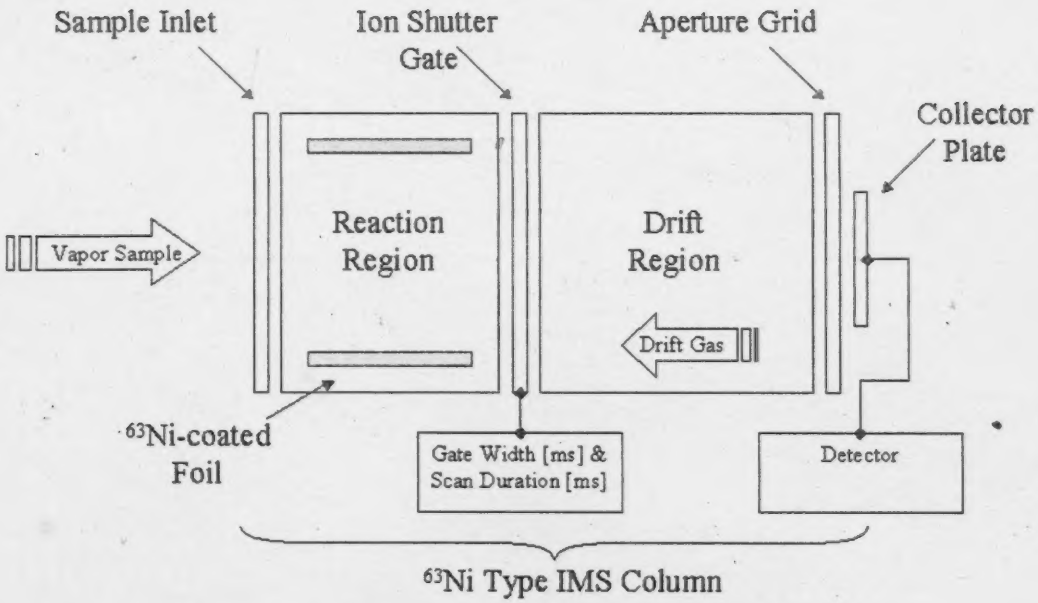

Figure 1-6. Schematic diagram of the ^{63}Ni type IMS column.

***Table 1-1.* Various Radioactive ^{63}Ni type IMS Column Designs**

References	Carrico (1983) [95]	Eiceman (1990) [98]	Eiceman (1991) [99]	Spangler (1993) [100]	Soppart (2000) [101]
Reaction Region[a]					
Length [cm]	6	5	-	-	-
I.D. [cm]	1.3	-	1	-	-
E - field [V/cm]	197	215	-	-	-
Ion Shutter Gate					
Type[b]	(B-N)	(B-N)	(B-N)	(B-N)	-
Gate Width [ms]	0.4	0.2	0.1 – 0.3	0.25 – 1.00	-
Drift Region					
Length [cm]	7.6	10	4.8	10.92	6
I.D. [cm]	3.8	-	4.25	-	1.5
E - field [V/cm]	-	215	-	-	~200
Typ. drift times [ms]	~20	-	-	16 – 22	8.3

[a] The Reaction Region for a ^{63}Ni type IMS is analogous to the Desolvation Region of an ES-IMS
[b] (B-N) refers to the Bradbury-Nielsen Type Ion Shutter Gate

1.3.6. Electrospray Ionization – Ion Mobility Spectrometry

The Electrospray ionization method, described above, has the advantage that it allows for the direct analysis of a liquid sample (either from a capillary ES source or from

a microchip ES source), and is capable of analyzing complex biomolecules such as proteins and peptides.

Other than the difference in ionization sources, the ES-IMS system consists of the same stages or similar ones as does the ^{63}Ni-IMS device described in the previous section, namely: (1) the sample reservoir and ES interface, (2) the desolvation region, (3) the drift region, and (4) the detector. Here the sample reservoir (1) is typically connected to a syringe pump that provides a sample flow rate of 1.0 – 10 μL/min [20,22,23,26,28] (sometimes referred to as the microspray regime), that can be varied or held stable, that transfers the liquid sample to the ES tip via a CE tube. (Nanospray or nano-ES is characterized by nL/min flow rates.[107,108]) The electrosprayed ion droplets are allowed to desolvate (or shed their solvent liquid via evaporation) within the desolvation region (generally measuring 4,[22] 5,[20] or 7.2 [26,28] cm long), aided in some cases by a desolvation and drift tube that can be set to high temperatures (e.g., 167 [22] or 250 [20,23] degrees Celsius). Like the ^{63}Ni-IMS device, an ion shutter gate, also typically of the Bradbury-Nielsen type,[20,26,28,95,106] can be found between the desolvation (2) and drift (3) regions of the IMS tube. The drift region typically measures 10,[22] 11;[20,23] or 13 [26,28] cm long, with inner diameters of 2.5 [22] or 4.9 [28,106] cm. The gate (pulse) width is also generally set between 0.1 – 1 ms (e.g., a 0.2 ms [23,26,28] or a 0.5 ms [20,22] pulse width is a common value). The "time-of-flight" detection (4) is the same. The aperture grid (of the same design as the focus grid) that lies between the drift region and the collector capacitively decouples the collector from the approaching ions; without the aperture grid, a broadening of the ion peaks and a loss in spectral resolution will result due to the ions being observed early by virtue of the coulombic interactions between the atoms in the collector plate and the incoming ions.[105] A pure, neutral drift gas can also be used, in the same manner as with the ^{63}Ni-IMS device, where typical gases include N_2,[25,109,110] He,[109] Ar,[109,110] CO_2 [109,110] – generally set to flow (at 400 to 900 mL/min) in the direction counter to the ion drift; here, the drift gases would also aid in the evaporation of the solvent liquid. [According to Asbury and Hill [109] different drift gases (particularly their polarizability and their size relative to the ion of interest) could change the mobility of ions in the drift region, thus affecting their drift times (and therefore their reduced mobility values), as well as their order of detection in relation of another ion.] Figure 1-7 depicts the general schematic of

the ES-type IMS. The various configurations for the ES type IMS column are listed in Table 1-2 below.

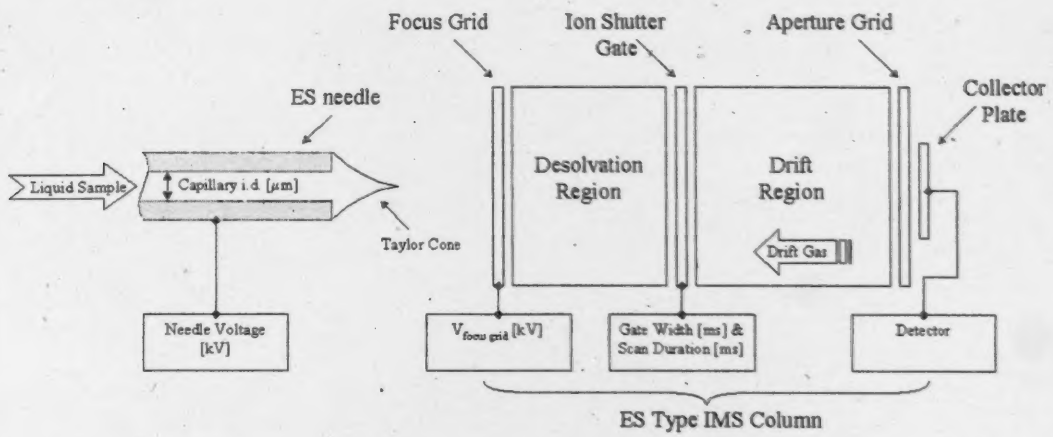

Figure 1-7. Schematic diagram of the ES type IMS column.

A common observation of ES-IMS systems is that incomplete desolvation/ desolution of ion clusters tend to lead to low resolution/sensitivity spectra. This can be solved by heating the drift tube, however, the heated drift gas (in the high temperature drift tube) would cause the ES needle to rise in temperature, usually above the boiling point of the solvent, thus causing solute precipitation in the needle itself that would lead to blockages and interruptions in the spray.[20,22] This means that one would need to cool the ES needle (Chen [20] notes that by cooling the ES source, one could also completely eliminate corona discharge).

The need for high temperatures is particular important when the goal is to utilize ES-IMS to obtain high resolution spectra of high mass molecules, such as proteins, which are important in biomolecular research. According to Hill and co-workers [20,22,28] and Guevremont *et al.*,[27] the high temperatures (~200 °C) help to evaporate the solvent molecules that are attracted to the highly charged ions of high molecular weight (MW) proteins (in their cases, cytochrome c), which leads to smaller, faster, better-resolved peaks. The latest research shows that modifications to the system parameters can lower the temperature requirement for the case of high MW samples. According to Matz *et al.* (2002),[45] one can achieve high resolution ion mobility spectra of high MW molecules (e.g., cytochrome c) at an optimum temperature of 150 °C and a 30 μm (i.d.) ES capillary

(compared with typical temperatures of 200 or 250 °C [20,23] and capillary sizes of 100 μm [20,22,23]), where shoulder (or multiple) peaks (corresponding to the conformations of each charge state) could be distinguished. The small capillary sizes and lower flow rates, coupled with a longer duration in the desolvation region lead to less solvent clustering on the ions, thus leading to higher resolution.[45]

Table 1-2. **Various ES type IMS Column Designs**

References[a]	Chen (1996) [20]	Chen (1996) [23]	Wittmer (1994) [22]	Wu (1998) [28]	Wu (2000) [26]
Electrospray Source					
Needle voltage [kV]	8.8	8.8	10	9.5	9.5
Capillary I.d. [μm]	100 (silica)	100 (silica)	100 (silica)	-	-
Liquid Sample[b]	50:50 (v/v) (H_2O/MeOH)	50:50 (v/v) (H_2O/MeOH)	47.5:47.5:5 (v/v/v) (H_2O/MeOH/HAc)	47.5:47.5:5 (v/v/v) (H_2O/MeOH/HAc)	50:50 (v/v) + 1% (H_2O/MeOH/HAc)
Liq. Flowrate [μL/min]	5	5	1.0 - 10.0	5	5
Desolvation Region[c]					
$V_{focus\ grid}$ [kV]	4.5	4.8	-	5.5	5.5
Length [cm]	5	-	4	7.2	7.2
E - field [V/cm]	-	-	-	280	279
Ion Shutter Gate					
Type[d]	(B-N)	-	-	(B-N)	(B-N)
Gate Width [ms]	0.5	0.2	0.5	0.2	0.2
Scan Duration [ms]	50	50	50	-	50
Drift Region					
Length [cm]	11	11	10	13	13
I.D. (O.D.) [cm]	-	-	2.5 (-)	4.9 (5.7)	4.9 (5.7)
{thickness}	{ - }	{ - }	{0.8}	{0.8}	{0.8}
E - field [V/cm]	~280	300	310	280	280
Temperature [°C]	250	250	167	-	-
Pressure [Torr]	-	689	-	-	-
Drift gas	N_2	N_2	N_2	N_2	N_2
{flow} [mL/min]	{~600}	{900}	{~600}	{630 (@ 25 °C)}	{630 (@ 25 °C)}
Typ. drift times [ms]	~10	-	~10	~20	~20
Typ. Ion current [pA]	1000 - 10000	-	-	10	-

[a] Note that Refs 20, 23, and 22 are related and do not involve MS; Note that Refs 28 and 26 are related and involve IMS/MS; Note also that the ES source is the same in Refs 22 and 26.

[b] Here, H_2O is water, MeOH is methanol, and HAc is acetic acid

[c] The Desolvation Region of an ES-IMS is analogous to the Reaction Region for a ^{63}Ni type IMS

[d] (B-N) refers to the Bradbury-Nielsen Type Ion Shutter Gate

1.4. Applications in Mass Spectrometry

As with an ion mobility spectrometer, the three main stages of any mass spectrometer are (a) the ionization source, (b) the ion separator or mass analyzer, and (c) the detector. The ionization sources (a) used for IMS – particularly, electrospray, radioactive ^{63}Ni, and MALDI – can be used with MS as well, in some cases (such as the ^{63}Ni or the flame ionization) perhaps with the IMS drift tube as the interface. Descriptions of these ionization sources were given in the section on *Ion Mobility Spectrometry* (*Section 1.3*). Other types of ionization sources [38] include electron bombardment otherwise known as electron ionization (EI), fast-atom bombardment (FAB), chemical ionization (CI), and inductively coupled plasma (ICP); these will not be covered in this dissertation. A list of ion separators or mass analyzers (b) is given below. The detector (c) is generally one of the following: (1) a Faraday cup/plate, (2) an electron multiplier, (3) a photomultiplier, or (4) a multichannel plate detector. The latter two stages (b, c) are implemented at vacuum pressures, typically between ~10^{-6} to 10^{-9} Torr.

As mentioned previously, mass spectrometers may employ one or more of the following mass analyzers: (1) the tandem MS (abbreviated MS/MS or MS^n); (2) the time-of-flight MS (TOFMS); (3) the quadrupole MS; (4) the ion trap MS (ITMS); and, (5) the Fourier Transform MS (FTMS). The MS/MS (1) [11,12,37,38] is a highly sensitive technique whereby the ions are subjected to two or more successive analysis stages in between which the ions are further fragmented typically employing collisionally-induced dissociation (CID), otherwise known as collisionally-activated dissociation (CAD). The TOFMS (2) [18,27,30,35,37-42] is the basis behind the IMS drift tube, which was described previously, except that it is operated at vacuum pressures. The quadrupole MS (3),[18,37,38,42] in which four parallel rods are set at a direct-current (DC) voltage potential with a radio-frequency (RF) potential superimposed over it, can operate in one of two settings. The first sets up under the effect of the static and high frequency quadrupole electric field a stable path that the ions with the desired mass-to-charge ratios would traverse. The second looks for the ions of different m/z ratios by their unstable paths. The ion trap MS (4),[30-34,37,38,42,43] which may employ a quadrupole device, uses high

frequency RF and DC potentials (not unlike the quadrupole MS) to create a field that stores (or traps) ions in a cavity. These ions can be released, in order from smallest to largest m/z ratio, by increasing the RF frequency. Finally, the FTMS (5) [26,37,38] employs an RF signal to excite ions that are orbiting within a magnetic field, then Fourier transforms the resultant time-dependent image current that the excited ions produce on the containment cell to obtain the component frequencies of the different ions corresponding to their m/z ratios.

The origin of mass spectrometry (MS), otherwise known as mass spectroscopy, is credited to the physicist Sir J.J. Thomson of the Cavendish Laboratory of the University of Cambridge.[38,111] ES-MS was introduced in 1984 by Yamashita and Fenn.[3] Since then the applications for ES-MS have existed in the field of biochemistry, where highly sensitive analysis of small quantities of such compounds as proteins [6,11,12,14,30,38,43,72,73] and peptides [1,13,14,26,29,38] take place (other applications were listed above).

1.5. Outline of this thesis

The structure of this dissertation will be as follows. Where this chapter has introduced the relevant subjects of (1) electrospray (ionization), (2) ion mobility spectrometry, and (3) mass spectrometry, the subsequent chapters will focus on the applications of these techniques/technologies (except mass spectrometry). *Chapter 2* will cover the preliminary design and testing of various electrospray ion sources (ESIS) – including a plastic microfluidic chip source, a glass microfluidic chip source, and a (tube-type) capillary electrophoresis (CE) source – as well as the design and evaluation of the preliminary (prototype) in-house-built ion mobility spectrometer, that would incorporate one of these ESIS concepts. *Chapter 3* will cover the design and evaluation of the second (successor or test model) ion mobility spectrometer, which would embody the design improvements over the prototype. *Chapter 4* will cover future work, such as the testing of a third IMS column and detector, the implementation of a microfluidic electrospray chip, and the applications of an ES-type device for space applications.

1.6. References

(1) Herring, C. J.; and Qin, J., "An on-line preconcentrator and the evaluation of electrospray interfaces for the capillary electrophoresis mass spectrometry of peptides," *Rapid Communications in Mass Spectrometry*, **13** (1999), pp. 1-7.

(2) Bateman, K. P.;White, R. L.; and Thibault, P., "Disposable emitters for on-line capillary zone electrophoresis nanoelectrospray mass spectrometry," *Rapid Communications in Mass Spectrometry*, **11** (1997), pp. 307-315.

(3) Kebarle, P.; and Tang, L., "From ions in solution to ions in the gas-phase: The mechanism of electrospray mass spectrometry," *Analytical Chemistry*, **65** (1993), pp. A972-A986.

(4) Tang, L.; and Kebarle, P., "Effect of the conductivity of the electrospray solution on the electrospray current. Factors determining analyte sensitivity in electrospray mass spectrometry," *Analytical Chemistry*, **63** (1991), pp. 2709 - 2715.

(5) Banks, J. F., "Recent advances in capillary electrophoresis electrospray mass spectrometry," *Electrophoresis*, **18** (1997), pp. 2255-2266.

(6) Kriger, M. S.;Cook, K. D.; and Ramsey, R. S., "Durable gold-coated fused silica capillaries for use in electrospray mass spectrometry," *Analytical Chemistry*, **67** (1995), pp. 385-389.

(7) Collins, D. C.;Tang, Q. L.;Wu, N. J.; and Lee, M. L., "Fast liquid chromatography/time-of-flight mass spectrometry using sol-gel bonded continuous-bed capillary columns," *Journal of Microcolumn Separations*, **12** (2000), pp. 442-449.

(8) Ikonomou, M. G.; and Kebarle, P.," Electrospray interface for mass spectrometer and method of supplying analyte to a mass spectrometer," United States Patent No. 5,349,186 (September 20, 1994).

(9) Dole, M.;Mack, L. L.;Hines, R. L.;Mobley, R. C.;Ferguson, L. D.; and Alice, M. B., "Molecular beams of macroions," *The Journal of Chemical Physics*, **49** (1968), pp. 2240-2249.

(10) Wen, J.;Lin, Y. H.;Xiang, F.;Matson, D. W.;Udseth, H. R.; and Smith, R. D., "Microfabricated isoelectric focusing device for direct electrospray ionization - mass spectrometry," *Electrophoresis*, **21** (2000), pp. 191-197.

(11) Figeys, D.;Gygi, S. P.;McKinnon, G.; and Aebersold, R., "An integrated microfluidics tandem mass spectrometry system for automated protein analysis," *Analytical Chemistry*, **70** (1998), pp. 3728-3734.

(12) Figeys, D.;Lock, C.;Taylor, L.; and Aebersold, R., "Microfabricated device coupled with an electrospray ionization quadrupole time-of-flight mass spectrometer: Protein identifications based on enhanced-resolution mass spectrometry and tandem mass spectrometry data," *Rapid Communications in Mass Spectrometry*, **12** (1998), pp. 1435-1444.

(13) Xue, Q. F.;Dunayevskiy, Y. M.;Foret, F.; and Karger, B. L., "Integrated multichannel microchip electrospray ionization mass spectrometry: Analysis of peptides from on-chip tryptic digestion of melittin," *Rapid Communications in Mass Spectrometry*, **11** (1997), pp. 1253-1256.

(14) Xue, Q. F.;Foret, F.;Dunayevskiy, Y. M.;Zavracky, P. M.;McGruer, N. E.; and Karger, B. L., "Multichannel microchip electrospray mass spectrometry," *Analytical Chemistry*, **69** (1997), pp. 426-430.

(15) Tang, K. Q.;Lin, Y. H.;Matson, D. W.;Kim, T.; and Smith, R. D., "Generation of multiple electrosprays using microfabricated emitter arrays for improved mass spectrometric sensitivity," *Analytical Chemistry*, **73** (2001), pp. 1658-1663.

(16) Fenn, J. B.;Mann, M.;Meng, C. K.;Wong, S. F.; and Whitehouse, C. M., "Electrospray ionization for mass spectrometry of large biomolecules," *Science*, **246** (1989), pp. 64-71.

(17) Patterson, S. D.; and Aebersold, R., "Mass spectrometric approaches for the identification of gel-separated proteins," *Electrophoresis*, **16** (1995), pp. 1791-1814.

(18) Li, J. J.;Wang, C.;Kelly, J. F.;Harrison, D. J.; and Thibault, P., "Rapid and sensitive separation of trace level protein digests using microfabricated devices coupled to a quadrupole-time-of-flight mass spectrometer," *Electrophoresis*, **21** (2000), pp. 198-210.

(19) Liu, H. H.;Felten, C.;Xue, Q. F.;Zhang, B. L.;Jedrzejewski, P.;Karger, B. L.; and Foret, F., "Development of multichannel devices with an array of electrospray tips for high-throughput mass spectrometry," *Analytical Chemistry*, **72** (2000), pp. 3303-3310.

(20) Chen, Y. H.;Hill, H. H.; and Wittmer, D. P., "Thermal effects on electrospray ionization ion mobility spectrometry," *International Journal of Mass Spectrometry and Ion Processes*, **154** (1996), pp. 1-13.

(21) Chen, Y. H.;Hill, H. H.; and Wittmer, D. P., "Analytical merit of electrospray ion mobility spectrometry as a chromatographic detector," *Journal of Microcolumn Separations*, **6** (1994), pp. 515-524.

(22) Wittmer, D.;Chen, Y. H.;Luckenbill, B. K.; and Hill, H. H., "Electrospray ionization - ion mobility spectrometry," *Analytical Chemistry*, **66** (1994), pp. 2348-2355.

(23) Chen, Y. H.;Siems, W. F.; and Hill, H. H., "Fourier transform electrospray ion mobility spectrometry," *Analytica Chimica Acta*, **334** (1996), pp. 75-84.

(24) Asbury, G. R.; and Hill, H. H., Jr., "Negative ion electrospray ionization ion mobility spectrometry," *International Journal for Ion Mobility Spectrometry*, **2** (1999), pp. 1-8.

(25) "Ultrahigh speed separations using gas-phase electrophoresis," Brigham Young University, Utah, 2001, website: http://www.byu.edu/capillary2001/extendedabstract.html. Accessed: (2001).

(26) Wu, C.;Siems, W. F.;Klasmeier, J.; and Hill, H. H., "Separation of isomeric peptides using electrospray ionization/high-resolution ion mobility spectrometry," *Analytical Chemistry*, **72** (2000), pp. 391-395.

(27) Guevremont, R.;Siu, K. W. M.;Wang, J. Y.; and Ding, L. Y., "Combined ion mobility time-of-flight mass spectrometry study of electrospray-generated ions," *Analytical Chemistry*, **69** (1997), pp. 3959-3965.

(28) Wu, C.;Siems, W. F.;Asbury, G. R.; and Hill, H. H., "Electrospray ionization high-resolution ion mobility spectrometry - mass spectrometry," *Analytical Chemistry*, **70** (1998), pp. 4929-4938.

(29) Srebalus, C. A.;Li, J. W.;Marshall, W. S.; and Clemmer, D. E., "Gas phase separations of electrosprayed peptide libraries," *Analytical Chemistry*, **71** (1999), pp. 3918-3927.

(30) Henderson, S. C.;Valentine, S. J.;Counterman, A. E.; and Clemmer, D. E., "ESI/ion trap/ion mobility/time-of-flight mass spectrometry for rapid and sensitive analysis of biomolecular mixtures," *Analytical Chemistry*, **71** (1999), pp. 291-301.

(31) Ramsey, R. S.;Vanberkel, G. J.;McLuckey, S. A.; and Glish, G. L., "Determination of pyrimidine cyclobutane dimers by electrospray ionization ion trap mass spectrometry," *Biological Mass Spectrometry*, **21** (1992), pp. 347-352.

(32) Ramsey, R. S.; and McLuckey, S. A., "Capillary electrophoresis electrospray ionization ion-trap mass spectrometry using a sheathless interface," *Journal of Microcolumn Separations*, **7** (1995), pp. 461-469.

(33) Ramsey, R. S.;Goeringer, D. E.; and McLuckey, S. A., "Active-chemical background-noise reduction in capillary electrophoresis/ion trap mass spectrometry," *Analytical Chemistry*, **65** (1993), pp. 3521-3524.

(34) Hoaglund, C. S.;Valentine, S. J.; and Clemmer, D. E., "An ion trap interface for ESI - ion mobility experiments," *Analytical Chemistry*, **69** (1997), pp. 4156-4161.

(35) Barnidge, D. R.;Nilsson, S.;Markides, K. E.;Rapp, H.; and Hjort, K., "Metallized sheathless electrospray emitters for use in capillary electrophoresis orthogonal time-of-flight mass spectrometry," *Rapid Communications in Mass Spectrometry*, **13** (1999), pp. 994-1002.

(36) Barnidge, D. R.;Nilsson, S.; and Markides, K. E., "A design for low-flow sheathless electrospray emitters," *Analytical Chemistry*, **71** (1999), pp. 4115-4118.

(37) "Mass Spectrometry Glossary," Cambridge Healthtech Institute (Newton Upper Falls, MA, USA), 2002, website: http://www.genomicglossaries.com/content/mass_spectrometry.asp. Accessed: (2002) August 19.

(38) "MS Information," Scripps Center for Mass Spectrometry, The Scripps Research Institute, website: http://masspec.scripps.edu/information/index.html. Accessed: (2002) August 14.

(39) Lazar, I. M.;Ramsey, R. S.;Sundberg, S.; and Ramsey, J. M., "Subattomole-sensitivity microchip nanoelectrospray source with time-of-flight mass spectrometry detection," *Analytical Chemistry*, **71** (1999), pp. 3627-3631.

(40) Stone, E.;Gillig, K. J.;Ruotolo, B.;Fuhrer, K.;Gonin, M.;Schultz, A.; and Russell, D. H., "Surface-induced dissociation on a MALDI - ion mobility - orthogonal time-of-flight mass spectrometer: Sequencing peptides from an 'in-solution' protein digest," *Analytical Chemistry*, **73** (2001), pp. 2233-2238.

(41) Karas, M.; and Hillenkamp, F., "Laser desorption ionization of proteins with molecular masses exceeding 10000 Daltons," *Analytical Chemistry*, **60** (1988), pp. 2299-2301.

(42) "Glossary of Common Mass Spectrometry Terms," Purdue University (West Lafayette, IN, USA), 2001, website: http://chemed.chem.purdue.edu/analyticalreview/mass_spec/. Accessed: (2002) August 19.

(43) Figeys, D.;Ning, Y. B.; and Aebersold, R., "A microfabricated device for rapid protein identification by microelectrospray ion trap mass spectrometry," *Analytical Chemistry*, **69** (1997), pp. 3153-3160.

(44) Lee, Y. J.;Hoaglund-Hyzera, C. S.;Barnes, C. A. S.;Hilderbrand, A. E.;Valentine, S. J.; and Clemmer, D. E., "Development of high-throughput liquid chromatography injected ion mobility quadrupole time-of-flight techniques for analysis of complex peptide mixtures," *Journal of Chromatography B*, **782** (2002), pp. 343-351.

(45) Matz, L. M.;Steiner, W. E.;Clowers, B. H.; and Hill, H. H., "Evaluation of micro-electrospray ionization with ion mobility spectrometry/mass spectrometry," *International Journal of Mass Spectrometry*, **213** (2002), pp. 191-202.

(46) Valentine, S. J.;Kulchania, M.;Barnes, C. A. S.; and Clemmer, D. E., "Multidimensional separations of complex peptide mixtures: A combined high-performance liquid chromatography/ion mobility/time-of-flight mass spectrometry approach," *International Journal of Mass Spectrometry*, **212** (2001), pp. 97-109.

(47) Matz, L. M.;Dion, H. M.; and Hill, H. H., "Evaluation of capillary liquid chromatography-electrospray ionization ion mobility spectrometry with mass spectrometry detection," *Journal of Chromatography A*, **946** (2002), pp. 59-68.

(48) Taraszka, J. A.;Counterman, A. E.; and Clemmer, D. E., "Gas-phase separations of complex tryptic peptide mixtures," *Fresenius Journal of Analytical Chemistry*, **369** (2001), pp. 234-245.

(49) McCooeye, M. A.;Mester, Z.;Ells, B.;Barnett, D. A.;Purves, R. W.; and Guevremont, R., "Quantitation of amphetamine, methamphetamine, and their methylenedioxy derivatives in urine by solid-phase microextraction coupled with electrospray ionization - high-field asymmetric waveform ion mobility spectrometry - mass spectrometry," *Analytical Chemistry*, **74** (2002), pp. 3071-3075.

(50) Matz, L. M.; and Hill, H. H., "Separation of benzodiazepines by electrospray ionization ion mobility spectrometry - mass spectrometry," *Analytica Chimica Acta*, **457** (2002), pp. 235-245.

(51) McCooeye, M. A.;Ells, B.;Barnett, D. A.;Purves, R. W.; and Guevremont, R., "Quantitation of morphine and codeine in human urine using high-field asymmetric waveform ion mobility spectrometry (FAIMS) with mass spectrometric detection," *Journal of Analytical Toxicology*, **25** (2001), pp. 81-87.

(52) Keller, T.;Miki, A.;Regenscheit, P.;Dirnhofer, R.;Schneider, A.; and Tsuchihashi, H., "Detection of designer drugs in human hair by ion mobility spectrometry (IMS)," *Forensic Science International*, **94** (1998), pp. 55-63.

(53) Lawrence, A. H., "Ion mobility spectrometry mass spectrometry of some prescription and illicit drugs," *Analytical Chemistry*, **58** (1986), pp. 1269-1272.

(54) Collins, D. C.; and Lee, M. L., "Developments in ion mobility spectrometry - mass spectrometry," *Analytical and Bioanalytical Chemistry*, **372** (2002), pp. 66-73.

(55) Asbury, G. R.;Klasmeier, J.; and Hill, H. H., "Analysis of explosives using electrospray ionization/ion mobility spectrometry (ESI/IMS)," *Talanta*, **50** (2000), pp. 1291-1298.

(56) Beegle, L. W.;Kanik, I.;Matz, L.; and Hill, H. H., "Effects of drift-gas polarizability on glycine peptides in ion mobility spectrometry," *International Journal of Mass Spectrometry*, **216** (2002), pp. 257-268.

(57) Kanik, I.;Beegle, L. W.; and Hill, H. H., "Ultra high-resolution electrospray ionization/ion mobility spectrometer system for in-situ detection of organic compounds," presented at the Conference of Lunar and Planetary Science, Lunar and Planetary Institute (Houston, TX, USA), 2001

(58) "Products," Smiths Detection, Smiths Group plc (London, UK), 2002, website: http://www.smithsdetection.com/Products/. Accessed: (2003) March 19.

(59) "Explosives and Narcotics Detection," GE Industrial Systems, General Electric Company (Plainville, CT, USA), 2003, website: http://www.geindustrial.com/ge-interlogix/iontrack/index.html. Accessed: (2003) March 19.

(60) Taylor, S. J.;Piper, L. J.;Connor, J. A.;FitzGerald, J.;Adams, J. H.;Harden, C. S.;Shoff, D. B.;Davis, D. M.; and Ewing, R. G., "Design aspects and operation characteristics of the lightweight chemical detector," *International Journal for Ion Mobility Spectrometry*, **1** (1998), pp. 58-63.

(61) Matz, L. M.;Clowers, B. H.;Steiner, W. E.;Siems, W. F.; and Hill, H. H., "Liquid-sheath-flow electrospray ionization feasibility study of direct water analysis with the use of high-resolution ion mobility spectrometry," *Field Analytical Chemistry and Technology*, **5** (2001), pp. 91-96.

(62) Swanson, L. W., "Electron and ion emission from liquid-metal surfaces," *Ieee Transactions on Plasma Science*, **19** (1991), pp. 746-748.

(63) Cloupeau, M.; and Prunetfoch, B., "Electrohydrodynamic spraying functioning modes: A critical review," *Journal of Aerosol Science*, **25** (1994), pp. 1021-1036.

(64) Batchelor, G. K., F.R.S., ed., *Mechanics of fluids: Miscellaneous papers*,The Scientific Papers of Sir Geoffrey Ingram Taylor (Vol. **4**), The Syndics of the Cambridge University Press, Cambridge, 1971.

(65) Juraschek, R.; and Rollgen, F. W., "Pulsation phenomena during electrospray ionization," *International Journal of Mass Spectrometry*, **177** (1998), pp. 1-15.

(66) Jones, A. R.; and Thong, K. C., "The production of charged monodisperse fuel droplets by electrical dispersion," *Journal of Physics D-Applied Physics*, **4** (1971), pp. 1159-1166.

(67) Tang, K. Q.; and Gomez, A., "Monodisperse electrosprays of low electric conductivity liquids in the cone-jet mode," *Journal of Colloid and Interface Science*, **184** (1996), pp. 500-511.

(68) Cloupeau, M.; and Prunetfoch, B., "Electrostatic spraying of liquids: Main functioning modes," *Journal of Electrostatics*, **25** (1990), pp. 165-184.

(69) Bruins, A. P., "Mechanistic aspects of electrospray ionization," *Journal of Chromatography A*, **794** (1998), pp. 345-357.

(70) Hulthe, G.;Petersson, M. A.; and Fogelqvist, E., "Coupling of open tubular liquid chromatography to electrospray mass spectrometry with a nanospray interface," *Analytical Chemistry*, **71** (1999), pp. 2915-2921.

(71) Loeb, L. B.;Kip, A. F.; and Hudson, G. G., "Pulses in negative point-to-plane Corona," *The Physical Review*, **60** (1941), pp. 714-722.

(72) Figeys, D.; and Aebersold, R., "Nanoflow solvent gradient delivery from a microfabricated device for protein identifications by electrospray ionization mass spectrometry," *Analytical Chemistry*, **70** (1998), pp. 3721-3727.

(73) Wang, C.;Oleschuk, R.;Ouchen, F.;Li, J. J.;Thibault, P.; and Harrison, D. J., "Integration of immobilized trypsin bead beds for protein digestion within a microfluidic chip incorporating capillary electrophoresis separations and an electrospray mass spectrometry interface," *Rapid Communications in Mass Spectrometry*, **14** (2000), pp. 1377-1383.

(74) Ramsey, R. S.; and Ramsey, J. M., "Generating electrospray from microchip devices using electroosmotic pumping," *Analytical Chemistry*, **69** (1997), pp. 1174-1178.

(75) Chiou, C. H.;Lee, G. B.;Hsu, H. T.;Chen, P. W.; and Liao, P. C., "Micro devices integrated with microchannels and electrospray nozzles using PDMS casting techniques," *Sensors and Actuators B-Chemical*, **86** (2002), pp. 280-286.

(76) de la Mora, J. F.; and Loscertales, I. G., "The current emitted by highly conducting Taylor cones," *Journal of Fluid Mechanics*, **260** (1994), pp. 155-184.

(77) Bell, A. E.;Schwind, G. A.;Rao, S.; and Swanson, L. W., "Lithium ion emission from a liquid-metal ion-source of $LiNO_3$," *International Journal of Mass Spectrometry and Ion Processes*, **88** (1989), pp. 59-68.

(78) Tang, K. Q.; and Smith, R. D., "Sensitivity enhancement of electrospray ionization MS for aqueous solutions in the corona-assisted cone-jet mode," *International Journal of Mass Spectrometry*, **162** (1997), pp. 69-76.

(79) Tang, K. Q.; and Gomez, A., "Generation of monodisperse water droplets from electrosprays in a corona-assisted cone-jet mode," *Journal of Colloid and Interface Science*, **175** (1995), pp. 326-332.

(80) Blades, A. T.;Ikonomou, M. G.; and Kebarle, P., "Mechanism of electrospray mass spectrometry: Electrospray as an electrolysis cell," *Analytical Chemistry*, **63** (1991), pp. 2109-2114.

(81) Kebarle, P., "A brief overview of the present status of the mechanisms involved in electrospray mass spectrometry," *Journal of Mass Spectrometry*, **35** (2000), pp. 804-817.

(82) Van Berkel, G. J.;McLuckey, S. A.; and Glish, G. L., "Electrochemical origin of radical cations observed in electrospray ionization mass spectra," *Analytical Chemistry*, **64** (1992), pp. 1586-1593.

(83) Smith, D. P. H., "The electrohydrodynamic atomization of liquids," *Ieee Transactions on Industry Applications*, **22** (1986), pp. 527-535.

(84) Zeleny, J., "Instability of electrified liquid surfaces," *The Physical Review*, **10** (1917), pp. 1-6.

(85) Gomez, A.; and Tang, K. Q., "Charge and fission of droplets in electrostatic sprays," *Physics of Fluids*, **6** (1994), pp. 404-414.

(86) Iribarne, J. V.; and Thomson, B. A., "Evaporation of small ions from charged droplets," *Journal of Chemical Physics*, **64** (1976), pp. 2287-2294.

(87) Collins, D. C.; and Lee, M. L., "Electrospray ionization gas-phase electrophoresis under ambient conditions and it's potential or high-speed separations," *Fresenius Journal of Analytical Chemistry*, **369** (2001), pp. 225-233.

(88) Wishart, D., private communication, 2003.

(89) Crabtree, H. J.;Cheong, E. C. S.;Tilroe, D. A.; and Backhouse, C. J., "Microchip injection and separation anomalies due to pressure effects," *Analytical Chemistry*, **73** (2001), pp. 4079-4086.

(90) Skoog, D. A.;Holler, F. J.; and Nieman, T. A., *Principles of instrumental analysis*, 5th Edition, Harcourt Brace College Publishers, Philadelphia, 1998.

(91) Eiceman, G. A.; and Karpas, Z., *Ion mobility spectrometry*, CRC Press, Inc., Ann Arbor, 1994.

(92) Smith, R. D.;Loo, J. A.;Loo, R. R. O.;Busman, M.; and Udseth, H. R., "Principles and practice of electrospray ionization - mass spectrometry for large polypeptides and proteins," *Mass Spectrometry Reviews*, **10** (1991), pp. 359-451.

(93) Matz, L. M.; and Hill, H. H., "Evaluating the separation of amphetamines by electrospray ionization ion mobility spectrometry/MS and charge competition within the ESI process," *Analytical Chemistry*, **74** (2002), pp. 420-427.

(94) Spangler, G. E.;Campbell, D. N.;Vora, K. N.; and Carrico, J. P., "Developments in ion mobility spectrometry," *Isa Transactions*, **23** (1984), pp. 17-28.

(95) Carrico, J. P.;Sickenberger, D. W.;Spangler, G. E.; and Vora, K. N., "Simple electrode design for ion mobility spectrometer," *Journal of Physics E-Scientific Instruments*, **16** (1983), pp. 1058-1062.

(96) Spangler, G. E.;Vora, K. N.; and Carrico, J. P., "Miniature ion mobility spectrometer cell," *Journal of Physics E-Scientific Instruments*, **19** (1986), pp. 191-198.

(97) Roehl, J. E., "Environmental and process applications for ion mobility spectrometry," *Applied Spectroscopy Reviews*, **26** (1991), pp. 1-57.

(98) Eiceman, G. A.;Blyth, D. A.;Shoff, D. B.; and Snyder, A. P., "Screening of solid commercial pharmaceuticals using ion mobility spectrometry," *Analytical Chemistry*, **62** (1990), pp. 1374-1379.

(99) Eiceman, G. A., "Advances in ion mobility spectrometry: 1980-1990," *Critical Reviews in Analytical Chemistry*, **22** (1991), pp. 471-490.

(100) Spangler, G. E., "Theory and technique for measuring mobility using ion mobility spectrometry," *Analytical Chemistry*, **65** (1993), pp. 3010-3014.

(101) Soppart, O.; and Baumbach, J. I., "Comparison of electric fields within drift tubes for ion mobility spectrometry," *Measurement Science & Technology*, **11** (2000), pp. 1473-1479.

(102) Dugourd, P.;Hudgins, R. R.;Clemmer, D. E.; and Jarrold, M. F., "High-resolution ion mobility measurements," *Review of Scientific Instruments*, **68** (1997), pp. 1122-1129.

(103) Baumbach, J. I.;Sielemann, S.; and Klockow, D., "Qualitative determination and quantitative analysis of volatile organic compounds using multi-capillary columns coupled to ion mobility spectrometers," *Institute of Spectrochemistry and Applied Spectroscopy* (1997), website: http://www.isas-dortmund.de/reports/1997/322_bb.pdf.

(104) Roch, T.; and Baumbach, J. I., "Laser-based ion mobility spectrometry as an analytical tool for soil analysis," *International Journal for Ion Mobility Spectrometry*, **1** (1998), pp. 43-47.

(105) St Louis, R. H.; and Hill, H. H., "Ion mobility spectrometry in analytical chemistry," *Critical Reviews in Analytical Chemistry*, **21** (1990), pp. 321-355.

(106) Bradbury, N. E.; and Nielsen, R. A., "Absolute values of the electron mobility in hydrogen," *Physical Review*, **49** (1936), pp. 388-393.

(107) Alexander, J. N.;Schultz, G. A.; and Poli, J. B., "Development of a nano-electrospray mass spectrometry source for nanoscale liquid chromatography and sheathless capillary electrophoresis," *Rapid Communications in Mass Spectrometry*, **12** (1998), pp. 1187-1191.

(108) Wilm, M.; and Mann, M., "Analytical properties of the nanoelectrospray ion source," *Analytical Chemistry*, **68** (1996), pp. 1-8.

(109) Asbury, G. R.; and Hill, H. H., "Using different drift gases to change separation factors (alpha) in ion mobility spectrometry," *Analytical Chemistry*, **72** (2000), pp. 580-584.

(110) Beegle, L. W.;Kanik, I.;Matz, L.; and Hill, H. H., "Electrospray ionization high-resolution ion mobility spectrometry for the detection of organic compounds, 1. Amino acids," *Analytical Chemistry*, **73** (2001), pp. 3028-3034.

(111) "What is Mass Spectrometry," American Society for Mass Spectrometry (Santa Fe, NM, USA), 2001, website: http://www.asms.org/whatisms/index.html. Accessed: (2002) August 14.

Chapter 2

Design and Testing of the Prototype Electrospray – Ion Mobility Spectrometry System

Page

Table of Contents

2.1. Introduction 41
2.2. Experimental Design and Testing of Various ES Source Types 42
2.2.1. Plastic Chip Electrospray Source 42
2.2.1.1. Fabrication of the Plastic Chip Electrospray Source 43
2.2.1.2. Evaluation of the Plastic Chip Electrospray Source 45
2.2.2. Microfluidic Glass Chip Electrospray Source 48
2.2.2.1. Fabrication of the Glass Chip Electrospray Source 48
2.2.2.2. Evaluation of the Glass Chip Electrospray Source 50
2.2.3. Capillary Electrospray Source 53
2.2.3.1. Fabrication of the Capillary Electrospray Source 53
2.2.3.2. Evaluation of the Capillary Electrospray Source 53
2.2.4. Preliminary ES Source Results 56
2.3. Experimental Design of the Preliminary ES-IMS System 57
2.3.1. Design and Fabrication of ES-IMS Device I 57
2.3.1.1. Electrospray Ion Source I (ESIS I) 57
2.3.1.2. IMS Drift Column I 60
2.3.1.3. Collector-Detector (C-D) Assembly I 69
2.3.1.4. External Equipment 73
2.4. Results and Discussion of the Preliminary ES-IMS System 74
2.4.1. Evaluation of the Fast Detection Circuit 74
2.4.2. Evaluation of ESIS I 80
2.4.3. Evaluation of Drift Column I 83
2.5. Conclusions 87
2.6. References 89

2.1. Introduction

As mentioned in *Chapter 1*, IMS can be interfaced with a variety of ion sources. The ES type seems to be the most versatile, especially where the study of samples (such as proteins) in solution is concerned. That is, the ES ion source can easily be implemented in microfluidic applications,[1-11] where microfluidics has proven to be an important technique in the fields of proteomics [12-15] and drug discovery [15,16]. For the ES sources, there exist various configurations. One method involves the use of a needle that acts as both the transport device for the liquid sample and the high voltage point in the point-to-grid (or point-to-plane) configuration. Other methods involve the use of microfluidic chip type ES sources [1,2,4-7,9,17-20] or other forms of micromachined ion source types [17] that were mentioned in the previous chapter. The use of a needle ES source allows for some variability in configuration (i.e., sheath flow, sheathless, liquid-junction, and direct electrode, see *Chapter 1*). Further, a capillary tube for capillary electrophoresis (CE) may be interfaced inside the ES needle [usually stainless steel (SS)] for transport of the liquid sample from a reservoir. This interface method would allow for a more convenient interface with a pump drive to control the liquid flow within the ES needle.

Section 2.2 below will highlight the design, fabrication, and evaluation three types of the electrospray ionization sources (ESIS): a plastic-chip ESIS (to be abbreviated p-μchip ESIS or simply plastic μ-chip, in *Section 2.2.1.*), the glass-chip based ESIS [or g-μchip (ESIS), in *Section 2.2.2.*], and the capillary-electrophoresis based ESIS (or CE ESIS, in *Section 2.2.3.*). The focus here is not the application of the ES source *per se*, but is instead the evaluation of the operational aspects of ES sources, centering on these three source types in particular.

The subsequent sections will focus on the preliminary ES-IMS system based upon the initial findings in *Section 2.2*. That is, the ES tip chosen for the system was a simple steel hypodermic needle whose point was ground flat. This ES tip interfaced at the end of a standard 1 mL syringe was used as our ES ion source, which will be described in further detail in the following sections. The remainder of this chapter will focus on the design, construction, and evaluation of the prototype in-house-built, printed-circuit-board

(PCB) -based IMS Column (or drift tube) and the prototype Collector-Detector Assembly in conjunction with this ES ion source.

2.2. Experimental Design and Testing of Various ES Source Types

The following sections will present the design, fabrication, and evaluation of the three types of ESIS. The main evaluation method for these source types was an Intel Play QX3 Microscope/Camera (Intel Corporation, Santa Clara, CA). A secondary method was a very preliminary ion mobility spectrometer arrangement, consisting of simply the grids and collector-detector, with no guard rings or ion shutter gate. The output of the detector (a simple amplifier circuit) was connected to a Tektronix TDS 3032 two-channel color digital phosphor oscilloscope (Tektronix, Inc., Beaverton, OR).

2.2.1. Plastic Chip Electrospray Source

The motivation for the use of plastic chip ES sources is that such devices are ideal for rapid prototyping, whereby the design-to-manufacturing stage is short. Because of this highly parallel design approach, such devices can be customized to interface with most (IMS and MS) analysis instrumentation quickly and at low costs.

The plastic chip ESIS was actually a construct produced by extruding and fusing (via heat) 0.375 mm diameter spools of a proprietary polyester compound (P1500) on a three dimensional, computer-controlled, heated stage of a Genisys Xs 3D printer (Stratasys, Inc., Eden Prairie, MN), available through the Multimedia Advanced Computational Infrastructure (MACI) research group headed by Dr. Robert Lederer of the University of Alberta Industrial Design Division. These chip emitters were designed and rendered in Rhinoceros 1.1 (Robert McNeel & Associates, Seattle, WA), a non-uniform rational b-splines (NURBS) modeling software for Windows; NURBS is a mathematical algorithm used in computer graphics or computer aided design (CAD) software packages. The output files of the Rhino program were converted to .STL format, which the Genisys printer was able to process.

2.2.1.1. Fabrication of the Plastic Chip Electrospray Source

Figure 2-1 below illustrates the basic design for the plastic μchip ESIS, which is basically a 39 (L) x 20 (W) x 10 (H) mm chip that consists of a funnel-shaped sample well feeding into the main channel. A pair of cylindrical holes was designed to intersect the bottom of the well and a point just inside the nozzle edge so that wire electrodes may be inserted. The reasoning behind the use of the pair of wire electrodes was to develop an electric field to create an ion flow within the channel, not unlike electrophoresis (EP) in a closed microfluidic chip (where "closed" refers to the lack of an opening or nozzle). This liquid flow is required for electrospray (ES) to occur.[21]

(a) (b)

Figure 2-1. A transparent rendered model of a chip-based electrospray ionization source. (a) A side view depicting the two electrode channels. (b) An angled view depicting the electrode channels as well as the ~0.5 mm diameter nozzle extending from the main channel of the chip. This chip has dimensions 39 (L) x 20 (W) x 10 (H) mm, and is made from 3-D printing of spools of 0.375 mm diameter P1500 (proprietary) polyester compound.

In the literature, another ES microfluidic chip was designed and described by Wen and co-workers (2000) [17] based on PET polymer film; this IEF–ES chip was described in *Chapter 1*. Another plastic chip ESI source reported in the literature is a star-shaped one constructed of PMMA, in which the eight-sided chip is set on a plastic box and liquid sample is allowed to be deposited into each of eight wells that are interfaced with the eight separate channels each of which ends in the sharp point of the star; eight sequential electrospray analyses of eight separate samples can be obtained with this disposable plastic octagonal plastic chip.[22] A method has also been reported for producing/prototyping a microfluidic device by 3D-printing a mold, which is then used to

make the (non-ES) plastic (e.g., PDMS) chip.[23] A more recent report (2002) describes a PDMS-ES chip (which was mentioned in *Section 1.2*).[24]

During the actual fabrication process of the p-μchip, it was found that due to the extremely small feature sizes of the microchannels of the chip – that is, on the order of the diameter of the extruded polyester material (i.e., 0.375 mm) – the channels ended up being reduced into slits, as shown in Fig. 2-2(left) below. The electrode openings [Fig. 2-2(right)], which were designed to be much larger, became more circular (as desired).

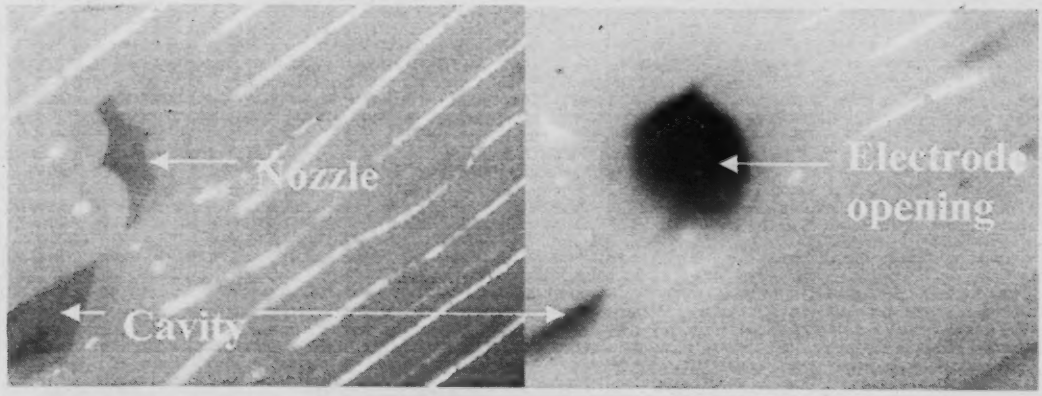

Figure 2-2. Photographs of the nozzle (left) and the electrode opening (right) of a plastic μchip ESIS. These images were taken with the Intel Play microscope set at a magnification of 60X. Notice that the nozzle, designed to be (~0.5 mm diameter) smaller than the (~0.7 mm diameter) electrode opening, is slit-like in either of the two cases. Notice also the cavities around the openings.

In the figure above, the nozzle is shown as a slit that is 2 fiber widths high (shown horizontally) by 1 fiber wide (shown vertically), when it should have been more circular. As it happens, the 3D printer, which is ideal for creating larger objects such as part of a skull, or models for cars, electronics equipment, was inadequate for such small dimension/feature products. In attempts to correct this, the channels were designed such that the channels were ~1.7 times that of the desired height. (Notice also in Fig. 2-2 that there appear to be cavities along the sides of the chip near the nozzle and the electrode openings. These can be attributed to the non-uniform heating/fusing of the polyester extrusions during 3-D printing; once again, these problems arise more with the smaller feature-size printed objects.) Also, it was found that when imaging from the side of the chip, the Intel Play microscope/camera set at 60X did not possess the adequate working

distance to focus on the axis of the expected liquid cone, especially with the width of the chip as it was (~20 mm). Therefore, a slimmer design was adopted, whereby the main channel would actual lie closer to the side of the chip that was closest to the camera. This "slim chip" design is depicted in Fig. 2-3. This 39 (L) x 12 (W) x 5 (H) mm "slim chip" features a main channel that is centered at 2 mm from one side edge of the chip and a funnel type extended well that is 7 (H from top surface) x 6 (top Diam) x 2 (bottom Diam) mm.

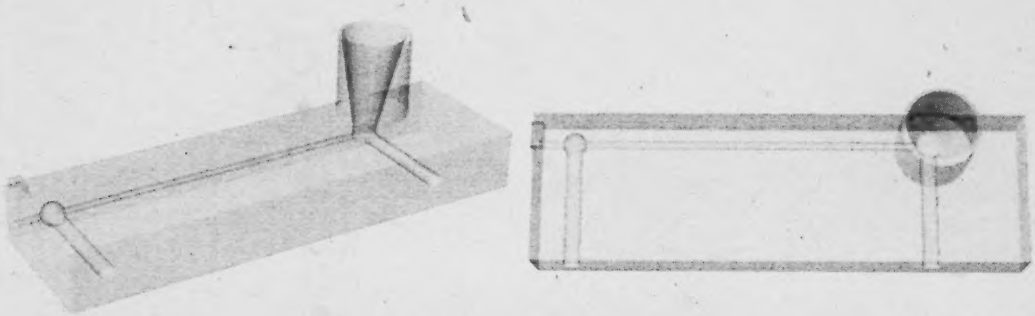

Figure 2-3. Designs of a modified ("slim") plastic μchip ESIS. Notice the oval channels that are larger horizontally to account for the tendency of the 3D printer to intrude on the channel space. Notice also that the right side (with the nozzle as the front) of the chip is essentially shortened to account for the short working distance of the Intel Play microscope set at 60X magnification.

2.2.1.2. Evaluation of the Plastic Chip Electrospray Source

A criterion for proper formation of a Taylor cone, prior to ES, is hydrophobicity of the nozzle region. Initial tests of hydrophobicity of these plastic microfluidic chips were undertaken, whereby individual droplets of water were introduced on the flat (top) surface of the chip. It was found that the liquid beads retained their shape over the span of several minutes, proving that this (P1500) plastic material maintained its hydrophobic nature, at least on the smooth top surface (not the nozzle edge).

For evaluating the plastic μ-chip ESIS during HV operation, it was necessary to seal the region around the electrode in the electrode opening (and this was done with a hot glue gun) to avoid leakage through this opening when the sample is loaded into the well of the chip.

To evaluate the "slim" plastic μchip ESIS, a metal screen was positioned at ~1 cm from the nozzle-end of the chip. A 30 kV high voltage power supply (NJE Corporation, Kenilworth, NJ) was used to provide the 10 kV source voltage, with a resistive divider connected in series to provide a 5.45 kV potential at the electrode in the well of the chip; the other electrode was left open-circuited, whereby an interfaced external well, or a 200 μL pipette tip sealed via parafilm, was filled with liquid sample [50:50 (v/v) methanol/water] to provide hydrostatic-pressure-induced flow. A Fluke 175 digital multimeter was connected in series between the (5.45 kV) resistive divider node and the electrode so that the current through the ESIS could be measured. A Keithley 417 picoammeter (Keithley Instruments, Inc., Cleveland, OH) was connected in series with the metal collector plate (i.e., a Faraday cup) to measure the current due to the impinging ions. Figure 2-4 illustrates this setup.

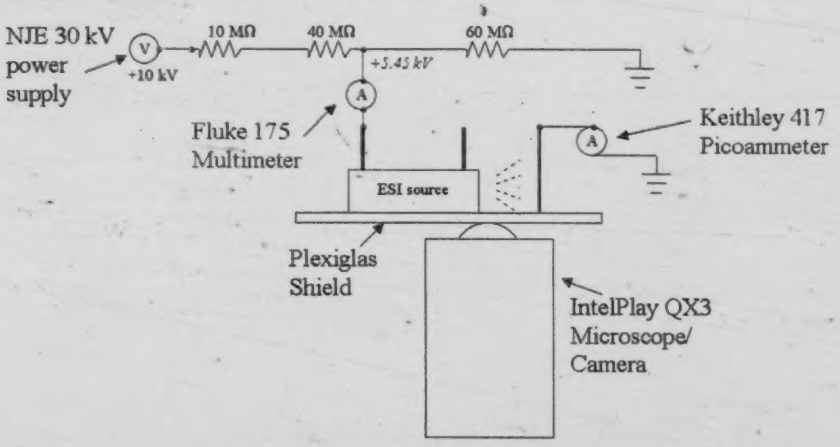

Figure 2-4. Schematic of the setup for observing the formation of a Taylor cone and electrospray during HV operation. This configuration allows for a Keithley 417 picoammeter to be interfaced with the collector plate so that ion current measurements may be taken.

Unfortunately, the results obtained were inconclusive, as the Keithley 417 was found to be erratic, regardless of whether the system was turned on or not; any movement near the system would influence the picoammeter reading. In testing this picoammeter with simulated currents it was found that it was inaccurate at the lower settings (i.e., 10^{-12} to 10^{-11} A), which represents the range of interest; the higher current settings (i.e., 10^{-7} to 10^{-6} A) proved to be more accurate. The Fluke digital multimeter (DMM) also produced

noise-like results, perhaps due to sporadic spray (if any) or interference from external sources. In addition to these electronic tests, a visual inspection of the formation of any cone tip was performed. However, the setup (also shown in Fig. 2-4) made it extremely difficult to locate the nozzle of the chip, and thus observation of the Taylor cone formation during HV operation was not possible.

With the HV connections taken off, and the "slim" chip was positioned such that the nozzle was pointed more toward the Intel Play microscope. This allowed for the observation of the formation of a liquid cone during non-HV operations. What was observed when liquid was pumped through the channel of the chip was a large bead covering the nozzle, with dimensions approximately 5 mm wide by 2.5 – 3 mm high by 1 mm thick (measured from the chip edge to the meniscus of the bead). The liquid bead flattened over time, such that its dimensions measured ~7 mm wide by ~3 mm high by less than 1 mm thick. It was also observed that the cavities in the chip "wall" seemed to affect the stability of the liquid bead – that is, these cavities acted as drains that allowed the liquid to leak elsewhere. Likely there were such cavities within the chip, near the main channel that allowed the liquid to leak out, and thus make it appear as if the well and channel had dried-up; in fact, due to the hydrophobic nature of the plastic material, the siphoning of liquid from the main channel was likely aided by capillary forces or Laplace pressures (not unlike those observed in capillary rise or pressure control experiments [25,26]). Figure 2-5 illustrates the loading and draining of the μchip.

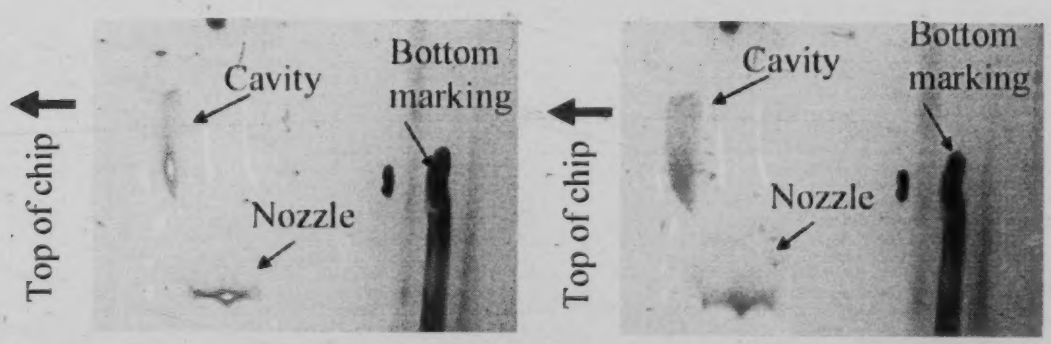

Figure 2-5. Photographs of the "slim" plastic μchip ESIS during loading. (left) When the liquid sample has just approached the end of the nozzle; (right) when the liquid has leaked out.

In summary, this technology, although ideal for quick prototyping of large-feature-sized objects, was unable to reliably produce the devices we required. Physical leakages and irreproducible features were unavoidable. An ESIS was required that would not be susceptible to this leakage problem. One such source is the glass microfluidic chip ES, which have been proven to be free of this problem in EP and EOF applications.

2.2.2. Microfluidic Glass Chip Electrospray Source

Since the plastic μchip proved troublesome in terms of leakage of the sample, it was hoped that the glass type, already established as ideal for microfluidic analyses, would overcome this problem. Previous glass microfluidic chip ES sources include the one described by Ramsey [9] that uses electroosmotic pumping to generate the liquid flow necessary to generate electrospray from a channel opening. Other glass chip ESIS, such as the ones described by Figeys and coworkers [2,4,5] involve a similar chip setup, except with a transfer capillary that was used to interface the chip with an analysis instrument (in their case, a quadrupole TOFMS).

Our glass chip ESIS was a standard "simple cross" microfluidic chip manufactured by Micralyne, Inc. (Edmonton, AB) that was diced in half (via a dicing saw) to expose the long channel. The exposed "nozzle" was shaped like a "D," where the width was 50 μm and the depth was 20 μm. It was hoped that a liquid cone would form from this nozzle once an electric field was set up between the liquid interface and a grid/screen cathode set a short distance from the nozzle. In this way, it is not unlike the glass chip used by Ramsey [9]. The following sections will describe more the design, fabrication, and evaluation of this glass μ-chip ESIS.

2.2.2.1. Fabrication of the Glass Chip Electrospray Source

The dimensions of the "simple cross" chip measure 16 (W) x 95 (L) x 2.2 (H) mm, with two channels, a long one (85 mm) and a short one (8 mm), that intersect 5 mm

from the end of the long one. At the end of each channel is a 2 mm diameter, 1.1 mm deep well (labeled BR, SR, SW, and BW in Fig. 2-6 to symbolize the buffer and sample reservoirs and the sample and buffer waste wells, respectively). This chip was actually fabricated using two 16 (W) x 95 (L) x 1.1 (H) mm Borofloat glass pieces, the bottom of which was wet-etched (using processes established at Micralyne) to create the channels, and the top of which had holes drilled through to create the wells. The two pieces were then aligned and anodically bonded together. Due to the wet-etching process, the channels actually end up being D-shaped, measuring 50 μm across at the interface between the top and bottom pieces, and 20 μm deep.

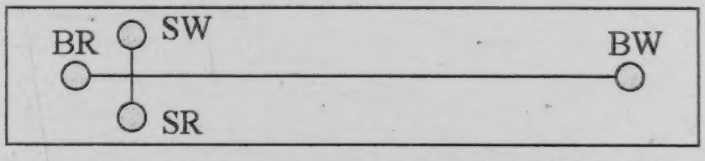

Figure 2-6. A schematic diagram of a Micralyne "simple cross" microfluidic chip.[25]

For the ES emitter, the main channel must be exposed. To that end, the microfluidic chip shown in Fig. 2-6 was diced in half. That left two potential ES emitters. The half with just the one well was chosen to simplify matters – that is, there would only be one sample reservoir, so that any source of blockages or such would be more readily evident.

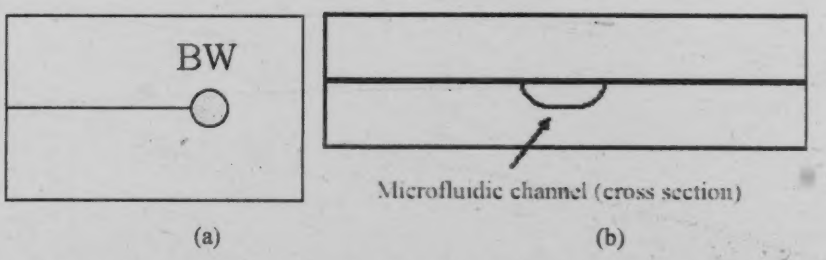

Figure 2-7. A diagram of a microfluidic chip that was cut for the purpose of implementing ES. (a) Here, a separation channel is exposed at the far (left) end of the chip. (b) Here, a cross-sectional view of the chip is shown (not to scale); this can also be seen as the rearview (or nozzle-end view) of the glass chip ES emitter.

2.2.2.2. Evaluation of the Glass Chip Electrospray Source

To evaluate the performance of this glass μ-chip emitter, two methods were employed. The first was visual inspection, where it was hoped that the formation of a liquid (Taylor) cone and perhaps electrospray might be observed. The second involved interfacing the emitter with a preliminary IMS arrangement.

For the first method, the glass μ-chip emitter was placed on a platform and positioned such that the nozzle-end faced the microscope, with a 5 mm thick plastic shield positioned between the two. (This plastic piece was used to shield the people in the laboratory against any electrical arcing or corona discharge during the actual experimentation with high voltages.) Due to safety concerns and the working distance of the microscope/camera, only a magnification of 10X could be employed. As such, the 20 μm high opening that was the nozzle was difficult to find, much less see, especially considering the relatively poor resolution of the camera at hand.

This same chip was also observed under a standard laboratory microscope (looking down on it) during loading of a liquid, in this case a 50:50 (v/v) methanol/water mixture; this mixture is commonly used in ES experiments. Here, it was necessary to interface a 200 μL pipette tip to the well to allow for more sample to be used at one time (and to avoid sample evaporation). It was observed that the main channel did indeed appear to wet. This meant that the liquid could potentially fill toward the nozzle. An optical instrument of sufficient working distance and magnification that was capable of inspecting the nozzle was not available due to cost factors.

A preliminary ion mobility spectrometer (shown in Fig. 2-8) was subsequently assembled in attempts to electrically observe electrospray, where visual attempts so far had failed. This spectrometer was constructed by simply placing three grids and one metal screen that were spaced 1.5, 6.5, 16.5 cm, and 17.5 cm, respectively, from the nozzle-edge of the chip, that was itself placed on top of a cardboard platform. A detection circuit, actually a simple amplifier circuit (shown in Fig. 2-9), with a gain of 1.15×10^{11} V/A was connected in series to the metal screen, which acted as a Faraday cup. The circuit consisted of an 11.3 MΩ input resistor that converts the incoming ion

current into a voltage, which is then amplified by two op-amp stages (LF 356; National Semiconductor Corporation, Santa Clara, CA) each with a gain of 101 V/V.

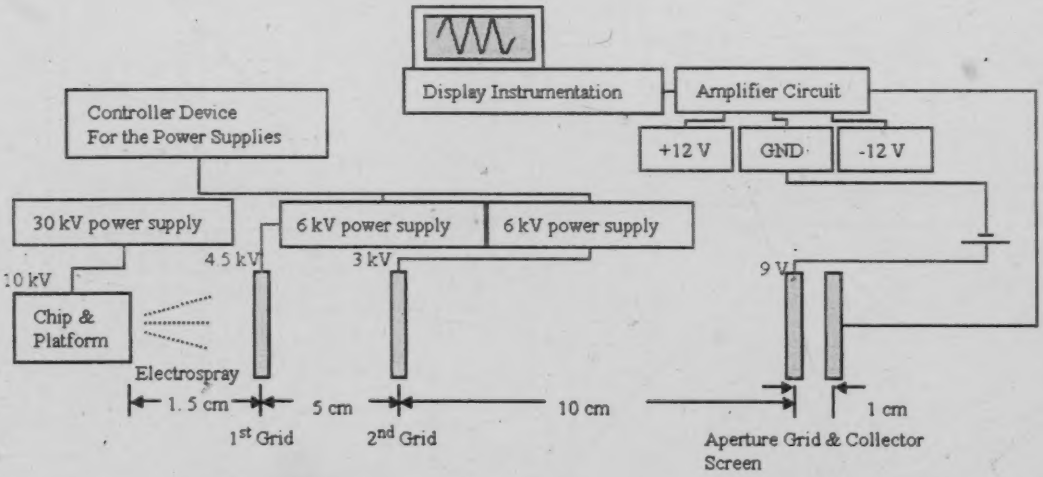

Figure 2-8. A schematic diagram of the preliminary IMS arrangement. Here, the three components were aligned as they had been on the wooden base plate (not shown).

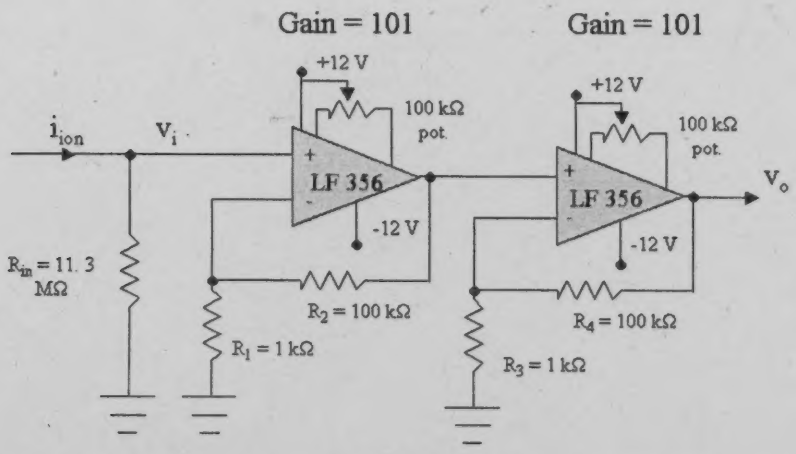

Figure 2-9. A circuit diagram of the detection circuit used in conjunction with the preliminary IMS arrangement. The ±12 V input power was actually ±11.85 V supplied by two Hewlett/Packard 6213A, 12V dc power supplies. The input of this circuit was connected to the metal collector plate, while the output was connected through a 5V zener diode to a Tektronix oscilloscope. The 100 kΩ potentiometers connected to pins 1 and 5 of each LF356 JFET op-amp is used to eliminate the input offset voltage (V_{OS} ~ 3 mV) that is inherent in this op-amp's internal circuitry.

Having connected the NJE 30 kV high voltage supply to the sample well on the chip via banana plug wires and a wire electrode, the two closest grids were connected to two of the outputs of the Microfluidic Tool Kit instrument (μTK; Micralyne Inc., Edmonton, AB, Canada) via HV wires. The last grid was connected in series with a 9 V_{dc} battery to provide a non-zero potential set before the collector plate; ideally this would be set to a potential that would allow for a uniform electric field between the previous grids and the collector plate, however the 9 V was close enough for an initial assessment. The voltages that were set for the chip electrode and the other two grids were 10 kV, 4.5 kV, and 3 kV, respectively. Having energized all these components, with the well having already been loaded, the oscilloscope was activated to capture any signal that appeared. However, the only signal that was received (shown in Fig. 2-10) turned out to be a ground loop effect or perhaps a transient pick-up by the antenna-like collector plate (perhaps not unlike the ringing effect observed later with the ES-IMS system, to be described later), where an inverse transient occurred following a downward spike coinciding with the activation of the HV power supplies. This effect persisted even when the liquid in the well had dried-up.

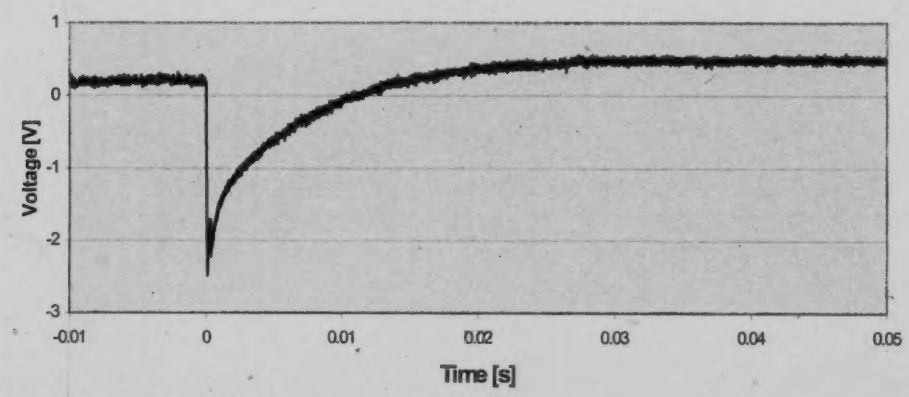

Figure 2-10. Transient signal obtained during μchip ES - IMS experiments. Here, time t = 0 corresponds with the activation of the μTK high voltage power supplies.

It has been noted in the literature that one possible problem with using an open-channel microfluidic chip is that while leakage within the microchannels is not a problem (as it was with the plastic chip described previously), the liquid may wet along this nozzle-edge (i.e., this surface may not be sufficiently hydrophobic).[10,11] This may

account for some of the difficulties encountered here, as hydrophobicity around the nozzle is required to maintain a Taylor cone (which is a requirement for electrospray). Although this is a problem that can be solved [i.e., by implementing a CE transfer line to an emitter (as described by Figeys and co-workers [2,4,5]), or by interfacing the microfluidic chip with an emitter tip alone (as described by Li *et al.*[27] and Wang *et al.*[7]), or by applying a hydrophobic coating/layer on the nozzle-edge of an open-channel microfluidic chip [10,11]], a source more suitable for prototyping was sought for this developmental stage.

2.2.3. Capillary Electrospray Source

Since the microfluidic chips (both plastic and glass) had proven difficult to work with in terms of obtaining and observing a stable spray, a different ESIS, one that was proven to previously produce a stable spray, was re-evaluated. The capillary-electrophoresis (CE) ESIS was of a design constructed years ago by Dr. Chris Backhouse, who had at the time begun studies on the electrified spraying of liquids.

2.2.3.1. Fabrication of the Capillary Electrospray Source

The CE ESIS, also known in the laboratory as the tube-type ESIS, was originally constructed by first fitting a 200 μm (ID) capillary tube inside the barrel of a standard 0.5 mm mechanical pencil tip, then applying silver epoxy at the tip to hold the two together. This emitter tip was then fitted inside a ~0.64 cm (¼ inch) i.d. vinyl tubing that was cut to a length of ~12 cm; appropriate amounts of Teflon tape were used to seal the fitting.

2.2.3.2. Evaluation of the Capillary Electrospray Source

The CE or tube-type ESIS was evaluated by two methods. The first was a visual observation, with a similar setup to those for observing the glass and plastic μ-chip emitters – that is, using the Intel Play microscope/camera and the appropriate support and

shielding structures. The tube-type emitter was held tip-down by laboratory clamps attached to a metal stand (not unlike the setup for supporting test-tubes in a chemistry laboratory). A metal plate was then placed on a stand ~1 cm below the emitter tip; the entire region below the stand and between the emitter and the observing camera was shielded using several-millimeter-thick, high-dielectric-strength plastic materials (> 10 kV/mm). It was found that the NJE 30 kV high voltage power supply was outputting a negative voltage. This meant that for a positive spray the metal plate (cathode) had to be set to the HV output of the NJE power supply and the emitter to virtual ground. A Keithley 417 picoammeter was used to measure the current at the emitter. The two configurations for this setup are presented in Fig. 2-11 below, where either an alligator clip attached to the emitter tip or a wire electrode inserted into the liquid-filled tube of the emitter was connected to the input of the Keithley 417.

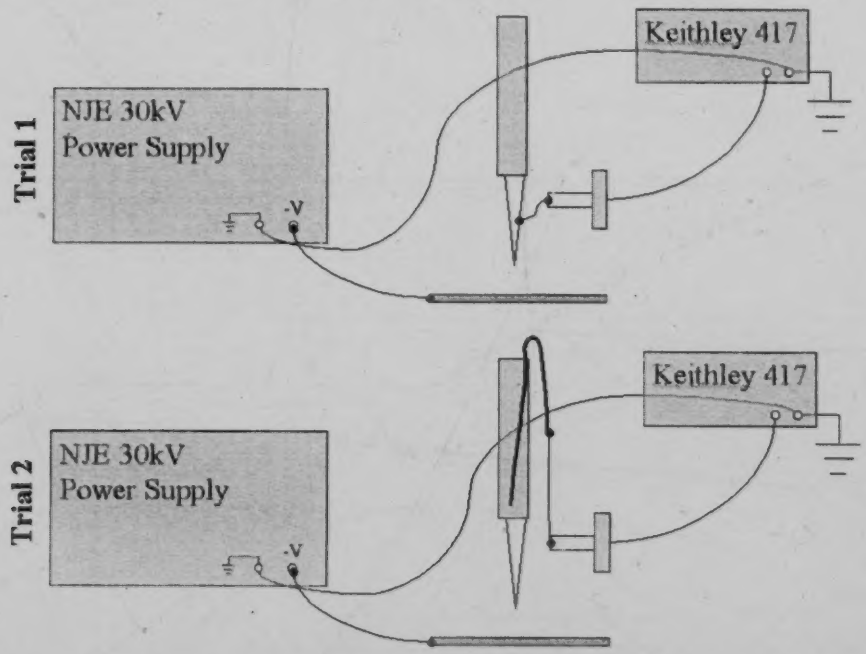

Figure 2-11. Schematic of the setup for electrically evaluating the (CE) tube-type ESIS. (Top) A trial where an alligator clip would connect the Keithley 417 to the ESIS metal tip; (bottom) a trial where an electrode would connect the Keithley 417 to the liquid sample in the ESIS reservoir. Notice the negative polarity of the NJE.

It was found that the currents obtained with the Keithley 417 (for varying scales ranging between 10^{-10} and 10^{-8} A) using the setup shown in Fig. 2-11 were still erratic

and because the system was not sufficiently shielded (i.e., the system was not operated in a grounded metal enclosure) it was extremely susceptible to noise. [In fact, any movement near the system could evoke a shift in the reading. As mentioned above in *Section 2.2.1.2*, the simulated current tests proved that the Keithley 417 was more accurate at the higher current ranges (i.e., 10^{-7} to 10^{-6} A).] So a visual observation of the ESIS tip was made using a setup similar to that shown in Fig. 2-4. Indeed, it was observed that an intermittent jet (not shown) would emanate from the bottom edge of the ESIS tip, which was actually closest to the metal plate collector due to the inherent setup. As the voltage was turned up to ~8kV (with the ESIS at virtual ground), however, a sizzling sound could be heard and a flash [captured in Fig. 2-12(top)] could be seen on the computer display (showing images taken by the Intel Play microscope) that was indicative of a corona discharge. Fortunately, the plastic shield between the ESIS emitter and the camera was sufficient to protect both the camera and the people in the lab. However, this discharge was sufficient to damage the tip of the ESIS, so that a charred tip remained [captured in Fig. 2-12(bottom)] that had to be replaced, not to mention that the input gain resistors of the Keithley 417 picoammeter were also found to have been significantly damaged (and also had to be replaced).

In summary, the CE (tube-type) ESIS was visually proven to produce at least an intermittent electrospray where a video capture of the electrospray was obtained (albeit at poor resolution), although electrical characterization required further calibration (and perhaps a more sensitive detector/picoammeter). It was also observed that corona discharge does indeed occur with the application of higher voltage potentials (as described in the literature). In our case, this discharge proved to cause significant damage to the ESIS (as well as some damage to the Keithley picoammeter).

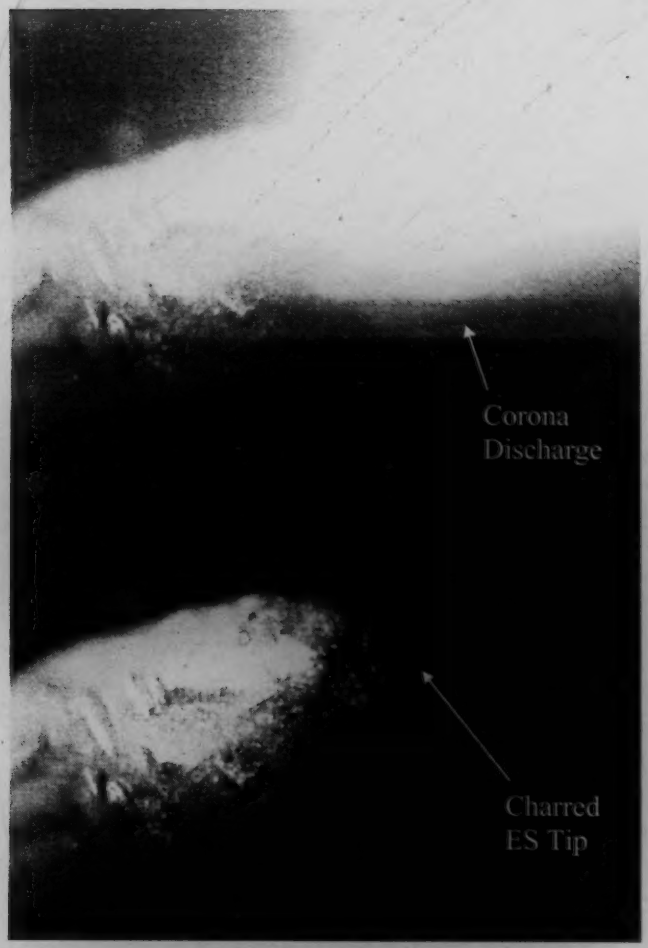

Figure 2-12. Still-photo-captures of electrospray (top), corona discharge (middle), and aftereffects of corona discharge (bottom) that were observed with the use of the (CE) tube-type ESIS emitter.

2.2.4. Preliminary ES Source Results

Both the evaluation of the chip type ESIS emitters (glass and plastic) were inconclusive, although the channels of both were observed to wet during non-HV operation, with the plastic one producing a bead over the nozzle. It was also found that the plastic emitter was prone to leak internally. The (CE) tube-type emitter produced the most promising result, in that a visual observation of both electrospray (not shown) and corona discharge [shown in Fig. 2-12(top)] was confirmed via use of the Intel Play microscope camera set at 60 times magnification.

2.3. Experimental Design of the Preliminary ES-IMS System

The basic design of an ES source includes the following components: (1) a reservoir for containing the liquid sample, (2) a high voltage potential to be applied to the tip, (3) a method for delivering the liquid sample to the tip, and (4) a tip that allows for electric field focusing. Additional components may include such tip accessories as those employed while implementing the sheath flow approach, the sheathless approach, or other such configurations (e.g., sheath liquids, sheath gases, pulled CE tips, etc.). (Please refer to *Chapter 1*, *Section 1.3.3* for more details on traditional ES-IMS, including a list of drift tube or IMS column parameters as reported in the literature.)

The next sections will describe the preliminary ES-IMS Device that was designed, constructed, and evaluated for this dissertation.

2.3.1. Design and Fabrication of ES-IMS Device I

Our first ES-IMS device consisted of four modules: the electrospray ionization source (ESIS I), the ion mobility spectrometry (IMS) Column I, the collector-detector (C-D) Assembly I, and (4) the supporting equipment.

2.3.1.1. Electrospray Ion Source I (ESIS I)

Considering this electrospray ion source to be a device used for preliminary tests, the design called for the simplest construction possible, without the liquid pump, or buffer (or sheath) gas flow, or capillary interfaces; future applications would allow for a microfluidic ES chip to be used. Here, the ES needle (shown in Fig. 2-13) was a 27-gauge (0.4 mm diameter) stainless steel (SS) needle with its normally sharp-pointed tip having been ground flat using a grinder and fine sandpaper. [The common configuration for an ES source is to interface a capillary electrophoresis (CE) capillary tube – typically a 100 μm diameter silica capillary [21,28,29] – between the reservoir and the tip, with the CE tube actually set inside a metal tip, such as a 27-gauge SS needle [21,28,29].] A standard 1

mL syringe to which the SS needle was attached acted as the reservoir for the liquid sample.

a)

b)

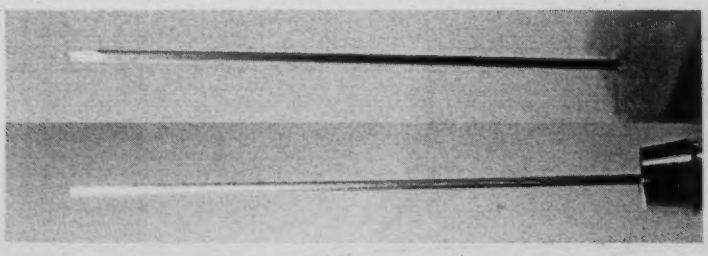

Figure 2-13. Photographs of (a) a 27-gauge SS hypodermic needle and (b) the flat-ground hypodermic needle tip of the (sheathless) electrospray ion source.

Without a (syringe) pump as used by other groups,[21,28-31] an alternate method was implemented to generate liquid flow within the source tip – that is, the entire ES-IMS apparatus was arranged in the vertical configuration to allow hydrostatic pressure within the syringe to maintain the liquid flow within the SS needle. This required that a mounting system be made to fit directly over a vertically oriented IMS column, the design of which is described in the sections below. The mount for this preliminary ES source was actually an assembly of cardboard pieces cut to fit the syringe, held together using two ~3 mm diameter plastic rods (similar to that used for the IMS column), and spaced using similar plastic ferrules. Figure 2-14 depicts the ES source within its mount prior to an ES-IMS experimental run. This type of ES interface closely resembles the sheathless type (see *Chapter 1*), except without any sheath gas and without a pulled tip. The μTK (described above) was used to provide the high voltage power to the ES needle and the IMS column (i.e., to the focus grid and resistor array, see next section for details).

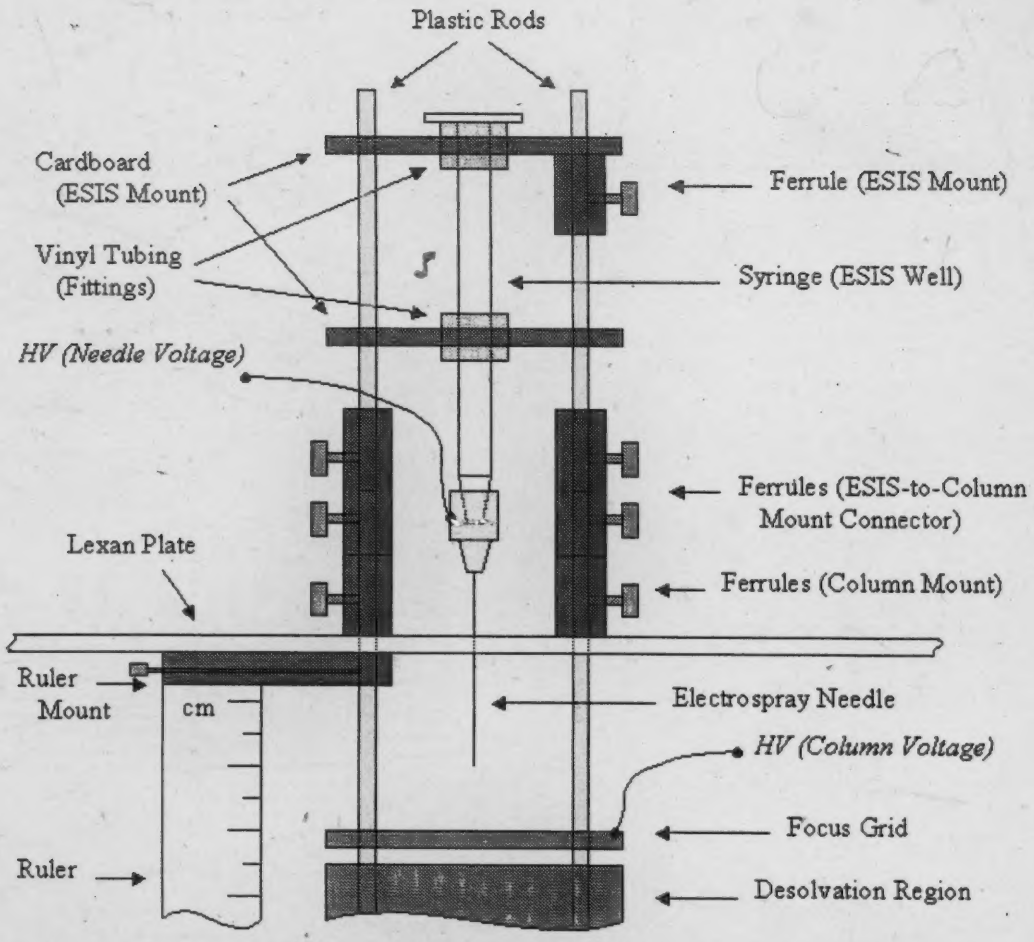

Figure 2-14. Schematic diagram of the electrospray ion source set in the ES-IMS system. An alligator clip connects "*HV (Needle Voltage)*" with the electrospray needle. Not shown are the banana jacks (input) and the RCA jack (output), which connect the column with the external instruments [e.g., "*LED-Hi & LED-Low*" (waveform generator to shutter gate controller), "*HV (Column Voltage)*" (μTK to focus grid), "± 12 V_{dc} & *GND*" (dc power supply to C-D Assembly), and "*Detector out to PMT in*" (detector to μTK). The aperture through which the needle is fitted is a 2 cm diameter hole.

As shown in Fig. 2-14, the ESIS, which consists of the syringe and SS needle held by its mount (i.e., the cardboard and plastic rods), was set above the IMS Column (with the first grid directly below the needle point), and was supplied with high voltage via a HV line (that was connected to the needle via an alligator clip).

The suspension plate, partially shown in the figure, was a 2 mm thick Lexan plate consisting of eleven circular holes: (a) three for the banana plugs for the detector input power; (b) two for the shutter control inputs; (c) two for the IMS column focus grid and GND HV connections; (d) one for the RCA jack for the detector output; (e) two for the plastic rods used to suspend the IMS column as well as to support/align the ESIS mounting assembly over the IMS column; and, (f) one 2 cm diameter aperture for the ES needle to fit through to hover above the focus grid of the column. To measure the distance between the tip of the ES needle and the top of the focus grid (FG), a plastic ruler attached to a custom (ferrule-like) bracket was inserted through one of the two plastic column mounting rods just before the (Lexan) Suspension Plate was fitted over the rods. A schematic diagram of the ES-IMS Device I setup (including the wire connections mentioned above) is shown in the next section.

During experimentation High Voltage (HV) was applied to the SS needle via an alligator clip and a HV wire that was interfaced with one of the HV outputs of the μTK. (As an aside, Micralyne's μTK contains two HV boards, each housing two 6 kV EMCO C60 positive power supplies, plus various HV switches.) By applying a lower voltage potential to the first grid (i.e., the focus grid) of the IMS column, a high electric field was developed between the tip of the SS needle and the grid, which encouraged the formation of the Taylor cone above an onset electric field. With an approximately 2.4 kV difference (with a needle-to-grid spacing ~1 cm), the Taylor cone will form a liquid jet at the tip, which would then release ion droplets that will enter the IMS column to drift toward the IMS detector. It was found during these high voltage experiments that one had to first inject the liquid (via air pressure) into the SS needle. This particular problem and its solution are described later.

2.3.1.2. IMS Drift Column I

The idea for using printed circuit board (PCB) pieces in the ion mobility drift column was conceived by Ben Bathgate, a technician working in the Electrical and Computer Engineering (ECE) Department at the University of Alberta. Where previous

research groups (taking Wu *et al.*[30,31] as an example) have used stainless steel (SS) rings [of dimensions 4.9 (ID) x 5.7 (OD) x 0.8 (Th) cm] separated by (insulator) spacer rings (i.e., 0.1 cm thick Alumina) and high impedance (i.e., 1 MΩ resistors), the present design involved pieces of single-sided PCB that contain a thin film (~ 35.56 μm thick) of copper on a dielectric material FR-4 (together measuring ~0.15 cm thick). Three types of PCB pieces were constructed to represent the guard rings, the grids, and the (Bradbury-Nielsen type) ion shutter gate.

The two grids (i.e., the focus and aperture grids) plus the Bradbury-Nielsen type ion shutter gate were constructed by the following process: (1) thoroughly cleaning each PCB piece with soap and water, then with acetone, followed by ethanol, and finally rinsing in de-ionized water; (2) partially milling out the front-side of the PCB piece [i.e., routing the perimeter of the circular aperture, but leaving the (extraneous) "button" in place to support the grid material during milling]; (3) soldering a layer of brass (6/1000 inch shim stock) to the partially-milled front-side, then milling out the features of the grid or gate; (4) milling out the back and removing the "button"; and, (5) applying selective acid etching to remove the burrs and edges of the grid wires [i.e., with a 5 M concentration of Nitric Acid (Fisher Scientific Ltd., Nepean, ON, Canada) poured through the aperture of the grid or gate that was placed grid-side down on risers such that the acid rises just above the brass layer]. The process for preparing the PCB guard rings was the same, except without steps #3 and 5. The PCB pieces were 4 x 4 cm square with 2 cm diameter apertures (that would act as the inner diameter of a guard ring). The "wires" of the grids (and shutter gate) were ~0.1 mm thick with a 1 mm separation. For the shutter gate, the milling process was modified to leave two separate, alternating (or interdigitating), conducting "combs" whose bases lie on either side of the PCB piece. For the PCB guard rings, grids, and shutter gate, two holes (3.175 mm or 1/8" in diameter) were milled out near two opposite corners of the PCB pieces so that guide/support rods (i.e., the previously mentioned plastic rods) placed through these holes would hold the stack or column together. Figure 2-15 below depicts the basic schematic designs of the PCB guard rings, grids, and ion shutter gate.

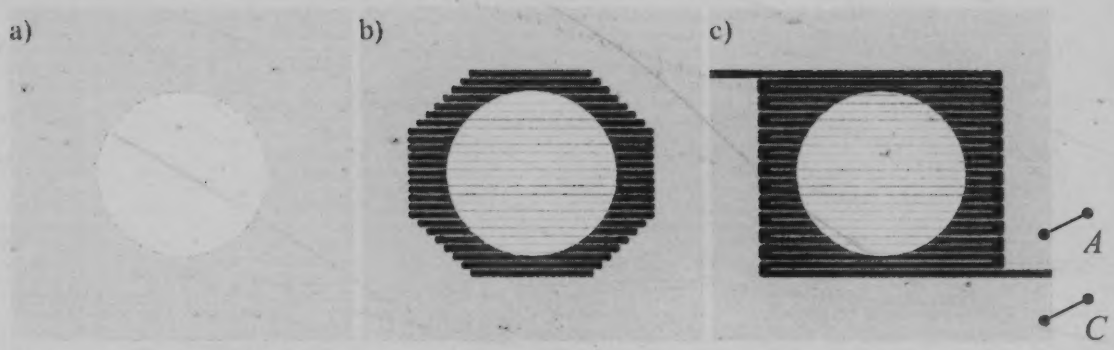

Figure 2-15. Schematic diagrams of the PCB (a) guard ring, (b) grid, and (c) shutter gate. (a-c) The lighter regions represent the conductive metal layer, while the darker regions represent the insulating (FR-4) layer; (c) leads *A* and *C* connect the individual "combs" to different voltage potentials.

To prevent corrosion (oxidation) on the surface of the metal film layer, all PCB pieces were submerged in Liquid Tin (421-500ML; MG Chemicals, Toronto, ON, Canada) – this resulted in a colour change from an orange-red copper to a dull grey. For the copper only grids and shutter gate (without the brass in step #3 above), it was found that simply milling the copper into "wires" resulted in bent or broken copper grids, as the copper was found to be too fragile during the milling process. The solution to this predicament was to apply (via solder) the layer of brass to a PCB guard ring prior to milling the grid features (described in step #3 of the PCB grid construction). The brass layer was found to be capable of surviving the milling process that sought to achieve parallel "wires" spaced ~1 mm (actually 0.9 mm) apart – this resulted in golden brass-coloured grids and shutter gate.

Where Wu *et al.*[30,31] had used 7.2 cm and 13 cm lengths for their desolvation and drift regions, respectively, our present design called for a total length of 10 cm (4 cm and 6 cm for the desolvation and drift regions, respectively), which was scaled down as were the PCB guard rings. This was done for two main reasons: (1) the test version did not require high temporal resolution (which would be limited by this short column) and (2) this short column would use (~30) less PCB pieces than would a 15 cm (5 cm / 10 cm) system (thus reducing the construction time and materials used). Figure 2-16 depicts the electrical schematic diagram of the IMS Column when interfaced with the ES source and the collector-detector (C-D) assembly.

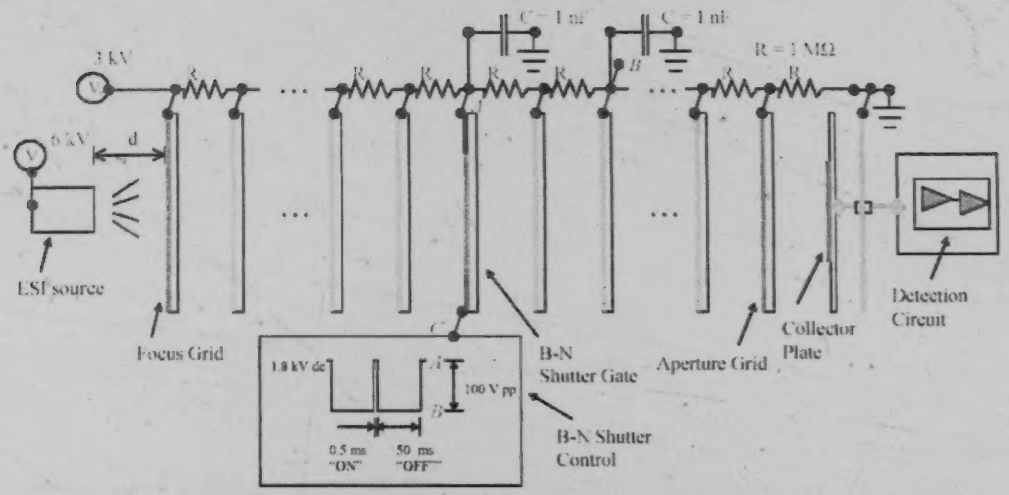

Figure 2-16. Electrical schematic diagram of the PCB IMS column including the ES source and the C-D. Dimensions/parameters: ESI source (~6 kV, ~4 mm o.d. SS needle), focus grid (3 kV, 0.9 mm grid spacing, 0.1 mm wide grid wires, d ~ 1 cm), B-N shutter control (-100 V_{pp}, 50 ms "OFF," 0.5 ms "ON," ~ 1000 V/cm electric field, ~1.8 kV_{dc} ON voltage), aperture grid (~50 V, same as focus grid), collector plate (~ 1 – 1.5 cm diameter, connected by feed through pin to input of detection circuit), detection circuit (> 10 pA, rise time < 0.5 ms, gain ~ 10^9 V/A), and general information ($L_{Focus\ Grid\ -\ Collector\ Plate}$ = 10 cm, $L_{Desolvation}$ = 4 cm, L_{Drift} = 6 cm, $N_{Guard\ Rings/Grids}$ = 65).

From Soppart and Baumbach's analysis of electric fields in drift tubes used for IMS,[32] there are two parameters that one must consider when assembling a drift tube: (1) the inherent field quality, Q_E, and (2) the shielding quality, Q_S. The former indicates the level of uniformity of the electric field that develops across the inner diameter of the drift tube based upon the dimensions of the guard rings within the drift tube, while the latter represents the degree to which the arrangement and the dimensions of these same guard rings within the drift tube would shield the interior of the drift tube from (external) electromagnetic interference. These two parameters can be expressed as follows:

$$Q_E = \frac{[\text{thickness of drift ring}]}{[\text{inner diameter of drift ring}]} \qquad (2.1)$$

$$Q_S = \frac{[\text{distance between drift rings}]}{[(\text{outer diameter - inner diameter}) \text{ of drift ring}]} \qquad (2.2)$$

These two parameters aid in determining the size and spacing for the drift or guard rings for the IMS device. According to Soppart and Baumbach,[32] a Q_E of < 1/10 provides for a

sufficient field quality. Although they state that Q_S should also be minimized, no benchmark values were given. Having designed the column as such, one must check these two parameters. Inserting the design values into these equations, respectively, results in:

$$Q_E = \frac{[35.56 \times 10^{-6}\ \text{m}]}{[0.02\ \text{m}]} = 0.001778 \ll \frac{1}{10} \qquad (2.3)$$

$$Q_S = \frac{[1.54 \times 10^{-3}\ \text{m}]}{[0.04\ \text{m} - 0.02\ \text{m}]} = 0.077 \qquad (2.4)$$

As a comparison, values of $Q_E = 0.04$ and $Q_S = 0.24$ were obtained by Soppart and Baumbach.[32] Therefore the present design satisfies the condition that the values for these two parameters be small, as the design values are an order of magnitude smaller than those listed in the literature.

In designing the IMS column the current drawn through the resistor array (i.e., the resistors coupling the individual guard rings and grids) was considered. For the 6 kV μTK high voltage module, which will be used as the power supplies for testing the column, the maximum rated output current that can be drawn is 85 μA. Therefore, for an array of 65 resistors (or for 65 PCB pieces) with 3 kV difference between the focus grid and the collector-detector (essentially at ground potential), the minimum resistor value is

$$R_{Min} = \frac{V_{column}}{N_{Res} \cdot I_{array}} = \frac{[3 \times 10^3\ \text{V}]}{[(65)(85 \times 10^{-6}\ \text{A})]} = 543\ \text{k}\Omega \qquad (2.5)$$

Assuming a 1 MΩ resistor array (which is larger than R_{Min}), the resultant array current is

$$I_{array} = \frac{V_{column}}{N_{Res} \cdot R} = \frac{[3 \times 10^3\ \text{V}]}{[(65)(1 \times 10^6\ \Omega)]} = 46.2\ \mu\text{A} \qquad (2.6)$$

Picking lower resistor values (e.g. 680 k or 820 kΩ) will result in higher currents. However, driving the power supply closer to its maximum rated current value on a continual basis will shorten its lifetime. (Capacitance considerations for the IMS Column have been made, and are noted in the *Appendix*.)

To connect each PCB piece (e.g., the guard rings, grids, and shutter gate) together electrically via resistors, solder flux (e.g. Kester "44" Rosin Core Solder) was applied to the metal surface of the PCB pieces to improve electrical contact. The process of assembly involved the following steps: (1) pre-cutting of the leads for the 1 MΩ

resistors; (2) pre-"tinning" of the PCB pieces [i.e., by melting some solder onto the surface of the metal (via soldering iron)]; (3) sliding each PCB piece down two plastic rods (each 1/8 inch or 3.175 mm in diameter) that had been anchored by raised temporary supports/platforms; (4) holding a resistor such that one of its leads is above the solder blob; (5) applying the soldering iron to the resistor lead to melt the solder around the resistor lead; and (6) repeating the process. The resultant desolvation (the shorter) and drift regions are depicted in the figure below, without the grids or the shutter gate.

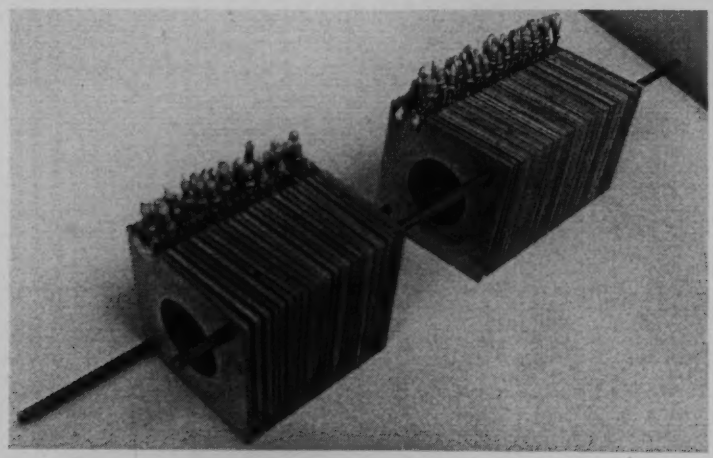

Figure 2-17. Photograph of the Column I desolvation and drift regions (without the grids or shutter gate. View of the front/top of the Column I desolvation (shorter stack) and drift (longer) regions

After the entire IMS column was assembled, several plastic ferrules (i.e., cylinders with orthogonal screw settings) were attached as anchors to hold up the column via the two plaster guide/mounting/support rods, and to interface the ES source mounting in a vertical arrangement as illustrated in the next section. It was found that after assembly of the column, the desolvation and drift region lengths were slightly longer than the designed 4 and 6 cm; this was due to excess solder flux (used to connect the resistors to the PCB pieces). This resulted in the removal of 4 PCB guard rings from the two regions, which reduced the total of PCB pieces to 61, 24 for the Desolvation Region and 37 for the Drift Region. The effective voltage drop across each of the resistors (i.e., across each of the PCB pieces) was actually [3 kV / 61 = 49.18 V ~] 49 V. The figure below shows a schematic of the IMS column to be suspended within a clear Plexiglas box, with the ES source mounted on top of the column's Lexan plate anchor.

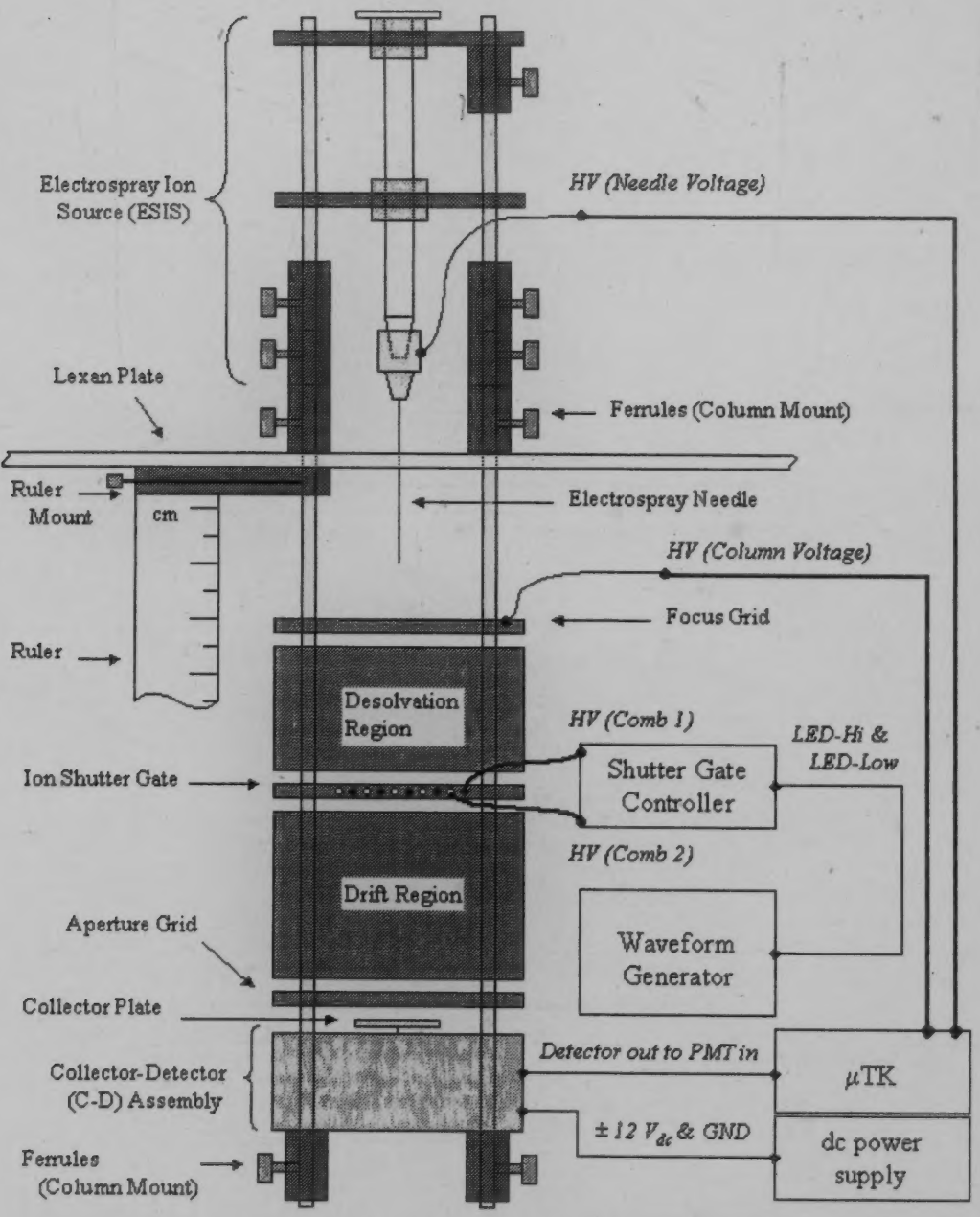

Figure 2-18. Schematic diagram of the ES-IMS Device I system setup. Note that the μTK and the waveform generator lie outside the Plexiglas box in which this device is suspended; the PCB-mounted shutter gate controller is suspended beside the column. The connections (from external sources) – "*LED-Hi & LED-Low*" (waveform generator), "*HV (Column Voltage)*" (μTK), "± 12 V_{dc} & *GND*" (dc power supply), and "*Detector out to PMT in*" (μTK) – interface with the column via banana jacks and an RCA jack (not shown). The aperture through which the needle is fitted is a 2 cm diameter hole. (See Fig. 2-14 for details on the ESIS.)

To control the ion shutter gate – that is, to set it "OPEN" (to allow ions into the drift region) and "CLOSED" (to restrict passage into the drift region) – a pair of 6 pin DIP high voltage (HV) phototransistor optocouplers (H11D1; Fairchild Semiconductor, South Portland, ME) were used as high voltage switches. (The "OPEN" and CLOSED" states are synonymous with the ion pulse being "ON" or "OFF".)

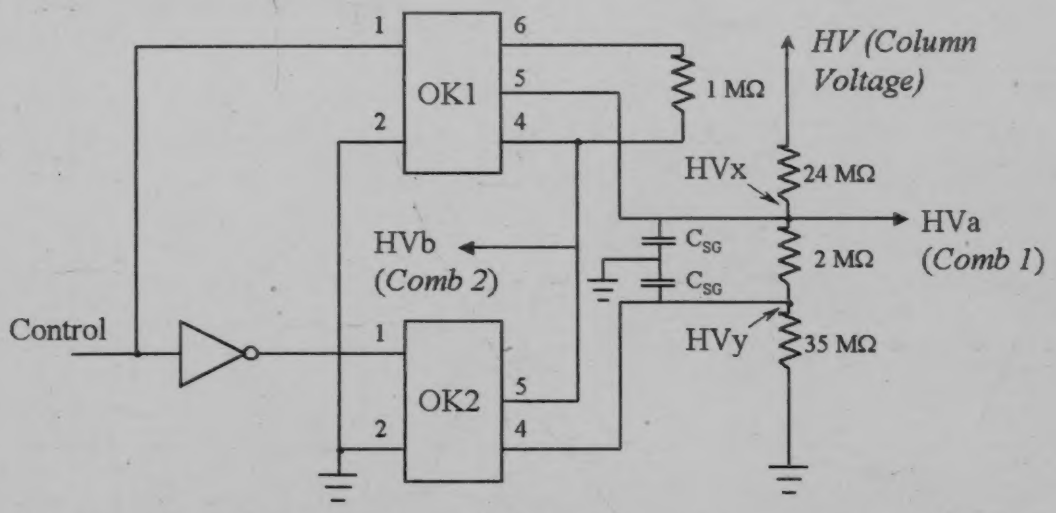

Figure 2-19. Electrical schematic of the Bradbury-Nielsen type ion shutter gate controller. *OK1* and *OK2* are high voltage phototransistor optocouplers (H11D1; Fairchild Semiconductor). C_{SG} represent 6 kV, 1 nF ceramic capacitors.

From the Fig. 2-19, *pin 5* (of *OK1*) is connected to HVa (or *comb 1*) of the shutter gate [which always stays at the corresponding voltage potential (HV_x) within the resistor array]. *Pin 4* (of *OK1*) and *Pin 5* (of *OK2*) are connected to HVb (or *comb 2*) of the shutter gate, while *pin 4* (of *OK2*) is connected to a guard ring two PCB pieces down-column, with a voltage potential HVy. In this case, *pin 4* (of *OK1*) and *Pin 5* (of *OK2*) act as floating switches that toggle between the positive (HVx) and negative (HVy) reference potentials. To switch to the OPEN state, one would trigger *pin 1* of *OK1* (i.e., *LED-Hi*), thus swinging the HVb of *comb 2* toward the same voltage as that of *comb 1* (i.e., HVx). To switch to the CLOSED state, one would trigger *pin 1* of *OK2* (i.e., *LED-Low*), thus swinging the HVb of *comb 2* of the shutter toward HVy [which is ~98 V less than HVx for *HV (Column Voltage)* equal to 3 kV]; this would essentially create an orthogonal electric field (for the actual 0.9 mm grid wire spacing) of ~109 V mm^{-1} in the

drift column that would bar ions from entering the drift region. Figure 2-20 further illustrates the operation of the shutter gate by depicting the circuit schematic during the two states of operation; the 6kV HV ceramic capacitors (C_{SG} = 1 nF) at the positive and negative reference points are included to attempt to stabilize the reference voltages during switching. For this first ES-IMS Device, the timing of the shutter gate will be handled by the function generator (i.e., the Agilent 33120A), whose output will connect to *LED-Hi* and *LED-Low* [shown in Fig.2-19 as "Control" and the inverter or (NOT gate)]; for steady-state operations a dc power supply will be used to connect to these two points on the SG controller.

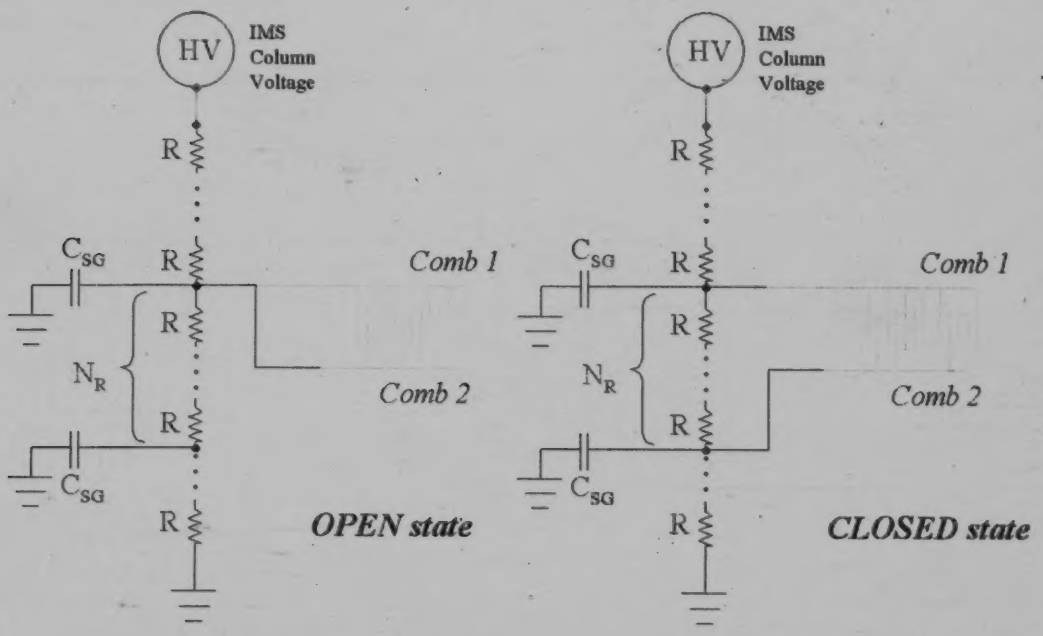

Figure 2-20. Schematic diagram of the operation of the shutter gate. Depiction of the gate in the OPEN state (left) and the CLOSED state (right). N_R = 2 for Shutter Gate I; HV = 3 kV; R = 1 MΩ; C_{SG} = 1 nF (6kV rated ceramic capacitors). *Comb 1*, *Comb 2*, and their respective connections correspond to the shutter connections shown in previous figures.

2.3.1.3. Collector-Detector (C-D) Assembly I

The design of the detector circuit for the first drift column was based on the High Speed Picoammeter circuit as found in the Keithley Low Level Measurements Handbook,[33] which is an op-amp with two feedback resistors (R_F and R_1) in series, a capacitor (C_1) to ground set between these two resistors, and a shunting capacitance (C_F) in parallel with R_F (as shown below). It should be noted that for low-level measurements, the presence of this shunting capacitance (C_F, that inadvertently develops between two conductors) may affect the measurement accuracy, by causing an RC delay that limits the rise time of the circuit. This shunting capacitance (also called stray or parasitic capacitance) in most cases can be reduced greatly by careful mechanical design of the circuit, however it will still be present, thus causing an RC delay that is not desirable for high speed measurements. To compensate for it, and consequently to achieve the desired speed, one needs to match the time constants R_FC_F and R_1C_1. This would cause the feedback loop of the op-amp circuit [shown in Fig. 2-21(left)] to reduce to a simple feedback resistor ($R_F + R_1$) without any shunting capacitance, as shown in Fig. 2-21(right). [The circuit analysis of Fig. 2-21(left) is provided in the *Appendix*.] Here, a 100 MΩ R_F feedback resistor was used for the picoammeter that is based on the OPA129 ultra-low bias current difet operational amplifier. Although C_F is an inadvertent value, we have tried to force a value on it that will hopefully dominate over pre-existing levels such that easier calculation of C_1 can be obtained; in other words, by setting a sufficiently large C_F we hoped to reduce the amount of trial and error required to find C_1. As such, the values of C_F, R_1, C_1 were selected to be 33 pF, 10 MΩ, and 330 pF, respectively.

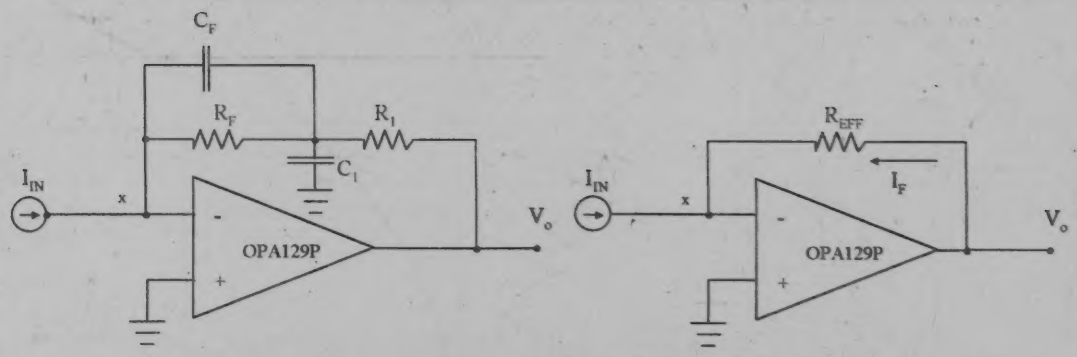

Figure 2-21. Circuit diagram of the Keithley high speed picoammeter. (left) the actual circuit and (right) the effective circuit. R_F = 100 MΩ, C_F = 33 pF, R_I = 10 MΩ, C_I = 330 pF.

To review how such a simple inverting feedback op-amp circuit [shown in Fig. 2-21(right)] would convert an input current to an output voltage, one would recall that the voltage at point "x" (i.e., at the inverting input) is the same as that at the non-inverting input for an ideal op-amp, that is, at ground potential. So, the output is simply the voltage drop across the feedback resistor. Assuming ideal conditions, the input current would be the same as the feedback current, so for this inverting configuration both would be directed at point "x". Then, the output voltage would be I_{IN} multiplied by R_{EFF}, and the gain would simply by R_{EFF} (or V_o divided by I_{IN}). Since any positive ions impinging on the Faraday or collector plate that is connected to the input of the detector would draw out electrons from the input, a current will be seen going into the input, and since the non-inverting input will be set at ground potential, the output voltage will be simply the product of the input current and the feedback resistance. Any input resistances would not affect this output. However, when simulating an input current by using an input voltage followed by input resistors – whereby I_{IN} equals V_{IN} divided by R_{IN} – any additional input resistances would drop the current by the new total R_{IN}.

The complete, three stage picoammeter circuit that was used for the ion detection is as shown below (Fig. 2-22), where an input current (as observed at the collector plate) is converted to a voltage via the first stage and the subsequent stages act as amplifiers for enhancing the input signal. C_{IN} and R_{IN} is a noise reduction circuit, whereby the former is a speed-up capacitor that allows the edges of the signal to be rapidly transferred into the input of the first stage and the latter is a resistor that cancels out the noise from the

feedback loop by producing the negative of the noise from R_F. The respective gains for the stages are ~1.10×10^8 V/A ($G \approx R_F + R_1 = 1.10 \times 10^8$), 10 V/V ($G = 1 + \frac{18k}{2k} = 10$), and 3 V/V ($G = \frac{15k}{4.7k} \approx 3$). For the input terminal (point "y" in Fig. 2-22) of the OPA129 op-amp, a "flying wire" technique was implemented,[34] whereby the connecting components were suspended in space above the circuit board (i.e., they were disconnected from the circuit board) via the use of an insulated (Teflon) solder terminal, press mount, pin type, feed through (Wearnes Cambion Ltd., Hope Valley, Derbyshire, UK). Though this "flying wire" pin connection method reduces the surface resistance (i.e., from the ohmic water layer that inevitably forms in atmosphere) and any additional circuit board capacitance, it is no longer a widely-used technique due to its labour-intensive implementation. (One of these insulated terminals, formerly known as turrets, was also used as a connecting pin between the collector plate and point "x", and is shown in a later section.)

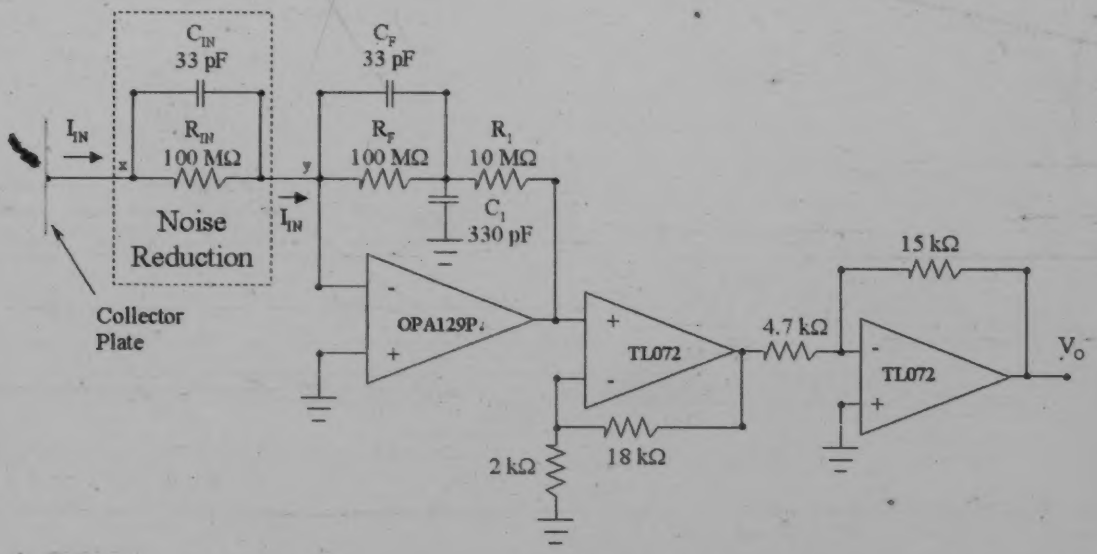

Figure 2-22. Schematic diagram of the picoammeter circuit that is the 1st detector. The stages have gains of ~100 MV/A, 10 V/V, and 3 V/V, respectively.

To summarize, the fast detection circuit used (also known as "Pico I") consisted of three stages. The first would convert the ion current as observed by the collector (Faraday) plate into a voltage using a high current-to-voltage (V/A) gain. This would

require an inverting operational amplifier (op-amp) configuration. The second stage is a a simple non-inverting, V/V gain stage. The third and final stage, another inverting op-amp, would ensure a positive output voltage for the incoming positive ion current, and would act as a voltage/voltage (V/V) gain stage. The input capacitor and resistor would reduce the noise from the feedback loop, while allowing for a faster detection (with the capacitor component).

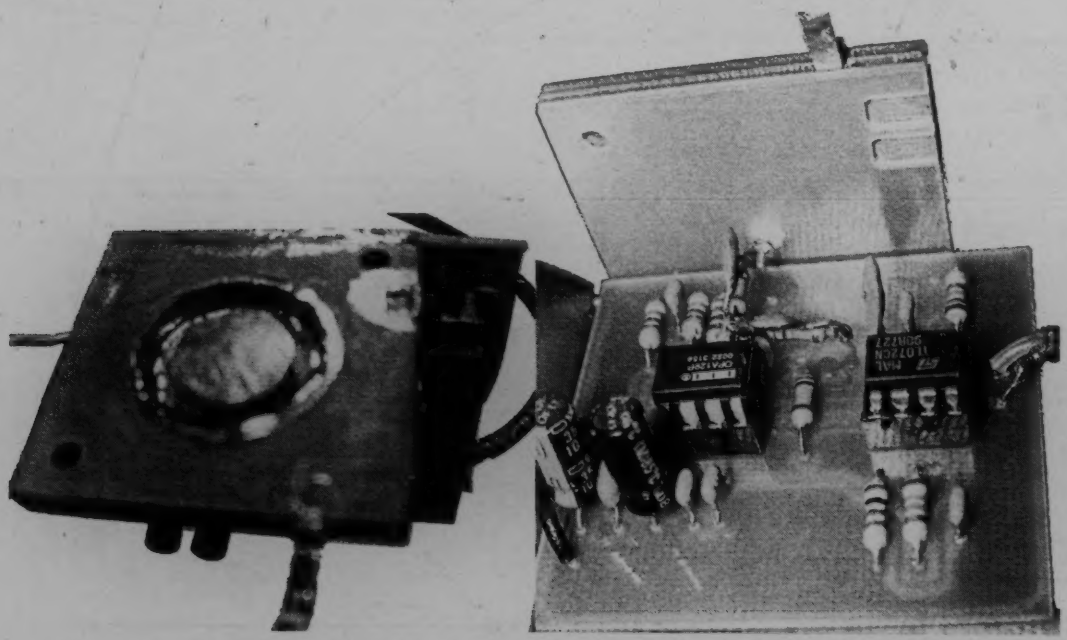

Figure 2-23. Photographs of Collector-Detector Assembly I. (Left) A front/top-angled view of the C-D assembly focusing on the circular collector plate that is set apart from the grounded region surrounding it and (right) a top view of the C-D assembly focusing on the picoammeter, with the 8-pin dip op-amps.

As shown in Fig. 2-23, the C-D Assembly I was composed of the single-sided detector circuit board soldered at right angles to the detector wall (constructed of a trio of single-sided piece of PCB material), which would line up parallel with the sixty-one single-sided PCB pieces in the Column. The collector (Faraday) plate – a 1.5 (D) cm cut piece of brass (6/1000 inch shim stock) was connected to the input of the picoammeter via the Teflon feed through (shown in the Fig. 2-23 as a metal pin in a white tab in the detector wall). The three-stage picoammeter circuit was milled and mounted on a single double-sided PCB piece measuring 4.9 (L) x 4.4 (W) cm. The two holes in the detector wall shown in the figure are for mounting the C-D assembly onto the IMS column via the

same plastic rods that hold the column together; a pair of plastic ferrules under the detector walls was secured to the plastic rods via set-screws in order to hold up the entire device (both the column and the collector-detector assembly). The three detector input wires (for ±12 Vdc plus GND) and the detector output coaxial cable were positioned on opposite sides of the detector PCB (shown on the left and the right in Fig. 2-23, respectively). [Note: Great care should be taken in the handling of high performance circuits, so as not to introduce leakage paths on circuitry from the collector plate to the input of the op-amp and to avoid any electrostatic discharges (ESD) that would damage the circuit components, thus affecting the response of the circuit. As such, the PCB should be cleaned with alcohol, and gloves should be wore when assembling the circuit.]

2.3.1.4. External Equipment

Here the External Equipment refer to the additional instrumentation necessary to operate the ES-IMS Device I, plus corresponding connector cables; this also includes the plastic (containment) box. These additional instruments consist of (1) the control computer, (2) Micralyne's μTK, (3) a pulse generator, and (4) the DC power supplies. The control computer (1) is a Pentium II PC running on the Windows 98 operating system. The software interface for the microfluidic toolkit is LabView (National Instruments, Austin, TX), which communicates with and controls the μTK (2) via the computer's serial communications port. The μTK (2) is an instrument that is primarily designed for microfluidic chip analysis; it contains four high voltage power supplies mounted on two boards that is normally coupled with a laser induced fluorescence (LIF) detection system. For the purposes of this project, the LIF system was disconnected, with the μTK acting as a HV supply. It also acted as the interface between the detector output and the LabView control program, which also displayed the signal on the computer display; this was accomplished by connecting the detector output into the 0-5 Vdc PMT input of the μTK, which would normally sample data from a PMT to monitor the level of fluorescence observed when implementing the LIF experiments. For the shutter gate control, an Agilent 33120A 15 MHz function/arbitrary waveform generator (Agilent

Technologies, Palo Alto, CA) (3) was set to output the necessary $10V_{pp}$ pulses for controlling the HV phototransistor optocouplers that acted as the shutter gate. In addition to these devices, a DC power supply (Model 1670; BK Precision, Yorba Linda, CA) was used to provide Detector I with the ±12 Vdc input voltages and GND. [A similar power supply was used to provide the dc signal to the shutter gate controller inputs (i.e., *LED-Hi* and *LED-Low*) to set the shutter gate either completely OPEN or completely CLOSED.] Finally, a simple 35 (L) x 26 (W) x 35 (H) cm clear plastic box that contained a single 13 cm diameter hole in its top panel, and that was found in the lab and used in conjunction with a small Lexan sheet (i.e., the suspension plate), was used as a containment and suspension device for the IMS column and the ESIS I.

2.4. Results and Discussion of the Preliminary ES-IMS System

In evaluating our prototype, the following testing sequence was utilized: (1) evaluation of the detector circuit (*Section 2.4.1*), (2) evaluation of the ESIS I (*Section 2.4.2*), and (3) evaluation of the shutter gate (*Section 2.4.3*).

2.4.1. Evaluation of the Fast Detection Circuit

For the initial version of the detection circuit (the picoammeter circuit shown in Fig. 2-22), the gain of the picoammeter was first determined by applying a small input voltage using the Hewlett Packard 6213A power supply, then measuring the output (V_o) with the Fluke 179 digital multimeter (DMM). The test conditions are illustrated in Fig. 2-24 below.

The current-to-voltage gain of the picoammeter was evaluated by simulating a (10 nA/V) current with the use of a 100 MΩ input resistor (R_{IN}) prior to the input of the OPA129 op-amp – that is, the input voltage was converted into a current that was then amplified by the gain of the picoammeter. [Note that R_{IN} and C_{IN} are permanent features of the circuit; with a current input (i.e., during ion detection) these components will not affect the amplifier gain (see the *Appendix*).] For the input power for the picoammeter,

the BK Precision Model 1670 DC power supply was used to supply ±12.15 Vdc. The results for this first test are shown in the Fig. 2-25.

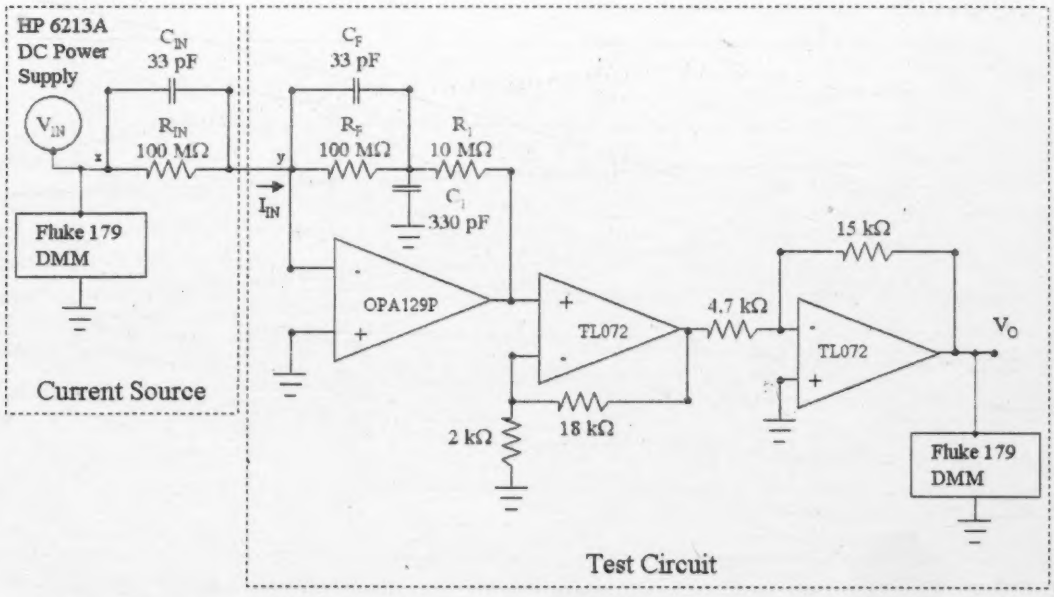

Figure 2-24. Schematic diagram for the testing of the precursor picoammeter circuit that was shown in Fig. 2-22.

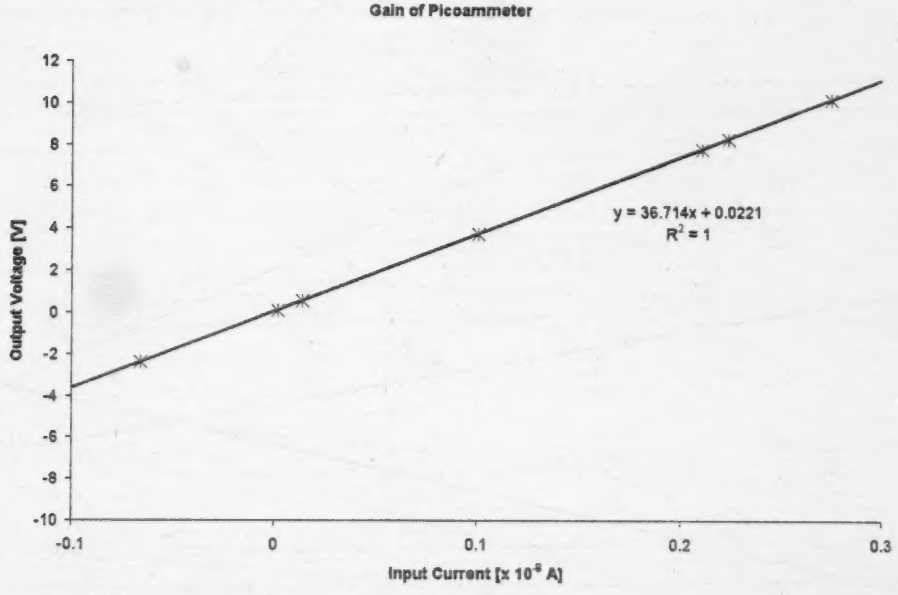

Figure 2-25. A plot of the gain of the picoammeter. The input currents are scaled in terms of 10 nA, with an input resistance of 100 MΩ for a dc input [Eqn.'s (A2.8a) and (A2.8b) for s = 0].

From the trend line in Fig. 2-25, one can see that the gain is 36.71 V / (10^{-8} A) = 36.71 x 10^8 V/A, which is expected as this stage was designed for a gain of 10^9 V/A – that is, the 100 MΩ input resistor would simulate a 10 nA input current (assuming a 1 V input voltage), which would be amplified by -1.1 x 10^8 V/A by the first stage of the operational amplifier (please refer to the *Appendix* for a more detailed analysis of this circuit). The additional 10 V/V gain was due to the non-inverting second stage of the picoammeter; the third stage was an inverting stage with a gain of 3 V/V (shown in Fig. 2-22). The perfect linearity of Fig. 2-25 (i.e., with $R^2 = 1$) can be attributed to there being no transient sources in the test circuit (shown in Fig. 2-24) – that is, the dc power supply provided a constant voltage within 1 mV [with a maximum standard deviation (σ) of 0.7 mV] that was converted to a current by R_{IN}, the noise pick-up was low (~10 mV, with σ ~ 7 mV), and any random spikes in dc mode were discarded by the DMM's.

The frequency/time response of this detector circuit was tested by simulating various sets of pulse trains at the input of the detector. For these experiments, a pair of Hewlett Packard 6213A DC power supplies was used to set the detector input voltages to ±12.06 V_{dc} and ground, the Agilent 33120A waveform generator was used as the input source and the Tektronix TDS 3032 oscilloscope was used to detect the input (generator output or detector input) and the detector output (via an RCA phonojack connector). Figure 2-26 illustrates the test circuit, where R_{Div1} and R_{Div2} are resistor values of a voltage divider used to simulate low currents (in conjunction with the 100 MΩ R_{IN}) at the input (marked "y").

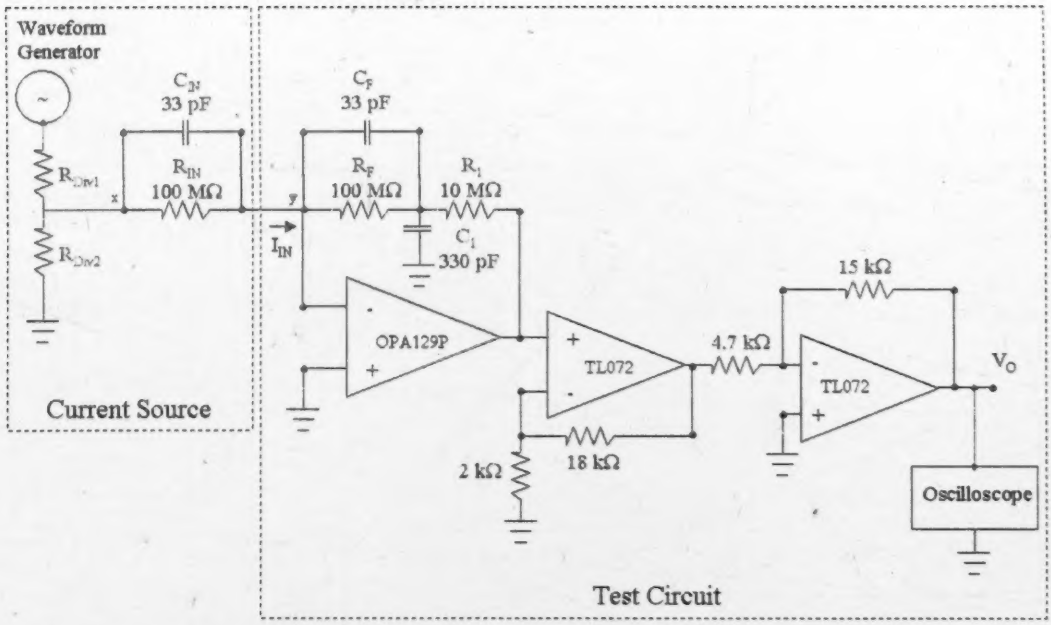

Figure 2-26. Schematic diagram for the testing of the modified picoammeter circuit that was shown in Fig. 2-22.

For these frequency and time response tests, the entire IMS column that was attached to the Lexan plate anchor (i.e., the suspension plate) was removed from the clear plexiglas box and set to suspend between an edge of the box and a convenient support column (i.e., a thick cardboard tube). For frequency response measurements, a 6/100 resistive divider (R_{Div1} = 94 kΩ, R_{Div2} = 6 kΩ in Fig. 2-26) was used to drop the 100 mV_{pp} sinusoidal sweep signal of the function generator to a 6 mV_{pp} detector input. Figure 2-27 (inset, top left) shows that the detector output amplitude decreases with decreasing frequency, despite the fact that the function generator amplitude was constant; this means that the gain is frequency-dependent. Figure 2-27 shows the plot of frequency versus gain, utilizing the amplitudes and frequencies obtained from the frequency sweep [Fig. 2-27(inset, top)] that was then normalized to the ~950 Hz amplitude [Fig. 2-27(inset, bottom right) shows a table of these values].

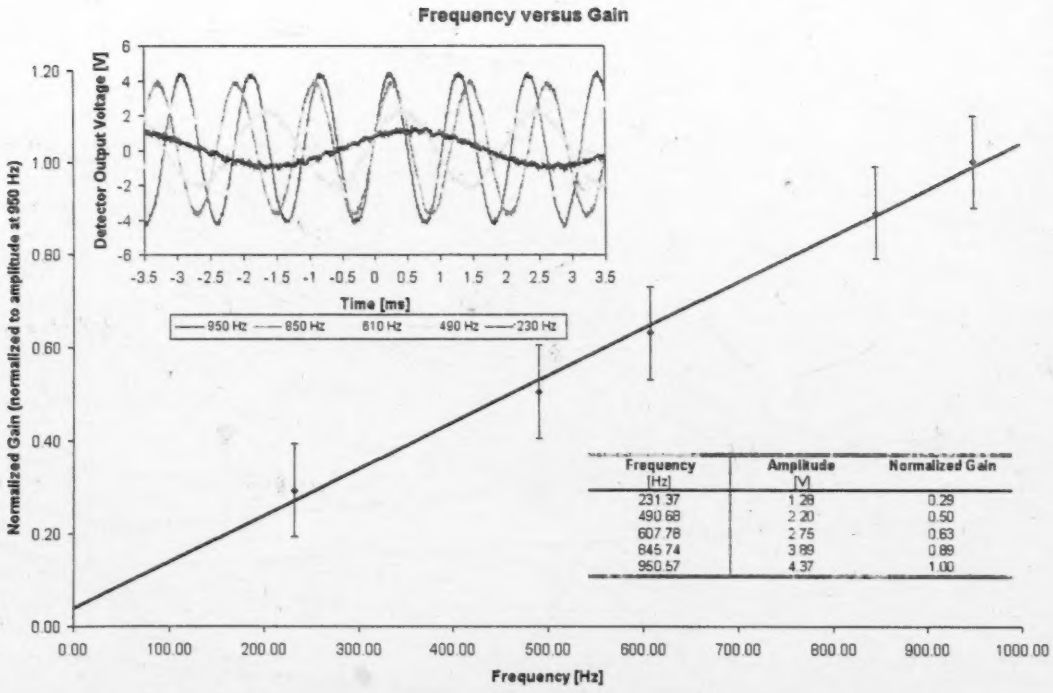

Figure 2-27. Frequency versus gain of the detector circuit shown in Fig. 2-22. Notice that the amplitude drops with decreasing frequency. Also shown is the graph of the frequency sweep (inset, top) and the corresponding table of measured frequency versus measured amplitudes (inset, bottom); values in the table were obtained from the average positive maximum points in the frequency sweep graph. The gain was normalized to the value obtained at ~950 Hz.

To investigate the time response of the circuit, a square wave burst input was used to simulate a small peak at the input of the detector. The input currents at point "y" (shown in Fig. 2-26) were varied (with values of 0.5, 1, 10, and 50 nA); this was done by varying the input voltages (i.e., 0.05, 0.1, 1, or 5 V_{pp}) and using a 6/100 resistive divider (that was mentioned above). The frequency was varied between 1 kHz and 200 Hz, with a burst rate of 20 Hz (to provide a 50 ms period). When the oscilloscope was connected to the output, however, it was found that a ringing or ripple phenomenon occurred (an example is shown in Fig. 2-28), whereby the response appears to be that of an under-damped circuit.

For the sensitivity measurements, an input current of approximately 1 nA was produced [using an input voltage of 100 mV_{pp} divided by 100 MΩ (R_{IN})]. The resultant output ripple waveform (shown in Fig. 2-28) was clipped at ±12 V. [The output voltages

were converted to a current using a gain of 36.71 x 10^8 V/A.] The signal limit of detection (sLOD) was found by focusing on two regions: (a) the interval between -1 and 0 ms (before the pulse) and (b) the interval between 34.95 and 49.95 ms (in the settled region during the pulse). The standard deviations (σ) for these two intervals were found to be 29.55 (for 1000 data points) and 31.52 pA (for 1500 data points), respectively. {The standard deviation was obtained by taking the sum of squared deviations of the region of interest, dividing by the number of data points in this region, then taking the square root of the resultant value [see Eqn. (2.7)].} The limit of detection can then be obtained by multiplying the σ values by three [see Eqn. (2.8)], which results in sLOD values of 88.66 and 94.57 pA, respectively, with an average sLOD of 91.62 pA.

$$\sigma = \sqrt{\frac{\sum_{i}^{n} (\bar{I} - I_i)^2}{n-1}} \tag{2.7}$$

$$sLOD = 3\sigma \tag{2.8}$$

As shown in Fig. 2-28, a ringing or ripple phenomenon (that was mentioned earlier) occurs with the rising edge of the (single or double) burst square wave input. This represents an under-damped condition, whereby the response of the op-amp circuit is not adequate enough to track the input signals but oscillates first before settling down to the steady-state value. In fact, this was found to be the case (not shown) for different input waveforms (e.g., sine, ramp, sawtooth, and sinc waveforms). Any signal that is received would be masked by this effect. This inadequate response of the picoammeter circuit is thus one of the main reasons for a second ES-IMS Device (to be covered in *Chapter 3*).

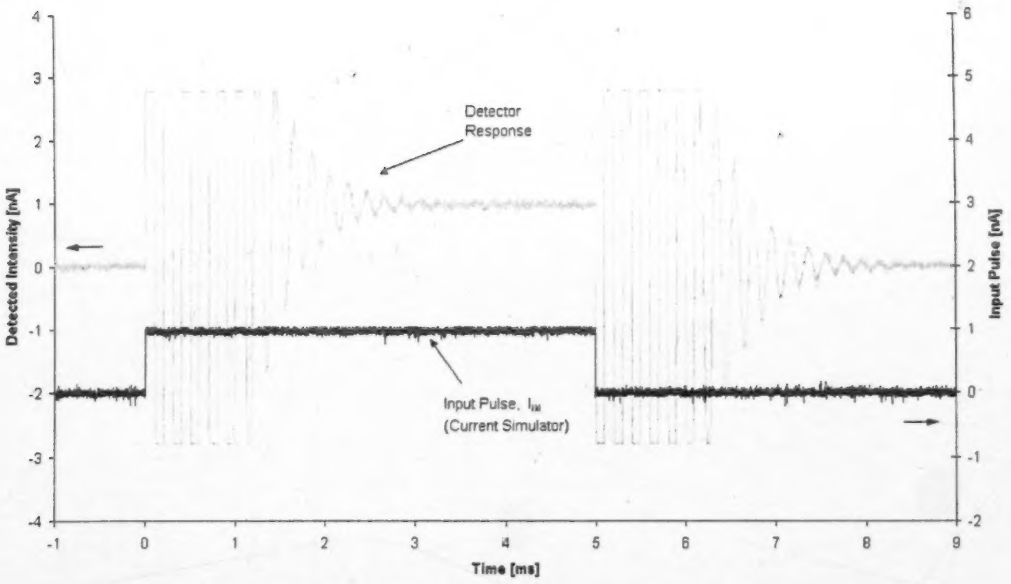

Figure 2-28. Observation of the ripple (or ringing) effect in the detector output for a square-wave burst input of 1 nA (20 Hz frequency). Note that with the left (detector intensity) and right (input pulse) axes aligned, "Input Pulse, I_{IN}" will overlap with the settled region of "Detector Response"; the axes were purposely misaligned to clearly distinguish the input and output waveforms.

2.4.2. Evaluation of ESIS I

It was found upon evaluation of the ESIS I that the OPEN (or "ON") state and the CLOSED (or "OFF") state could be clearly distinguished (see Fig. 2-29). This was done while the ESIS I was interfaced with the rest of the ES-IMS device components – that is, with the focus grid of the IMS column set ~1 cm below the needle tip and with the C-D assembly already interfaced with the bottom part of the IMS column. By connecting the flat-grounded 27-gauge needle of the ES source via an alligator clip attached to the HV (*1A*) input of the μTK, the voltage output (of the μTK power supply) was varied via a program in LabView. Here, the shutter gate was set to be always OPEN [in Fig. 2-29(top)] or always CLOSED [in Fig. 2-29(bottom)], resulting in the former signal being significant larger than the latter. It should be noted that the non-zero ion current observed during the CLOSED state of the ion shutter gate was most likely due to the presence of large droplets (due to an uncontrolled flow and high liquid flow rate, see *Chapter 3*), which overwhelm the shutter gate because the orthogonal electric field is insufficiently

large enough to deflect such large droplets. Alternatively, because the system was operated in the vertical configuration, the droplets could have been large enough to be affected by gravity. Droplets emitted from the Taylor cone that are too large tend to cluster, making evaporation difficult.

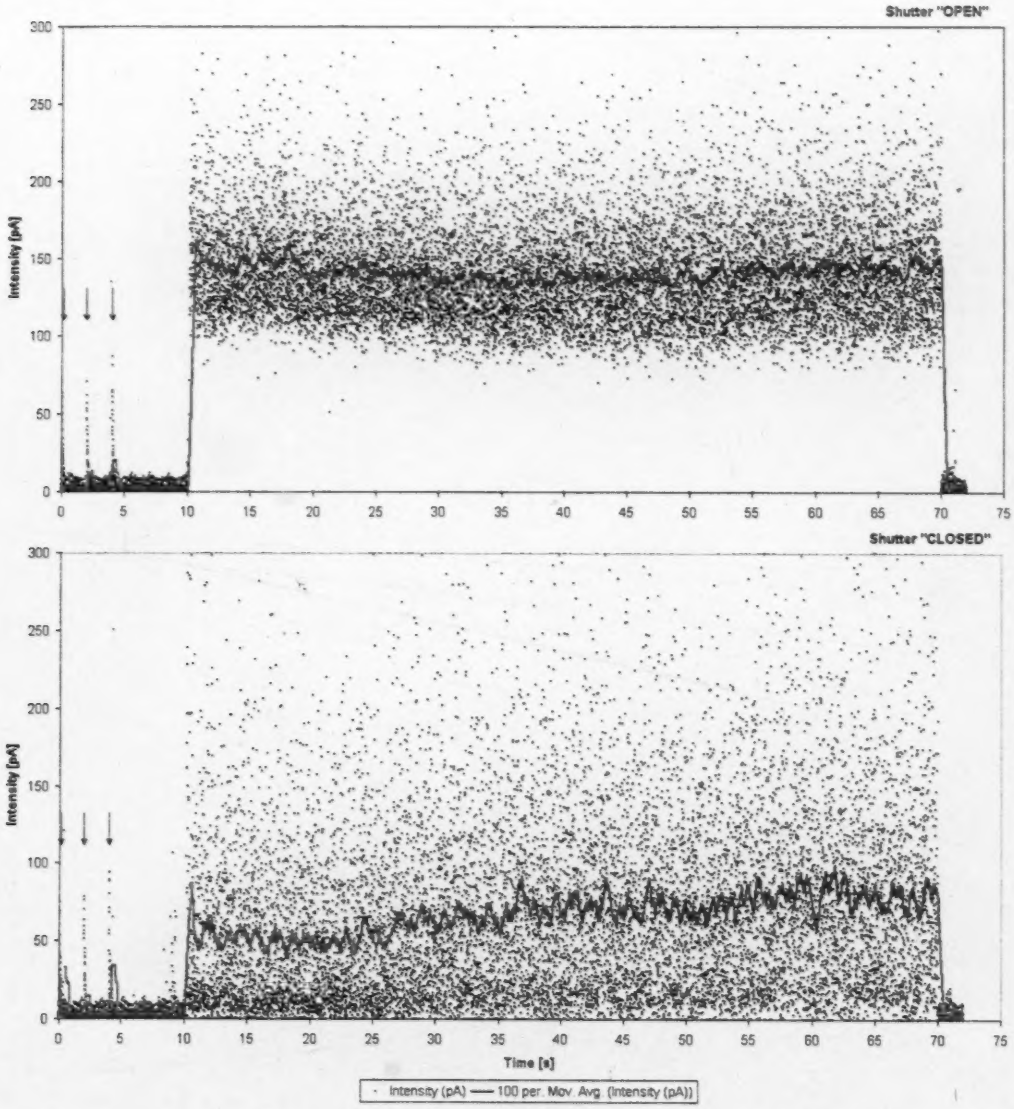

Figure 2-29. Ion spectra for the steady-state OPEN (top) and CLOSED (bottom) states of the shutter gate. Note that the dots represent the ion intensity (pA) detected, while the line represents 100 point moving averages of the raw spectrum data. The three arrows (↓) between 0 and 5 s correspond with the ramp up of the IMS column voltage to 3 kV by steps of 1 kV. (See text for details)

Zero-signal spectra corresponding to a cessation of the liquid flow (in the ESIS) would occasion occur (perhaps due to air bubbles in the needle). Sometimes, these stoppages in flow correct themselves [as in Fig. 2-30(top)], so that the signal is recovered. Other times, manual correction is required, where one must physically apply air pressure to reinitiate flow (e.g., via a fixed-volume micropipette fit into the 1 mL syringe opening of the ES source). If flow is not initiated the zero signal will persist [as shown in Fig. 2-30].

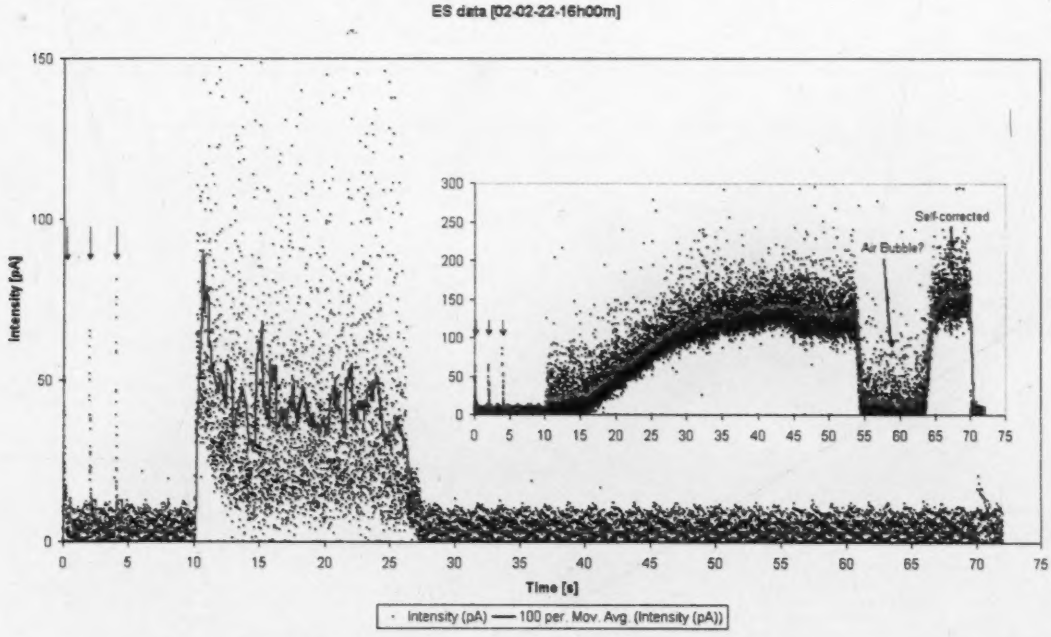

Figure 2-30. Indications of blockages in the ES needle that cause disruptions in the detected ion current. The ion spectrum shown indicates a persistent blockage in the ESIS needle (see text for details). The inset shows a self-corrected blockage (perhaps an air bubble). Note that the dots represent the ion intensity (pA) detected, while the line represents 100 point moving averages of the raw spectrum data. The three arrows (↓) between 0 and 5 s correspond with the ramp up of the IMS column voltage to 3 kV by steps of 1 kV.

Although the data obtained can distinguish between the continuously OPEN and continuously CLOSED states of the ion shutter gate in terms of ion intensity, the acquisition and maintenance of a stable electrospray is somewhat cumbersome. This present system cannot electrically distinguish between spray modes; the successor system has shown such capabilities (see *Chapter 3*). The next steps are high speed tests of the

shutter gate controller (see *Chapter 3*), which were not performed here due to limitations in equipment – that is, the μTK (with a sampling rate of 50 Hz or once every 20 ms) is too slow to resolve expected ~1 ms wide peaks.

2.4.3. Evaluation of Drift Column I

Knowing that the shutter gate was capable of stopping ions, it was still necessary for the shutter gate's response to be measured to determine the reliability of the ion shutter gate. This was accomplished via a Hewlett Packard 6200B 50 V DC power supply to perform low voltage operation to assess the speed of the shutter gate. A major assumption here is that operation at low voltages is the same as at high voltages. A setting of 30 V_{dc} was applied to at the focus grid of the IMS column (where at high voltages a setting of 3 kV_{dc} would normally be applied). A 500 MHz, 8.0 pF, and 10 MΩ oscilloscope probe (connected to a Tektronix TDS 3032 oscilloscope) was used to measure the voltage difference between the switching comb of the shutter and the column ground. Recall that the designed shutter is comprised of 2 "combs" whose "teeth" alternate and are separated by ~1 mm (actually 0.9 mm), one of which is set to the voltage corresponding to its position in the voltage divider of the column and the other that is switched between this voltage and ~100 V less than this voltage. Here, all the voltage values are expected to be ~100 times less because a column voltage of 30 V is used, which is 100 times less than the 3 kV. Figure 2-31 depicts the connections for the waveform generator, where the generator positive lead was connected to *LED-Hi* and the generator negative lead to the *LED-Low*.

Figure 2-32 illustrates the shutter response when a 10 V_{pp} square-wave burst signal (from the waveform generator) is used to trigger the optocouplers of the shutter gate controller.

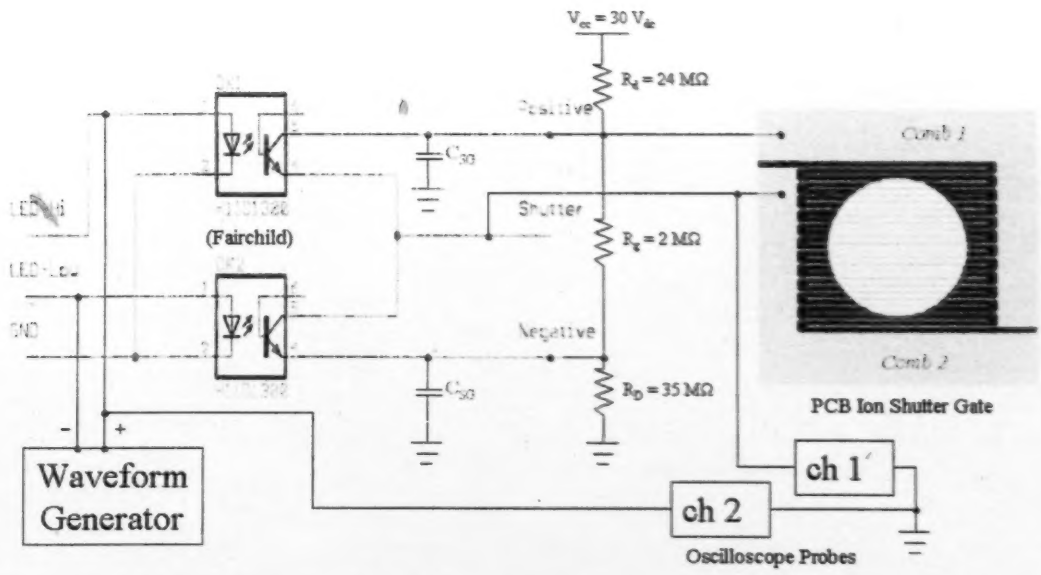

Figure 2-31. Circuit schematic for the testing of the Bradbury-Nielsen type ion shutter gate controller (shown in Figs. 2-19 and 2-21). Notations are the same as in Fig. 2-19. R = 1 MΩ, C_{SG} = 1 nF (6 kV).

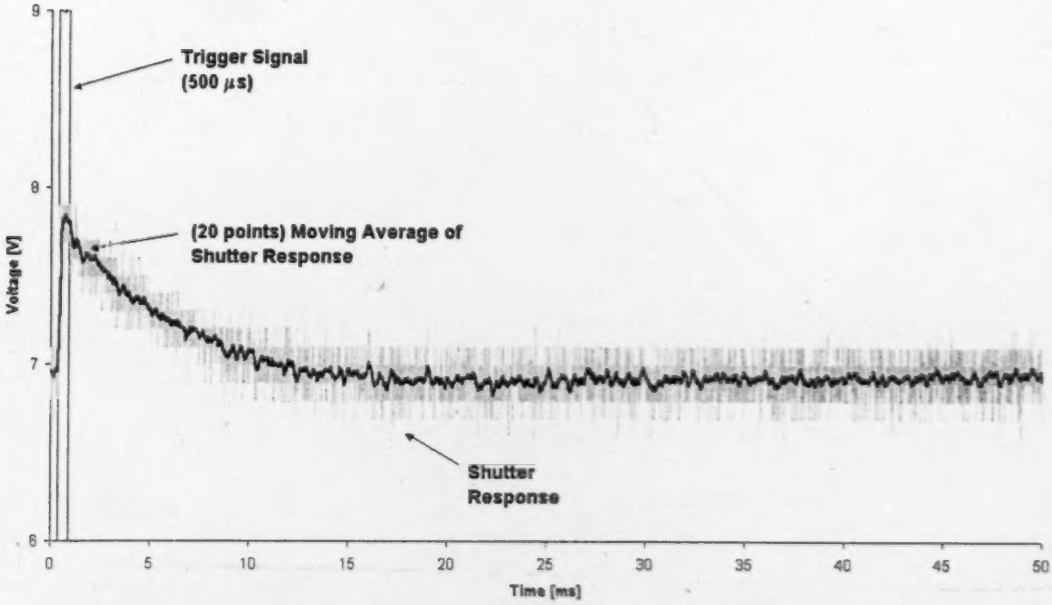

Figure 2-32. Shutter response for 1 kHz square burst shutter inputs. (top) close view and (bottom) wide view. Note the ~10 – 12 ms transient delay (see *Chapter 3* for an explanation).

Here, one can clearly observe a transient delay (exponential decay). It was later found that the shutter was not switching adequately – that is, the inherent capacitance coupled with the column resistance may be the cause of the RC transient shown in Fig. 2-32; this will be evaluated to a greater extent in *Chapter 3*.

The ES source performed its purpose, as designed and as evidenced by the nonzero signals (shown in Fig. 2-29 in *Section 2.3.3.2* above) that returned to normal when the liquid sample was forced through the (air bubble-filled) ES needle. The shutter gate, too, performed well. This was confirmed with the significant drop in ion current as observed by the detector for the CLOSED state as compared with the OPEN state, and was shown in Fig. 2-30. The fact that the CLOSED state ion current was non-zero could be attributed to the overwhelming of the shutter gate by large droplets that could not be sufficiently deflected; alternatively, the large droplets produced in the vertical arrangement may be affected by gravity. This is likely given that the overflow of liquid at the ESIS tip leads to the formation of large (charged) liquid droplets within the drift region (that have been observed visually on the FG of the column). To remedy this, two solutions exist: (1) the shutter gate orthogonal electric field could be increased by connecting the "negative" lead (i.e., *pin 4* of *OK2*) of the shutter control to a lower position in the column resistor array (e.g., six resistors down shutter) to increase the voltage between the two alternating combs (to ~300 V from ~100 V); and, (2) the entire device could be modified to operate in the horizontal configuration. However, two problems exist with the latter solution. The first problem is the reliance on an uncontrolled (liquid sample) flow system (i.e., the hydrostatic pressure-driven flow system), whereby the height of the liquid within the syringe tube of the ESIS induces a pressure-driven flow at the SS tip; this problem requires the use of an alternate flow system (e.g., microfluidic ES chip, with flow control). The second is that the current support structure, namely the plastic rods, was too flimsy to support the column, thus resulting in a non-uniform electric field between the guard rings of the IMS column, as well as an inability of the structure to support the weight of the PCB pieces at the unsupported (i.e., collector-detector) end of the IMS Column: This would require the use of stronger materials for supporting the PCB pieces. During and after each experiment, it was observed that certain regions – namely the area around the shutter gate and the area

near the collector plate, including the collector itself – were noticeably wet. The wetness of the FR-4 layers (of each PCB piece) around the shutter gate is possibly due to ions that have been successfully deflected by the ion shutter gate but accumulate and condense as larger neutral droplets that permeate through the FR-4 layer; the droplets are assumed neutral due to the expected annihilation of the ions that contact the grid wires of the shutter gate. The wetness around and on the collector plate was merely an accumulation of the ions throughout each run (that condense as at the shutter gate region). This wetness may adversely affect the operation of the system; prevention of this condensation is therefore desirable (*Chapter 3* describes an IMS column design that allows for such).

The ringing response of the detector was once again observed on the oscilloscope (not shown) with trials involving the use of the 50:50 (v/v) MeOH/H_2O mixture and with the Agilent 33120A set to output square-burst outputs to simulate a 10 V_{pp}, 0.5 ms (OPEN), 49.5 ms (CLOSED) shutter pulse.

Two types of trigger signals were used for the ES-IMS Device I. For the case of the μTK interface for the detector output (as well as the HV control), the trigger indicating the onset of the shutter gate (1) was the time stamp (corresponding to the voltage control program's onset times). It should be noted that the μTK interface cannot be relied upon for ES-IMS studies because the sampling rate of the μTK optical detection PCB is a (fixed) 50 samples per second, translating to a sample every 20 ms, which is obviously too slow for resolving any of the expected methanol/water peaks. In fact, the ringing behavior would actually have damped out within this time span. For the case of the oscilloscope interface for the detector output (set to ch. 1 of the osc.), the trigger signal was the output of the function generator (i.e., the shutter control pulse set to ch 2 of the osc.); for this case, the voltage control was still being handled by the μTK.

During the longer experimental runs it was observed that after a time, the detector would drop to a zero-signal that would persist even when the air pump technique was applied (involving the use of a fixed volume micropipette to force the liquid into the ES needle via air pressure). It was observed that when the system was shutdown and disconnected (as a safety protocol), and the PCB pieces near the collector were shifted out of the way, the (cup-shaped) collector region was found to be filled up with a pool of the liquid sample that would cause a short circuit between the Faraday plate and the

grounded cup surrounding the plate. The immediate solution for this was to leave the system partially disassembled and left to dry for the course of a day or two; this would also allow the region around the shutter gate, found to be wet after operation, to dry out. After drying out the column, the system was checked by simply turning on the high voltages without introducing any liquid sample/solvent (this type of test was referred to as a "control run"). A return to the baseline (i.e., a zero-signal) would indicate that the system was back to "normal." This "control run" was also used prior to and during the experiments to indicate continued normal operation, and to allow for any real signals to be distinguished.

2.5. Conclusions

In summary, the (prototype) system, constructed from printed circuit board (PCB) components, did demonstrate successful slow-speed operation. Firstly, it was shown that the electrospray source was indeed producing ions, which could be deflected by the shutter gate. This was observed with a drop in the ion signal at the detector during the CLOSED state; a visible wetting of the region around the shutter gate may also be indicative of ion production (if ions were not present, this particular region would not be wet at all – that is, only ions, not neutral molecules, could be swept aside by the shutter gate). The shortcomings of the design, however, lie in (1) the flimsiness of the ESIS mount, (2) the use of plastic guide rods that were too flexible, (3) the unprotected suspension of the shutter gate controller from the column, (4) the inadequate response of the detector, and (5) the bulkiness of the entire system. The first concern resulted in the imprecision and inaccuracies regarding the positioning of the needle within the device. The second led to non-uniformity in the drift electric fields within the column. The third may lead to possible external effects, such as physical damage and perhaps even electromagnetic interference. The fourth, and probably the most important, likely led to the rippling phenomenon, which completely blocked any real signal that would have been observed. The fifth (arising due to the present need of external instruments such as the μTK and the numerous DC power supplies) would play a much larger role once the

above problems are resolved, and when portability and ease of use become more of an issue.

The condensation of liquid (especially around the collector plate and the shutter gate region) can be attributed to two main reasons: (1) the closed design of the column, which would discourage the evaporation of the liquid sample, and (2) the relatively uncontrolled flow system of the ESIS, which would sometimes require the brute force application of (too much) air pressure to force the liquid into the ES needle. To solve the first problem, an IMS column could be designed using double-sided PCB pieces that would be separated by air, thus promoting the evaporation of the liquid sample via the passive airflow between the guard rings and especially around the collector plate. (The capabilities and the possible consequences of this open design will be addressed in *Chapter 3*.) As for the second problem, with the eventual interface of a microfluidic chip-based ES source, where flow rates would be controlled by electro-osmotic flow (for example), this would no longer be a problem. Also, this microchip ES system would allow for portability in the form of a miniaturized system (compared with a syringe-pump-based system). For now, this flow problem cannot be avoided.

2.6. References

(1) Figeys, D.;Gygi, S. P.;McKinnon, G.; and Aebersold, R., "An integrated microfluidics tandem mass spectrometry system for automated protein analysis," *Analytical Chemistry*, **70** (1998), pp. 3728-3734.

(2) Figeys, D.;Lock, C.;Taylor, L.; and Aebersold, R., "Microfabricated device coupled with an electrospray ionization quadrupole time-of-flight mass spectrometer: Protein identifications based on enhanced-resolution mass spectrometry and tandem mass spectrometry data," *Rapid Communications in Mass Spectrometry*, **12** (1998), pp. 1435-1444.

(3) Liu, H. H.;Felten, C.;Xue, Q. F.;Zhang, B. L.;Jedrzejewski, P.;Karger, B. L.; and Foret, F., "Development of multichannel devices with an array of electrospray tips for high-throughput mass spectrometry," *Analytical Chemistry*, **72** (2000), pp. 3303-3310.

(4) Figeys, D.;Ning, Y. B.; and Aebersold, R., "A microfabricated device for rapid protein identification by microelectrospray ion trap mass spectrometry," *Analytical Chemistry*, **69** (1997), pp. 3153-3160.

(5) Figeys, D.; and Aebersold, R., "Nanoflow solvent gradient delivery from a microfabricated device for protein identifications by electrospray ionization mass spectrometry," *Analytical Chemistry*, **70** (1998), pp. 3721-3727.

(6) Lazar, I. M.;Ramsey, R. S.;Sundberg, S.; and Ramsey, J. M., "Subattomole-sensitivity microchip nanoelectrospray source with time-of-flight mass spectrometry detection," *Analytical Chemistry*, **71** (1999), pp. 3627-3631.

(7) Wang, C.;Oleschuk, R.;Ouchen, F.;Li, J. J.;Thibault, P.; and Harrison, D. J., "Integration of immobilized trypsin bead beds for protein digestion within a microfluidic chip incorporating capillary electrophoresis separations and an electrospray mass spectrometry interface," *Rapid Communications in Mass Spectrometry*, **14** (2000), pp. 1377-1383.

(8) Tang, K. Q.;Lin, Y. H.;Matson, D. W.;Kim, T.; and Smith, R. D., "Generation of multiple electrosprays using microfabricated emitter arrays for improved mass spectrometric sensitivity," *Analytical Chemistry*, **73** (2001), pp. 1658-1663.

(9) Ramsey, R. S.; and Ramsey, J. M., "Generating electrospray from microchip devices using electroosmotic pumping," *Analytical Chemistry*, **69** (1997), pp. 1174-1178.

(10) Xue, Q. F.;Dunayevskiy, Y. M.;Foret, F.; and Karger, B. L., "Integrated multichannel microchip electrospray ionization mass spectrometry: Analysis of peptides from on-chip tryptic digestion of melittin," *Rapid Communications in Mass Spectrometry*, **11** (1997), pp. 1253-1256.

(11) Xue, Q. F.;Foret, F.;Dunayevskiy, Y. M.;Zavracky, P. M.;McGruer, N. E.; and Karger, B. L., "Multichannel microchip electrospray mass spectrometry," *Analytical Chemistry*, **69** (1997), pp. 426-430.

(12) Figeys, D.; and Pinto, D., "Proteomics on a chip: Promising developments," *Electrophoresis*, **22** (2001), pp. 208-216.

(13) Figeys, D., "Array and lab on a chip technology for protein characterization," *Current Opinion in Molecular Therapeutics*, 1 (1999), pp. 685-694.

(14) Pinto, D. M.;Ning, Y. B.; and Figeys, D., "An enhanced microfluidic chip coupled to an electrospray Qstar mass spectrometer for protein identification," *Electrophoresis*, **21** (2000), pp. 181-190.

(15) Figeys, D., "Adapting arrays and lab-on-a-chip technology for proteomics," *Proteomics*, **2** (2002), pp. 373-382.

(16) Oleschuk, R. D.; and Harrison, D. J., "Analytical microdevices for mass spectrometry," *Trac-Trends in Analytical Chemistry*, **19** (2000), pp. 379-388.

(17) Wen, J.;Lin, Y. H.;Xiang, F.;Matson, D. W.;Udseth, H. R.; and Smith, R. D., "Microfabricated isoelectric focusing device for direct electrospray ionization - mass spectrometry," *Electrophoresis*, **21** (2000), pp. 191-197.

(18) Kriger, M. S.;Cook, K. D.; and Ramsey, R. S., "Durable gold-coated fused silica capillaries for use in electrospray mass spectrometry," *Analytical Chemistry*, **67** (1995), pp. 385-389.

(19) Barnidge, D. R.;Nilsson, S.;Markides, K. E.;Rapp, H.; and Hjort, K., "Metallized sheathless electrospray emitters for use in capillary electrophoresis orthogonal time-of-flight mass spectrometry," *Rapid Communications in Mass Spectrometry*, **13** (1999), pp. 994-1002.

(20) Barnidge, D. R.;Nilsson, S.; and Markides, K. E., "A design for low-flow sheathless electrospray emitters," *Analytical Chemistry*, **71** (1999), pp. 4115-4118.

(21) Chen, Y. H.;Hill, H. H.; and Wittmer, D. P., "Thermal effects on electrospray ionization ion mobility spectrometry," *International Journal of Mass Spectrometry and Ion Processes*, **154** (1996), pp. 1-13.

(22) Yuan, C. H.; and Shiea, J., "Sequential electrospray analysis using sharp-tip channels fabricated on a plastic chip," *Analytical Chemistry*, **73** (2001), pp. 1080-1083.

(23) McDonald, J. C.;Chabinyc, M. L.;Metallo, S. J.;Anderson, J. R.;Stroock, A. D.; and Whitesides, G. M., "Prototyping of microfluidic devices in poly(dimethylsiloxane) using solid-object printing," *Analytical Chemistry*, **74** (2002), pp. 1537-1545.

(24) Chiou, C. H.;Lee, G. B.;Hsu, H. T.;Chen, P. W.; and Liao, P. C., "Micro devices integrated with microchannels and electrospray nozzles using PDMS casting techniques," *Sensors and Actuators B-Chemical*, **86** (2002), pp. 280-286.

(25) Crabtree, H. J.;Cheong, E. C. S.;Tilroe, D. A.; and Backhouse, C. J., "Microchip injection and separation anomalies due to pressure effects," *Analytical Chemistry*, **73** (2001), pp. 4079-4086.

(26) Petrucci, R. H.; and Harwood, W. S., *General chemistry: Principles and modern applications*, 7th, Prentice-Hall, Inc., Upper Saddle River, New Jersey, 1997.

(27) Li, J. J.;Wang, C.;Kelly, J. F.;Harrison, D. J.; and Thibault, P., "Rapid and sensitive separation of trace level protein digests using microfabricated devices coupled to a quadrupole-time-of-flight mass spectrometer," *Electrophoresis*, **21** (2000), pp. 198-210.

(28) Wittmer, D.;Chen, Y. H.;Luckenbill, B. K.; and Hill, H. H., "Electrospray ionization - ion mobility spectrometry," *Analytical Chemistry*, **66** (1994), pp. 2348-2355.

(29) Chen, Y. H.;Siems, W. F.; and Hill, H. H., "Fourier transform electrospray ion mobility spectrometry," *Analytica Chimica Acta*, **334** (1996), pp. 75-84.

(30) Wu, C.;Siems, W. F.;Asbury, G. R.; and Hill, H. H., "Electrospray ionization high-resolution ion mobility spectrometry - mass spectrometry," *Analytical Chemistry*, **70** (1998), pp. 4929-4938.

(31) Wu, C.;Siems, W. F.;Klasmeier, J.; and Hill, H. H., "Separation of isomeric peptides using electrospray ionization/high-resolution ion mobility spectrometry," *Analytical Chemistry*, **72** (2000), pp. 391-395.

(32) Soppart, O.; and Baumbach, J. I., "Comparison of electric fields within drift tubes for ion mobility spectrometry," *Measurement Science & Technology*, **11** (2000), pp. 1473-1479.

(33) Keithley, J. F., *Low level measurements: precision DC current, voltage and resistance measurements*, 5th Edition, Keithley Instruments, Inc., Cleveland, 1998.

(34) An example of the "flying wire" connection also referred to as "air wiring" can be found in the datasheet for a precision CMOS dual micropower operational amplifier (LMC6062; National Semiconductor).

(35) Kebarle, P.; and Tang, L., "From ions in solution to ions in the gas-phase: The mechanism of electrospray mass spectrometry," *Analytical Chemistry*, **65** (1993), pp. A972-A986.

Chapter 3

Follow-up Design of a PCB-based Electrospray – Ion Mobility Spectrometer*

Table of Contents

Page

3.1. Introduction 93
3.2. Follow-up Design and Testing of a Novel ES-IMS System 93
3.2.1. Description of ES-IMS Device II 95
3.2.1.1. Description of ESIS II 95
3.2.1.2. Description of IMS Drift Column II 96
3.2.1.3. Description of C-D Assembly II 105
3.2.1.4. Description of the Control Box 109
3.2.1.5. Description of (ES-IMS) Clear Box 111
3.2.1.6. Description of the External Equipment 113
3.3. Results and Discussion 114
3.3.1. Cytochrome c 125
3.4. Conclusions 136
3.5. References 138

* A portion of this chapter has been accepted for publication as "A novel electrospray – based ion mobility spectrometer" in the *American Journal of Physics* **(2003)**, by Bathgate, B.; Cheong, E. C. S.; and Backhouse, C. J.

3.1. Introduction

The need for a second ion mobility spectrometry (IMS) drift column arose from the various shortcomings of the first. Namely, the IMS Column I was prone to non-uniform and inconsistent drift electric fields (due to the overly flexible plastic support rods), to the ringing/ripple effect (partially due to a slow and under-damped picoammeter circuit), and to inaccuracies and imprecision in ES needle positioning within the device (due to a non-rigid ES source mount). The first device was also not suitable for portable operations due to the high voltage (HV) and shutter gate (SG) controls (including power supplies) being housed in two separate external instruments – Micralyne's microfluidic tool kit instrument (μTK) and an Agilent 33120A Waveform Generator; the detector also required its own external power supplies, in the form of two Hewlett Packard 6213A DC power supplies that provided the ±12 V_{dc} inputs.

The second ES-IMS device was designed to correct these initial design shortfalls, by slotting the guard rings and grids in a rigidly-held structure, by constructing a more stable ESIS and IMS assembly, and by using a self-contained control unit (in place of the external HV and SG controls). The Device II design, and its evaluation, will be described in greater detail in this chapter.

3.2. Follow-up Design and Testing of a Novel ES-IMS System

As mentioned in the *Introduction* above, the second ES-IMS device was designed to surpass the first in terms of performance. As such, it incorporates various components built with the following design goals in mind: (1) portability, (2) safety, and (3) user-friendliness. In order to accomplish these goals, the device had to be housed in one single box, with the minimum of external connections allowable, and with a communication line between the box and a computer. Within the box must be housed the HV and the SG controls, thus their requisite power supplies had to be added to the list of external equipment. Finally, both the ESIS and the column must be made rigid, so as to avoid inaccuracies and imprecision in experimentation – that is, to prevent the ES needle

from inadvertently shifting position from the central axis of the IMS column during operation and to prevent inconsistencies in the uniformity of the drift electric field.

To that end, the ES-IMS Device II can be described as containing the following six modules, as illustrated in Fig. 3-1: (1) the ESIS II, (2) the IMS Column II, (3) the Collector-Detector (C-D) Assembly II, (4) the Control Box, (5) the (ES-IMS) Clear Box, and (6) the External Equipment.

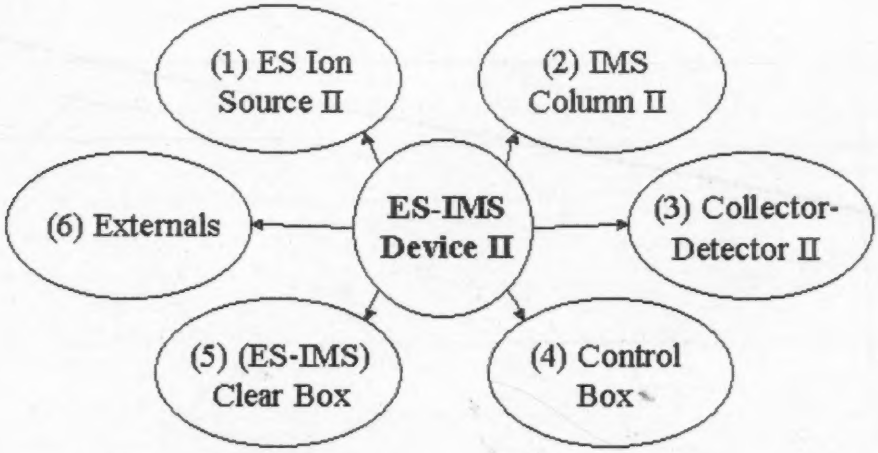

Figure 3-1. A schematic illustration of the various modules of ES-IMS Device II.

The novel aspects of this design center mainly around the utilization of the PCB material as the building material for the IMS column [which allows for easy modification (e.g., miniaturization or expansion), quick and simple construction, and mass production] and the utilization of a PIC-Microboard system for supplying the operations of the device (i.e., the shutter gate timing, the detector power supply, the high voltage supply, the safety interlocks for the high voltage components, the trigger signals for the data acquisition). Future designs would eliminate the need for the external equipment (which presently limit the portability of the system). With some modifications (e.g., adding a liquid crystal display, external control buttons, and additional RAM chips or a USB connection, etc.), this microboard-based approach could provide for self-contained operation. Because of the PCB and Microboard elements of this design, our IMS could potentially be as compact, field portable, and simple as commercially available ^{63}Ni-IMS systems (that are unsuitable for non-volatile substances, such as proteins), but allows for

the power of ES-based systems, namely the ability to analyze non-volatile (e.g., proteins, peptides, drugs) as well as volatile materials (e.g., explosives). Furthermore, our modular IMS column can be easily interfaced with microfluidic chip-based electrospray sources, thus giving the myriad advantages of microfluidic chip systems (i.e., on-chip separations, on-chip PCR, on-chip protein digestion, highly parallel implementation, etc.). In addition due to the relative ease of construction and design of the system, parallel (multiple) IMS columns can be used to simultaneously study such effects as the varying of drift gases, the varying of drift temperatures, the varying of drift lengths, and the varying of detector systems, among other effects, on the mobility of ions in atmosphere. These parallel columns could also be interfaced with a single, wide ES chip for example, wherein loading a single well with the sample leads to parallel sets of microchannels/ microchambers (each set of which allows for the following on-chip features to be set in parallel that would interface with each IMS column: no separation, pre-separation, PCR, and protein digestion, etc.), each microchannel ending in an electrospray tip.

The following sections do more to describe the design concepts, the fabrication of the components (highlighted in Fig. 3-1), and their evaluation.

3.2.1. Description of ES-IMS Device II

3.2.1.1. Description of ESIS II

The ESIS II remained the same in terms of design as the ESIS I – that is, it consisted of a standard 1 mL syringe with a blunt (i.e., flat-ground) 27-gauge SS needle. The difference here was in the mounting for this component within the ES-IMS device. In other words, a mounting structure was designed such as to secure the ESIS directly above the IMS column, in a manner that would allow the ES needle to be centered along the axis of the column. This mounting structure comprised a 7 (ID) x 16 (OD) x 20 (L) mm ferrule (basically a tube with a set-screw positioned in the middle of the length of the tube) mounted on a 5 mm thick mounting surface built directly onto the Cover Plate of the Clear Box (see *Section 3.2.1.5.*). This effectively limited any possible, inadvertent,

lateral ES needle position shifts during operation; vertical shifts, on the other hand, are still possible if great force is applied downward on the vertically-aligned syringe of the ESIS, although the nylon bolt (that is part of the ferrule) mostly limits this occurrence when tightened. Once again, note that this particular ESIS is essentially a sheathless interface, except without either a sheath gas or a pulled tip (see *Chapter 1*).

3.2.1.2. Description of IMS Drift Column II

Design of the IMS Column II

The second Drift Column – composed of double-sided PCB pieces separated by air – would have the same inherent electric field quality [Q_E, Eqn. (2.3)] and shielding quality [Q_S, Eqn. (2.4)] as the first column, since the thickness, the circular aperture diameter, and the separations of the guard/drift rings were essentially the same.

Because the 6 kV EMCO high voltage power supplies (previously mounted on the HV boards of the μTK) are now used separately (i.e., by themselves and not within the μTK), the maximum output current that can be drawn is 166 μA, compared with the 85 μA maximum current for the μTK; just to be safe, the design would limit this to a 100 μA maximum current draw. Therefore, for an array of 61 resistors (or for 62 PCB surfaces) with 3 kV difference between the focus grid (FG) and the collector-detector (essentially at ground potential), the minimum resistor value is

$$R_{Min} = \frac{V_{column}}{N_{Res} \cdot I_{array}} = \frac{[3 \times 10^3 \text{ V}]}{[(61)(100 \times 10^{-6} \text{ A})]} = 492 \text{ k}\Omega. \qquad (3.1)$$

Assuming a 1 MΩ resistor array (which is larger than R_{Min}), the resultant array current is

$$I_{array} = \frac{V_{column}}{N_{Res} \cdot R} = \frac{[3 \times 10^3 \text{ V}]}{[(61)(1 \times 10^6 \ \Omega)]} = 49.2 \ \mu\text{A} \qquad (3.2)$$

Even operating with a parallel set of resistor arrays [to be described in *Section 3.2.3.1* for the segregated (shutter) HV configuration], the total current drawn would be twice I_{array} or 98.4 μA, which is still under our "safe limit" of 100 μA.

In terms of the physical design, the second IMS column calls for a 4 cm desolvation region and a 6 cm and drift region, using a combined total of sixty-two, 4 x 4 cm PCB surfaces with 2 cm diameter apertures all stacked together. The IMS Column II was actually constructed of 31 double-sided PCB pieces (each of which acts as both the guard ring and insulator) sandwiched between two (single-sided PCB) side-boards such that the insulator between the guard rings would alternate between air and the FR-4 layer of the PCB. [This may lead to capacitive effects that may or may not affect the ion drift, however, it would provide a more uniform electric field (assuming that the voltage differences between the 1 MΩ resistor-separated guard rings, and the spacing between the PCB pieces, are approximately equal). Also, with the guard rings soldered in place within the sandwiching plates (or side-boards), the structure is rigid enough to be placed on its side (for implementation in the horizontal mode to eliminate any gravity effects), although a vertical reservoir or manometer (plus fittings and seals) would have to be designed to interface with a horizontal ES-IMS Device.] These two side-boards would serve three purposes: (1) to act as the mounting points for the IMS column, such that a clamping/mounting structure built into the Cover Plate of the Clear Box (see *Section 3.2.1.5.*) can be made to suspend the column; (2) to secure the guard rings in set positions, via solder joins, for ensuring consistency and uniformity of the drift electric field and for maintaining a rigid structure that would allow a change in overall device orientation from vertical to horizontal; and, (3) to house the C-D Assembly II, and to shield it from electromagnetic interference (by way of grounded conducting regions). Furthermore, it was hoped that this open design would allow for the sample liquid to evaporate faster, thus avoiding the dry-up time as was required for the first column, where the liquid would pool at the "cup" between the collector (Faraday) plate and the grounded detector wall, thus short-circuiting the detector input signal (see *Chapter 2*). This open scheme would also hopefully allow evaporation of the region around the shutter gate, which was previously observed to be wet after operation.

The focus grid (FG), the Bradbury-Nielsen type ion shutter gate (SG), and the aperture grid (AG) were the same as for Column I (see *Chapter 2*), except that they were constructed on double-sided PCB (not single-sided), where the "bottom-side" is actually just an adjacent guard ring.

Fabrication of the IMS Column II

The construction of the individual IMS column components (i.e., the guard rings, grids, and shutter gate) was similar to that for the first IMS column (see *Chapter 2, Section 2.3.1.2* for details regarding the milling process for the IMS column pieces; see Fig. A3-2 in the *Appendix* for more precise schematic diagrams of these components). The major differences are the use of double-sided copper clad boards (which reduces the number of PCB pieces by roughly two for the similar length drift tube), the use of two single-sided copper clad boards as side-boards (to replace the overly flexible plastic support rods of IMS Column I), and the use of large PCB pieces for the grids and shutter gate. The latter (i.e., the larger grid and shutter gate IMS column pieces) is to accommodate the extra current limiting resistor for the focus grid, the shutter control circuitry for the B-N shutter gate, and the grounding plane for the drift ring after the aperture grid (that would actually fit with the collector plate shielding structure). This relatively simple construction of the Bradbury-Nielsen type ion shutter gate (as described in *Chapter 2*) differs from the methods currently available, whereby one is left with the options of either laying down alternating sets of wires,[1,2] likely by threading them through guide holes, or alternatively weaving/threading two separate wires through the appropriate holes in a pre-machined, insulated ring-shaped frame [3]. Both of these other methods present themselves as time-consuming methods for constructing the B-N type shutter gates (especially in terms of mass production and precision construction).

Column II consists of 24 PCB surfaces (of the double-sided boards, including one focus grid) in the desolvation region and 38 PCB surfaces (which includes one ion shutter gate, one aperture grid, and one grounded guard ring that surrounds the Faraday/collector plate) in the drift region, for a total of 62 PCB surfaces. The total length from the top surface of the focus grid to the surface of the detector plate is 9.65 cm. The drift region itself, from the top surface of the ion shutter gate to the collector plate, measures 5.85 cm. The average spacing between any two PCB surfaces is ~1.55 mm. The guard rings were connected electrically by sixty-one 1 MΩ, ¼ W surface-mount resistors on one side-board ("resistor-side") and another sixty-one 100 nF, 50 V ceramic capacitors on the other side-board ("capacitor-side"), with another 1 MΩ, ¼ W current-limiting resistor

mounted on the FG PCB board between the 3.05 kV Column voltage connection and the focus grid features. A segregated resistor array (of ~ 61 MΩ) was connected in parallel to the resistor-side to provide the reference voltages for the shutter gate controller, where the negative reference was 1 MΩ down-column from the positive. This meant that the shutter gate in the OPEN state would be held at ~1.8 kV, so that the drift region electric field would be ~310 V cm^{-1}. In the CLOSED state, the orthogonal electric field would be ~550 V cm^{-1}, about twice the drift field, which would accelerate and deflect the incoming ions toward the grid wires (not unlike the deflection of ink droplets in an ink-jet printer [4]), annihilating them in the process. Figure 3-2 depicts this assembly (where side views of both side-boards are shown). (The purpose of the segregated array and the capacitors is detailed in the next section.)

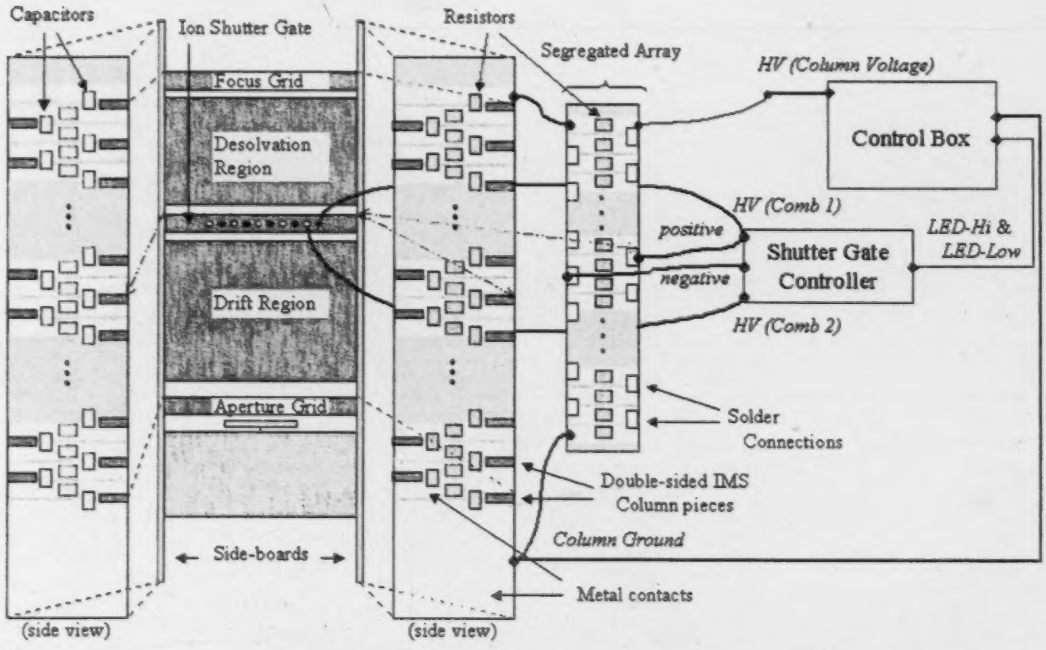

Figure 3-2. Schematic diagram of IMS Column II. The resistors on the (side-view of the right) side-board are 1 MΩ surface-mount resistors, while the ones on the segregated array are equivalent impedance ceramic resistors (~ 61 MΩ total); the capacitors on the (side-view of the left) side-board are 100 nF surface-mount ceramic capacitors. The dotted lines indicate a correspondence between a point on the IMS column and a point on the side-view of each side-board. The dotted arrows indicate the point on the segregated array corresponding to the ion shutter gate in the IMS column.

The shutter gate control inputs (i.e., *LED-Hi* and *LED-Low*) and the detector input power (± *12* V_{dc} and *GND*, not shown) are accessible via a 9-pin hooded D-Sub connector that mates with the Control Box (see *Section 3.2.1.4* and the *Appendix*); the Column Voltage and Column Ground are accessible via their respective banana plug connectors, which are connected directly to the HV fly leads (one from each EMCO high voltage supply). The Electrospray Needle Voltage connection is accessible via a banana-banana-alligator clipped high voltage wire (see *Section 3.2.1.5*). The output of the detector circuit and the trigger signal from the control box (both not shown) are interfaced with the probes of an oscilloscope.

Evaluation of the IMS Column II

It was found early on in the evaluation of the system (with simply the resistor-side connected, and with the shutter gate references connected to these resistors) that the ringing/ripple effect (mentioned in *Chapter 2*) persisted despite the general design modifications (i.e., the double-sided design and rigid mounting structures). In numerous tests it was observed that any voltage pulse introduced at any point in the resistor array (i.e., at the shutter gate reference points) would propagate down the rest of the array. In other words, a pulse introduced at the shutter gate voltage references by the switching of the gate will translate down the array to the aperture grid (positioned ~ 1.5 mm from the collector plate), and would subsequently be detected by the picoammeter circuit – resulting in the ripple or ringing effect. [The picoammeter circuit is sufficiently sensitive to detect electrical pulses transmitted through air, whereby the floating collector plate (i.e., input of the picoammeter) acts as an antenna. Simulations of this in-air pulse detection have been performed, where the resultant ripple resembles the one described above (see the *Appendix*, *Section A3.0.3* for test conditions and results).]

To reduce this effect to negligible levels, the following modifications were administered: (1) the separate (or segregated) resistive array [shown in Figs. 3-2 and 3-3(a)] was used to provide the reference voltages for the shutter gate control circuit and (2) the 100 nF capacitors were mounted in series along the second side-board of the column (mirroring the resistor-side). The segregated array greatly reduced this effect by

providing an electrical buffer between the voltage pulses (created by the switching shutter gate) and the aperture grid (which would in-turn transmit the pulses to the antenna-like collector plate). The addition of the series capacitors (100 nF ceramic) further reduces the effects of the ripple (i.e., they improve the damping of the ripple response); the response worsens with the absence of some or all of the capacitors (please refer to the *Appendix*, for "More on the Ripple/Ringing Phenomenon").

The Ion Shutter Gate (SG) Control Circuit

With the improvement of the response (i.e., the reduction of the ripple effect), it was found that the shutter gate speed became a factor to be considered. That is, with the segregated array and the 100 nF capacitors, the response was tens of milliseconds [with or without the 1nF, 6 kV ceramic capacitors at the reference points (C_{SG})], several orders of magnitude slower than the desired gate pulse width (0.2 – 0.5 ms; see *Chapter 1* for other pulse width values reported in the literature). Figure 3-3(a) depicts the electrical schematic for the system including the segregated array, while Fig. 3-3(b) shows the response with and without the 6kV, 1 nF ceramic capacitors at the reference points (C_{SG}).

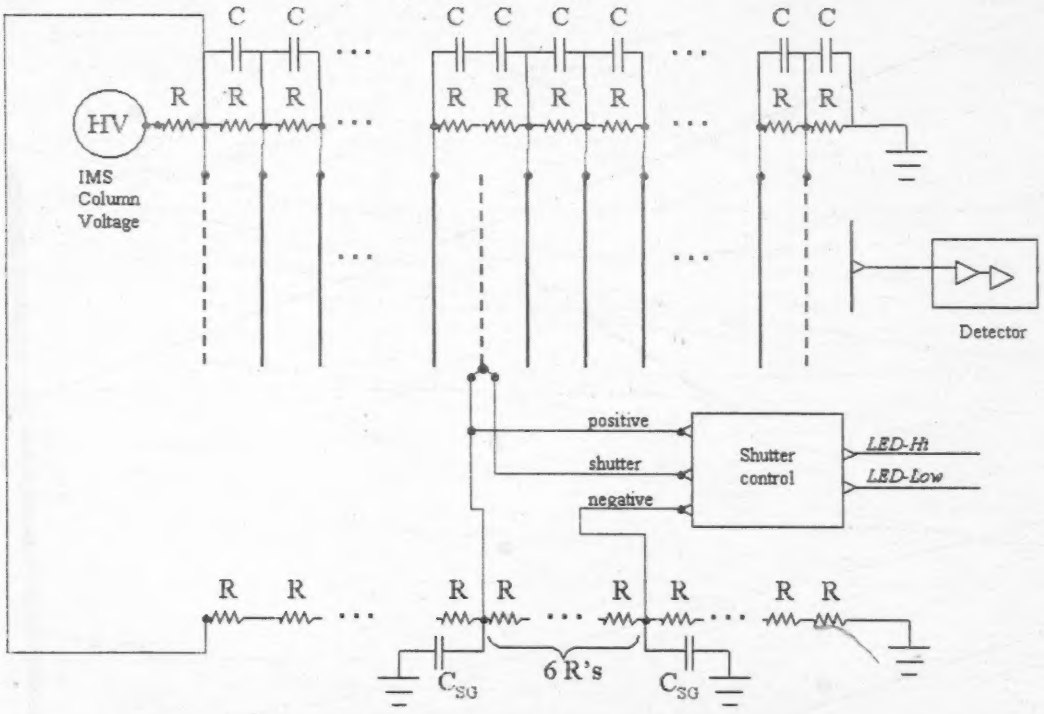

Figure 3-3(a). Electrical schematic of the segregated (shutter) HV column configuration. Note that the capacitors (C = 100 nF, rated for 50 V) were mounted in parallel to the upper resistor array (the one not connected to the SG). R = 1 MΩ; HV = 3.05 kV; C_{SG} = 1 nF (6kV rated ceramic capacitors). The dotted lines indicate the focus grid (left), the ion shutter gate (middle), and the aperture grid (right).

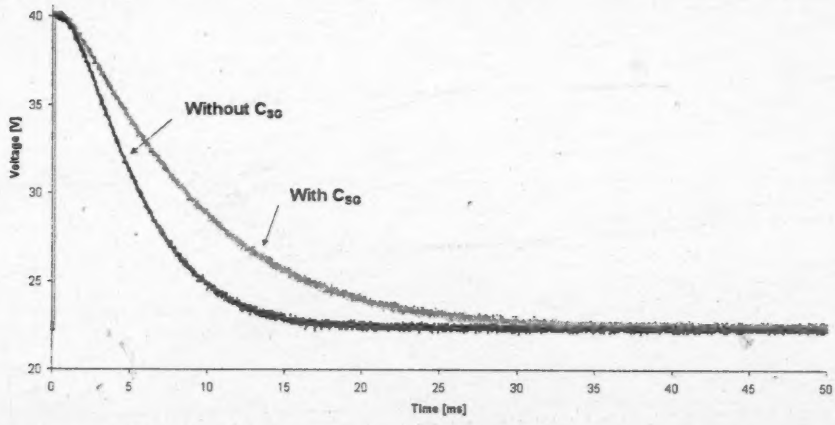

Figure 3-3(b). Comparison between the shutter gate responses before (with) and after (without) the removal of the shutter gate capacitors (C_{SG}). Note the significant decrease (by approximately half) in the settling time of the shutter response after removal of the capacitors, from ~ 30 ms to ~ 15 ms. This response was obtained by simulating a 40 V_{dc} voltage at "positive" [see Fig. 3-3(a)].

The implications of a slow shutter gate are that significant tailing of the peaks in the spectrum would occur (not shown), thus resulting in truly slow signals where multiple peaks would smear together (i.e., as unresolved signals). After exhaustive testing with the system, the shutter gate slowness was traced to the phototransistor optocouplers (H11D1; Fairchild Semiconductor, South Portland, ME) of the shutter gate control circuit. When the phototransistor optocoupler is triggered (with a 5 V input, either *LED-Hi* or *LED-Low*), the LED in the optocoupler emits photons that are converted to charges at the junction of the phototransistor. Since there is only one path for the charge to dissipate (i.e., through the emitter of the phototransistor), coupled with the extremely low currents (due to the high load resistance, 61 MΩ), the phototransistor would essentially stay ON for a much longer period (i.e., tens of milliseconds, which is ~ 2 orders of magnitude slower than desired).

It was found that the best response resulted by placing a 1 MΩ resistor at R_{BE1} (i.e., between the base and emitter of the first phototransistor optocoupler, OK1). The purpose of R_{BE1} is to facilitate the dissipation of charge at the junction of the first phototransistor. The response with R_{BE1} reduced the gate closing time to a few hundred microseconds, a significant improvement over the milliseconds (see Fig. 3-4 for the schematic of the shutter gate controller with R_{BE1} and for the improved response), and smaller than the ~1 ms features we expect in our spectra.

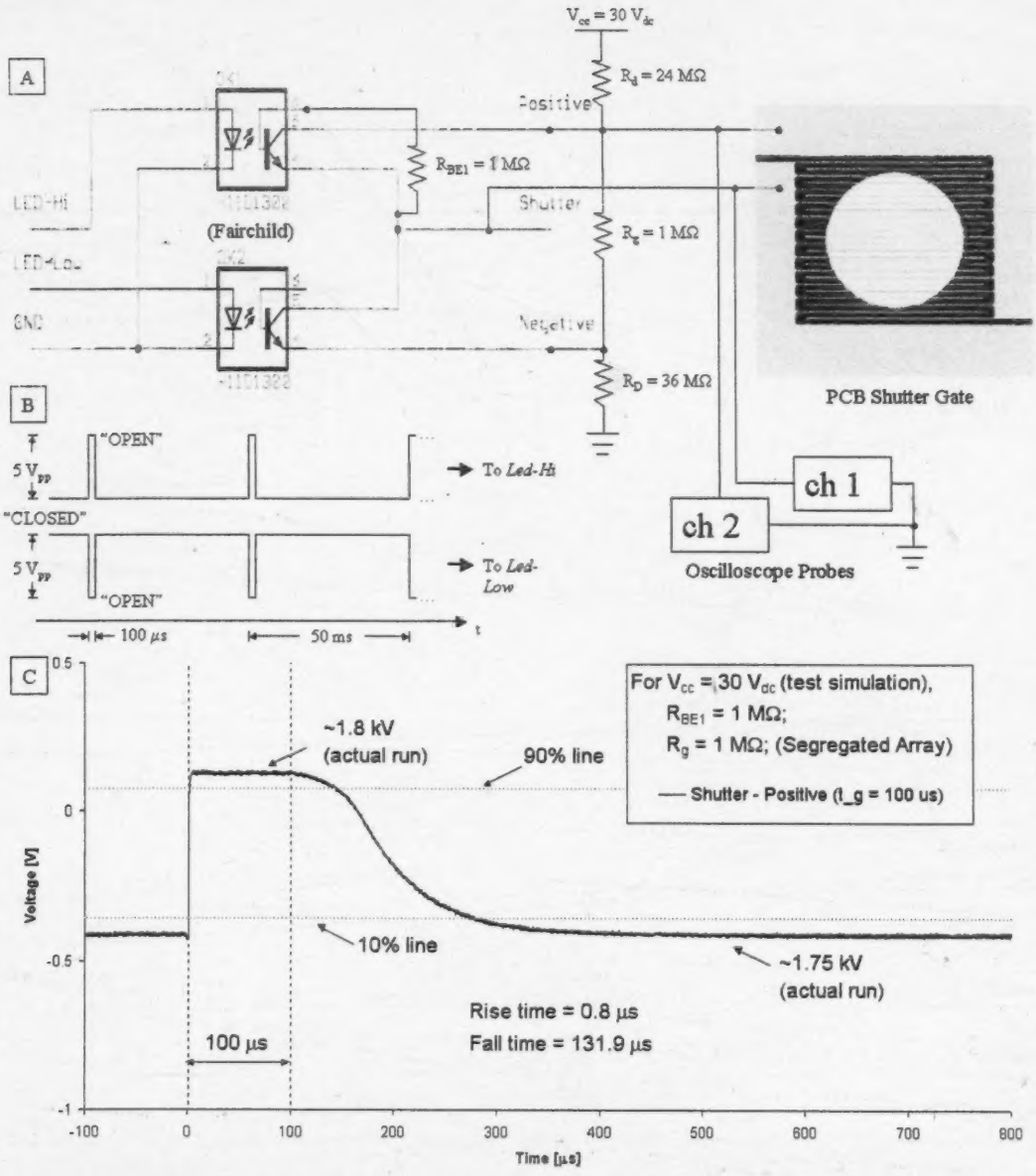

Figure 3-4(a-c). The schematic (A), trigger signals (B), and response (C) of the shutter gate controller with R_{BE1} = 1 MΩ, R_g = 1 MΩ. The vertical, dotted lines indicate the opening and closing of the ion shutter gate – that is, they represent the boundaries of the 100 μs gate pulse width. The rise and fall times were found to be 0.8 and 131.9 μs, respectively, with an absolute closing time of ~250 μs [approximately 2 orders of magnitude faster than before (see Fig. 3-3)].

Figure 3-4(c) shows the improved response of the shutter gate, with a fall time of 131.9 μs and an absolute closing time of ~250 μs, which is two orders of magnitude faster than the response of the shutter gate circuit without R_{BE1} (shown in Fig. 3-3). [Note that the two vertical, dotted lines in Fig. 3-4(c) indicate the 100 μs gate pulse signal sent from the PIC microcontroller to the optocouplers.]

3.2.1.3. Description of C-D Assembly II

The design of the detector circuit for the second drift column, like that for the first, was based on the High Speed Picoammeter circuit as found in the Keithley Low Level Measurements Handbook,[5] and as was shown (in Fig. 2-24 of *Chapter 2*) and described/analyzed in detail in *Section 2.3.1.3.* In this case, a 1 GΩ feedback resistor was used for the picoammeter that is based on the OPA129 ultra-low bias current difet operational amplifier.[6] The applications notes for the OPA129 describe the use of a 1 GΩ resistor for their -1 V/nA current-to-voltage converter, thus one was used here to further increase the gain of the first stage of the picoammeter by 10 times.

The complete, three stage picoammeter circuit is as shown below, where an input current (as observed by the collector plate) is converted to a voltage via the first stage and the subsequent stages act as amplifiers for enhancing the input signal. The respective gains for the stages are 1.01×10^9 V/A ($\text{Gain} = R_F + R_1 = 1.01 \times 10^9$), 10 V/V ($\text{Gain} = \frac{22\,\text{k}}{2.2\,\text{k}} = 10$), and 4 V/V ($\text{Gain} = 1 + \frac{10\,\text{k}}{3.3\,\text{k}} = 4$). The values for R_1 and C_1 were obtained by tuning the system until these values produced the best (i.e., fastest) response, with the components at hand. [Note that unlike Detector I (also known as "Pico I"), Detector II (or "Pico II") does not have any input capacitors or resistors (i.e., no R_{IN} or C_{IN}).]

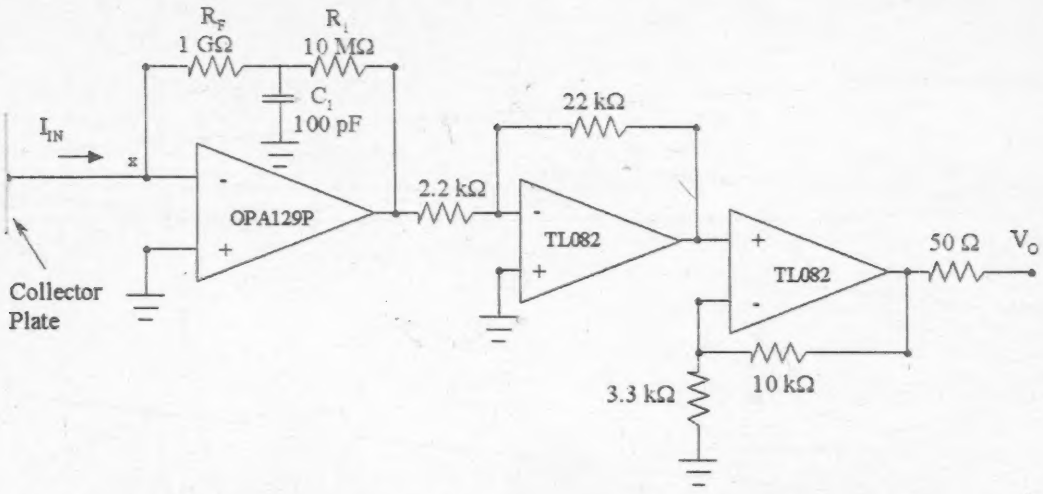

Figure 3-5. Schematic diagram of the picoammeter circuit that is the 2nd detector. The stages have gains of 1.01 GV/A, 10 V/V, and 4 V/V, respectively.

As shown in Fig. 3-6 below, the C-D Assembly II was composed of the double-sided detector circuit board soldered at right angles to the detector wall, which would line up parallel with the thirty-one PCB pieces in the column. [Recall that Detector I (or "Pico I") was mounted on a single-sided board.] The collector (Faraday) plate – a 1.5 (D) cm cut piece of brass (6/1000 inch shim stock) – was connected to the input of the picoammeter via an insulated (Teflon) solder terminal, press mount, pin type, feed through (shown in the figure as a metal pin in a white tab in the detector wall that was also used in the first C-D assembly). A grounded wire-mesh cage was built around the collector plate for shielding purposes (which differs from the solid "cup" design of C-D I that was prone to short circuits to ground potential due to the accumulation of the liquid sample).

To prevent current leakages at the input of the picoammeter circuit, several precautions were undertaken, including the use of the "flying wire" technique [7] at the inverting input of the OPA129 op-amp, and the use of gloves during handling of the resistors (especially with the 1 GΩ) because residues left by fingerprints would present lower resistance paths that would short circuit these high impedance resistors. The three-stage picoammeter was milled and mounted on a single double-sided PCB piece measuring 4.2 (L) x 3.7 (W) cm. The two white plastic stand-offs shown in the figure are

for mounting the C-D assembly onto one of the Column side walls/plates. The three wires shown in the bottom right corner of the (left) figure and the coaxial cable shown on the bottom left corner are for the detector input power (±12 V_{dc} plus GND) and the detector output, respectively.

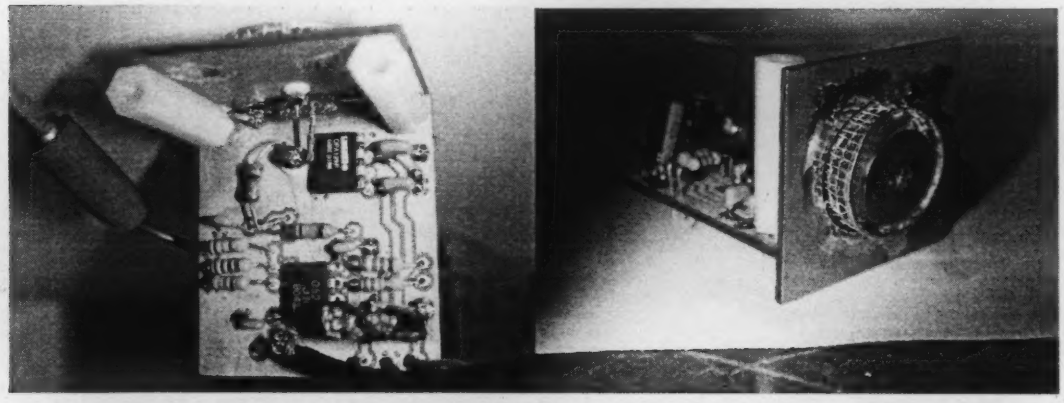

Figure 3-6. Photographs of Collector-Detector Assembly II. (left) a view of the detector circuit, where the collector plate is mounted on the top of the picture; and (right) an angled view of the collector-detector, where the detector is surrounded by a cylindrical grid structure that acts as shielding.

In evaluating the entire ES-IMS Device II, it was found that even before the high voltage was activated, the detector was producing a noise-like signal that persisted despite efforts to better shield the collector plate by soldering a ring of brass (shim stock) onto the grounded, bottom-most PCB surface of the column so as to surround the collector plate, and despite connecting 100 nF, 50V ceramic capacitors in parallel with the resistors (on the opposite column sideboards), as shown in Figs. 3-2,3-3(a). This noise-like signal (an example of which is shown in Fig. 3-7) was eventually traced to a feedback problem from the second stage to the feedback loop of the (OPA129) first stage. This was corrected by cutting the traces for the (±12 Vdc) input power supplies to the TL082 dual op-amp (i.e., stages two and three of the picoammeter circuit shown in Fig. 3-5), and creating a short circuit between the output of the 1st stage to the output of the 3rd stage (see Fig. 3-8); this effectively dropped the overall gain by ~40 times. (The TL082, whose input power traces were cut, was not removed from the circuit board.)

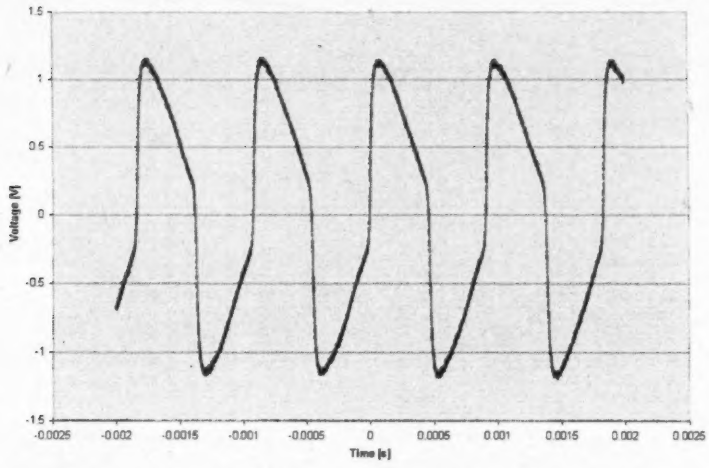

Figure 3-7. An example of the feedback noise signal observed with the inclusion of the second and third stages of Detector II.

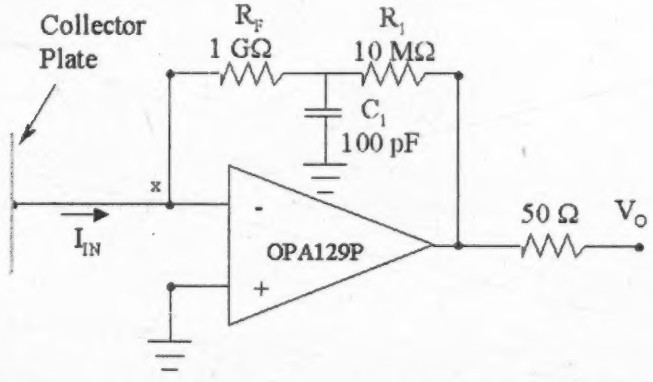

Figure 3-8. Schematic diagram of Detector II. The first stage has a gain of 1.01 x 10^9 V/A; the second and third stages (in Fig. 3-5) have effectively been removed.

High (HF) and low frequency (LF) noise measurements were also made, without any efforts to shield against electromagnetic interference and without any noise filters, where ~150 mV_{pp} LF and ~ 50 mV_{pp} HF noise was detected with the input to the amplifier (Fig. 3-8) open-circuited. During the experiments, the input (i.e., the collector plate) was partially shielded by the column, yielding ~50 mV_{pp} LF noise, before averaging. (Averaging over 512 scans or more considerably reduced this noise signal.) The standard deviation was 5 mV (before averaging) and 0.7 mV (after averaging over 512 scans).

3.2.1.4. Description of the Control Box

The Control Box was designed as a means of making the ES-IMS device more portable by eliminating the excess instrumentation – for example, the μTK and the Agilent arbitrary waveform generator. As such, the Control Box (described in much greater detail in the *Appendix*) would house two EMCO C60 6 kV power supplies and one PIC16F877-based Microboard controller. (The EMCO power supplies will henceforth be referred to simply as the EMCO's.) As a safety feature, interlocking switches built into the control box would open-circuit the input power to the EMCO's should the control box be operated outside of the Clear Box (see *Section 3.2.1.5* below) or should the cover plate be removed. Besides providing the HV to the ES needle and the IMS column, it would also provide the shutter gate control voltage pulses, the ±12 V_{dc} detector input power, a trigger pulse to the oscilloscope to mark time for the detector output, and to provide a means of communication with a control computer (via the RS-232 serial communications port connection).

The control box was constructed using a 5 x 4 x 3 inch natural finish, two-piece aluminum minibox (CU-3005-A; Bud Industries Inc., Willoughby, OH), which will henceforth be referred to as "the minibox" (consisting of three 5 x 4 inch panels shaped in a "U") and the "minibox lid" (consisting of one 5 x 4 inch panel between two 4 x 3 inch panels, all shaped in a "U", with overhanging sleeves that fit over the side panels of the minibox). One side panel of the minibox will act as the "top" of the control box during ES-IMS operations. This side panel consisted of five holes: two for the banana jacks for the EMCO inputs (+12 V_{dc} and GND); one for the RCA jack for the shutter trigger to be connected to channel two of the oscilloscope (via a BNC-BNC cable with a BNC-RCA connector); one for the 12 V_{dc}, 1.2 A input power for the Microboard; and, one for the RS-232, 9-in D-Sub serial connector that interfaces the Microboard with the control computer. The bottom of the minibox (actually the column-facing side of the control box during ES-IMS operations) contained one groove and ten holes: four for the mounting screws for the circuit boards within the box; two for each of the two interlocking switches [TM-Series Unimax Miniature Snap-Action Switch (C&K Components Inc., Clayton, NC)]; one for the banana jack for the column ground; and one for the 9-pin D-Sub

connector for the shutter control *LED-Hi* and *LED-Low*, and for the detector input power *±12 Vdc* plus *GND*. The groove would be for a ribbon cable used for connecting each of the two interlocking switches in series with the input power to each of the EMCO's; the normally open-circuited interlock switches require that the snap-action switches be depressed to close the circuit between the EMCO input power and the EMCOs. The minibox lid featured a keyhole that was sized to fit an 8 (ID) x 15 (OD) x 11 (D) mm rubber grommet, through which the two EMCO HV fly-leads would be threaded through the box. A 1.57 mm thick, pre-punched insulating board (Vectorbord®; Vector Electronics & Technology Inc., North Hollywood, CA), with 1.1 mm diameter holes, was cut to fit within the 5 x 4 inch dimensions of the minibox, and was used to mount the two EMCO's. This HV-mounted Vectorbord® was spaced from the bottom of the minibox interior by four 2.5 cm long plastic stand-offs. Likewise, the Microboard (which already fits into the minibox) was raised over the Vectorbord® using another four similar plastic stand-offs. Figure 3-9 (as well as Fig. A3-5) depict(s) the Control Box in its finished form.

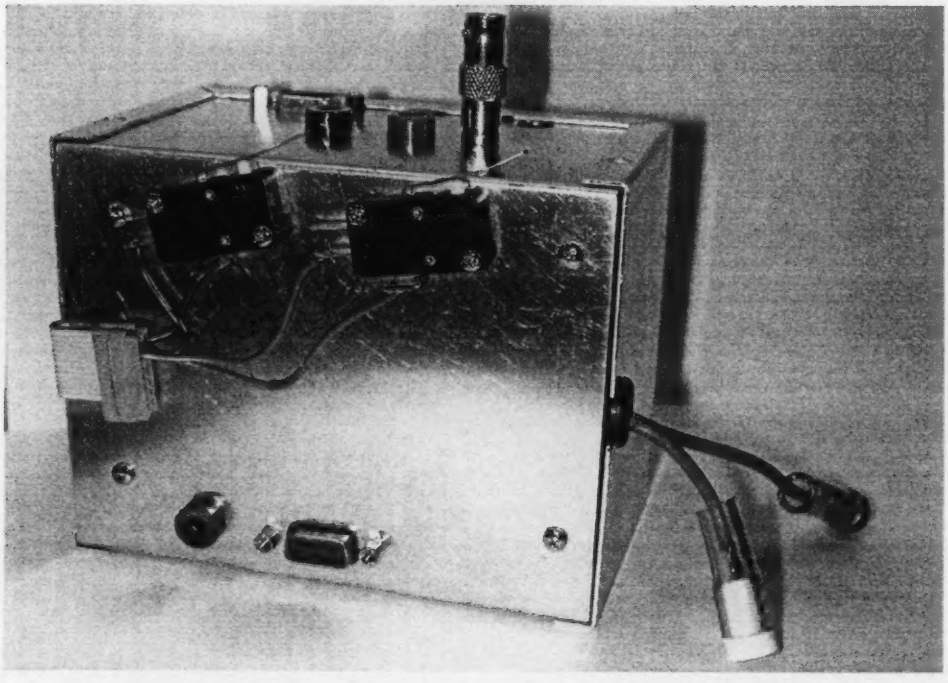

Figure 3-9. Photograph of the control box. (Photographs of this unit in its various stages of disassembly can be found in the *Appendix*)

3.2.1.5. Description of (ES-IMS) Clear Box

The main purpose of the (ES-IMS) clear box is to provide a safe containment structure for the ES-IMS device. In other words, it is to house the high-voltage-exposed components out of reach of human hands during HV operation. As such, a clear plastic box with outer dimensions measuring 35 (W) x 26 (Dp) x 35 (H) cm, constructed using 6 mm thick plastic sheets, included (a) a shelf that would hold the control box (see *Section 3.2.1.4*) and (b) a cover plate (made of the same material) that would support and secure the ESIS II and the IMS Column II (see *Sections 3.2.1.1. & 3.2.1.2.*), as well as depressing the interlocking switches on the control box to close the circuit between the EMCO's and their corresponding input voltages. A keyhole was cut into the top panel of the clear box such that the center of curvature of the keyhole was set ~22 cm from the inner face of the right panel (one of the two 26 cm by 35 cm side panels of the clear box). The diameter and the width of the keyhole are both 13.1 cm. Inside the clear box is a 10 cm deep shelf (made of the same plastic material) that spans the right side of the clear box, flush against the right panel interior, and set such that the top surface of the shelf is ~9.5 cm from the interior (bottom) surface of the top panel.

The cover plate, which is mounted on top of the clear box using four (finger-tightened) set screws, supports the ESIS mount (see *Section 3.2.1.1*) and the column mount (actually a disc with four round, nylon stand-offs connected via two set-screws to each bracket holding the column), both aligned along the center of curvature of the clear box top panel keyhole. A rectangular hole was cut into the cover plate on the right side, directly above the shelf to allow the five wire connections on the top of the control box to be accessed from outside of the ES-IMS device (i.e., the clear box). Additionally, the cover plate consisted of a hole set slightly off from the ESIS mount that was fitted with an RCA jack reserved for the detector output connection to channel one of the oscilloscope. Figure 3-10 shows a schematic diagram with the various components of ES-IMS Device II connected. [Figure A3-1(b) in the *Appendix* shows a photograph of the system.]

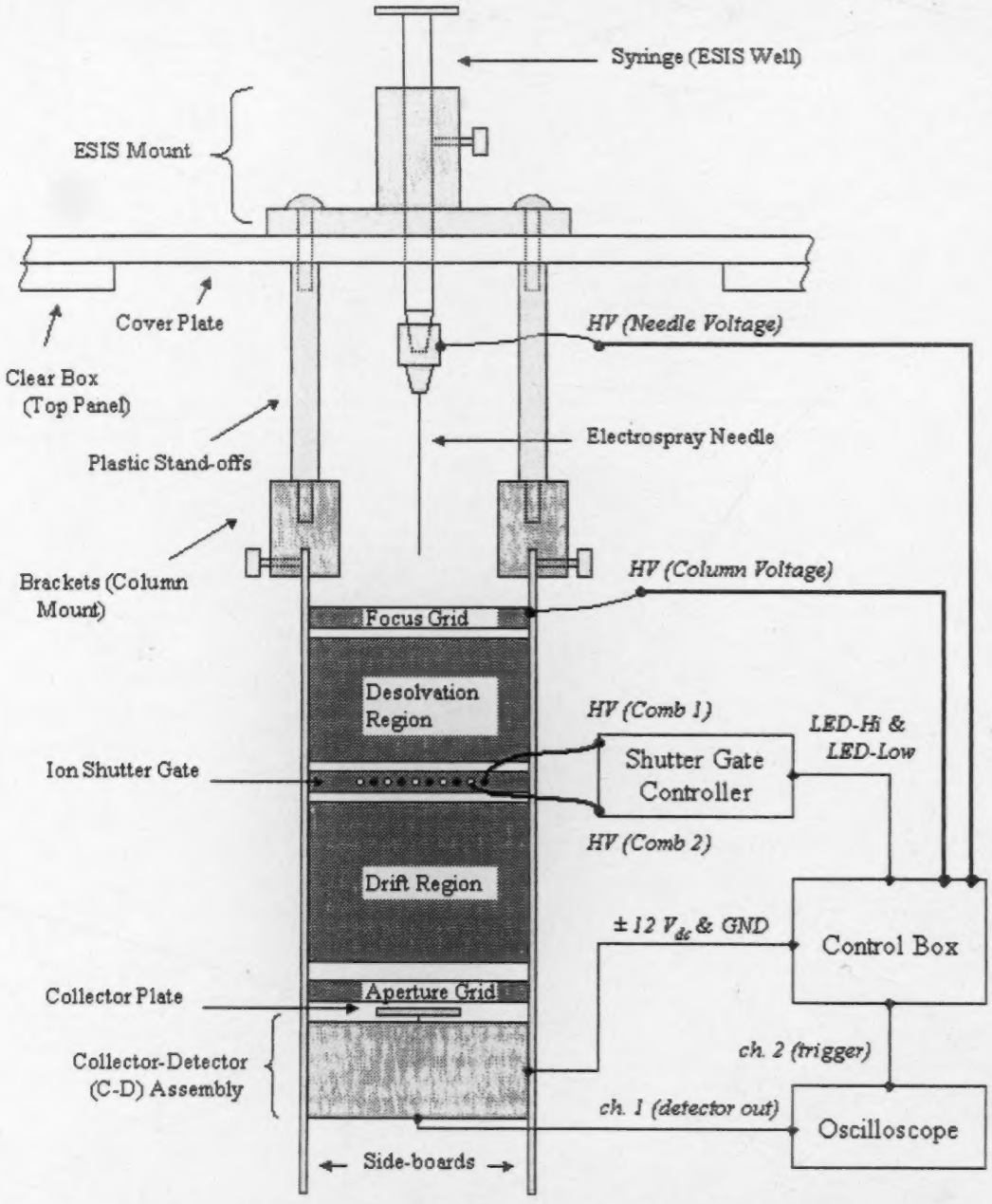

Figure 3-10. Schematic diagram of ES-IMS Device II. Note that the oscilloscope and the dc power supplies for the EMCO's (not shown) lie outside the clear box in which this device is suspended. The shutter gate controller is mounted on the same board as the shutter gate; the control box sits on a shelf in the clear box. (See *Section* 3.2.1.1 for details on the ESIS and mount; see Figs. 3-2, 3-3 for details of IMS Column II.)

3.2.1.6. Description of the External Equipment

Here the external equipment refers to the additional/external instruments necessary to operate the ES-IMS Device II, plus their corresponding connector cables. These include (1) the control computer, (2) the measuring oscilloscope, (3) the EMCO input voltage supply, and (4) the Microboard power supply. The control computer (1) was a Pentium III – 700 MHz PC running on a Windows 98 operating system. The software interface for the PIC16F877 was HyperTerminal (Hilgraeve Inc., Monroe, MI), which communicated with the Microboard via a 9600 Hz baud rate RS-232 serial line. A program on the 40-pin PIC16F877 microprocessor chip (that is listed in the *Appendix*) was activated and shutdown via this HyperTerminal Interface. The measuring oscilloscope (2) was a 300MHz, 2.5 GS/s Tektronix TDS 3032 two channel color digital phosphor oscilloscope (Tektronix, Inc., Beaverton, OR). The first channel input was dedicated to monitoring the Detector II output, while the second channel received the trigger pulse (actually a duplicate *LED-Hi* pulse, please refer to the *Appendix* for details on this feature of the control box). The EMCO input voltage supply (3) was a single Hewlett Packard 6213A power supply set to +12 V_{dc}. (Note: the EMCO's allow for a wide range of input voltages: 11.5 to 16 V_{dc}.) Finally, the Microboard power supply was a 12 V_{dc}, 1.2 Ampere AC adapter that takes in a 120 V_{ac}, 60 Hz, 24 W input.

An eventual design goal would be to dispense with these external instruments altogether, resulting in a more self-contained device. This was mentioned previously (i.e., with suggestions for the implementation of an LCD and keypad, and the utilization of the ADC input of the PIC processor with additional memory). One other possibility is the use of a positive 12 V regulator (on the Microboard) as the input voltage supply for the EMCO's; however, one must be careful not to drive the regulator to overload. Ideally, one would only require either one power cable to power the Microboard (which would supply the EMCO's as well), or a series of batteries. This self-contained, multi-tasking approach represents the power of a (PIC) Microboard-based system.

3.3. Results and Discussion

For any ion mobility spectrometer, there are three important factors that determine the efficacy of the system: (1) the signal limit of detection (sLOD; the lowest intensity signal that can be distinguished from the background noise); (2) the concentration (or sample) limit of detection [LOD; the lowest amount of a sample that can be detected in a much larger proportion of solvent (or air in the case of ^{63}Ni-based systems)]; and, (3) the (temporal) peak resolution (the ability of the system to distinguish between two closely spaced peaks). When these factors have been optimized, the ion mobility spectra obtained by the system for any substance can be compared with that obtained by the same system (or other systems) for the same substance by comparing the mobility (or reduced mobility) values of the ion peaks in the spectra. This constitutes the common means of identification of a species. Alternatively, one can build up a library of spectra for a number of different known sample species.

For the optimized system described in this chapter, the signal limit of detection was obtained by running the system without any liquid sample/solvent (or alternatively, by not initiating flow in the ESIS). The subsequent "control" spectra would typically look like that shown in Fig. 3-11, after averaging over 512 individual spectra (each spectrum with a period of 50 ms). Unless otherwise stated, the conditions for obtaining the data (i.e., the experimental setup) were as described in *Section 3.2.1*.

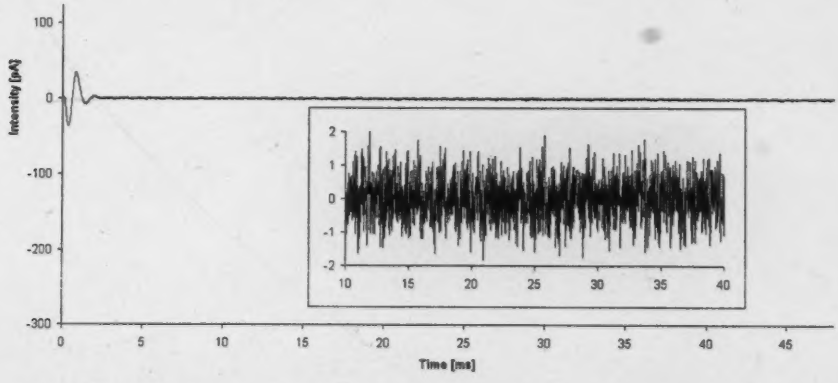

Figure 3-11. Typical "control" spectrum detected by ES-IMS Device II. A zoom view of the spectrum (inset) is also shown. This spectrum was taken by averaging over 512 scans (where one scan is 50 ms period in length). Averaging was done using the pre-set function on the oscilloscope.

The standard deviation (σ) and the signal limit of detection (sLOD) were calculated using the following equations respectively, where $\bar{I}$ and I_i are the mean intensity (in pA) and data point intensity (in pA), and n is the number of data points:

$$\sigma = \sqrt{\frac{\sum_{i}^{n} (\bar{I} - I_i)^2}{n-1}} \qquad (3.3)$$

$$sLOD = 3\sigma \qquad (3.4)$$

Focusing on the interval between 5 ms and 49.8 ms, the number of data points (n) equals 4481, which results in an average σ of 0.70 ± 0.17 pA, using Eqn. (3.3). The sLOD value – generally derived by taking three standard deviations from the mean [Eqn. (3.4)] – was 2.09 ± 0.51 pA. For un-averaged spectra (shown in the *Appendix*), the sLOD value was found to be 16.89 ± 4.39 pA, which is an order of magnitude larger than the averaged data; this is due to occasional random noise and an occasional high frequency (kHz) noise (of unknown origin, but possibly an artifact of one of the electrospray modes) that skew the standard deviation values, thus skewing the sLOD values. By averaging the spectra 512 times (with a scan time of 25.6 s) the sLOD improves dramatically (by an order of magnitude). (If the averaging function on the oscilloscope is stopped before 25.6 s has elapsed, the resultant sLOD values become larger, with values lying somewhere between ~1 and ~30 pA.) Averaging over a larger number of scans (or individual spectra) will further improve the signal limit of detection.

With the uncontrolled-flow system described above (i.e., without the aid of a syringe pump or a microchip ES to control the liquid flow in the ESIS), it was necessary to inject air into the ESIS reservoir (i.e., to pump liquid through the syringe of the ESIS) in order to initiate liquid flow. This leads to various cone-jet modes: Spray Mode 1 (SM-1, "ink-jetting" mode), SM-2 ("stable" mode), and SM-3 ("over-spray" mode). SM-1 and SM-3 represent the unstable, polydisperse spray modes (i.e., characteristic of droplets of varying sizes), while SM-2 represents the stable, monodisperse mode (i.e., characteristic of droplets of uniform size). [The characteristics of SM-2 are well known.[8-10] There actually exists another spray mode between SM-1 and SM-2, which Juraschek and Rollgen (1998) [8] describe as producing spectra containing low frequency pulses (< 5 kHz) of constant amplitude and consistent peak shape.] The "ink-jetting"

mode (also referred to as the "pulsating" [8,9,11] or the "spitting" mode [12]) corresponds to a low flow rate. Here, the emission rate of ion droplets exceeds the supply of liquid to the tip of the liquid (Taylor) cone so that the Taylor cone collapses then replenishes as the tip is resupplied, thus resulting in low frequency (low kilohertz) pulses [shown in Fig. 3-12(a) and in the *Appendix*], which agrees well with the findings by Juraschek and Rollgen (1998) [8] (who obtained these low frequency pulsations with current measurements at the electrospray source). The "over-spray" mode corresponds with high sample flow rates at the liquid cone, where the opposite occurs. That is, the supply of liquid to the cone tip exceeds the emission rate of droplets, thus leading to a high overall emission rate (i.e., pumping) of droplets of varying sizes; this "pumping" of the liquid typically leads to the accumulation of large droplets on the focus grid, which may affect the mobility of ions in this region (although it does not seem to have much effect on the detected signal once one enters into SM-2). [It should be noted that the multi-spray aspect of SM-3 is typically initiated by increasing the applied (electrospray) voltage beyond a certain threshold (dependent upon the liquid used).[8,9]] The spectral observation of these unstable modes seems to indicate that the average droplet size is relatively large (large enough so that the orthogonal electric field of the shutter gate becomes incapable of deflecting them, or alternatively, they become large enough for gravity to affect their drift), as illustrated by the random occurrence of the SM-1 droplets [shown in Fig. 3-12(a)] and by the "blanketing" effect of SM-3 [Fig. 3-12(b)].

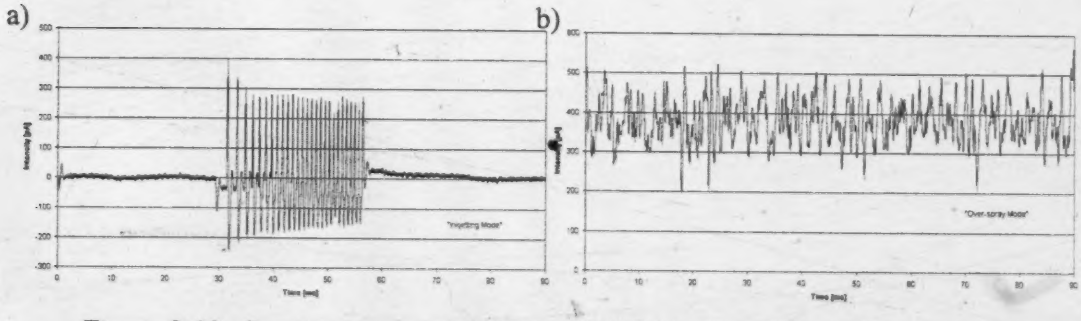

Figure 3-12. Spectra representing (a) the "ink-jetting" and (b) the "over-spray" modes. The "ink-jetting" mode corresponds with low flow rates, while the "over-spray" mode corresponds with high flow rates (see text for details). Both represent polydisperse modes, in which the spray droplets are of varying (non-uniform) sizes. (a) un-averaged; (b) averaged over ~20 scans.

As the liquid supply rate (at the cone tip) matches the emission rate, we enter into the "stable" spray mode, which corresponds with "clean" spectra. Typically with the injection of air pressure (for the initiation of flow), the order of modes is from SM-3 to SM-2, where SM-1 occasionally appears. It was observed by Kebarle [13] that ion-solvent interactions lead to "clustering," whereby the neutral solvent (e.g., H_2O) will attach themselves to the ions (e.g., H_3O^+). This means that when the ion-enriched droplets undergo evaporation (after SM-1) they will reach a critical charge density (i.e., the Rayleigh limit), and will thus undergo fission (according to the Charge Residue Model, see *Chapter 1*). This cycle will continue until the droplet arrives at a stable state where the charge density is under the Rayleigh limit (despite evaporation). Although this may lead to more than one ion per droplet, the size is sufficiently small to be considered as an individual gas-phase ion (this is even more so for large biomolecules such as cytochrome c). According to Hill and co-workers [14-16] and Guevremont *et al.*,[17] high drift temperatures serve to thermally de-cluster the ion-solvent pair – that is, heating allows for better desolvation or evaporation of the solvent. One could then take advantage of the well-documented [8-10,18] monotonic decrease in droplet size with a decrease in the liquid flow rate (for the spray mode in the monodisperse or stable regime). For example, a study by Matz *et al.* found that smaller capillary sizes and lower flow rates (< 1 μL/min) generally leads to smaller, faster ions at lower temperatures likely due to less solvent clustering to begin with.[19]

Figure 3-13 shows spectra of 50:50 (v/v) methanol/water where the peak positions are shown to shift toward faster drift times during a single run (with one sample loading). (The methanol was obtained from Fisher Scientific, while the water was Milli-Q water that was additionally autoclaved and filtered.) We observed that over the course of the run, the liquid level in the ESIS lowers, thus decreasing the flow rate (due to a lower hydrostatic pressure), which as Matz and co-workers found would decrease the amount of solvent clustering, resulting in smaller parent droplets and thus faster ion drifts. The decrease in signal amplitude with a decrease in flow rate (Q) seems to agree with at least the proportionality component of the well-established and experimentally confirmed model (known as the Hendricks model [18]), which predicts that the (ion) current (I_{ion}) is

proportional to $Q^{\frac{4}{7}}$. (Whether our results match to the $4/7^{th}$ power of Q is unknown, as our flow rates are unknown.)

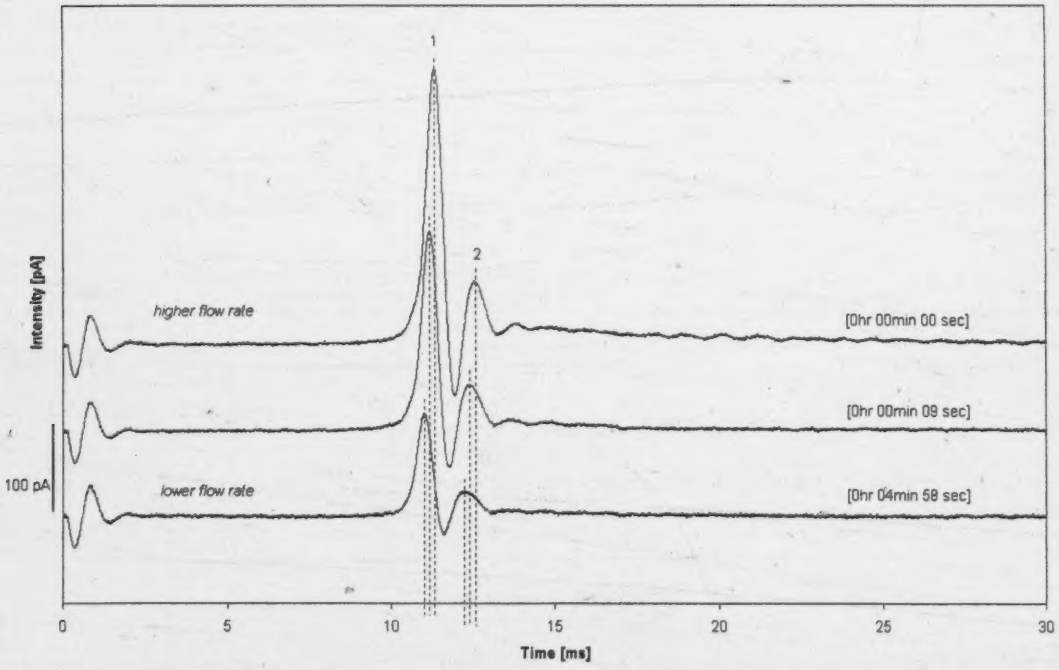

Figure 3-13. Ion mobility spectra of 50:50 (v/v) methanol/water. (ES-IMS system described in *Section 3.2.1.*)

The values of significance from any ion mobility spectrum are the drift times (t_d), the ion peak currents/intensity (I_{ion}), the reduced mobility values (K_o), the peak resolutions (R_p), and the peak-to-peak resolutions (R_{pp}). t_d relates to the velocity of the ions (where the drift length, L_d is known), while I_{ion} relates to the number of charges the ions possess. K_o is a comparative value for the ion mobility of the ions (indirectly representative of the ions' relative mass, charge, and size) that is normalized to 273.15 K and ambient pressure (to allow for comparisons amongst various different experimental setups). This is given by Eqn. (3.5), for $L_d = 5.85$ cm, $V_d = 1820$ V, $T_d = 293.15$ K, and $P_d = 710$ Torr.

$$K_o = \frac{(L_d)^2}{t_d (V_d)} \left(\frac{273.15\,K}{T_d} \right) \left(\frac{P_d}{760\,Torr} \right) \qquad (3.5)$$

In Fig. 3-13 the average drift time for peak 1 [peak 2] was 11.16 ± 0.16 [12.38 ± 0.16] ms, with an average ion peak current of 224.61 ± 101.43 [51.62 ± 21.38] pA. The corresponding average K_o (Eqn. 3.1) value for peak 1 [peak2] was 1.46 ± 0.02 [1.31 ± 0.01] $\frac{cm^2}{V \cdot s}$. As a comparison, Hill *et al.*[20] listed three peaks for 50:50 (v/v) methanol/water (shown in Fig. 3-14), with K_o of 2.88, 2.53, and 2.38 $\frac{cm^2}{V \cdot s}$, respectively, which is roughly two times larger than those obtained here; their first peak was attributed to NH_4^+ contaminant (shown as an "†" in Fig. 3-14), and their second and third peaks due to methanol ("1" in Fig. 3-14) and water ("2" in Fig. 3-14), respectively.

Possible reasons for the difference in values (by almost a factor of 2) include the fact that no drift gases or high temperatures were used for our system, which would affect the ion drifts (see Table 1-2 for a summary of drift tube parameters listed by the Hill group). [A discrepancy was found when their given parameters [20] (i.e., L_d = 11 cm, E_d = 300 V/cm, T_d = 523.15 K, and P_d = 689 Torr) were entered into Eqn. (3.5) for their drift times of ~7.9, ~8.9, and ~9.5 ms (as measured from their spectrum), which resulted in K_o values of 2.20, 1.95, 1.82 $\frac{cm^2}{V \cdot s}$, which are closer to our values. Their stated values and the values calculated from their stated parameters are plotted in Fig. 3-15 for their solvent peaks ("1" and "2" in Fig. 3-14).]

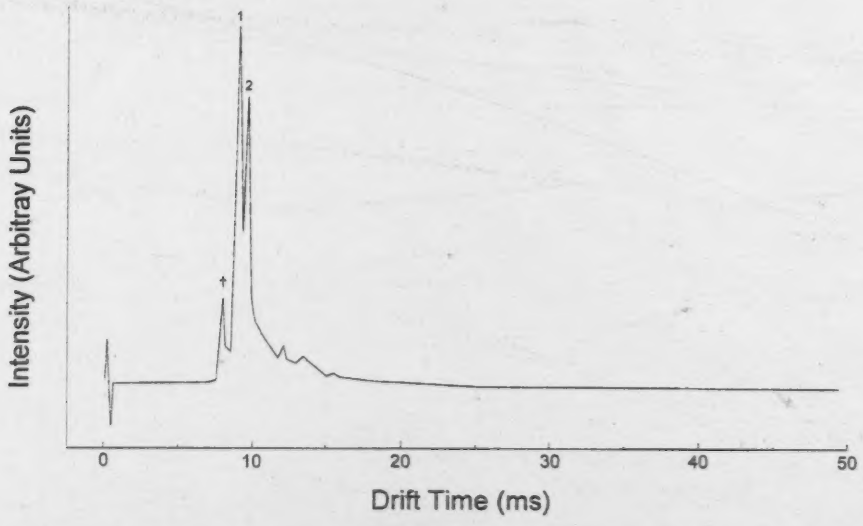

Figure 3-14. Ion mobility spectrum of 50:50 (v/v) methanol/water obtained by Hill and co-workers. "1" and "2" represent methanol and water, respectively, while "†" represents an ammonium contaminant. Modified from Ref. 20.

Figure 3-15 shows a plot of the reduced mobilities (K_o) for the solvent peaks (50:50 methanol/water), comparing the literature values with our own for differing temperatures. From the plot, our values (shown with an "x") are similar to a set of values (shown as solid diamonds connected by a dotted line) obtained for an unresolved solvent peak at various temperatures,[17] but slightly less than those obtained by the Hill group [15,20] [shown with the solid diamonds (connected by two solid lines for the two solvent peaks), and the open circles and squares for the two solvent peaks obtained]. The K_o for solvent peaks 1 & 2 are indicated by numbers (1, 2) and arrows. An important point to note is that resolving the two solvent peaks is not always possible. In fact, at a drift temperature of 100 °C, Wu *et al.*[15] obtained a single unresolved peak for their solvent spectrum [using 47.5:47.5:5 (v/v/v) methanol/water/acetic acid].

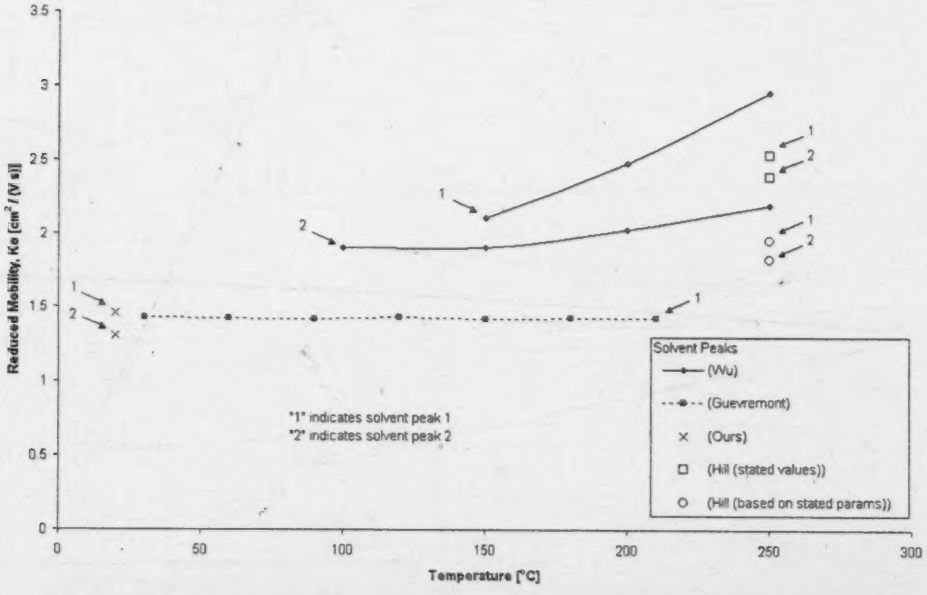

Figure 3-15. Plot of the reduced mobility (K_o) values for 50:50 methanol/water for various temperatures, comparing among literature results. The lined plots are based on the solvent peak(s) that was/were obtained for a series of temperatures.[15,17] From the Hill group's results,[20] it was found that their stated K_o values ("□") did not match their stated parameters (which when accounted for are shown as "○"). The multiple data points given for the single temperature point represent the multiple solvent peaks that were obtained by Hill *et al.* and by us (shown as "x").

R_p [in Eqn. (3.6)] is one of the key indicators of a system's performance, as it speaks to the spectrometer's ability to produce individual sharp spectral peaks that can be

distinguishable from other closely spaced peaks. R_{pp} is a similar parameter that is mainly applicable to two closely spaced peaks. These are given as follows:

$$R_p = \frac{t_d}{w_{½}} \tag{3.6}$$

$$R_{pp} = \frac{2(t_{d2} - t_{d1})}{w_1 + w_2} \tag{3.7}$$

The full-width-half-maximum ($w_{½}$) value for peak 1 [peak 2] in Fig. 3-13 was 0.54 ± 0.01 [0.71 ±0.09] ms. This leads to a peak resolution (R_p) value (Eqn. 3.2) of 20.79 ± 0.14 [17.72 ± 2.28], which compares well with that of Hill and co-workers,[20] whose values (obtained from their spectrum) are 23, 18, and 19, respectively, for their three peaks. Other values obtained by the same group (e.g., 15.7 – 58.7 for varying drift gases [21] and 26 – 96 for varying gate widths and measurement modes [15]) are also similar. These other systems feature the use of high drift temperatures, drift gases, syringe pumps, and longer drift times, all of which can affect the mobility of the ions.

The corresponding R_{pp} value (Eqn. 3.3) is 0.60 ± 0.02, which is simply another way to represent peak resolution. To compare with the results obtained by Hill and co-workers,[20] their "$w_1 + w_2$" (as measured from their spectrum) was ~3.4 ms. Focusing on their solvent peaks (i.e., the 8.9 and 9.5 ms peaks), their R_{pp} value would be ~0.4. In other words, without the benefit of a drift gas or high drift temperatures, our system still performs well in terms of resolution.

When methanol was sampled alone [shown in Fig. 3-16], it was found that the main peak centered between 11 and 13 ms, indicating that peak 2 is due to the methanol, which opposes the findings of Hill *et al.*[20] that was shown in Fig. 3-14, where their methanol peak came before their water peak. Although, Asbury and Hill [21] have found that certain drift gases can change the order of the peaks. From Fig. 3-16, peak 1 seems to be present but diminished in amplitude, possibly due to residual water in the system. The peaks marked with asterisks (*) are also likely due to air contaminants; since methanol has a much lower surface tension than either water alone or the methanol/water mixture, one need not apply as high a voltage (for example) for the onset of ES. Because the electric field is higher than is required for the ES of methanol, corona discharge/ ionization of the air surrounding the Taylor cone may be taking place, which would result

in the "*" peaks. (The relatively high amplitude peak centered about 17 ms may be due to a dominance in the corona ionization effect.) Furthermore, while the positions of peaks 1 and 2 tend to shift slightly during a single run (due to solvation/clustering issues, mentioned above), these "*" peaks (especially the one centered about the 17 ms point) do not seem to shift in position (not shown), which seems to indicate that they are not related to the liquid in the ESIS. Ideally, one would run water alone to confirm the peak identities, however, effective electrospray of water alone is not possible without significant modifications to either the system or the electrospray source (also noted by others [11]), therefore a comparison cannot be made directly. Peaks can be identified via use of a mass spectrometer set to measure the m/z ratio for ions within a certain drift time window, however, we do not have access to such an instrument, therefore complicating the identification process. (Similar contaminant peaks have been obtained by others.[16,19])

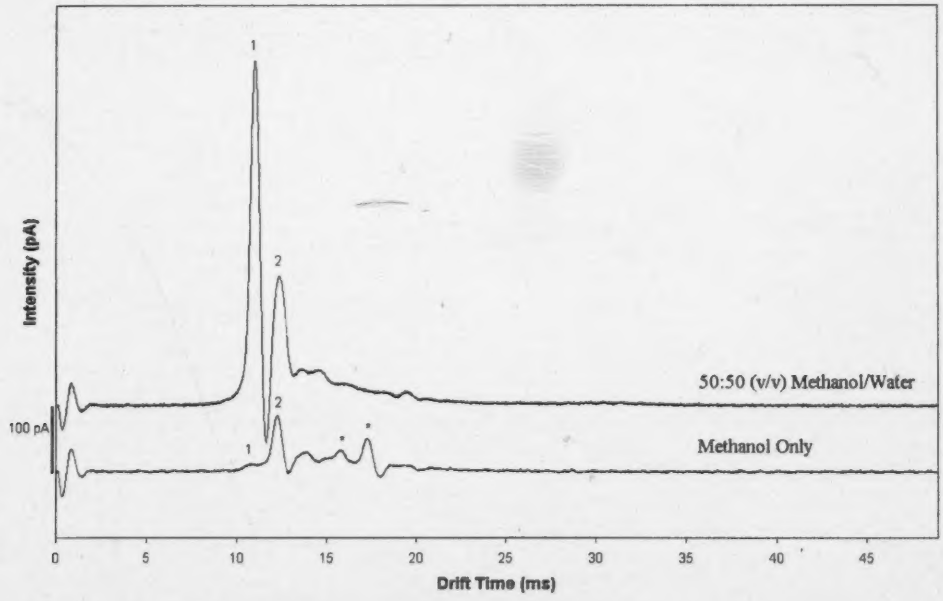

Figure 3-16. A comparison of the ion mobility spectra of the solvent only and the methanol only runs. Peak 2 seems to be the methanol peak, peak 1 is likely due to water, the peaks marked with "*" are likely air contaminants (see text).

Changes in the system response corresponding to changes in the drift electric field were also examined, where the "IMS Column Voltage" shown in Fig. 3-3(a) and 3-10 is decreased [such that the focus grid voltage (V_{FG}) is lowered from 3 kV to 1 kV], which

in-turn decreases the orthogonal electric field at the ion shutter gate (by decreasing the voltage between the positive and negative references). In other words, when V_{FG} is halved, V_p and V_n (= V_s for the CLOSED state) will decrease by the same proportion, so that "$V_g = V_p - V_s$" (for the CLOSED state) will also be halved – example, when V_{FG} is decreased from 3 kV to 2.5 kV, V_g will decrease from 49 V to 41 V. Figure 3-17(a) illustrates the spectra obtained for drift fields of ~310 to ~160 V/cm. At ~100 V/cm and below [shown in Fig. 3-17(b)], the shutter gate becomes ineffective in deflecting the ions, which results in an effective continuous ON state or dc signal [not unlike the condition for total ion current (TIC) measurements,[14] where the shutter gate is set in the continuously open state]. The variations in Fig. 3-17(b) – that is, the shift in baseline amplitude – result from the "overspray" of ions with the initiation of the run [i.e., with manual application of air pressure at Figs. 3-17(a)1 and 3-17(a)4] that settles down over time as the hydrostatic pressure in the ESIS decreases with the emission of liquid in the form of ions [shown in Figs. 3-17(a)2, 3-17(a)5], until the liquid in the ESIS dries up [shown in Fig. 3-17(a)3]. (Unless otherwise stated, the drift field used for the experiments was ~310 V/cm.)

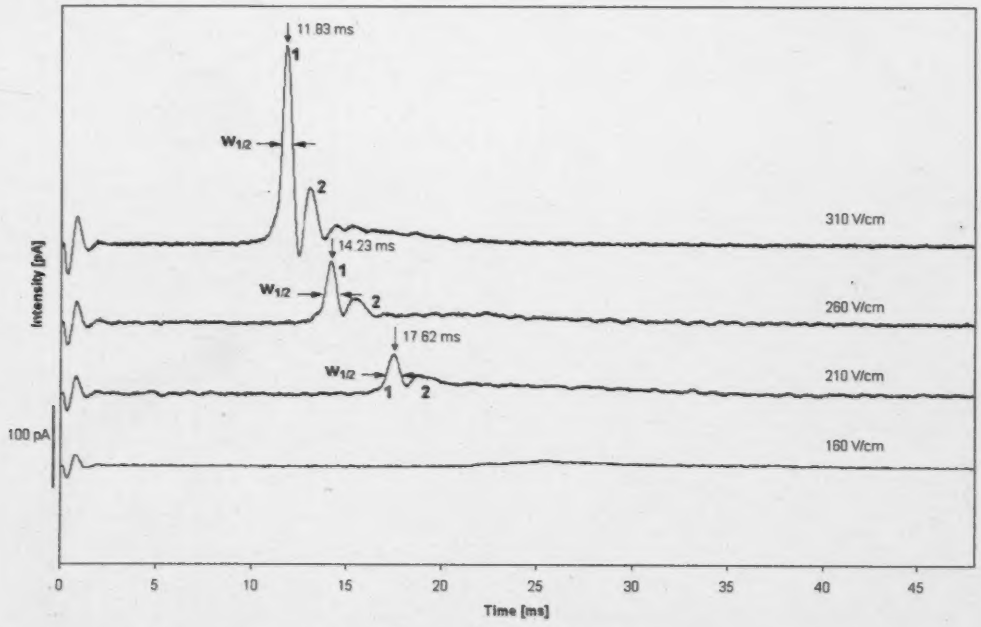

Figure 3-17(a). Time resolved spectra of 50:50 (v/v) methanol/water for varying drift electric fields.

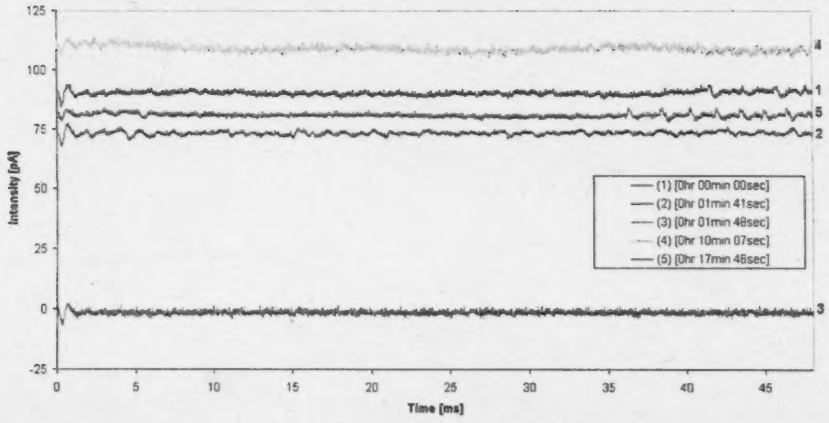

Figure 3-17(b). Time resolved spectra of 50:50 (v/v) methanol/water for a drift electric field of ~100 V cm^{-1}. Sample was loaded before (1) and before (4). (3) represents a zero-signal spectrum when liquid in the ESIS had dried up.

In Fig. 3-17(a) the peak positions are shown to shift to longer drift times for lower drift electric fields. The reduced mobilities given by Eqn. (3.5) for these peaks (peak 1) with drift times of 11.83, 14.23, and 17.62 ms are 1.38, 1.39, and 1.40 $\frac{cm^2}{V \cdot s}$, respectively; as expected, these values are the same (to within 1/100 of a decimal point) from Eqn. (3.5). (These K_o are also within ~5% of the average value obtained for peak 1 in Fig. 3-13.) The temporal widths ($w_{1/2}$) are 0.57, 0.65, 0.79 ms, respectively, thus resulting in R_p values of 20.75, 21.77, and 22.15. These values are actually somewhat comparable to those of Hill and co-workers [15,20,21] (see above), more so considering that their experiments were made with a significantly more complex systems with a longer drift column and with different drift gases [where they [22] had found that certain (high polarizability) drift gases would actually increase the drift times of the ions, thus resulting in high R_p values, as defined by Eqn. (3.6)].

3.3.1. Cytochrome c

Cytochrome c, found in plants and animals, is a small electron-carrying heme protein (~12.3 kDa) that is important for photosynthesis and respiration.[22] The samples of cytochrome c that were studied using ES-IMS Device II were bovine heart (C3131, MW 12.327 kDa) and horse heart (C7752, MW 12.384 kDa), both from Sigma-Aldrich (St. Louis, MO). The concentrations used were between 1 mg/mL (1 part in one thousand) and 5 mg/mL (5 parts in one thousand) for the bovine heart (C3131), and ~3 mg/mL (3 parts in one thousand) for the horse heart (C5572).

To prepare a 1 mg/mL sample, 1 mL of filtered, Milli-Q water (dd H_2O) was first pipetted into the 10 mg vial of cytochrome c (bovine heart). [The Milli-Q (de-ionized and distilled) water had previously been autoclaved, then 0.45 mm filtered.] The vial was vortexed for several minutes, then left to sit under an aluminum foil in a dark room (cytochrome c is light sensitive). 0.5 mL of certified ACS spectranalyzed (100%) methanol (A408-1; Fisher Scientific Ltd., Nepean, ON, Canada) was pipetted into an Eppendorf tube that was covered in aluminum foil. To this foil-covered Eppendorf tube was added a 0.4 mL aliquot of filtered dd H_2O. The vial of cytochrome c was vortexed for several more minutes, then 0.1 mL of the cytochrome c solution (observed under light as a consistent, faint red-brown colour) was extracted then added to the contents of the foil-covered Eppendorf tube, which in turn was vortexed for another several minutes. Both the vial of cytochrome c (9 mg in 0.9 mL of water) and the foil-covered Eppendorf tube (labeled with 1 mg/mL cytochrome c) were either used immediately or refrigerated until needed.

Figure 3-18 shows a comparison of the spectra for the "Control run" (without any liquid, with only the HV turned on), the "Solvent-only" run (with the methanol/water mixture, with the HV turned on), and the 1 mg/mL and the 5 mg/mL concentrations of cytochrome c. As can be seen, the "Control run" spectrum looks like that in Fig. 3-11. The solvent-only run produced peaks 1-5, where peaks 1 and 2 can be attributed to the solvent peaks (see Fig. 3-16). The later (weak) peaks (i.e., peaks 3-5) seen in Fig. 3-18 are not attributed to any particular component, as they are not always present. Hill and co-workers also observed these "bumps" (shown in Fig. 3-14), although they did not

speculate as to their identity.[16] [They may be due to the air around the tip of the Taylor cone being ionized (via corona ionization), which agrees with the belief by some in the field that these peaks are air contaminants.[16,19]] The addition of the lower concentration sample of cytochrome c resulted in peaks 6-8, which increase in signal amplitude for the higher concentration. To better show the resolution of ES-IMS Device II [our peak resolution (R_p) values of ~20 were comparable with those obtained by Hill *et al.* [20]], we obtained resolved solvent peaks (peaks 1 and 2) even with the addition of the protein (cyt-c), which differed from that of some systems reported in the literature. For example, Hill and co-workers [20] noted that typically when an analyte was added (in their case 0.05 mg/mL glucosamine or n-tetradecylamine), their solvent peaks become unresolved (i.e., the solvent typically showed up as a single peak in their ion mobility spectrum), which these researchers attributed to either ion chemistry reactions in the liquid of the ESIS during ES or ion-molecule interactions in the gas-phase that occurred in the desolvation region.

Figure 3-19 shows a (zoom view) comparison of the 1 mg/mL cytochrome c and the solvent spectra. The discrimination of two different samples/solvents is done on the basis of the ion mobility spectra, which are system dependent. For example, one ES-IMS system will produce a slightly different spectrum for a 50:50 (v/v) methanol/water mixture than another system, depending on the types of drift gases, drift temperatures, etc. that are used. If used with a microfluidic chip, IMS is more robust than the more commonly used laser induced fluorescence (LIF) as used with the microfluidic toolkit [23] in terms of (1) the types of samples that can be analyzed (see *Section 1.3.1.*) and (2) the fact that separation can occur on-chip followed by a signal confirmation using the TOF measurement of the IMS.

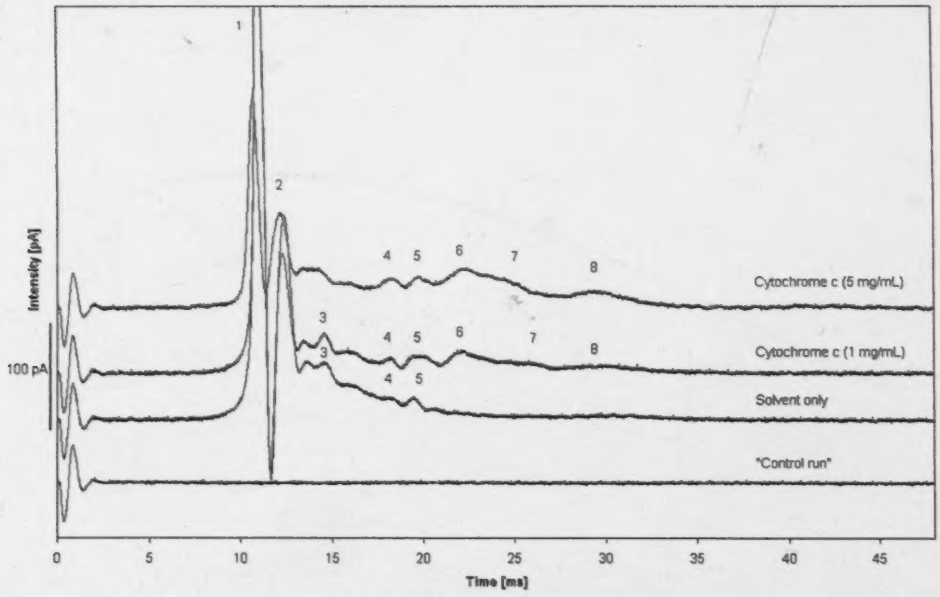

Figure 3-18. A comparison of the ion mobility spectra of cytochrome c (C3131; 1 and 5 mg/mL in 50:50 (v/v) methanol/water) with the solvent only and "control" runs. With the addition of solvent only, peaks 1-5 appear, where peaks 1 and 2 are due to the solvent while peaks 3-5 are likely air contaminants (see text). When the low concentration sample (Cyt-c) is added, peaks 6-8 appear, which increase in signal amplitude with the higher concentration.

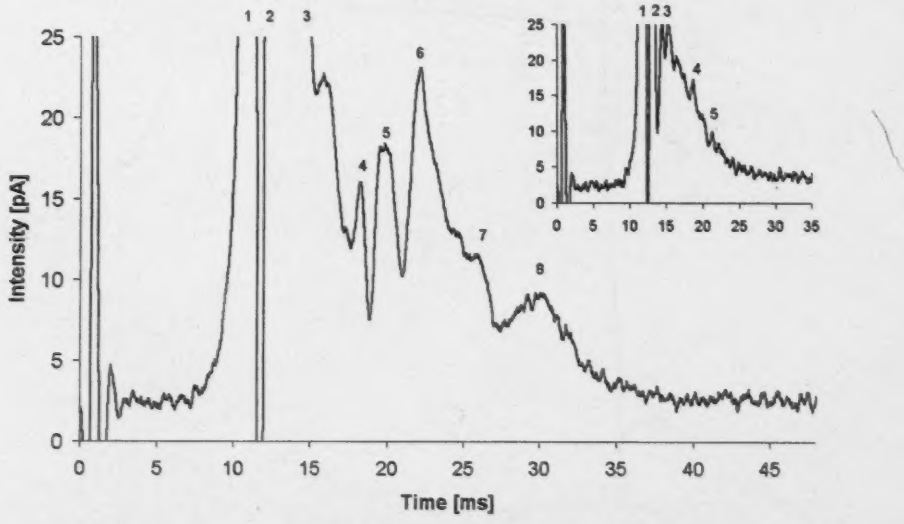

Figure 3-19. A comparison of the ion mobility spectra of 1 mg/mL cytochrome c with solvent only (inset). Peaks 1 and 2 are the solvent, peaks 3-5 are likely air contaminants, and peaks 6-8 are the cytochrome c peaks (see text).

For the 1 mg/mL cytochrome c samples (C3131), the average drift times for the (two) solvent peaks are 10.96 ± 0.25 ms and 12.22 ± 0.23 ms [an example shown in Fig. 3-18], and 22.39 ± 0.30 and 30.13 ± 0.18 ms, respectively for cytochrome c (cyt-c) peaks 6 and 8 (Fig. 3-19). [Peaks 3-5, with average drift times of 14.56 ± 0.25, 18.27 ± 0.06, and 20.07 ± 0.21 ms are the air contaminant peaks.] The reduced mobility values for cyt-c peaks 6 and 8 are 0.73 and 0.54 $\frac{cm^2}{V \cdot s}$. (Peak 7 was not sufficiently resolved from peak 6, and so will be associated with peak 6 for now.) What is clear from Fig. 3-19 is that when cytochrome c is added, peaks 6-8 appear after the solvent peaks (peaks 1 and 2), whereas they are not present for the solvent only runs [Fig. 3-19(inset)]. This means that, as a method of identification, we can pre-separate a sample on-chip (on a microfluidic ES chip) prior to ES, then use the IMS data as a confirmation.

Thus far it has been mentioned that peak positions shift with time under un-controlled flow conditions. However, when the flow conditions are ideal [i.e., with the initiation of a very low flow, thus by-passing SM-3 (and SM-1)], we have observed a very highly reproducible and repeatability series of spectra (shown in Figs. 3-20 and 3-21). Once low-flow conditions were achieved, we managed to obtain a single run (with a single sample loading of <100 μL) that lasted over 2 hours. However, this is not typical of the system (due to the flow issues).

For Figs. 3-20 and 3-21 (C3131, 5 mg/mL), t_d for the solvent peaks center around 10 and 11.8 ms, and for the cytochrome c peaks, around 22 (peak 6), 26 (peak 7), and 39 ms (peak 8). This translates to reduced mobilities (K_o) of 0.74, 0.63, and 0.42 $\frac{cm^2}{V \cdot s}$, respectively, for the cytochrome c (peaks 6-8). The other peaks (peaks 3-5) are centered about 14, 18.2, and 19.7 ms, with corresponding K_o of 1.17, 0.90, and 0.83 $\frac{cm^2}{V \cdot s}$. The variations in Fig. 3-21 can be attributed to the varying liquid flow rates in the ESIS, which as mentioned earlier would lead to changes in spray modes (or in this case, simply a change in droplet sizes due to a decreasing flow rate, thus resulting in amplitude variations). The decrease in amplitude to the zero-signal level indicates a drying up of the sample in the ESIS.

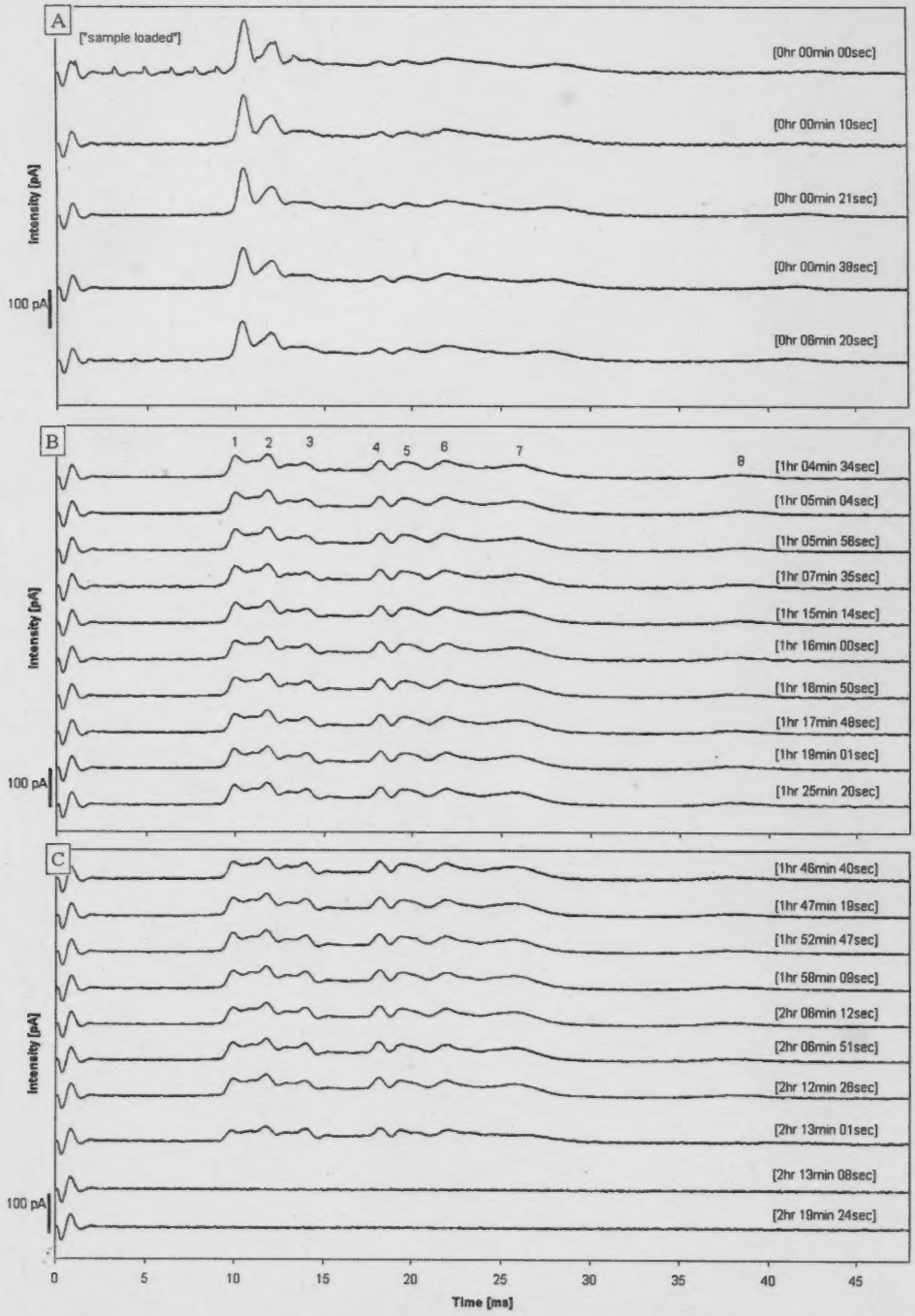

Figure 3-20. Time resolved spectra of cytochrome c (C3131; 5 mg/mL in 50:50 (v/v) methanol/water). (A) represents the start of the run immediately following the loading of 50 to 100 μL of sample; (B) represents ten consecutive spectra during the middle of this one run (notice the consistent shape of the peaks); and, (C) represents

the end of the over two hour long single run (when the liquid in the ESIS ran out). Each curve represents an average of 512 individual spectra. (See text for details.)

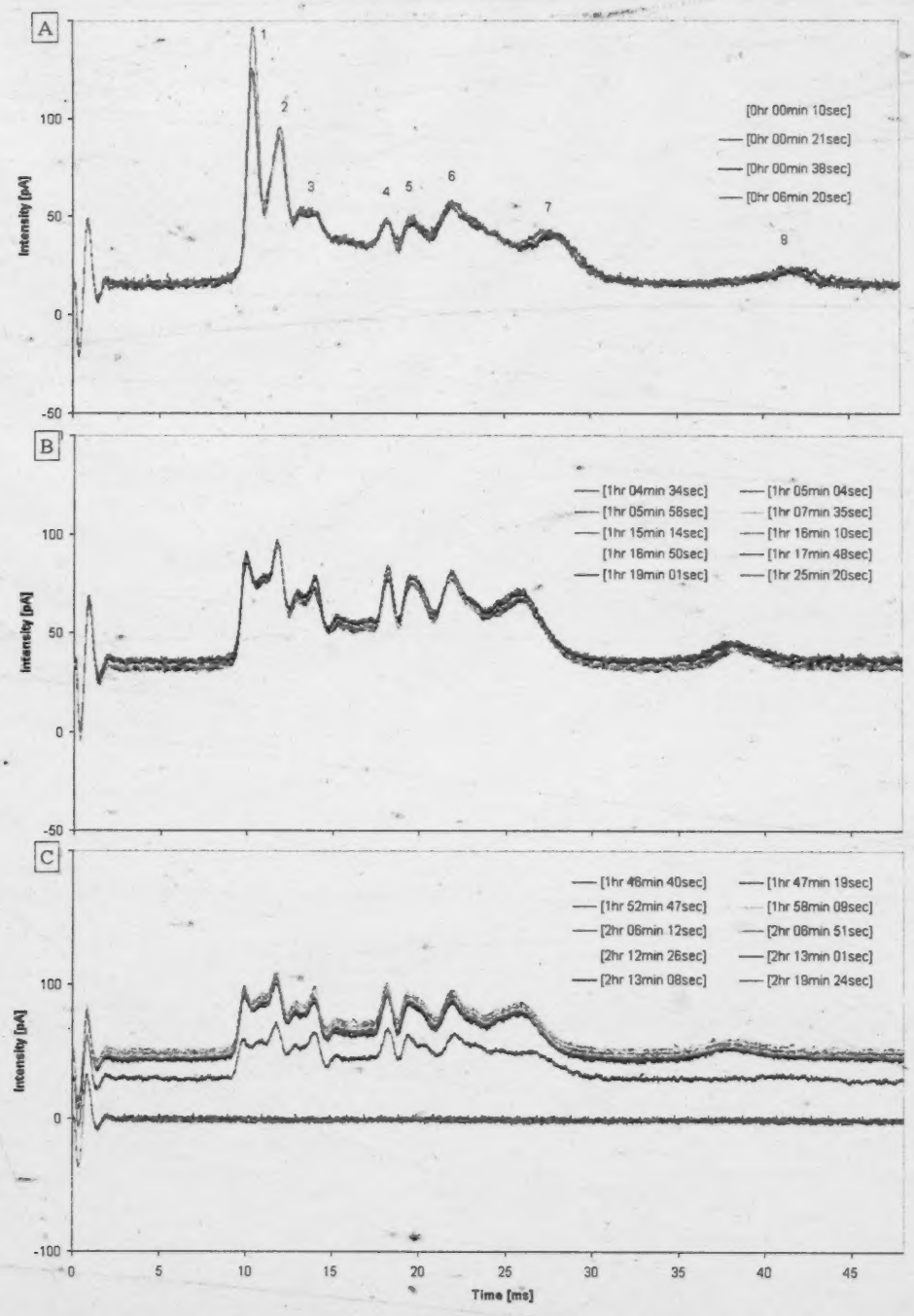

Figure 3-21. Overlapping spectra of cytochrome c (C3131; 5 mg/mL in 50:50 (v/v) methanol/water; from Fig. 3-20). (See the text and Fig. 3-20 caption for details.)

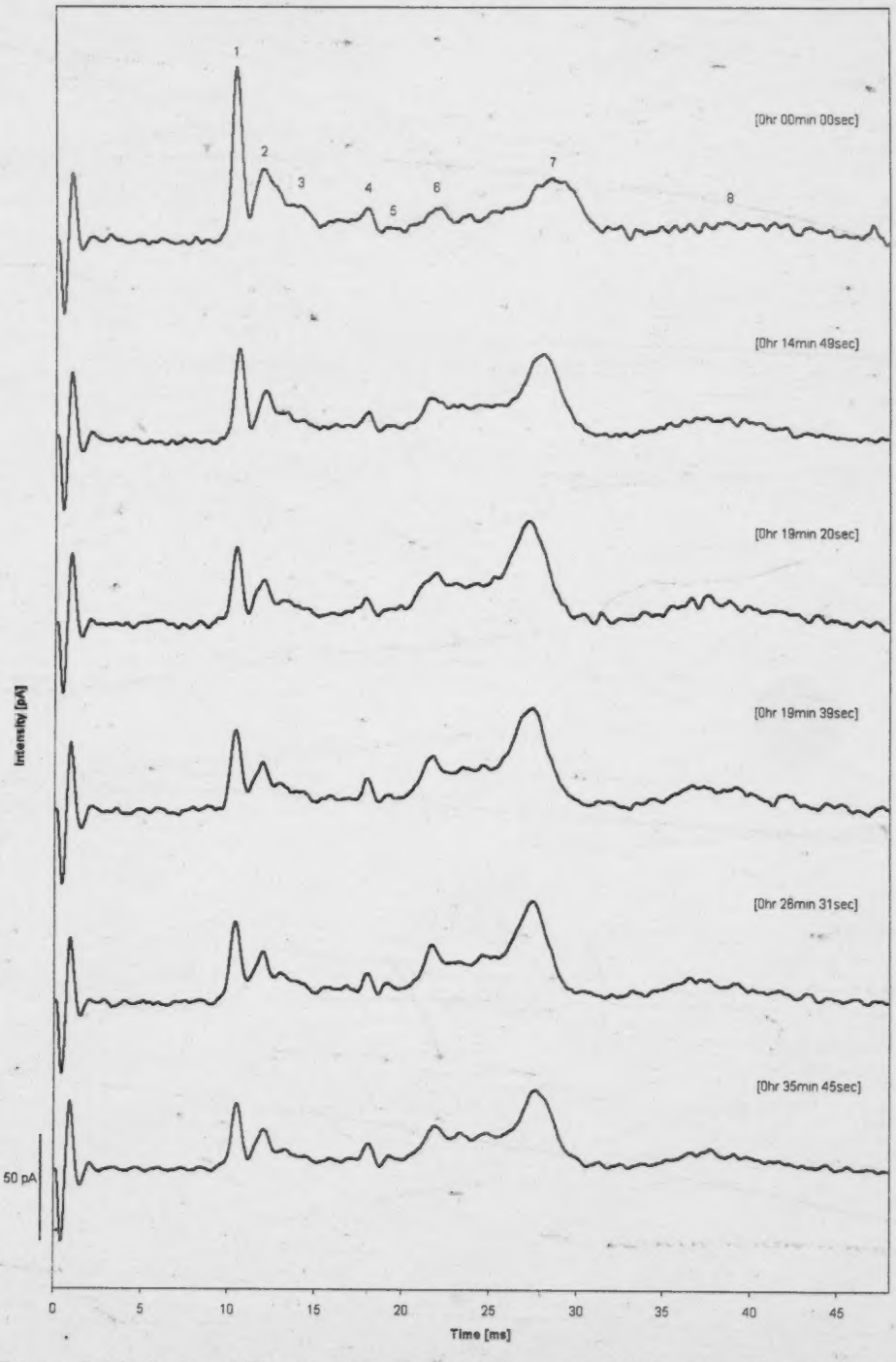

Figure 3-22. Ion mobility spectra of cytochrome c (C7752; ~3 mg/mL in 50:50 (v/v) methanol/water). Each curve represents a 20 point moving average of a spectrum that had already been averaged over 512 individual spectra (or scans).

From Fig. 3-22 (C7752, ~3 mg/mL), t_d for the solvent peaks are ~10.5 and ~12 ms, and for cytochrome peaks, ~22 (peak 6), ~27.5 (peak 7), and ~38 ms (peak 8); here, peak 4 (and sometimes, peak 5) also appear(s). The dominance of peak 7 in Fig. 3-22 (compared to peak 7 in previous figures) is most likely due to the differences in chemical composition between horse heart (Fig. 3-22) and bovine heart cytochrome c (Figs. 3-18 – 3-21). In Figs. 3-20 – 3-22 the signal amplitudes of the cytochrome c peaks (peaks 6-8) are approximately the same as for the solvent peaks (peaks 1 and 2), as opposed to the relative amplitudes in Figs. 3-18 – 3-19, where the cytochrome c peaks are considerably subdued in relation to the solvent ones. One reason is that over the course of a single run, the flow rates decrease, thus resulting in a more efficient electrospray with smaller initial droplets (as mentioned above). This means that there is less neutral solvent to evaporate during the desolvation process, therefore resulting in less solvent being detected at the end of the column (i.e., lower amplitude for the later spectra as opposed to the higher amplitude of the first spectrum); this is especially true for the 2 hour long run (Figs. 3-20 and 3-21), which represents the ideal condition, where a very stable, very efficient run occurs that spans over several hours from a single loading of a sample.

To compare these peak assignments with those found in the literature, the cyt-c peaks [i.e., the ~22, 26, and 39 ms peaks (peaks 6-8) in Figs. 3-20 and 3-21] are approximately in the right relative positions as those obtained by Smith *et al.*[16] and by Wittmer *et al.*[24]. In terms of resolution, the peaks in the above figures are slightly more resolved than the Smith cytochrome c peaks, but are less resolved than the Wittmer ones. Also, for one of the spectra obtained by Wittmer and co-workers, there were extraneous peaks centered about ~14 and 16 ms, which somewhat resemble the peaks 4 and 5 in Figs. 3-17 – 3-21, albeit a little closer to their solvent peak(s). Although they did not explicitly explain the origins of these extra peaks, they observed that with a closed configuration (i.e., by isolating their drift tube from their laboratory air) they were able to eliminate these peaks. Table 3-1 below compares the K_o values for cytochrome c obtained using ES-IMS Device II with those obtained by others [14,16,24] (where values were provided or calculated from given parameters). From the table it can be seen that our cyt-c values are somewhat similar, although with fewer peaks (shown as fewer K_o values). The bold-faced values represent the dominant cytochrome c peaks, where our

value of 0.74 cm^2 $(V\ s)^{-1}$ is similar to the 0.86 cm^2 $(V\ s)^{-1}$ obtained by Chen *et al.*[24] and Wittmer *et al.*,[16] who are both associated with the Hill group at Washington State University (which would explain their almost equal values).

Table 3-1. **Comparison of the Reduced Mobilities (K_o) of Cytochrome c Peaks**

Reference	Solvent $[cm^2\ (V\ s)^{-1}]$	Air Contaminants $[cm^2\ (V\ s)^{-1}]$	Cytochrome c [a] $[cm^2\ (V\ s)^{-1}]$
Ours	1.46, 1.31	1.17, 0.90, 0.83	**0.74**, 0.63, 0.42
Chen [b]	-	-	0.94, 0.91, **0.86**, 0.83, 0.80, 0.76, 0.72, 0.67
Wittmer [c]	2.40	1.69, 1.48	0.87, **0.84**, 0.81, 0.76, 0.72, 0.66, 0.61
	2.37	-	0.92, 0.89, **0.86**, 0.83, 0.81, 0.76, 0.72, 0.67

[a] Multiple K_o values reflect multiple Cytochrome c peaks, where the bold-faced values represent the dominant peaks.
[b] Cytochrome c data was given in Table IV of Ref. 24.
[c] Cytochrome c data was calculated from spectra in Ref. 16 and system parameters given in Ref. 14. Data was given for two different system configurations.

For the spectra obtained in Figs. 3-20 – 3-21, the 2 hour electrospray of 50 to 100 μL amounts to an effective sample flow rate of ~380 to ~770 nL/min. This means that the system is capable of achieving nano-ES (at least the high end of that regime). However, one should note that this was not a typical run, which generally lasts 2 to15 minutes for the same amount of sample/solvent (still ~3.3 to 50 μL min^{-1}). This is because of the uncontrolled flow of the sample, which requires coaxing (in the way of a slight application of air pressure) to start the flow; once flow has begun, the surface tension of the liquid, coupled with hydrostatic pressures will maintain the flow. The problem arises with the manual application of air pressure (with the mixture), which results in the various undesired spray modes (namely, SM-3 and SM-1, stated above).

$$\mathrm{LOD} = \frac{[\mathrm{Concentration}]}{[\mathrm{Peak\ Intensity}]} \cdot \mathrm{sLOD} = \frac{[\mathrm{Concentration}]}{[\mathrm{Peak\ Intensity}]} \cdot 3\sigma \qquad (3.8)$$

To arrive at a sample or concentration limit of detection (LOD), varying concentrations of (bovine heart, C3131) cytochrome c were studied. The 22 ms peaks (i.e., peak 6) of the resultant spectra (not shown) were baseline corrected (i.e., peak

height minus baseline height), then the average signal amplitudes were used to obtain the data points (shown in Fig. 3-23) for 1, 1.25, 1.65, 2.5, and 5 mg/mL concentrations. A linear regression of this plot was used to approximate the relationship between the signal strength (in pA) and the concentration (in mg/mL). However, when the signal amplitudes were plotted (shown in Fig. 3-23), the significant deviations from the linear regression proved that accurate LOD calculations could not be obtained by this method. These deviations are due to the changes in amplitude (as shown in Fig. 3-21) that results from the variance in the sample flow rate (as mentioned previously). In fact the error bars (which account for the largest difference in signal strength for any of the concentration levels) are ±13.87 pA wide, therefore control of the sample flow rate must first be achieved (which would allow for more consistent peak amplitudes) before this calculation can be made in the standard fashion (which is to input the sLOD into the linear equation obtained from the chart, then solve for LOD [25]). However, an estimated value of LOD can be arrived at by simply taking the lowest concentration used (i.e., 1 mg/mL), multiplying by the sLOD (i.e., the 2.09 pA obtained above), then dividing by the signal amplitude for the cytochrome c peak (in our case, peak 6 for the 1 mg/mL spectrum shown in Fig. 3-19, which was 20 pA), as follows:

$$\mathrm{LOD} = \mathrm{conc} \cdot \frac{\mathrm{sLOD}}{\mathrm{I_{peak}}} = 1 \tfrac{\mathrm{mg}}{\mathrm{mL}} \cdot \frac{2.09\,\mathrm{pA}}{20\,\mathrm{pA}} = 0.105 \tfrac{\mathrm{mg}}{\mathrm{mL}} = 105\,\mathrm{ppm} \qquad (3.9)$$

The resultant estimated LOD was thus found to be 0.105 mg/mL or 105 ppm. This LOD can be represented as ~8.5 pmol/μL or ~8.5 x 10^{-6} M. Although LOD values are frequently not specified in the literature (especially for cytochrome c), one example of an LOD is 7.5 x 10^{-7} M for atrazine,[12] which was obtained using an ES-based IMS of far greater cost and complexity (i.e., with syringe pumps, drift and sheath gases, drift tube heaters, etc.).

With more sensitive electronics (especially with noise reduction), and with the averaging of a larger number of scans (which will reduce the sLOD), the level of sample concentration detectable by the system (LOD) can be decreased by a significant amount, perhaps even down to a few ppm or even ppb. [See *Chapter 4* for sLOD and LOD values for a detector circuit (Pico IV) that incorporates active noise filtering.]

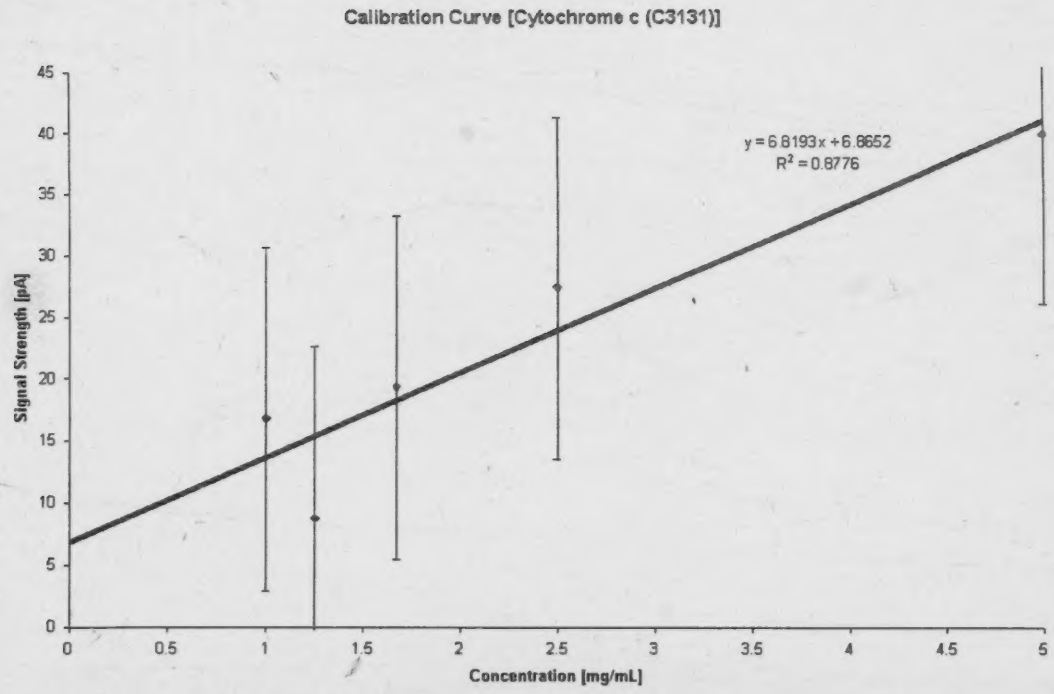

Figure 3-23. Calibration curve obtained for the ES-IMS Device II, for the protein cytochrome c (C3131). A linear regression is shown for the average amplitudes (both base-line corrected and converted to pA) of the 22 ms peaks for concentrations of 1.25, 1.67, 2.5, and 5 mg/mL (or parts per thousand). The error bars take into account the largest difference in signal strength for any one of these concentration levels (in this case, ±13.87 pA); the large error is due to the uncontrolled/ unpredictable sample flow rate at the ESIS (see text).

3.4. Conclusions

Firstly, the optocoupler phototransistor-based SG controller has been proven to provide extremely fast switching times for the gate voltages (0.1 ms; with rise and fall times of 0.8 and 131.9 μs, respectively, with an absolute closing time of ~200 – 300 μs) using the configuration shown in Fig. 3-4(a) (see *Section 3.2.1.2*), which includes the use of a segregated array for the reference voltages, an R_{BE} value of 1 MΩ at the first optocoupler (*OK1*), and an R_g value of 1 MΩ (which translates to a voltage of ~49 V across 0.9 mm for the FG at 3 kV for an orthogonal field of ~550 V cm^{-1}, which is almost twice the drift electric field of ~310 V cm^{-1}).

The system was tested with 50:50 (v/v) methanol/water [Figs. 3-13 and 3-17(a)], a common solvent used for ES-IMS experiments, where two dominant peaks were observed that centered around 11.2 and 12.4 ms, corresponding to water and methanol respectively (Fig. 3-16). The peak resolution (R_p) was found to be 20.8 and 17.7 for two peaks respectively. When we compare with the solvent spectrum obtained by the Hill group [20] – whose order of methanol and water peaks are reversed from ours (Fig. 3-14), with R_p of 18 and 19 – we see that our peak resolution values (obtained with a much simpler system, that is, without drift gases or high temperatures, and with a shorter drift length, all of which have been reported to improve the performance of an IMS [14-16]) are similar.

In terms of the repeatability of the system performance, Figs. 3-20 and 3-21 (both representing the same run) show that the spectra can indeed remain virtually the same over the course of over two hours for a 50 – 100 μL sample/solvent solution (in our case, for the protein cytochrome c), which means that we have attained the (high-end) of nano-ES, so long as the "over-spray" mode (SM-3) is by-passed. This, however, is not typical of the system due to problems arising from the manual application of air pressure to initiate flow in the ESIS, which generally results in a system that first enters SM-3 before setting into SM-2 (the stable regime characterized by clean spectra). It should be noted that the flow rates of typical runs are actually somewhat comparable to those reported in the literature (see *Chapter 1*), once the stable mode has been initiated. That is, the same

amount of sample/solvent solution typically lasts anywhere from 5 to 15 minutes, thus translating to flow rates of ~3.3 and 20 μL min^{-1}.

The signal limit of detection (sLOD) of the device (i.e., the lowest intensity signal that can be distinguished from the background noise) was found to be ~2.09 pA, after averaging over 512 spectra, while the concentration limit of detection (LOD) was estimated to be ~100 ppm or ~8.1 μM for the cytochrome c analyte. By averaging over a larger number of spectra, sLOD and thus LOD will be decreased a few ppm [Eqn. (3.4)]. Coupled with better detection circuit (i.e., with active noise filtering), LOD could perhaps even be brought below ppm.

In conclusion, the system has been proven to function as designed. The portable, modular, and light-weight construct allows for integration with microfluidic ES chips, which among other advantages allows for highly parallel analyses of samples both on-chip and in-IMS (e.g., separation versus no-separation of proteins on-chip could simultaneously interface via multiple spray tips into parallel IMS columns, each of which uses different drift gases or different detection modes to study the differences in ion mobilities). Such a system is less costly than most systems (especially ones that utilize commercial high voltage pulsers and/or high voltage supplies), with costs of a few hundred dollars (US); replacing the EMCO's (the most expensive components) with an in-house-built HV circuit would reduce the cost further. And, since it is PCB-based, it is capable of being easily mass produced, with any changes to the design being made just as easily. Future designs would integrate the data-acquisition and averaging using the ADC inputs of the PIC Microboard, thus completely replacing the oscilloscope to make a more compact analysis instrument; this represents the power of a microcontroller design.

3.5. References

(1) Bradbury, N. E.; and Nielsen, R. A., "Absolute values of the electron mobility in hydrogen," *Physical Review*, **49** (1936), pp. 388-393.

(2) Spangler, G. E., "Theory and technique for measuring mobility using ion mobility spectrometry," *Analytical Chemistry*, **65** (1993), pp. 3010-3014.

(3) Nowak, D. J.;Rice, J. E.; and Bianco, D. R.," Ion gating grid," United States Patent No. 4,150,319 (April 17, 1979).

(4) Halliday, D.;Resnick, R.; and Walker, J., *Fundamentals of physics*, 4th Edition, John Wiley & Sons, Inc., Toronto, 1993.

(5) Keithley, J. F., *Low level measurements: precision DC current, voltage and resistance measurements*, 5th Edition, Keithley Instruments, Inc., Cleveland, 1998.

(6) datasheet for OPA129 (Burr-Brown Corporation, Tucson, AZ).

(7) An example of the "flying wire" connection also referred to as "air wiring" can be found in the datasheet for a precision CMOS dual micropower operational amplifier (LMC6062; National Semiconductor).

(8) Juraschek, R.; and Rollgen, F. W., "Pulsation phenomena during electrospray ionization," *International Journal of Mass Spectrometry*, **177** (1998), pp. 1-15.

(9) Tang, K. Q.; and Gomez, A., "Monodisperse electrosprays of low electric conductivity liquids in the cone-jet mode," *Journal of Colloid and Interface Science*, **184** (1996), pp. 500-511.

(10) Jones, A. R.; and Thong, K. C., "The production of charged monodisperse fuel droplets by electrical dispersion," *Journal of Physics D-Applied Physics*, **4** (1971), pp. 1159-1166.

(11) Tang, K. Q.; and Gomez, A., "Generation of monodisperse water droplets from electrosprays in a corona-assisted cone-jet mode," *Journal of Colloid and Interface Science*, **175** (1995), pp. 326-332.

(12) Smith, R. D.;Loo, J. A.;Loo, R. R. O.;Busman, M.; and Udseth, H. R., "Principles and practice of electrospray ionization - mass spectrometry for large polypeptides and proteins," *Mass Spectrometry Reviews*, **10** (1991), pp. 359-451.

(13) Kebarle, P.; and Tang, L., "From ions in solution to ions in the gas-phase: The mechanism of electrospray mass spectrometry," *Analytical Chemistry*, **65** (1993), pp. A972-A986.

(14) Chen, Y. H.;Hill, H. H.; and Wittmer, D. P., "Thermal effects on electrospray ionization ion mobility spectrometry," *International Journal of Mass Spectrometry and Ion Processes*, **154** (1996), pp. 1-13.

(15) Wu, C.;Siems, W. F.;Asbury, G. R.; and Hill, H. H., "Electrospray ionization high-resolution ion mobility spectrometry - mass spectrometry," *Analytical Chemistry*, **70** (1998), pp. 4929-4938.

(16) Wittmer, D.;Chen, Y. H.;Luckenbill, B. K.; and Hill, H. H., "Electrospray ionization - ion mobility spectrometry," *Analytical Chemistry*, **66** (1994), pp. 2348-2355.

(17) Guevremont, R.;Siu, K. W. M.;Wang, J. Y.; and Ding, L. Y., "Combined ion mobility time-of-flight mass spectrometry study of electrospray-generated ions," *Analytical Chemistry*, **69** (1997), pp. 3959-3965.

(18) Ikonomou, M. G.;Blades, A. T.; and Kebarle, P., "Electrospray ion spray: A comparison of mechanisms and performance," *Analytical Chemistry*, **63** (1991), pp. 1989-1998.

(19) Matz, L. M.;Steiner, W. E.;Clowers, B. H.; and Hill, H. H., "Evaluation of micro-electrospray ionization with ion mobility spectrometry/mass spectrometry," *International Journal of Mass Spectrometry*, **213** (2002), pp. 191-202.

(20) Chen, Y. H.;Siems, W. F.; and Hill, H. H., "Fourier transform electrospray ion mobility spectrometry," *Analytica Chimica Acta*, **334** (1996), pp. 75-84.

(21) Asbury, G. R.; and Hill, H. H., "Using different drift gases to change separation factors (alpha) in ion mobility spectrometry," *Analytical Chemistry*, **72** (2000), pp. 580-584.

(22) "Life Science Dictionary," Biotech Resources, University of Texas at Austin (Austin, TX, USA), 2000, website: http://biotech.icmb.utexas.edu/search/dict-search.html. Accessed: (2003) March.

(23) Crabtree, H. J.;Cheong, E. C. S.;Tilroe, D. A.; and Backhouse, C. J., "Microchip injection and separation anomalies due to pressure effects," *Analytical Chemistry*, **73** (2001), pp. 4079-4086.

(24) Chen, Y. H.;Hill, H. H.; and Wittmer, D. P., "Analytical merit of electrospray ion mobility spectrometry as a chromatographic detector," *Journal of Microcolumn Separations*, **6** (1994), pp. 515-524.

(25) Long, G. L.; and Winefordner, J. D., "Limit of Detection," *Analytical Chemistry*, **55** (1983), pp. A712-A724.

Chapter 4

Future Work

Page

Table of Contents

4.1. ES-IMS Device III 141
4.1.1. Collector-Detector Assembly III 146
4.2. Microfluidic Electrospray Chip Applications 150
4.3. Ion Thruster Applications 151
4.3.1. Theoretical Analysis and Estimates of Thrust 152
4.3.2. Low Vacuum Design and Testing of an Ion Thruster – Propelled Craft 155
4.3.2.1. Design of IT Pendulum I 158
4.3.2.2. Design of the Control Tube for IT Pendulum I 160
4.3.2.3. Experimental Setup for Testing IT Craft III: "Vac I" 162
4.3.3. Ion Thruster Arrays 163
4.4. References 164

4.1. ES-IMS Device III

In *Chapter 3*, an electrospray ionization - ion mobility spectrometry (ES-IMS) system (Device II) was described that utilized double-sided copper-clad boards [i.e., printed circuit board (PCB) material] as the guard rings, grids, and shutter gate, as well as the side-boards that held them in place. On these side-boards (single-sided copper-clad boards) was mounted a resistor array (61 - 1 MΩ surface-mount resistors in series) that divided the (typically) 3 kV focus grid voltage across the 62 surfaces such that the voltage difference between two adjacent guard rings was ~49 V. The drift length was measured to be 5.85 cm, with average guard ring separations of ~1.55 mm.

The third ES-IMS Column represents an alternative method of assembly. The individual components (i.e., the guard rings, the grids, and the shutter gate) were constructed in the same manner, except that this time 2 x 2 mm dual-row headers (soldered on either side of each PCB piece) were slotted into holes set in the side-boards instead of tabs slotted into slits in the side-boards. The original idea was that this pin-slotting arrangement (where two clusters of 4 header pins soldered on either side of each double-sided Column piece) would allow for more flexibility in the IMS design – that is, the shutter gate position (for example) could be changed at will. [Note that four pins, two on each side would be electrically connected to each PCB surface (i.e., to each guard ring or grid), where the two sides are electrically disconnected save for 1 MΩ resistor mounted between them.] This proved not to be the case due to the considerable amount of flex that these pins had, which countered any hopes of equal spacing of the PCB components. Apparently, with the copper-clad boards from MG Chemicals, the thickness varied between ~1.4 and ~1.6 mm. Permanent soldering of these to the side-boards (like with the tabs in Column II) was the only option in order for the spacing to be guaranteed (whereby prior to soldering, extra pieces of the same material were used as spacers).

For the shutter gate control, a new design called for surface mounting of the components. This essentially eliminates instances (as with Column II) where the metal tabs around through-holes would come off with excessive soldering. Also, this would allow for easy attachments of resistors (such as the 1 MΩ base-to-emitter resistor for optocoupler 1, see *Chapter 3*). Jumper cables in conjunction with headers/receptacles

soldered on a few points along the resistor-side of the column (near the shutter gate) allowed for easy reconfiguration of the positive and negative references (whereas re-soldering was required with Column II each time one wished to change the references). Figure 4-1 depicts the components of the fully assembled Column III (shown in Fig. 4-2).

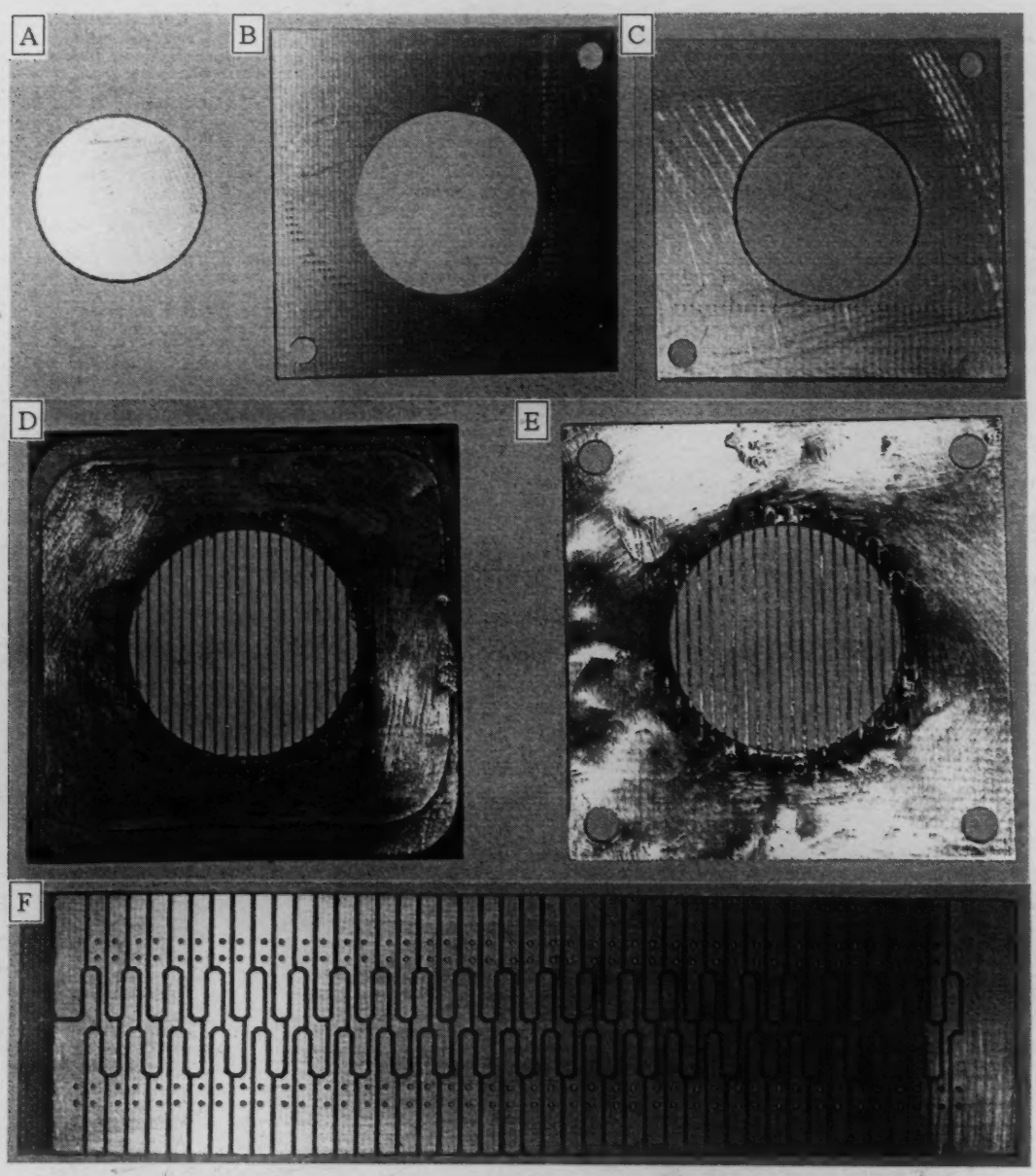

Figure 4-1. Photographs of the various components for IMS Column III. Shown are (A) the extraneous "button", (B) the un-"tinned" and (C) "tinned" guard ring, (D) the focus grid, (E) the aperture grid, and (F) one of the two side-boards.

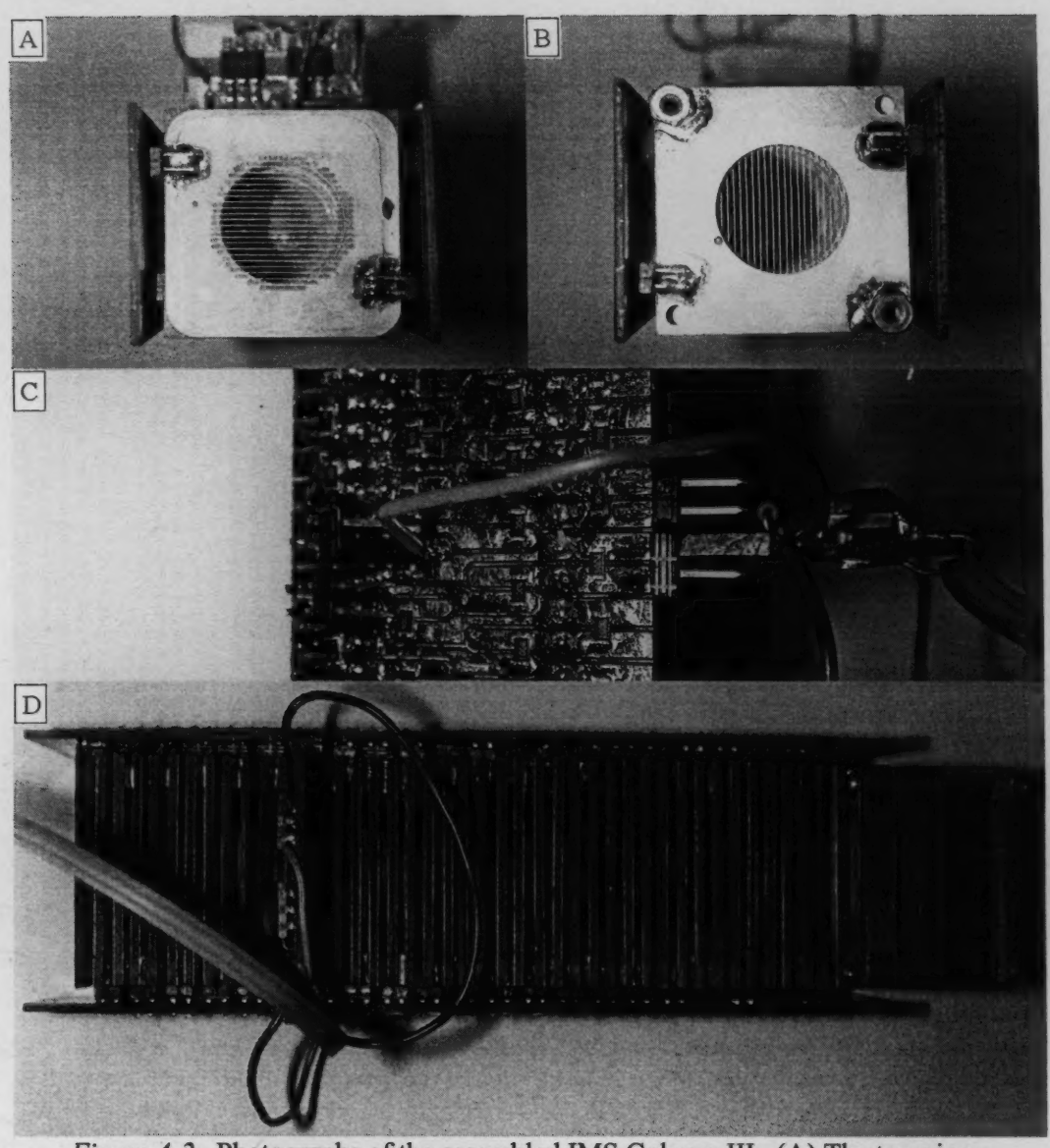

Figure 4-2. Photographs of the assembled IMS Column III. (A) The top-view shows the focus grid and the shutter gate control; note the double-headers on either side of the grid. (B) The bottom-view shows the aperture grid; note the brass ¼ inch nuts soldered to opposing corners [these are for attaching the Collector-Detector (C-D) Assembly III]. (C) A close-up view of the column shows the region of the resistor-side around the shutter gate (and controller); note the attached headers and jumpers that allow for easy reconfiguration of the shutter gate references. (D) A wide view shows the fully assembled Column III with the attached C-D III (shown on the right, and described in the next section). The length of the drift region is ~9.1 cm, with the total (FG to collector plate) length being ~13.1 cm (which is longer than the Column II for improved temporal resolution). The ribbon wire is for *LED-Hi*, GND, and *LED-Low* (see *Chapter 2*).

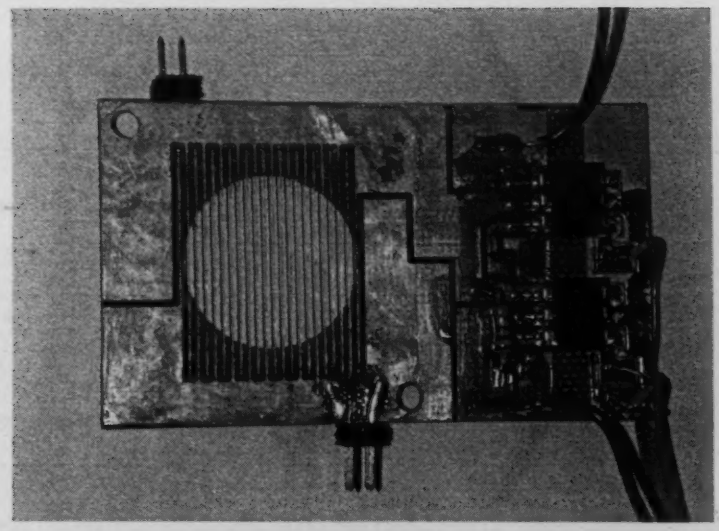

Figure 4-3. Photograph of the ion shutter gate and controller for IMS Column III. Here, the use of surface mount components allows for easy modification of the circuit (should that be necessary). Note that the positive and negative references (represented by the two jumper wires, shown at the top and bottom) are not electrically connected to the grid. This allows for the floating half of the grid to be more positive or more negative than the non-floating half. Note also that one set of wires (bottom) has part of a dual-row header soldered to it (that will be connected to the resistor array along the side-board), while the other does not [but is actually electrically connected via traces to the emitter of optocoupler 1 (bottom) and the collector of optocoupler 2 (top)] The ribbon wire is for *LED-Hi*, GND, and *LED-Low* (see *Chapter 2*).

Figure 4-3 shows the shutter gate and controller for IMS Column III, which is essentially the same as that for Column II (see *Chapter 3*) except that the components are surface mount (which would allow for easier replacement of components). Please refer to *Section 3.2.1.2* for a description of the operation of the shutter gate.

The next steps would involve testing this system and comparing it with the previous ones [particularly Device II, which has been shown to perform well (see *Chapter 3*)]. Other samples, such as polyethylene glycol (PEG600) and bovine serum albumin (BSA), would also be tested with the system. Ion mobility spectra of PEG600 (an oligomer) are readily available for comparison, however, only mass spectra [1] of BSA (a protein) are available. According to Chen *et al.*[2] the peak amplitudes for PEG600 are similar to those for cytochrome c. Figure 4-4 depicts a sketch of a PEG600 ion mobility spectrum, modified from Ref. 2. The first peak (about 10 ms) is the unresolved 50:50

(v/v) methanol/water solvent, while the broad peak (about 25 ms) is due to the PEG600. Actually, the spectrum obtained by Chen and co-workers shows multiple peaks within the 25 ms main peak, where these peaks become better resolved with a higher drift temperature (~250 °C) due to de-clustering of the solvent.

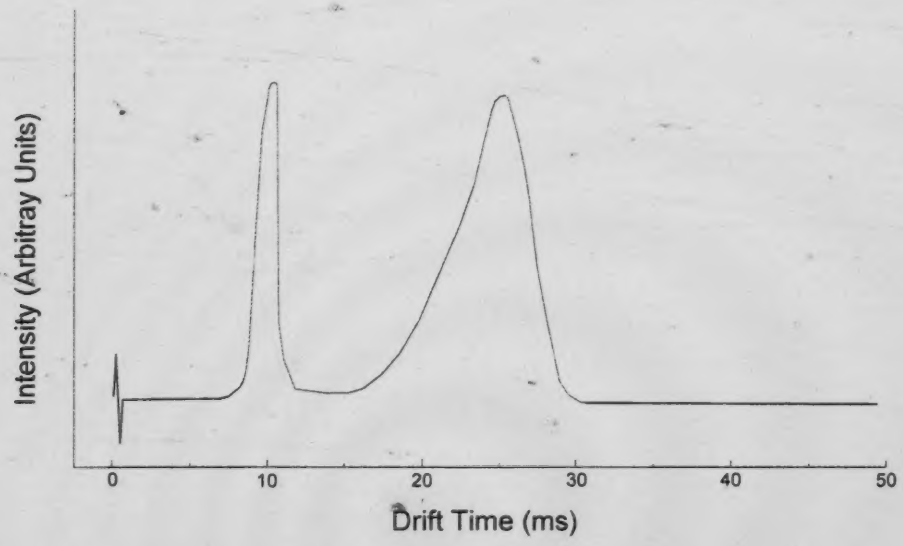

Figure 4-4. Ion mobility spectrum of PEG-600 obtained by Chen and co-workers. The peak centered about 10 ms is the solvent peak, while the peak about 25 ms is the PEG600. Note that the spectrum obtained by Chen shows multiple peaks within the 25 ms peak. Modified from Ref. 2.

4.1.1. Collector-Detector Assembly III

The third detector (or picoammeter, also referred to as "Pico IV") is a redesign of the second detector ("Pico II," see *Chapter 3*), this time including active noise filtering of the op-amp input power. ["Pico III" is a transition model that was used to test the effectiveness of "Pico IV." Pico IV is a modular, compact version of Pico III (not shown).] The 1 GΩ feedback resistor is the same, however, the 10 MΩ resistor and the 100 pF capacitor have been replaced by 20 kΩ and 2 kΩ resistors, respectively. An offset stage (set via a 50 kΩ potentiometer) is connected to the non-inverting input of the OPA129, while the feedback loop connected to the inverting input looks similar to that of "Pico II." This first stage has a nominal gain of -1.1×10^{10} V/A [-1 GΩ + 20 kΩ (1 - 1 GΩ / 2 kΩ)]. The second stage is an inverting (OPA228) op-amp stage utilizing a gain of -10 V/V (-47 kΩ / 4.7 kΩ), whose output goes through a 47 Ω resistor that connects to the outside via one of the 9-pin port connections. The ±12 V_{dc} and GND connections are also wired through this 9-pin port. Figure 4-5 depicts the individual circuit schematics for the 1st and 2nd stages, as well as the 9-pin port connections with the active noise filtering for the ±12 V_{dc} supplies.

The first stage and the 9-pin port connections are mounted on their own respective double-sided boards, while the second stage shares space with a noise filtering circuit (based on two OPA2228 op-amps), that although electrically disconnected from the rest of the gain stages (except for the ±12 V_{dc} and GND connections) filters any low frequency noise from the (±12 V_{dc}) inputs. The collector plate is attached to the opposite side of the same board as the first stage (board #1). Between this first board and the next (board #2 which consists of the 2nd stage and the low frequency filter) are three "border" plates that enclose the circuit components that act as spacers [an example of which is shown in Fig. 4-6(a)], two of which were cut to allow the 50 kΩ potentiometer to fit with the dial accessible on the outside. Three more "border" plates separate this second double-sided board from the one with the 9-pin connector (board #3). A "border" box [shown in Fig. 4-6(b)] separates this third board from the bottom cover plate (board #4) of the collector-detector assembly. The first two boards are shown in Figs. 4-6(c), 4-6(d) as mounted and partially assembled.

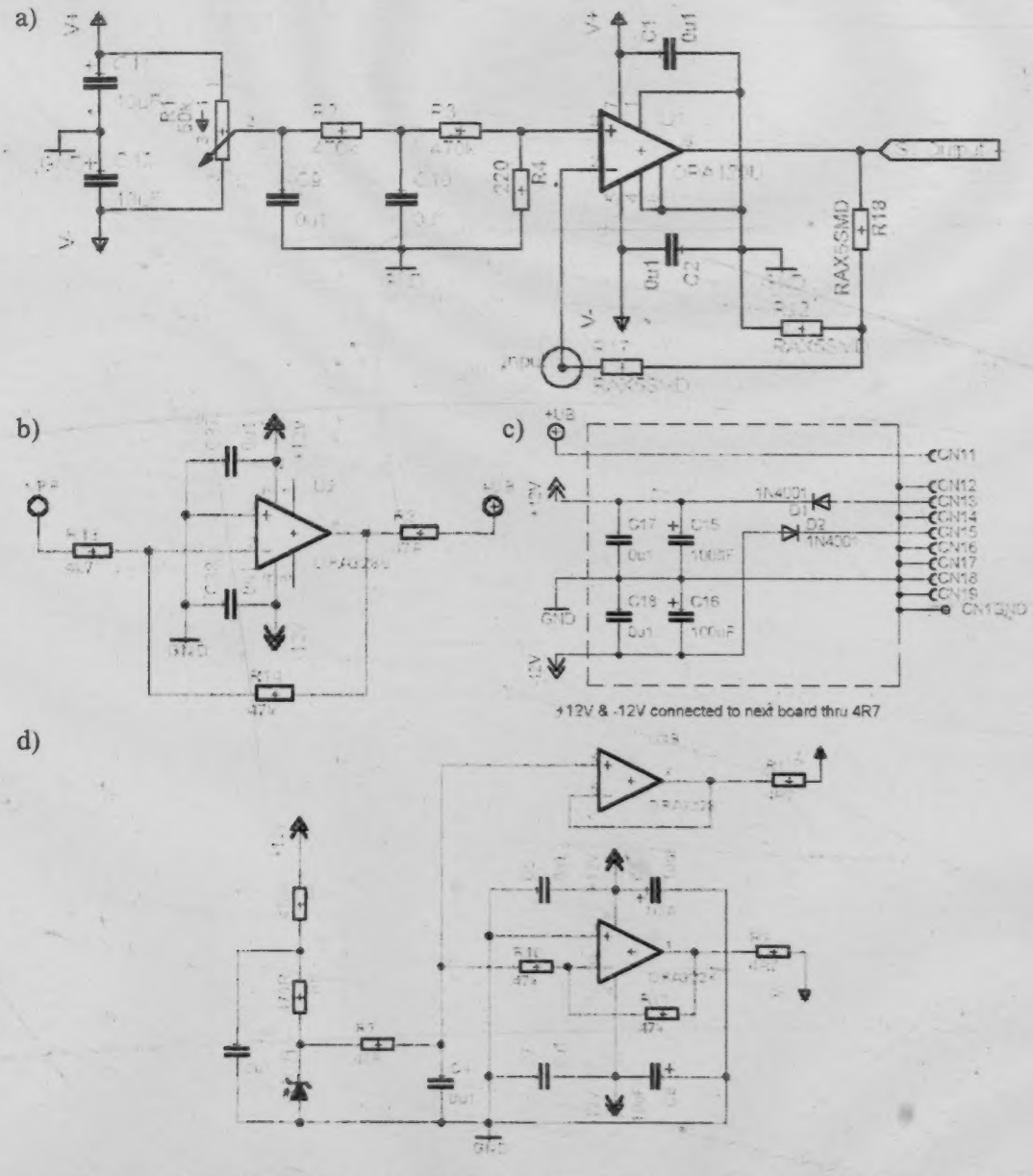

Figure 4-5. Individual circuit schematics of the Detector III stages. Shown are the -1.1 x 10^{10} V/A gain 1st stage with a 50 kΩ offset control (a), the -10 V/V gain 2nd stage (b), the 9-pin port connections (c), and the low frequency noise filter for the ±12 V_{dc} op-amp inputs (d).

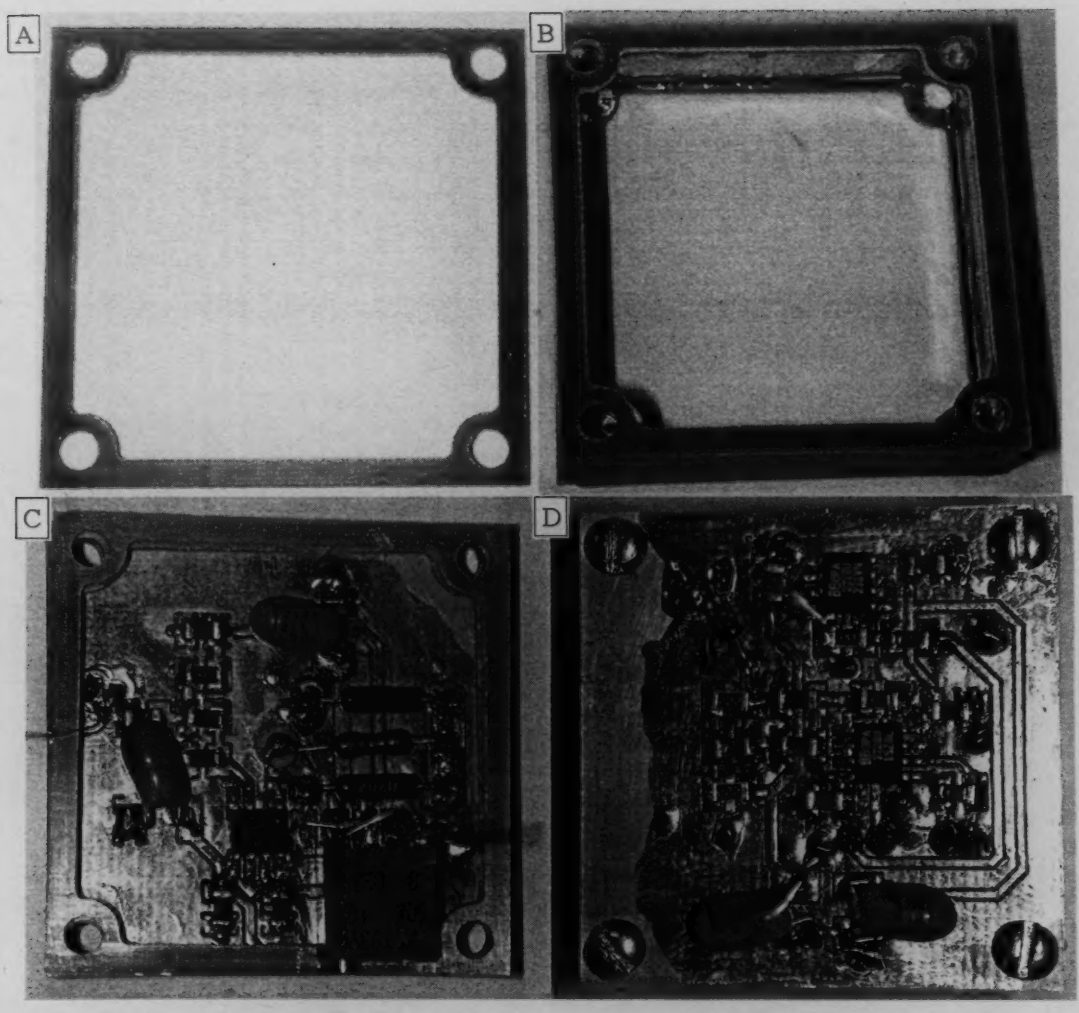

Figure 4-6. Photographs of the various components for C-D Assembly III. Shown are (A) an example border plate, (B) the border box, and (C) the mounted and partially assembled 1st board with the first stage and (D) the 2nd board with the second stage and low frequency noise filter.

When fully assembled, the sides of this modular and enclosed third collector-detector assembly measure 3.9 x 3.9 cm. The length measures 2.75 cm (just the casing), 3 cm (including the collector plate), and 3.4 cm (including both the collector plate on one end and the 9-pin port at the other end). Figure 4-7 shows the front (or top) (a) with and (b) without the aperture grid, (c) the side with the offset control, and (d) the back (or bottom) with the 9-pin port.

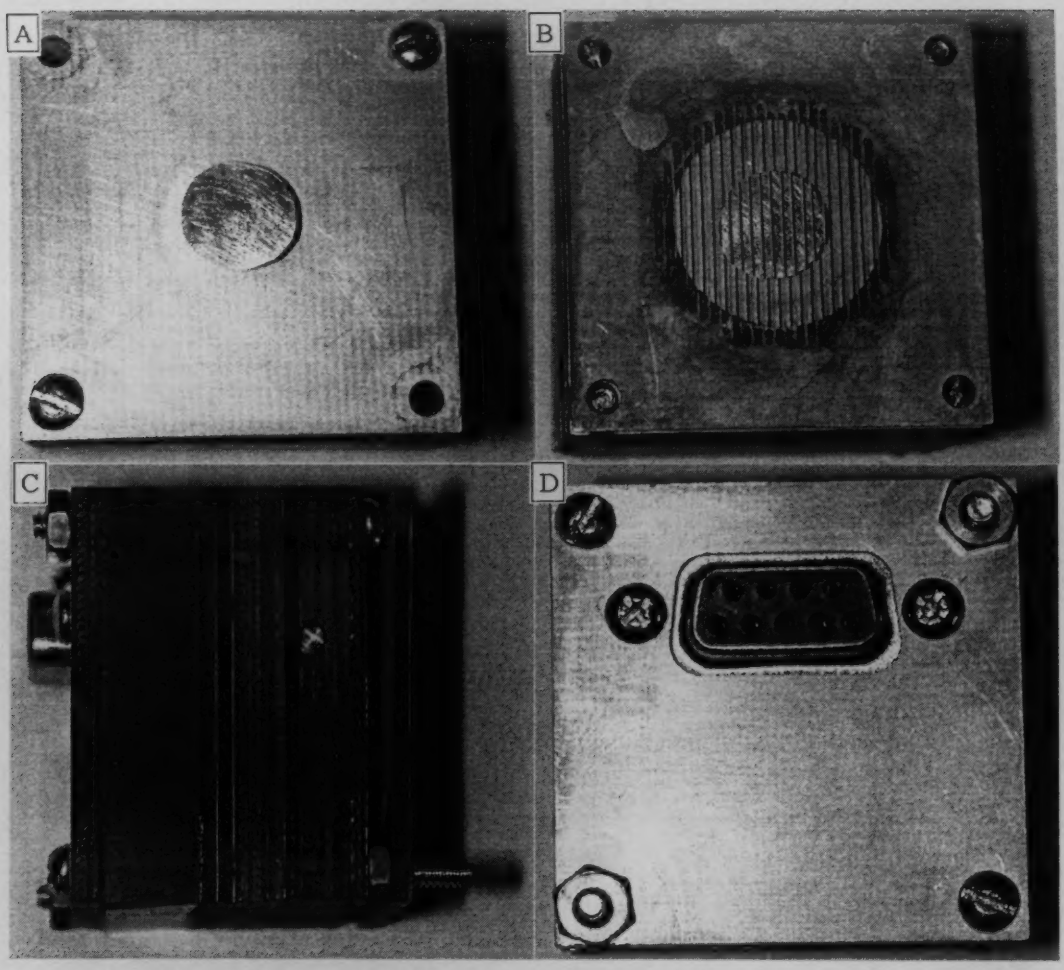

Figure 4-7. Photographs of the fully-assembled C-D Assembly III. Shown are (A) the front or top with and (B) without the aperture grid, (C) the side with the offset control, and (D) the back or bottom with the 9-pin port.

Noise (i.e., signal limit of detection or sLOD) values (each of which are averaged over 10 consecutive spectra) that were obtained by the various picoammeters Pico's I – IV are compared and listed in Table 4-1, where it can be observed that the active noise filtering of the latter two detectors (Pico III and Pico IV) reduces the sLOD by one or two orders of magnitude compared to Pico II. This lower sLOD would allow for much lower values for LOD (see *Chapter 3*). For example, the mean sLOD obtained by Pico IVa for the case of "HV," and "Ave512" is 0.063 pA, compared with a mean sLOD of 2.41 pA (for the same conditions) obtained by Pico II. From *Chapter 3*, the LOD for cytochrome c was estimated to be ~100 ppm. Assuming similar peak amplitudes for cytochrome c,

we would expect the LOD of Pico IVa to be ~3 ppm for an average of 512 scans. By averaging over a larger number of scans (e.g., over a few thousand spectra), we can lower the sLOD value, thus lowering the LOD of Pico IVa, perhaps even below the parts per million range. [Note that the sLOD for Pico IVb is approximately the same or worse than that for Pico II. This may be due to some leakage in the circuitry or a malfunctioning integrated circuit (IC) component.]

Table 4-1. **Comparison of the Noise Pickup of the Various Detector Circuits**

			Signal LOD (sLOD = 3 σ), pA			
			no HV		HV	
Pico Name	Alias/Marking	Gain, x 10^9 V/A	no Ave	Ave512	no Ave	Ave512
Pico I	-	3.3	435.53	16.27	352.64	18.09
Pico II	-	1.01	14.31	1.53	16.39	2.41
Pico III	1G	10	2.09	0.212	5.77	0.367
Pico IVa	10G	110	0.35	0.023	0.91	0.063
Pico IVb	1G	10	25.33	1.506	41.45	2.161
Pico IVc	3G	30.6	10.92	0.359	10.92	0.513

[a] Pico I is the prototype picoammeter (used in Column I), Pico II is the test model (used in Column II), Pico III is the transition model (used to evaluate the redesign of Pico II), and Pico IV is the new model (a compact version of Pico III, used in Column III). The three versions of Pico IV only differ in their 1st stage gain resistances, although Pico IVb may contain components that may be malfunctioning.
[b] Here, "no HV" refers to operation with high voltages turned OFF, while "HV" refers to the high voltages being turned ON. No liquid sample/solvent was introduced in either case.
[c] Here, "no Ave" refers to the "sample" mode of the oscilloscope, while "Ave512" refers to the "average" mode over 512 scans.
[d] Here, all the sLOD values were obtained by taking the mean of values from 10 consecutive spectra.

4.2. Microfluidic Electrospray Chip Applications

As mentioned previously, the ultimate goal for a portable IMS is to interface with a microfluidic chip type ES device, such as one described in *Chapter 2*, *Section 2.2* or the PDMS ES chip described in *Chapter 1*, *Section 1.2* that was developed by Chiou *et al.*[3] In our lab, microfluidic PDMS electrophoresis (EP) chips have been coupled with external peristaltic pump devices to control on-chip liquid flow. One possible future approach is to incorporate such a design in an ES chip. Figure 4-8 shows an example, where a "finger" extending from a servo-motor-controlled axial shaft would press down on the looped channel of a PDMS ES chip, thus providing the peristaltic action to control

the liquid flow (by temporarily closing portions of the channel of the relatively soft PDMS chip).

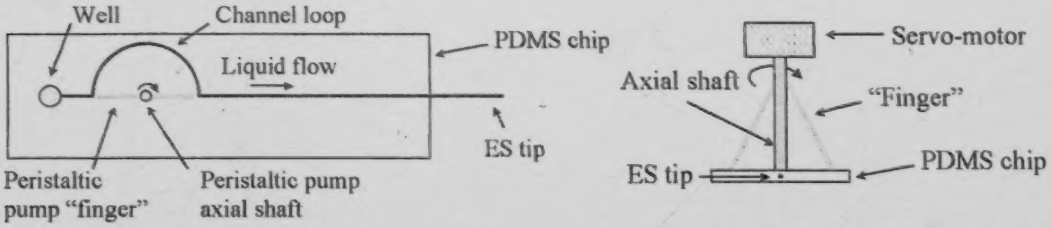

Figure 4-8. Schematic diagrams of the peristaltic pump-driven PDMS ES chip. (a, left) a top view showing the hemispherical loop and the "finger" position and sweep range; (b, right) a side view looking toward the ES tip showing the servo-motor-controlled peristaltic pump (including axial shaft and "finger").

4.3. Ion Thruster Applications

Because it is able to provide a stream of ions, an ESI-type source would represent an alternative to the propulsion systems currently used for spacecraft (i.e., chemical propulsion). Such a system would be classified as an Electrostatic Propulsion System, which falls under the field of Electric Propulsion (that also includes Electrothermal and Electromagnetic propulsion systems). The most well-known Electrostatic Propulsion System is the Xenon-Ion Propulsion System implemented as the main engine for NASA's Deep Space 1 (DS1) spacecraft that was launched in 1998.[4] This propulsion system was based on electron bombardment systems developed by Harold R. Kaufman and co-workers.[5-10]

Due to the extremely small thrusts that such systems are capable of – that is, on the order of micro-Newtons – Electric Propulsion is not suitable for propelling a craft beyond the gravitational sphere of a planet. The appeal for these systems, however, comes from the fact that deep space operations over the course of months or years allows for incredible velocities to be achieved, velocities far beyond what combustion or other conventional systems are capable of. Furthermore, the amount of fuel required for achieving these phenomenal speeds over its operation period is insignificant compared with what a convention system would burn up within a short period of time.

4.3.1. Theoretical Analysis and Estimates of Thrust

One of the difficulties in analyzing the data from a measurement of the current inherent in an ion spray issuing from a solid needle ion source [SNIS; basically, a sharp-tipped needle shown in *Chapter 2*, Fig. 2-13(a) that is operated without a liquid] is the conversion from the current that is measured and the effective velocity of the ions themselves, which translates to thrust. The following outlines one such approach.

To begin, one would have to start with the force relation for a charge in an electric field, shown in Eqn. (4.1). The energy required to move this charged particle a distance *d* is given by Equation (4.2). If one equates this relation to the kinetic energy relation, one obtains the equality shown in Equation (4.3). Since the current (i.e., the number of charges or ions impinging on the detector surface per second) was the quantity that was measured, we would replace the charge *q* with $I_{ion}\ t$ to arrive at Equation (4.4)

$$F = m_{ion}\ a_{ion} = q\ E_f \tag{4.1}$$

$$E = F\ d = m_{ion}\ a_{ion}\ d = q\ E_f\ d \tag{4.2}$$

$$\tfrac{1}{2}\ m_{ion}\ v_{ion}^2 = q\ E_f\ d \tag{4.3}$$

$$\tfrac{1}{2}\ m_{ion}\ v_{ion}^2 = I_{ion}\ t\ E_f\ d \tag{4.4}$$

where F = the force required to accelarate a charge in an electric field [N];
m_{ion} = the mass of the ion [kg];
a_{ion} = the acceleration of the ion [m s^{-2}];
q = the charge of the ion [C];
E_f = the electric field [V m^{-1}];
E = the energy required to move a charge a distance *d* [J];
d = the distance that a charge is moved [m];
v_{ion} = the velocity of the ion [m s^{-1}];
I_{ion} = the ion current that one would measure [A];
t = the period of interest [s];

Rearranging Eqn. (4.4), then putting back Eqn. (4.1) into the resultant relation, then rearranging once more, one obtains the following relation for the velocity of the ion (v_{ion}) with respect to the ion current (I_{ion}).

$$v_{ion} = \frac{2\ I_{ion}\ d}{q} \tag{4.5}$$

Equation (4.5) relies on a distance, which we can take to be the distance from the needle tip to the grid, which is ~ 1 cm (a value we can set and change). As for charge q, we can assume either a +1 or a +2 ion assuming that Fe^{+} or Fe^{2+} ions are being emitted. If it is the needle which is emitting the ions (in this case, Fe^{2+} from the stainless steel hypodermic needle, with perhaps impurity metals, etc.), instead of the air being ionized, we can take the velocity of the Fe^{2+} ions so that (taking a current of ~ 1.25 nA, for a 3 kV voltage difference)

$$v_{ion} = \frac{2\left(1.25 \times 10^{-9}\ \text{A}\right)\left(0.01\,\text{m}\right)}{2\left(1.6 \times 10^{-19}\ \text{C}\right)} \tag{4.6}$$

$$v_{ion} = 78.13 \times 10^{6}\ \tfrac{\text{m}}{\text{s}} \tag{4.7}$$

Note, that this ion velocity corresponds to the velocity of the ions at or just after the grid to which they are accelerated by the electric field between the needle and the grid (which is only valid between these two points). This translates to an ion momentum of

$$p_{ion} = m_{ion}\, v_{ion} \tag{4.8}$$

$$p_{ion} = \left(52 \cdot 1.67 \times 10^{-27}\ \text{kg}\right)\left(78.125 \times 10^{6}\ \tfrac{\text{m}}{\text{s}}\right) \tag{4.9}$$

$$p_{ion} = 6.78 \times 10^{-18}\ \text{kg}\,\tfrac{\text{m}}{\text{s}} \tag{4.10}$$

This means that each Fe^{2+} ion would impart a momentum transfer of 6.78×10^{-18} kg m s^{-1} to a spacecraft assuming similar conditions to produce similar currents. So, over the course of time t, we get the following number of ions

$$N_{Fe^{2+}} = \frac{I_{ion}\, t}{q_{Fe^{2+}}} \tag{4.11}$$

$$N_{Fe^{2+}} = \frac{\left(1.25 \times 10^{-9}\ \text{A}\right)t}{2\left(1.6 \times 10^{-19}\ \text{C}\right)} \tag{4.12}$$

$$N_{Fe^{2+}} = \left(3.91 \times 10^{9}\right)t \quad \text{[ions]} \tag{4.13}$$

The total momentum then for time t of spray is then given by the following.

$$p_{total} = \sum_{i}^{N} m_i\, v_{ion} \tag{4.14}$$

$$p_{total} = N_{Fe^{2+}}\, m_{ion}\, v_{ion} \tag{4.15}$$

$$p_{total} = \left(3.91 \times 10^{9}\right)t\left(6.78 \times 10^{-18}\ \text{kg}\,\tfrac{\text{m}}{\text{s}}\right) \tag{4.16}$$

$$p_{total} = 2.65 \times 10^{-8}\ t \quad \left[kg\,\frac{m}{s}\right] \tag{4.17}$$

The expected thrust would then be the time derivative of p_{total}, which is 26.5 nN. The thrust *T*, as shown in Section (1.5.2) and modified for this case, is expressed as

$$T = R_m\, v_{ion} = -\left(-\dot{m}\right) v_{ion} = \dot{p}_{total} \tag{4.18}$$

where T = the thrust that the ion source is capable of producing [N];
R_m = the negative of the rate of change of the mass of the propellant [kg s^{-1}];
$\dot{m}$ = the rate of change of the mass of the propellant [kg s^{-1}];
$\dot{p}_{total}$ = the rate of change of the total momentum [kg m s^{-2}];

Looking at Equation (4.18), one can arrive at the estimated value of thrust that this particular SNI source is capable by simply taking the time derivative of Equation (4.17), which results in a value of 26.5 nN of thrust. In order for one to achieve micro-Newtons of thrust with this SNI source, one would essentially have to use an array of (say) 100 or more such sources. (*Section 4.3.3* contains some design ideas regarding multiple sources for future consideration and evaluation.)

Viewed in practical terms, a craft with a total mass of 1 kg (for example), the velocity (v_{craft}) that is imparted to it by the spray of Fe^{2+} ions over time *t* is obtained via the following method.

$$p_{total} = p_{craft} \tag{4.19}$$

$$N_{Fe^{2+}}\, m_{Fe^{2+}}\, v_{Fe^{2+}} = m_{craft}\, v_{craft} \tag{4.20}$$

$$v_{craft} = \frac{N_{Fe^{2+}}\, m_{Fe^{2+}}\, v_{Fe^{2+}}}{m_{craft}} = \frac{p_{total}}{m_{craft}} \tag{4.21}$$

$$v_{craft} = \frac{\left(2.65 \times 10^{-8}\ kg\,\frac{m}{s}\right)t}{(1\ kg)} \tag{4.22}$$

$$v_{craft} = \left(2.65 \times 10^{-8}\right)t \quad \left[\frac{m}{s}\right] \tag{4.23}$$

Therefore, from Equation (4.23), the longer we leave the spray on, the more ions will be pushing the craft along (and since we have assumed no impedance in the craft's forward motion, i.e., we are essentially matching to free space conditions), therefore, velocity increases with time, as is the current understanding with ion thruster propelled spacecraft. In fact, this particular inherent quality of the ion thruster is what makes it so attractive for long duration and long distance interstellar travel. Figure 4-9 below

illustrates the velocity of craft over time for varying craft mass, whereby an array of 1000 SNI sources as described above is assumed. Here, a craft of mass 1 kg at the end of 10 years of thrusting will ideally achieve a velocity of 8320 m s^{-1}.

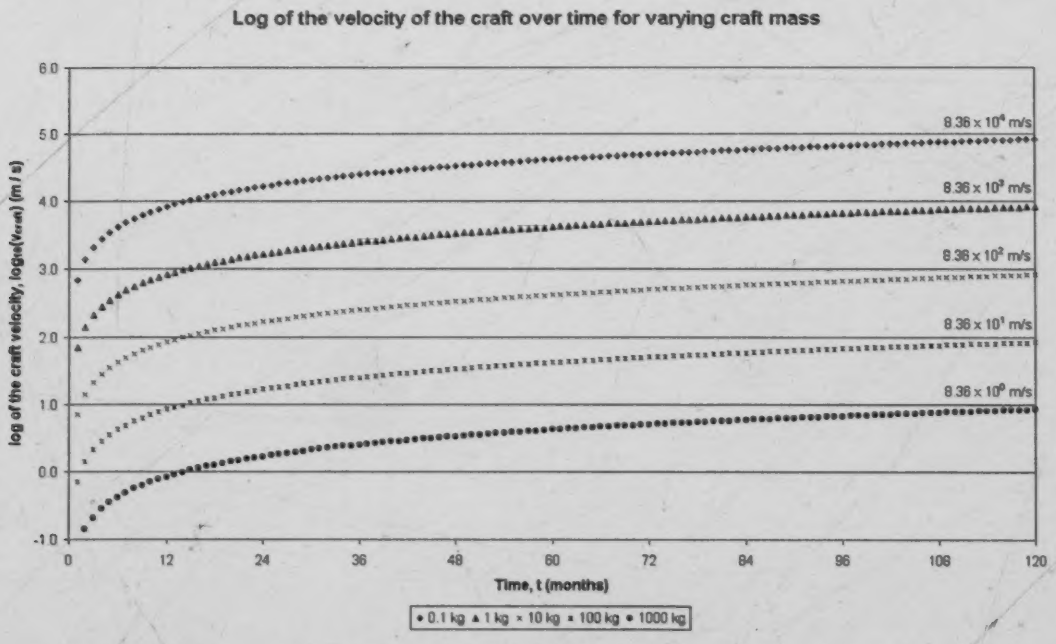

Figure 4-9. Plot of the velocity of a craft of varying mass over time. Here, an array of 1000 SNI sources is assumed.

4.3.2. Low Vacuum Design and Testing of an Ion Thruster – Propelled Craft

Thrust Measurement Set-up

The design for the measurement of thrust calls for the use of a torsion pendulum, which would involve suspending the thruster, the control module, and a mirror on a 25 μm diameter tungsten fiber (perhaps gold-coated). The ion thruster – basically, a sharp-tipped needle [shown in *Chapter 2*, Fig. 2-13(a) to henceforth be referred to as the SNIS; that would be operated without a liquid] and grid assembly – would be suspended on one half of a dumbbell (the other half of which will act as the counterbalance). The control module is a coke-can-sized/shaped box/tube containing the two EMCO positive high

voltage supplies, the PIC16F877 controlled microboard (probably trimmed down to size), and the necessary number of batteries.

The system could be operated in two modes: (1) the Deflection (Static) mode and (2) the Oscillating (Dynamic) mode. The former calls for the measurement of angular displacement following the activation of the thruster from rest position in order to calculate thrust. The latter calls for an extension of the former, whereby the thruster is left on for a time then shut down, such that the subsequent periods of oscillation and their respective deflections from rest can be used to calculate thrust. The following equation [11] illustrates this second method:

$$\Gamma_w = lR = \kappa\xi \qquad (4.24)$$

where Γ_w = the torque applied to the fiber [N m];
l = the lever arm length [m];
R = the thrust, or equivalently the force required to deflect the pendulum an angle ξ from rest position [N];
κ = the torsional constant of the fiber [N m rad^{-1}];
ξ = the angle of deflection from rest position [rad];

Because this design of the torsion pendulum involves complicated geometry (due to the inclusion of an ion thruster on one end of a dumbbell), one must determine the torsion constant using a dumbbell and a cylinder of equal masses, and their respective periods of oscillation.[11] The use of both calibration devices serves to eliminate changes in the torsion constant of the fiber.[11] As described by Cook *et al.*,[11] the determination of this constant can be accomplished by first mounting the regular dumbbell to the central axis of the torsion pendulum and measuring the period of oscillation with this arrangement, then doing the same with the cylinder in its place. This calls for an attachment to be set at the central axis of the pendulum for these modular calibration devices to be easily interchangeable. Once these values have been measured, and the torsion constant for the particular fiber used has been calculated, this process need not be repeated unless one is concerned about the long-term effects to the torsion constant due to inelastic stress endured by the fiber. The following equation [11] enables one to calculate the torsion constant using both these calibration devices (the dumbbell and the cylinder):

$$\kappa = 4\pi^2 \frac{I_d - I_C}{\Pi_d^2 - \Pi_c^2} \qquad (4.25)$$

where I_d = the moment of inertial of a dumbbell [kg m^2];
I_c = the moment of inertial of a cylinder [kg m^2];
Π_d = the period of oscillation of the dumbbell [s];
Π_c = the period of oscillation of the cylinder [s];

The more familiar equation for the period of oscillation of a torsion balance is given by the following:

$$\Pi = 2\pi\sqrt{\frac{I}{\kappa}} \tag{4.26}$$

where Π = the period of oscillation of the torsion balance [s];
I = the moment of inertia of the balance [kg m^2];
K = the torsion constant [N m rad^{-1}].

The torsion constant (K) cannot be easily determined from this equation because the moment of inertia (I) of the complicated geometry of the thruster/counterbalance or beam stop/counterbalance assembly is difficult to calculate. However, the moments of inertia for a dumbbell and a cylinder, individually, can be determined using formulae from various texts.

What are left then are the measurements of thrust applied by the expulsion of ions from the thruster. This can be determined by operating the system in the oscillating mode and applying Eqn. (4.24) to calculate the thrust using a series of deflections from rest position. The value obtained by Cook *et al.*[11] for the torsion constant of their 25 μm diameter, gold-coated tungsten wire was 6.04×10^{-8} N m rad^{-1}. Taking this value in our estimate of thrust per degree radian, one obtains for a 3.5 cm lever arm length (l):

$$R/\xi = \frac{\kappa}{l} = \frac{6.04 \times 10^{-8}\ \text{N m rad}^{-1}}{0.035\ \text{m}} = 1.73 \times 10^{-6}\ \text{N rad}^{-1} \tag{4.27}$$

This means that if one sets the detection screen (say a wall with rule-marks on it) at a distance of several meters, one could easily and quite accurately obtain deflection measurements of <1° (or 0.01745 rad).[11] This method of deflection measurement could also be sensitive enough for the Deflection (Static) Mode of operation for the torsion pendulum. For an electric field of 3×10^5 V m^{-1} (or 3 kV potential difference over 1 cm), one would obtain a thrust of 26.5 nN, as estimated in *Section 4.2.1.1* above, for ion currents of ~1.25 nA for an Fe^{2+} ion stream generated from a solid needle ion source.

Using the value obtained from Eqn. (4.27), this value of thrust would result in an angular deflection of 0.015 rads (or 0.86°).

The schematic diagram below represents the pendulum setup.

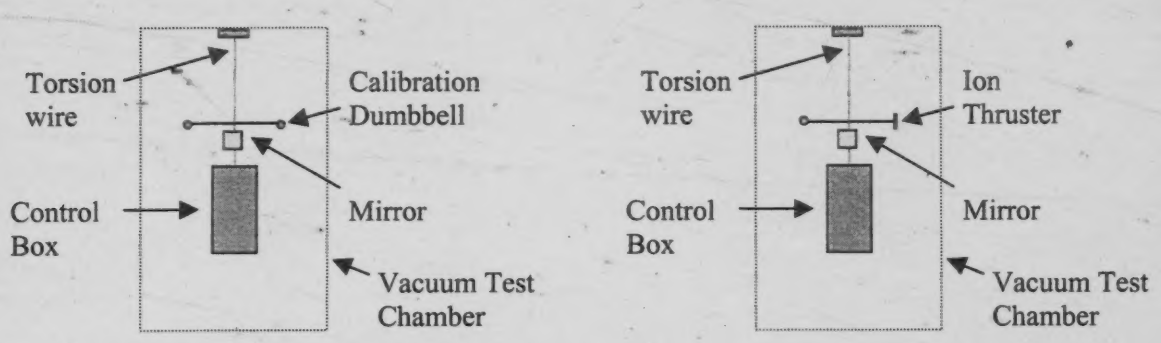

Figure 4-10. Schematic diagrams of the torsion pendulum vacuum setup. (left) the calibration setup to determine the torsion constant of the fiber and (right) the thrust measurement setup.

4.3.2.1. Design of IT Pendulum I

The Pendulum support structure (a schematic of which is shown in Fig. 4-10) is based around a 15.5 cm o.d., 14.2 cm i.d., 30.7 cm long (from exterior base to top of dome) glass bell jar, which consists of a 0.7 cm thick, rim (at the base) that extends 1 cm from the exterior side of the jar. In other words, a (metallic) cover plate that is perhaps 20 cm in diameter, and at least 1 or 2 cm thick would serve as the pendulum suspension structure, with 4 metallic legs that extend from the four corners of this disk-shaped cover plate to rest on the bell jar support plate, which itself would consist of a wooden board approximately 20 x 20 cm square and several centimeters thick that has two other boards mounted normally in a cross-shaped manner (looking down) with the curvature of the dome of the bell jar cut out of the two vertical boards; that is, the bell jar support would consist of 3 wooden boards: 1 square base plate and 2 vertical plates with the cross-sectional shape of the bell-jar cut out of each of them. The cover plate, also serving as the suspension apparatus, would have a threaded hole set just slightly off-center (and perhaps raised slightly from the top surface) such that a hairline groove cut down one

side of the threaded hole would be centered on the cover plate. The suspension wire, a very thin (a 25 – 75 μm diameter) tungsten wire (preferably gold-coated) would fit in this groove, a washer and bolt would then screw into this hole to firmly secure the suspension wire and thus support the weight of the entire torsion pendulum.

The suspension fiber will suspend three distinct components: (1) the torsion balance assembly (either the calibration dumbbells or the IT assembly), (2) the mirror and mount, and (3) the Control Tube (to be described in detail in the next section). The torsion balance bar, a 5 cm long x 3 mm diameter rod with threaded screws on each end, would be used for both the calibration and the IT assembly. The middle 1 cm of the rod would be flattened with 2 holes set a small distance apart from the mid-point, at which point is set a third hole, and one slit cut outward/orthogonally from the middle hole to the edge of one side of this flattened region. To hold this balance bar in place on the pendulum, two small inner diameter, large outer diameter ferrules with rubber-tipped set screws would be used, where the one would be placed below and the other above the balance bar. The bottom would have a male connection, while the top the female connection, such that the balance bar would slot in place and be secured by the sandwiching pair. Cylindrical weights (3) with threaded holes would screw onto the ends of the balance bar; each of these weights would be set to equal the mass of the IT assembly.

The IT assembly would consist of two L-shaped struts: (1) a plastic one for supporting the HV needle and banana plug connector and (2) a metal one for supporting the mesh grid that will be positioned ~1 cm away from the tip of the needle. One end of each of these struts would be bonded or welded to a washer (either plastic or metal) that will fit around the protruding threaded screws of the balance bar and secured using a stand-off (made of either plastic or metal). When it is set up, the "L's" would lie in a horizontal plane extending from the axis of the balance bar. The other end of the metal L-strut would be welded to a mesh grid, which will be connected to ground due to its contact with the grounded metal suspension wire via the metal balance bar and metal L-strut. The other end of the plastic L-strut, on the other hand, would serve to secure the banana plug connector of a high voltage wire, which would snake along the axis of the balance bar and then along the axis of the suspension wire, through the top cover of the

control tube to plug into the EMCO power supply flying output. If necessary, a similar wire could be snaked to the other end of the balance bar for symmetry or for ease of calculation of the moment of inertia. The 27-gauge SS hypodermic needle would simply fit over the banana plug to complete the IT assembly.

To measure the deflection of the torsion balance, a laser pointer (class III) would be positioned outside the (vacuum) chamber (window) with the beam incident on a mirror that is also suspended on the wire. A wall or other (flat or arc-shaped) surface would be placed at least a meter away from the mirror, perhaps with ruled markings set on the surface to measure displacement of the beam spot on the wall. The angular displacement of the torsion balance, as well as the period of oscillation, would be inferred from this beam spot displacement. To improve sensitivity of the measurement, a HeNe laser (which is often used as a laser system alignment instrument) could be borrowed and used in place of the laser pointer. As for the mirror, a small silicon wafer (cut to size) would be mounted on a ferrule (say) that would be secured to the suspension wire via a set screw (rubber tipped).

All in all, the control tube would suspend 10 cm from the bottom surface of the cover plate, the balance bar would be centered 5 cm from above the top of the tube, and the mirror would be mounted halfway between the tube and the balance bar.

4.3.2.2. Design of the Control Tube for IT Pendulum I

The Control Tube – based on the use of NiMH (nickel metal hydride rechargeable) AA batteries – would consist of a 3 cm radius metal cylinder with threaded caps ("top cap" and "bottom cap"), the total length of which would measure 10-15 cm. The bottom half of the Tube would house the ten 1.2 Vdc NiMH AA batteries, while the top half would house the control circuitry and the EMCO C60 6 kV HV power supply(ies). The battery array would actually be mounted right onto the bottom cap, with two trapezoidal risers to hold the batteries in place on top of the spring contacts. Grooves would be cut into the interior wall of the cylinder such as to press a piece of vector board with the complementary spring contacts against the top surface of the battery array. The

arrangement of the array, for achieving a series connection of the ten batteries for acquiring the 12 Vdc supply, is shown in the diagrams below. The leads from the two contact points would be made in the form of a dangle wire connection to its mate that is connected to the vector board and Microboard.

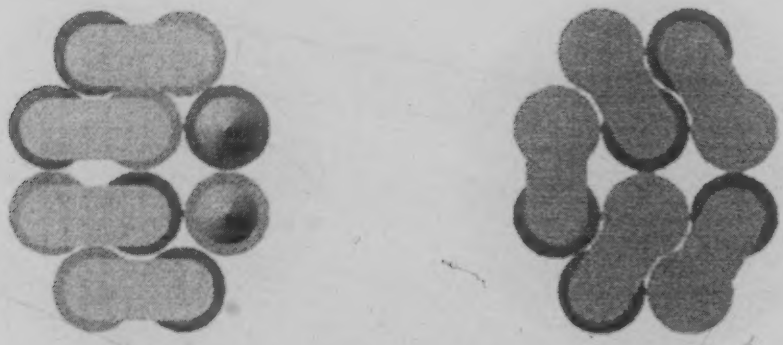

Figure 4-11. Schematic diagrams of the battery array within the control tube of the torsion pendulum setup. (left) top view of the battery array and (right) bottom view of the battery array. Note: the lighter and darker cylinders represent the positively and negatively aligned batteries, the darker elongated ovals represent the bottom contacts, the lighter elongated ovals represent the top contacts, and the lighter cones represent the positive and negative terminals of this 12 Vdc power supply.

The top half of the cylinder would have two sets of grooves – one to fit the EMCO C60 6 kV power supply mounted vector board and the other to fit the microboard PIC controller. Another set of wires would be used to connect the EMCO output (HV wires in this case) and the infrared receiver leads with the top cap.

The top cap would comprise a reversed version of the bolt/groove arrangement used on the top plate to suspend the suspension wire; that is, the bolt would screw upwards, with the small hole seen from the outside. Two holes with attached HV wires would be set ~1 cm from the vertical plane created by aligning the screen hole and the groove. The IR receiver would be placed ~ 1.5 cm equidistant from these two HV wire holes and opposite the bolt aperture. This IR receiver would be set just below the silicon wafer mirror (see Fig. 4-10), so that only one window for the chamber would be necessary (a) to communicate with the control tube and (b) to allow for laser-aided angular displacement measurements. An RCA SystemLink 3 Universal Remote control

(RCU300WG) will be used to communicate with the microboard via the IR receiver. The simplest settings would call for an ON and an OFF state for the Ion Thruster on the torsion pendulum, where ON calls for a 6 kV voltage difference across the 1 cm spacing between the needle tip and the grid and OFF calls for a shut down of all the voltages. Figure 4-12 below depicts the (top view) cut-away schematic of the control tube, showing the lower half (with the batteries), the upper half (with the electronics), and the top cap (with the interface).

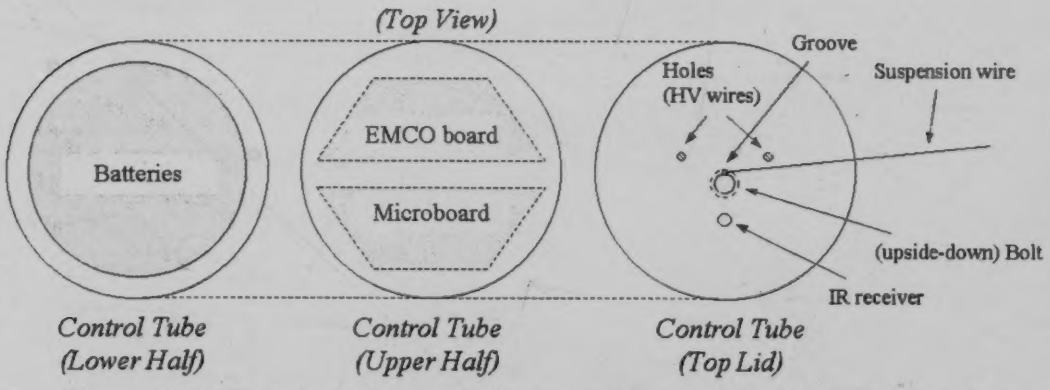

Figure 4-12. (Top view) Schematic diagram of the control tube. Shown are the lower half for the batteries (left), the upper half for the electronics (middle), and the top cap for the interface with the rest of the torsion pendulum (right).

Future options for the control unit may include an accelerometer that would average over 100 readings (say) and save to the memory (perhaps expanded) of the PIC module.

4.3.2.3. Experimental Setup for Testing IT Craft III: "Vac I"

Assuming chamber dimensions of 30 cm diameter x 40 cm height with an access port that is >20 cm, the entire hanging assembly described above for the bell jar setup (i.e., the torsion pendulum suspended from the ~20 cm diameter, four-legged cover plate) would fit through the access aperture with the 30.7 cm long rubber-tipped legs resting on the bottom of the chamber. This means that at least one window must be centered 20-25 cm above the resting place for the legs in order for the mirror and the IR receiver to be in

line of sight. If necessary – that is, if an available chamber with these specifications is not found – the entire hanging assembly can be slightly modified in terms of height and width, while still keeping the torsion pendulum design the same.

4.3.3. Ion Thruster Arrays

For the thrust calculations given above (in *Section 4.3.1*) the desired thrust (i.e., micro-Newtons) via the use of the SNIS can only be achieved by using an array of parallel SNIS's. One such configuration, called a Spindt-type field emitter array (FEA) is described in the literature.[12-14] Named after Charles Spindt of the MicroSystems Engineering Center of SRI International (Menlo Park, CA), the FEA cathode (when operated in the negative mode, emitting electrons in the process) is a microfabricated array that consists of tens of thousands to millions of metal tips separated by a layer of insulating material (essentially a honey-comb structure with the openings for the tips and the walls as the dielectric, except it need not be hexagonal in configuration), with a metal grid layer (whose openings coincide with the tip positions) deposited on top of the insulator (base). Figure 4-13 shows a schematic of this structure. Aguero notes that a single FEA cathode containing millions of tips per square centimeter would be capable of over ~ 5 kA cm^{-2}.[12]

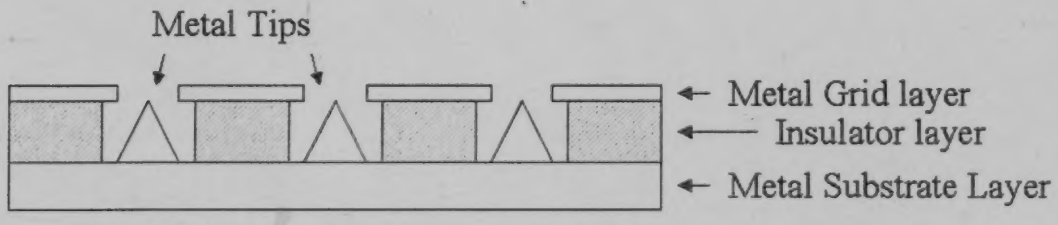

Figure 4-13. Schematic diagram of the Spindt field emitter array (FEA).

For our applications, we would perhaps operate in the positive mode, perhaps with a liquid metal flowing over the tips, so that erosion over time (due to the emission of positive ions, from the metal tips themselves) would not occur. However, the use of a liquid metal would involve designing a liquid interface and associated equipment (i.e.,

liquid reservoir, transfer lines, and pumps). Alternatively, instead of a liquid metal, a liquid solvent (e.g., a methanol/water mixture, as used in the ESIS described in previous chapters) could be used instead (for a system with this liquid interface).

4.4. References

(1) Wang, C.;Oleschuk, R.;Ouchen, F.;Li, J. J.;Thibault, P.; and Harrison, D. J., "Integration of immobilized trypsin bead beds for protein digestion within a microfluidic chip incorporating capillary electrophoresis separations and an electrospray mass spectrometry interface," *Rapid Communications in Mass Spectrometry*, **14** (2000), pp. 1377-1383.

(2) Chen, Y. H.;Hill, H. H.; and Wittmer, D. P., "Thermal effects on electrospray ionization ion mobility spectrometry," *International Journal of Mass Spectrometry and Ion Processes*, **154** (1996), pp. 1-13.

(3) Chiou, C. H.;Lee, G. B.;Hsu, H. T.;Chen, P. W.; and Liao, P. C., "Micro devices integrated with microchannels and electrospray nozzles using PDMS casting techniques," *Sensors and Actuators B-Chemical*, **86** (2002), pp. 280-286.

(4) "Deep Space 1," Jet Propulsion Laboratory, the California Institute of Technology, and the National Aeronautics and Space Administration, 2002, website: http://nmp.jpl.nasa.gov/ds1/. Accessed: (2002) August 14.

(5) Kaufman, H. R., "Origin of the electron-bombardment ion thruster," *Journal of Spacecraft and Rockets*, **18** (1981), pp. 289-292.

(6) Kaufman, H. R.;Harper, J. M. E.; and Cuomo, J. J., "Developments in broad-beam, ion-source technology and applications," *Journal of Vacuum Science and Technology*, **21** (1982), pp. 764-767.

(7) Kaufman, H. R.; and Robinson, R. S., "Plasma processes in inert-gas thrusters," *Journal of Spacecraft and Rockets*, **18** (1981), pp. 470-476.

(8) Kaufman, H. R.; and Robinson, R. S., "Electric thruster performance for orbit raising and maneuvering," *Journal of Spacecraft and Rockets*, **21** (1984), pp. 180-186.

(9) Kaufman, H. R.; and Robinson, R. S., "Minimum hole size in ion optics," *Journal of Spacecraft and Rockets*, **22** (1985), pp. 381-382.

(10) Kaufman, H. R.;Robinson, R. S.; and Trock, D. C., "Inert gas thruster technology," *Journal of Spacecraft and Rockets*, **20** (1983), pp. 77-83.

(11) Cook, S. R.;Hoffbauer, M. A.;Cross, J. B.;Wellenstein, H.; and Fink, M., "Specialized torsion balance designed to measure the absolute flux density of hyperthermal molecular beams containing reactive species," *Review of Scientific Instruments*, **67** (1996), pp. 1781-1789.

(12) Aguero, V. M., "Cubesats: A technology and science mission low-cost test bed," presented at the AIAA/USU Conference on Small Satellites, AIAA (Utah State University (Logan, UT, USA)), 2001

(13) Makishima, H.;Miyano, S.;Imura, H.;Matsuoka, J.;Takemura, H.; and Okamoto, A., "Design and performance of traveling-wave tubes using field emitter array cathodes," *Applied Surface Science*, **146** (1999), pp. 230-233.

(14) Ogiwara, N.;Suganuma, K.;Miyo, Y.;Kobayashi, S.; and Saito, Y., "Application of the field emitter array to the vacuum measurements," *Applied Surface Science*, **146** (1999), pp. 234-238.

Appendices

Page

Table of Contents

A1.0. Chapter Appendices 167
A2.0. Chapter 2 Appendices 167
A2.0.1. IMS Column I Design Considerations 167
A2.0.1.1. IMS Column I Capacitance Considerations 167
A2.0.1.2. Circuit Analysis of the Keithley High Speed Picoammeter 170
A3.0. Chapter 3 Appendices 174
A3.0.1. More Images of the ES-IMS System 174
A3.0.2. Details of the Control Box 176
A3.0.2.1. Schematic (Block) Diagrams of Control Box Components 176
A3.0.2.2. Description of Control Box Components 178
A3.0.2.2. C-Program for ES – IMS Controller (or Control Box) 182
A3.0.3. More on the Ripple/Ringing Phenomenon 193
A3.0.4. Comparison Between the Averaged and Un-averaged Control Signals 198
A3.0.5. More on the Unstable, Polydisperse Spray Modes (SM-1 and SM-3) 199
A4.0. References 200

A1.0. Chapter Appendices

The following sections contain the appendices to *Chapters 2* and *3*. The notations and conventions used here are described in *Notations* in the prefatory pages.

A2.0. Chapter 2 Appendices

A2.0.1. IMS Column I Design Considerations

A2.0.1.1. IMS Column I Capacitance Considerations

The capacitance of the IMS column was considered, as it may adversely affect the operation of the system. To begin, the capacitance between two guard rings (i.e., from the start of one PCB surface to the interface between the metal film layer and the dielectric FR-4 layer of the next PCB square) was calculated. The capacitance ($C_{FR\text{-}4}$) of the guard/drift rings that are separated by the FR-4 layer can be calculated using the following relation (that assumes a parallel plate configuration):

$$C_{FR\text{-}4} = \varepsilon_o \, \kappa_{FR\text{-}4} \, A_{PCB} \, / \, d_{FR\text{-}4} \qquad \text{(A2.1a)}$$

$$C_{FR\text{-}4} = 3.51693 \times 10^{-11} \text{ F} = 35 \text{ pF} \qquad \text{(A2.1b)}$$

where $\kappa_{FR\text{-}4}$ and $d_{FR\text{-}4}$ are the dielectric constant (~ 4.75) and the thickness (~ 1.54 mm) of the insulating FR-4 layer of the PCB squares, respectively. A_{PCB} is the surface area (~ 1.29×10^{-3} m^2) of the copper film layer of the (4 x 4 cm, 2 cm diameter aperture) PCB squares, and ε_o the permittivity of free space (8.85×10^{-12} C V^{-1} m^{-1}).

Since the 65 PCB squares are in series (and assuming that there is negligible capacitance due to the presence of the "wires" on the "grids" and the shutter gate, please refer to Fig. A2-1 below), the overall capacitance of the column would be

$$C_{Column} = \frac{C_{FR\text{-}4}}{N_{PCB}} = \frac{35 \text{ pF}}{65} \qquad \text{(A2.1c)}$$

$$C_{Column} = 0.541 \text{ pF} = 541 \text{ fF} \qquad \text{(A2.1d)}$$

This is an extremely small value. Assuming that we have a 100 MΩ resistance (which is far larger than the 65 MΩ noted above for the column resistance) for example, the resultant transient RC delay would be 20.3 μs, which is faster than the 500 μs pulse width of the shutter (hence smaller than the millisecond time scales of interest), so it can generally be ignored.

For the two grids and the shutter gate, whose (rectangular) wires are designed to be 0.1 mm wide and separated by ~1mm, the capacitance was once again calculated assuming we have parallel plate capacitors of equal total surface areas as the grid surfaces.

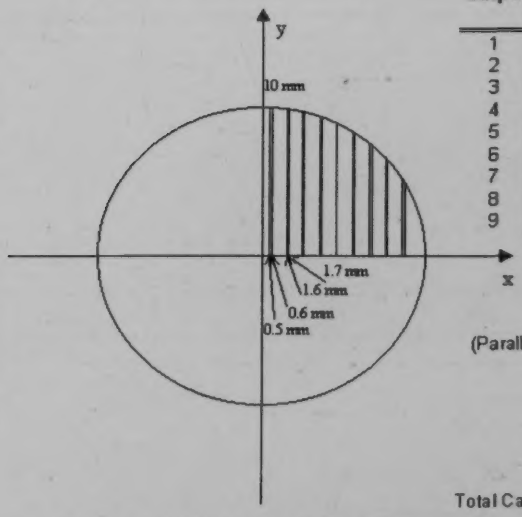

Strip #	x [mm]	y [mm]	Area (// grids) [mm²]	Surface Area [mm²]	Capacitance [F]
1	0.500	9.987	0.355	0.999	3.145E-15
2	1.600	9.871	0.351	0.987	3.108E-15
3	2.700	9.629	0.342	0.963	3.032E-15
4	3.800	9.250	0.329	0.925	2.912E-15
5	4.900	8.717	0.310	0.872	2.745E-15
6	6.000	8.000	0.284	0.800	2.519E-15
7	7.100	7.042	0.250	0.704	2.217E-15
8	8.200	5.724	0.204	0.572	1.802E-15
9	9.300	3.676	0.131	0.368	1.157E-15

Quadrant Total Surface Area =	7.190	mm²
Quadrant Total Surface Area =	7.190E-06	m²
Grid Total Surface Area =	**2.876E-05**	**m²**
(Parallel Plate) Capacitance Estimate =	**1.656E-13**	**F**
"Ring" Thickness =	0.03566	mm
"Ring" Spacing =	0.001000	m
"insulator" Thickness =	0.001538	m
Permittivity of Free Space =	8.85E-12	C / V m
Total Capacitance (between grid wires) =	**2.437E-16**	**F**

Figure A2-1. Calculation of the estimated capacitance of the column grids. (left) a schematic diagram of a grid, with focus on one quadrant; (right) a table of the calculation for the capacitance (1) between the wires of the grid on the left and (2) assuming a parallel plate configuration with another grid of equal surface area parallel with the shutter gate.

The above calculation assumes that the "wires" of the grids are all layered exactly in the manner shown in the diagram, which is most likely not the case (i.e. the "wires" may be shifted by a small amount along the x direction). The parallel plate estimate is 0.166 pF (assuming a grid of equal surface area and arrangement is in parallel to and spaced ~1.54 mm from the shutter gate); this is less than the capacitance from Eqn. (A2.1d), so it too can be ignored. As for the capacitance between the "wires" of the "grids" (or shutter gate),

$$C_{wires} \approx \varepsilon_o A_{wires}/d_{wires} = (8.85 \times 10^{-12})(20\,\text{mm})(35.56\,\mu\text{m}) / (1\,\text{mm}) \qquad \text{(A2.1e)}$$

$$C_{wires} \approx 6.297 \times 10^{-15}\ \text{F} = 6.3\ \text{fF} \qquad \text{(A2.1f)}$$

The capacitance between the "wires" can also be ignored; this calculation assumes that all the wires are of equal length (or 20 mm long), which is an over-estimation. Taking into account the fact that the length of the parallel wires decreases as one moves along the (positive/negative) x-direction away from the y-axis, the capacitance is closer to 0.244 fF (from Fig. A2-1) than the estimated 6.297 fF [from Eqn. (A2.1f)]. The capacitance between the "wires" can thus be ignored.

Because the capacitance near the ion collector may affect the detection of ions, that area must be more closely examined. With the aperture grid spaced ~1.54 mm away from the collector plate, and with the aperture grid having the same geometry as the grid configuration shown in Fig. A2-1 (at least as seen within the column inner diameter) and the collector plate having a diameter of 1.5 cm centered axially, the estimated calculation for the capacitance (assuming, say, an average of two parallel plate capacitors with areas equal to the grid surface area and the collector plate, respectively) was as follows.

Strip #	x [mm]	y [mm]	Surface Area [mm^2]
1	0.500	9.987	0.999
2	1.600	9.871	0.987
3	2.700	9.629	0.963
4	3.800	9.250	0.925
5	4.900	8.717	0.872
6	6.000	8.000	0.800
7	7.100	7.042	0.704
8	8.200	5.724	0.572
9	9.300	3.676	0.368

Quadrant Total Surface Area =	7.190	mm^2
Quadrant Total Surface Area =	7.190E-06	m^2
Grid Total Surface Area =	**2.876E-05**	m^2
Aperture Grid - Collector Separation =	0.001538	m
Collector Radius =	0.007500	m
Collector Area =	**1.767E-04**	m^2
Voltage (grid - collector) =	**49.180**	V
(Parallel Plate Est.) Capacitance (grid) =	**1.656E-13**	F
(Parallel Plate Est.) Capacitance (collector) =	**1.018E-12**	F
Average Estimated Capacitance =	**5.916E-13**	F

Table A2-1. Calculation of the Estimated Capacitance of the Aperture Grid - Collector Plate. Shown is a table of the capacitance calculation (parallel plate estimate) for this region.

The average capacitance was found to be 0.592 pF; this value can also be ignored because it is approximately the same as the capacitance from Eqn. (A2.1d).

A2.0.1.2. Circuit Analysis of the Keithley High Speed Picoammeter

To analyze the Keithley High Speed Picoammeter circuit [shown in Fig. 2-21(left)], it is convenient to replace the parallel R_FC_F components with an equivalent impedance (Z_F), as shown in Fig. A2-2 below.

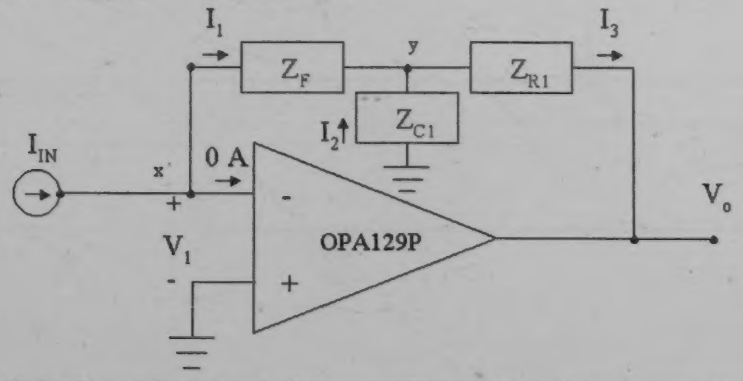

Figure A2-2. Simplified circuit diagram of the Keithley high speed picoammeter.

The complex impedances Z_F, Z_{C1}, and Z_{R1} can be expressed as follows, where "s" can be replaced with "jω" (to represent physical circuits).

$$Z_F(s) = \frac{R_F}{1 + s C_F R_F} \qquad \text{(A2.2a)}$$

$$Z_{C_1}(s) = \frac{1}{s C_1} \qquad \text{(A2.2b)}$$

$$Z_{R_1} = R_1 \qquad \text{(A2.2c)}$$

Assuming an ideal op-amp, the input voltage (V_x) and the current I_1 would, respectively be …

$$V_x = V_1 = 0\,V \qquad \text{(A2.3a)}$$

$$I_1 = I_{IN} \qquad \text{(A2.3b)}$$

The voltage at point "y" would be as follows.

$$V_y(s) = V_x - I_1 \cdot Z_F(s) = -I_{IN} \cdot \frac{R_F}{1 + s C_F R_F} \qquad \text{(A2.4)}$$

It follows that the currents I_2 and I_3 are …

$$I_2(s) = \frac{0 - V_y(s)}{Z_{C_1}(s)} = I_{IN} \cdot \frac{s C_1 R_F}{1 + s C_F R_F} \qquad \text{(A2.5)}$$

$$I_3(s) = I_1 + I_2(s) = I_{IN} \cdot \left(1 + \frac{s C_1 R_F}{1 + s C_F R_F} \right) \qquad \text{(A2.6)}$$

The (op-amp) output voltage (V_o) can then be expressed as …

$$V_o(s) = V_y(s) - I_3(s) \cdot Z_{R_1} \qquad \text{(A2.7a)}$$

$$V_o(s) = - I_{IN} \cdot \frac{R_F}{1 + s C_F R_F} - I_{IN} \cdot \left(R_1 + \frac{s C_1 R_1 R_F}{1 + s C_F R_F} \right) \qquad \text{(A2.7b)}$$

$$V_o(s) = - I_{IN} \cdot \left(\frac{R_F + R_1 + s C_F R_F R_1 + s C_1 R_1 R_F}{1 + s C_F R_F} \right) \qquad \text{(A2.7c)}$$

The terms within the round brackets can be grouped as follows.

$$V_o(s) = - I_{IN} \cdot \left(\frac{R_F \cdot (1 + s C_1 R_1) + R_1 \cdot (1 + s C_F R_F)}{1 + s C_F R_F} \right) \qquad \text{(A2.7d)}$$

If the time constants C_1R_1 and C_FR_F are equal, where $\tau = C_F R_F = C_1 R_1$, the result would simplify into a relation without any dependence on capacitance [Equation (A2.7f)], thus avoiding any RC delay (transients), therefore resulting in the very fast (op-amp) gain circuit (as suggested by Keithley).

$$V_o(s) = - I_{IN} \cdot \left(\frac{R_F \cdot (1 + s\tau) + R_1 \cdot (1 + s\tau)}{1 + s\tau} \right) \qquad \text{(A2.7e)}$$

$$V_o = - I_{IN} \cdot (R_F + R_1) \qquad \text{(A2.7f)}$$

Here, one can see that the resultant current-to-voltage gain does indeed resemble the response of the circuit shown in Fig. 2-21(right), where (1st stage) output voltage decreases linearly with increasing input (ion) current; the phase would be zero.

For the case of the circuit shown in Fig. 2-22, it is convenient to ignore the 2nd and 3rd stages, as these are simple inverting and non-inverting (op-amp) gain stages. What is left then is simply the circuit shown in Fig. A2-2, except with an additional input impedance (Z_{IN}). It can be noted that the current I_1 would still equal any input current (I_{IN}) regardless of the additional input impedance. However, any (rf) noise signal that is received by the (antenna-like) collector at the input of the picoammeter will influence the output of the circuit due to the additional input impedance. The simplified circuit is shown in Fig. A2-3 below.

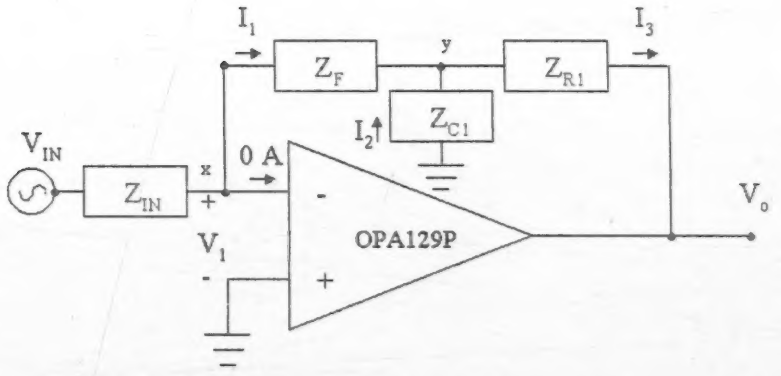

Figure A2-3. Simplified circuit diagram of the modified high speed picoammeter.

Assuming that the time constants $C_F R_F$ and $C_1 R_1$ are equal, the feedback loop of the op-amp will reduce to that shown in Fig. 2-21(right), where $Z_{EFF} = R_{EFF} = R_F + R_1$. In fact, the only difference here would be that the ion current (I_{IN}) would be replaced by the current (I_1) that results from the interaction between the input (noise) voltage (V_{IN}) and the additional input impedance (Z_{IN}).

$$I_1 = \frac{V_{IN}}{Z_{IN}} \tag{A2.8a}$$

$$\text{where } Z_{IN}(s) = \frac{R_{IN}}{1 + s\,C_{IN} R_{IN}} \tag{A2.8b}$$

Replacing I_{IN} in Eqn. (A2.7f) with I_1 in Eqn. (A2.8a) and expressing the resultant equation in terms of a gain, we obtain the following relation.

$$\frac{V_o(s)}{V_{IN}(s)} = -\frac{(R_F + R_1)}{R_{IN}} \cdot (1 + sC_{IN} R_{IN}) \tag{A2.9a}$$

Replacing "s" with "jω", the physical gain becomes the following.

$$\frac{V_o(j\omega)}{V_{IN}(j\omega)} = -\frac{(R_F + R_1)}{R_{IN}} \cdot (1 + j\omega\, C_{IN} R_{IN}) \tag{A2.9b}$$

The magnitude ($\left|\frac{V_o}{V_{IN}}\right|$) and phase ($\phi$) of Eqn. (A2.9b) can be expressed, respectively, as

$$\left|\frac{V_o}{V_{IN}}\right| = \frac{(R_F + R_1)}{R_{IN}} \cdot \sqrt{(1 + \omega^2 C_{IN}^2 R_{IN}^2)} \tag{A2.10}$$

$$\phi = \arctan(-\omega\, C_{IN} R_{IN}) \tag{A2.11}$$

Recalling the values of R_F, R_1, R_{IN}, and C_{IN}, Eqn.'s (A2.10) and (A2.11) reduce to their simplified forms, resulting in magnitude and phase plots shown in Fig. A2-4.

$$R_F = 100\,M\Omega;\ R_1 = 10\,M\Omega;\ R_{IN} = 100\,M\Omega;\ C_{IN} = 33\,pF$$

$$\tau_{IN} = C_{IN}R_{IN} = 0.0033\,s \qquad \text{(A2.12a)}$$

$$G = \frac{(R_F + R_1)}{R_{IN}} = 1.1 \qquad \text{(A2.12b)}$$

$$\left|\frac{V_o}{V_{IN}}\right| = (1.1)\cdot\sqrt{\left(1+\omega^2\,(0.01)^2\right)} \qquad \text{(A2.13)}$$

$$\phi = \arctan\left(-\omega\,(0.01)\right) \qquad \text{(A2.14)}$$

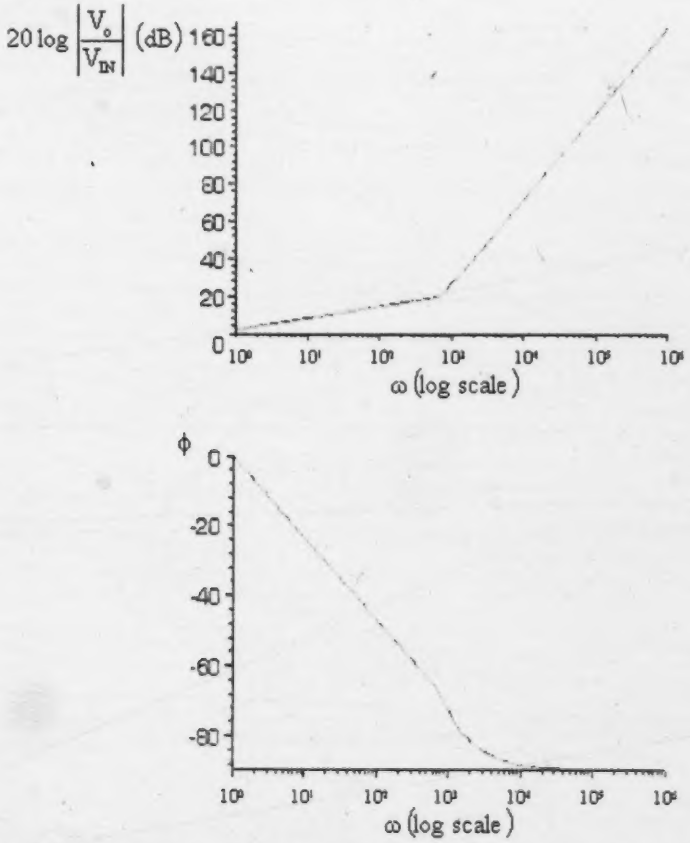

Figure A2-4. (Top) Magnitude and (bottom) phase response of the modified high speed picoammeter for the case of noise pick-up.

For the Magnitude, the response is ~7 dB/decade up to the critical point (i.e., ~660 rads s^{-1} or ~105 Hz), then it increases to ~45 dB/decade. For the Phase, the response is –24°/decade up to the critical point, then it levels off at –90°.

A3.0. Chapter 3 Appendices

A3.0.1. More Images of the ES-IMS System

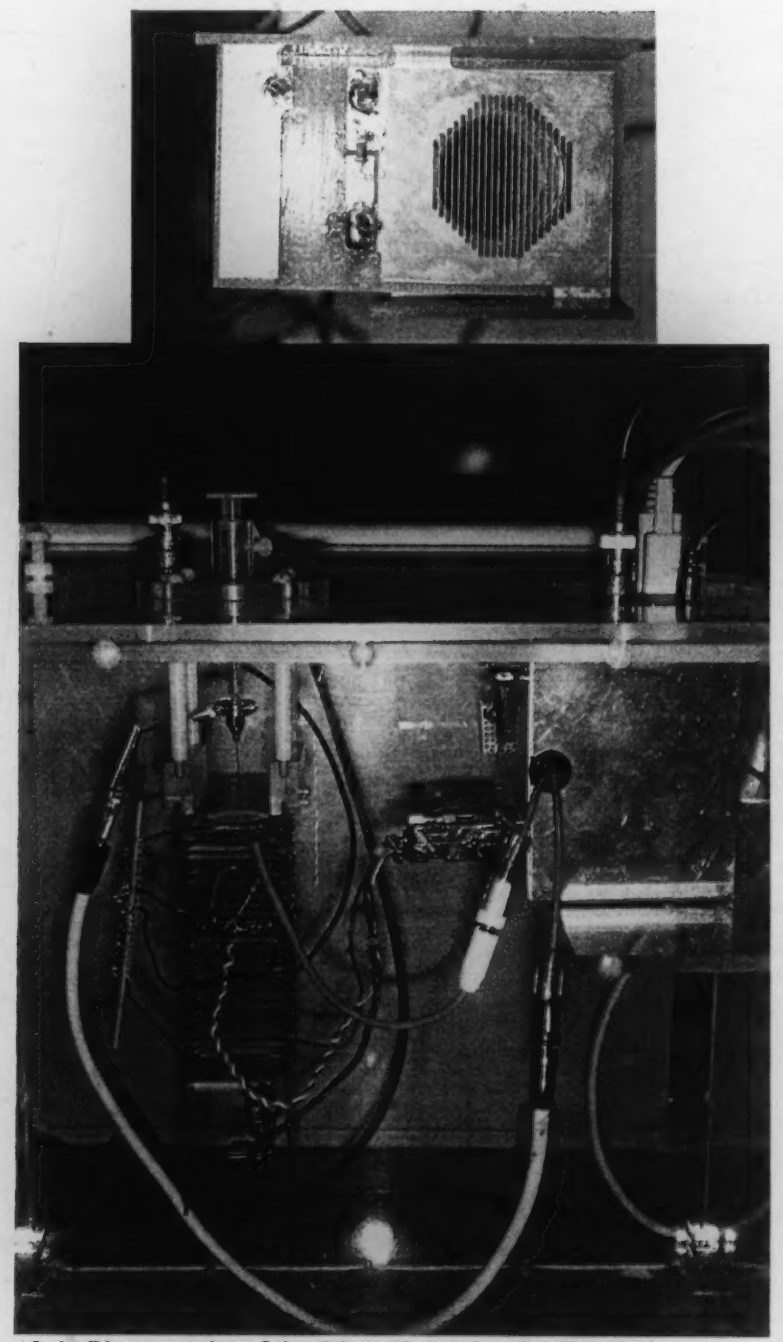

Figure A3-1. Photographs of the ES-IMS Device II. (ES-IMS system described in *Section 3.2.1.*)

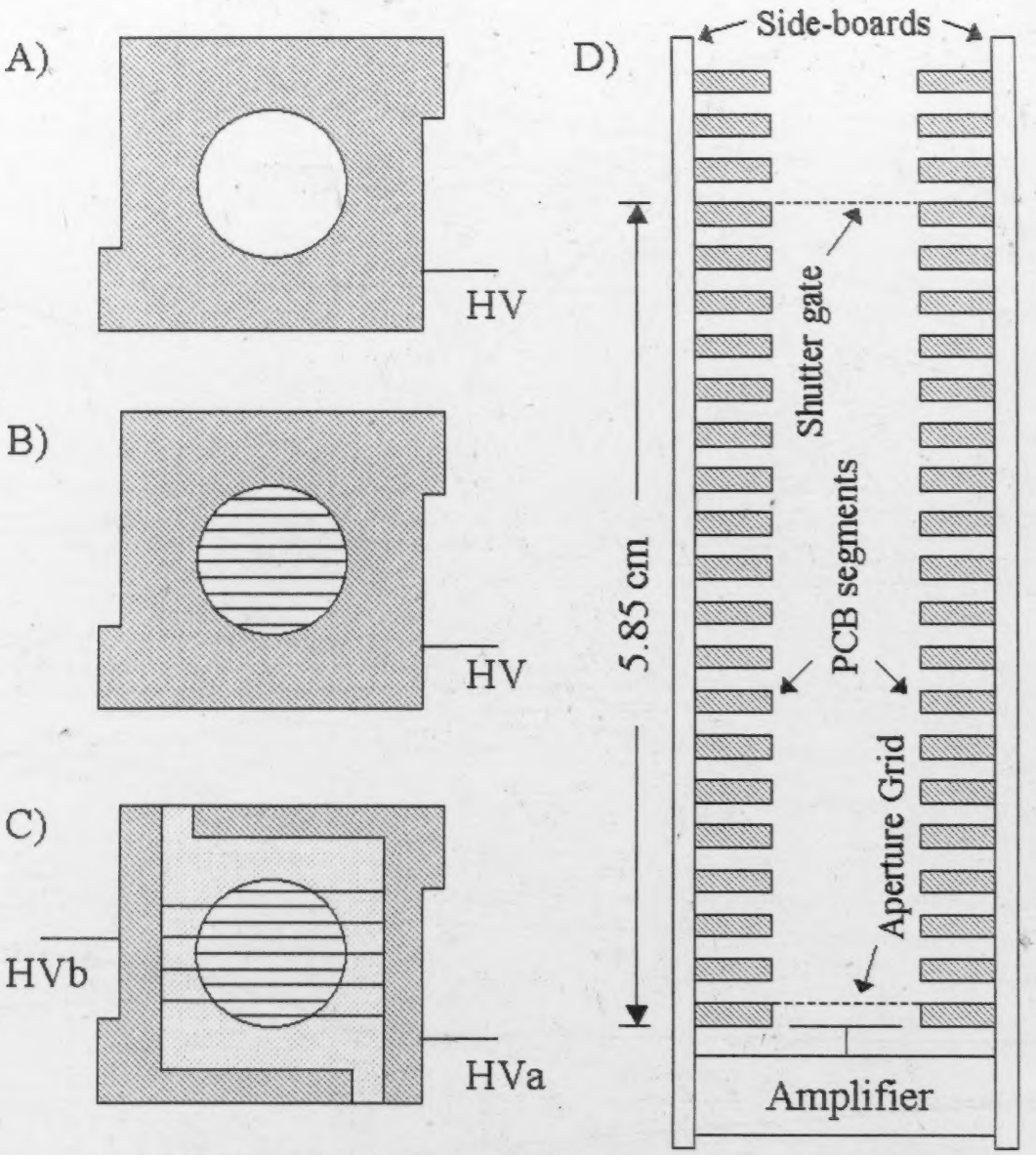

Figure A3-2. Schematic diagram showing the components for ES-IMS Device II: (A) a guard ring, (B) a grid, (C) the shutter gate, and (D) a cross-sectional view of the drift region of the IMS column. The dimensions are: sides = 4 cm, aperture diameter = 2 cm, tab [on either side of elements in (A)-(C)] = 1.1 (L) x 0.3 cm (W). The dot-dash line represents the shutter gate, while the dashed line represents the aperture grid; the horizontal line connected to the amplifier represents the Faraday (or collector) plate.

A3.0.2. Details of the Control Box

A3.0.2.1. Schematic (Block) Diagrams of Control Box Components

Microboard Component Connections

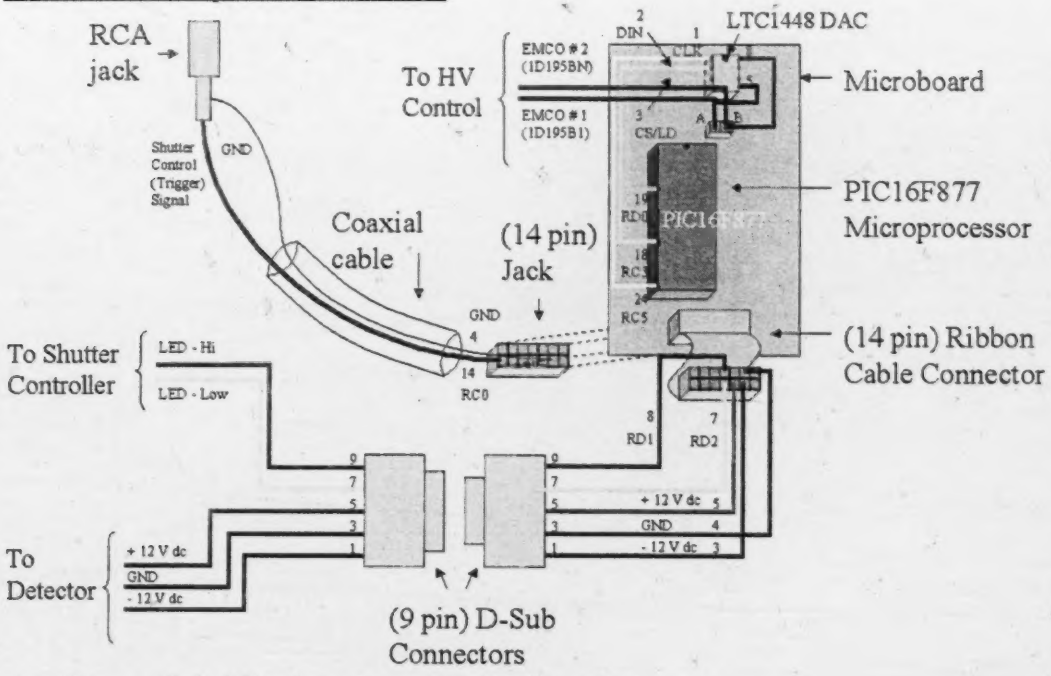

Figure A3-3. Microboard component schematic.

The RCA jack would interface with an oscilloscope to provide a visual trigger for when the shutter is set to the OPEN or ON state. The reader would obtain a better understanding of this schematic by glimpsing the photographs of this component (see the next section). The Detector Rails provided via the 9-pin D-Sub connector actually measure ±11.98 Vdc.

High Voltage (HV) Input/Output Connections

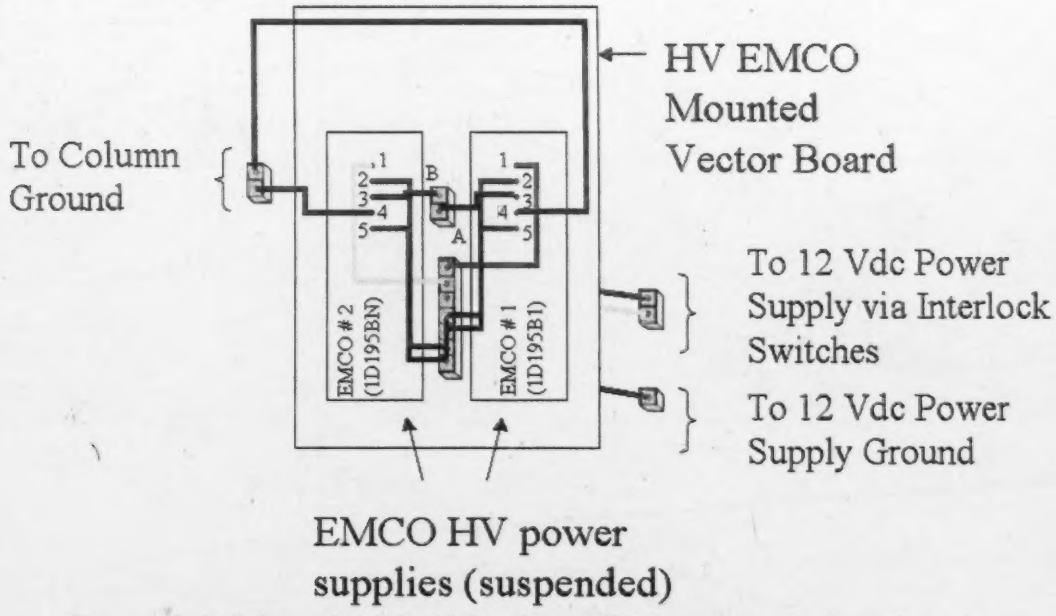

Figure A3-4. Schematic of the high voltage (HV) input/output connections.

The 3 connectors shown outside the Board indicate connections to be made with other components (e.g., pin connections with banana plugs or ribbon connectors, etc.). In the schematic, the view is looking down inside the disassembled Control Box at the upside-down HV EMCO Mounted Vector Board. The red and orange wires (to pins 1) indicate the connections for the HV inputs, the brown wires (to pins 1 and 5) for the HV input grounds, the black wires (to pins 4) the HV returns, and the blue (to pin 3, EMCO #2) and black (to pin 3, EMCO #1) wires the HV controls; the pin connections on the EMCO's and the DAC outputs are noted next to their corresponding wires.

A3.0.2.2. Description of Control Box Components

This section details the components found in the Control Box.

Microboard Controller

The PIC16F877-based Microboard was used (1) to provide the detector input power (±12 Vdc and GND), (2) to control the settings for the two EMCO C60 High Voltage (HV) Power Supplies (EMCO High Voltage Corporation, Sutter Creek, CA), (3) to provide interlock switches that would cut off the input power to the two EMCO Power Supplies, and (4) to provide a trigger to the oscilloscope (ch. 2) in the form of a parallel/duplicate line from the shutter (*LED-Hi*) line (i.e., to provide timing for the experimental runs; ch. 1 of the oscilloscope will be monitoring the detector output of the IMS Column II). An RS-232 cable was interfaced with a computer (using Hyper Terminal) via the 9-pin connector mounted on the Microboard. An AC adapter provided the Microboard with the requisite 12 Vdc power.

Internal Ribbon Wire

The Internal Ribbon Wire connection provided the detector input power (actually ±11.98 Vdc and GND) as well as the shutter control inputs (*LED-Hi* and *LED-Low*). The schematic above depicts the connection at the ribbon connector end (which mounts over the 14-pin setting situated near the bottom of the PIC, on the top of the Microboard). The other end of the ribbon will interface to a 9-pin D-sub connector (please refer to the schematic diagrams in section 2.1. for information about the D-sub pin connections).

(14 – Pin) Trigger Lead

The (14-Pin) Trigger Lead connection is intended to provide a visual trigger using the second channel of the oscilloscope (while the first channel is used to monitor the detector output); this allows for proper time of flight (TOF) measurements which would allow velocity and mobility information of the ions to be inferred. The schematic above

depicts the connection at the (14-Pin) Jack end (which mounts over the same 14-pin setting as the Ribbon Wire, but on the bottom of the Microboard). The other end of the Trigger Lead will interface with an RCA jack mounted on the side of the Control Box (please refer to the photographs in Fig. A3-5 for a visual depiction of this arrangement).

High Voltage (HV) Control

The High Voltage (HV) Control Leads (black and blue wires) are intended to connect to a 2-pin port on the vector board on which the two EMCO C60 6 kV HV Power Supplies are mounted. The two leads are connected from the bottom to the VoutA and VoutB ports of the DAC LTC1448 that is mounted on the Microboard. The other end is a double pin jack to which the two leads are soldered. This double pin jack would slot into place over a double pin-pin connection that was soldered onto the HV vector board and connected to the control pin (pin 3) of the two EMCO power supplies.

High Voltage (HV) EMCO Mounted Vector Board

The HV EMCO Mounted Vector Board consisted of two EMCO C60 Power Supplies mounted upside-down (with respect to the Microboard). A 7-pin jack was also mounted upside-down (with respect to the Microboard) and between the two EMCO's such that the metal pins are on the same side of the vector board as the pins of the EMCO's. Two of these pins were connected to each Input Pin (pin 1) of each EMCO power supply, while four of these pins were shorted together and connected to the Input Ground and Case Ground Pins (pins 2, 5) of each EMCO power supply. The (orange and red) wires that would interface will two Input pins via the 7-pin jack would connect to a (red) banana plug mounted on the side of the Control Box via an external ribbon wire leading to the outside of the box and two TM-Series Unimax Miniature Snap-Action Switch (C&K Components Inc., Clayton, NC) (one switch for one EMCO Input). These Snap-Action Switches (with the leads soldered to the NO, normally open-circuited, connection and common) would act as interlock switches, cutting off the Input power to

the EMCO's and essentially cutting out the HV power if their metal arms are not held down.

A double pin-pin connector was mounted near this 7-pin jack and also between the two EMCO's, and a connection was made with the Control Pin (pin 3) of each EMCO; the pins sticking upward (toward to bottom of the Microboard) would allow a double pin jack to slot into place. The remaining pin on each EMCO (pin 4) is the HV return pin to which was connected a high voltage wire each to one (green) banana plug mounted to the side of the Control Box (via a double pin jack soldered onto the banana plug and a double pin-pin connector soldered to the two wires). The HV fly leads (one from each EMCO) were threaded through a 5/16" (~8mm) inner diameter rubber grommet that would slot into place in a slit that was cut into the side of the cover of the Control Box.

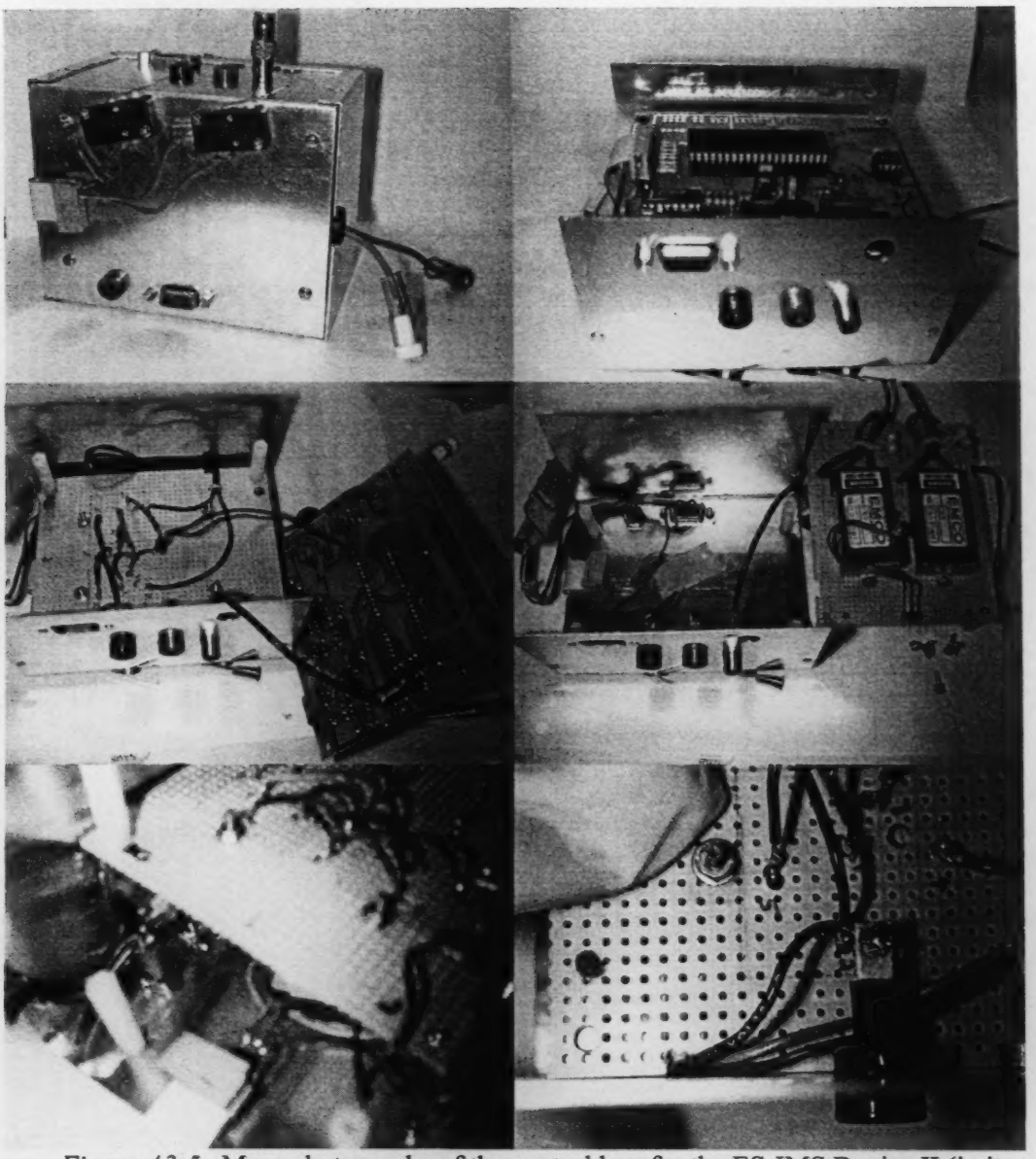

Figure A3-5. More photographs of the control box for the ES-IMS Device II (in its various stages of disassembly/reassembly). Views of the fully assembled control box (left, top) and with the minibox lid removed (right, top); views of the Microboard (left, middle) and the HV-mounted Vectobord® (right, middle) being placed to the side; views of the HV-mounted Vectorbord® (left, bottom) in relation to the HV input wires (right, bottom) within the control box.

A3.0.2.2. C-Program for ES – IMS Controller (or Control Box)

This section lists the PIC C program used to control the Control Box functions.

```
/*****************************************************************/
/*                                                               */
/* Project:      ESI-IMS controller                              */
/*                                                               */
/* Author:       Eric Cheong                                     */
/*                                                               */
/* Date:         February 12, 2003 (version "ES12_A7")           */
/*                                                               */
/* Description:  This program runs in one mode:  ES-IMS column mode. */
/*      It will run with two EMCO C60 power supplies and with the IMS*/
/*      column.  It will control the ion shutter gate, regulate the  */
/*      ES and column voltages, and provide a trigger pulse for each */
/*      run.  It will set the IMS Column (V_IMSc) and ES needle      */
/*      (V_ESn) to user-defined voltages between 1 kV (683) and 5 kV */
/*      (3413) and between V_IMSc and 6 kV (4095), respectively.  It */
/*      will ramp up V_IMSc by 200 V steps and V_ESn by 1000 V steps.*/
/*      A TIC Mode is also available.                            */
/*      This program also comes with a kill switch.              */
/*                                                               */
/*****************************************************************/

// An ES-IMS controller

// Routines:
//      ESI_IMS_Mode
//      get_values
//      summary
//      IMS_Energize
//      Run_cycle
//      pulse_ctrl
//      get_long        {written by Loi Hua in timztc1.c}
//      str_long        {written by Loi Hua as "get_string" in timztc1.c}
//      Set_HV
//      Set_DACs        {modified by Loi Hua in timztc1.c}

// PIC16F877 PIN Assignments
//   Pins     #       Wire                    Duties / Functions
//  ------ -----  --------     ---------------------------------------
//    C3     18     yellow       (DAC LTC1448) system clock (SCK)
//    C5     24     tan          (DAC LTC1448) SPI Data Out (SDO)
//    D0     19     white        (DAC LTC1448) Chip Select (CS)
//    A0      2     blue         (Detector) voltage measurement (ADC)
//    C4     23     orange       Indicator for HV#1 (LTC1448, pin5) ON
//    C3     22     blue         Indicator for HV#2 (LTC1448, pin8) ON
//    D1     21     yellow       (Shutter) LED-Low, Yellow Wire (Hi=OFF)
//    C0     15     coaxial      (Trigger) LED-Hi, copy

#include <16f877.h>
#device PIC16F877 ADC=10
#fuses HS, NOWDT, NOPROTECT, NOPUT, NOLVP, NOBROWNOUT
#use delay(clock=20000000)
```

```
#use rs232(baud=9600, xmit=PIN_C6, rcv=PIN_C7)

#include <stdlib.h>
#include <stdio.h>

#define INTS_PER_SECOND 15 // (4000000/(4*256*256))
byte seconds;              // A running seconds counter
byte int_count;            // Number of interrupts left before a second
                           // has elapsed

#int_rtcc                  // This function is called every time
clock_isr()                // the RTCC (timer0) overflows (255->0).
{                          // For this program this is apx 15 times
       if(--int_count==0) // per second.
       {
       ++seconds;
       int_count=INTS_PER_SECOND;
       }
}

//***********************************
//Declare Global Variables
long int        N_scans = 0;     // The desired number of scans per run
long int        V_IMSc = 0;      // The final desired IMS column voltage
long int        V_ESn = 0;       // The final desired ES needle voltage
long int        t_ON = 0;        // The desired Shutter Gate Pulse Width
long int        t_period = 0;    // The desired period

//Declare Functions
void ESI_IMS_Mode(void);
void get_values(void);
void summary(void);
void IMS_Energize(void);
void Run_cycle(void);
void pulse_ctrl(long int i);
long get_long(void);
void str_long(char * s, int max);
void Set_HV(long int lDac1, long int lDac2, long int dur_sec);
void Set_DACs(long int lDac1, long int lDac2);

/*************************************************************************/
/* Function:     void main(void)                                         */
/* Description:  This function runs with ESI-IMS circuit and PICmicro*/
/*      16F877board.  This program will prompt user for a mode (ESI- */
/*      IMS or Exit).  For the ESI-IMS mode, it will run a pre-      */
/*      defined program (i.e., ramping up the column to 3 kV by 200 V*/
/*      increments, ramping up the needle to a user-defined voltage  */
/*      between 5.8 kV (3413) and 6 kV (4095) by 1 kV increments,    */
/*      toggling the ion shutter gate ON or OFF for N cycles         */
/*      {N, t_ON, andt_period being input at a prompt}).  A kill     */
/*      switch (any key, except y or Y) will set all voltage control */
/*      pin outputs to 0V, and initialize the rest of the pins.      */
/* Parameters:   none                                                 */
/* Return:       none                                                 */
/*************************************************************************/
```

```
void main(void)
{       char            answer, ch_mode;

      // **OPTIONAL** //
        int_count=INTS_PER_SECOND;
        set_rtcc(0);
        setup_counters(RTCC_INTERNAL, RTCC_DIV_128);
        enable_interrupts(INT_RTCC);
        enable_interrupts(GLOBAL);

        // spi and ADC initialization
        setup_spi(spi_master | spi_h_to_l | spi_clk_div_64);
        setup_adc_ports(ALL_ANALOG);
        setup_adc(ADC_CLOCK_INTERNAL);
        set_adc_channel(0);

    do
    {
        // Clear all outputs (C4, C5, D0, D1, D2, and D3)
        output_low(PIN_D3);         // Indicator for HV#2 (LTC1448, pin8)
        output_low(PIN_C4);         // Indicator for HV#1 (LTC1448, pin5)
        Set_HV(0,0,1);              // Make sure HV supplies are off

        // Set shutter to OFF state
        output_high(PIN_D2);
        output_low(PIN_C0);
        output_low(PIN_D1);
        printf("\r\n\nWelcome to the ESI-IMS Control System!");

        // Display Mode Menu & Run Modes
        printf("\r\nPlease Choose an Option!");
        printf("\r\n\t1) Run ES - IMS Mode");
        printf("\r\n\tX) Exit Program\r\n");
        ch_mode = getch();

        switch(ch_mode)
        {
            case '1':
                printf("\r\nEntering ES - IMS Mode!\r\n");

                // Goto ESI-IMS Mode Function
                ESI_IMS_Mode();

                printf("\r\n\n\n\nEnd of ES - IMS run!\a\n");
                printf("\r\n\nDo you wish to run again?\n");
                printf("\r\n\nPress y or Y to continue");
                printf(" or any other keys to exit the program.\r\n");
                answer = getc();
                putc(answer);
                break;

            case 'x':
                answer = ' ';
                printf("\r\nExiting Program!");
                break;
```

```
            case 'X':
                answer = ' ';
                printf("\r\nExiting Program!");
                break;

            default:
                answer = 'y';
                printf("\r\nIncorrect Input!  Please try again!");
                break;
        }
    }while((answer == 'y') || (answer == 'Y'));
    // De-energize IMS column and ES needle
    Set_HV(0,0,1);                  // Make sure HV supplies are off

    printf("\r\nEND PROGRAM!  Have a nice day!\a\n");
}//end of main()

/*************************************************************************/
/* Function:     Void ESI_IMS_Mode(void)                                 */
/* Description:  Control Function for the ESI-IMS Mode, including        */
/*      prompts, displays, function calls, etc.                          */
/* Parameters:   none                                                    */
/* Return:       none                                                    */
/*************************************************************************/

void ESI_IMS_Mode(void)
{
        // Prompt for the various times
        get_values();

        // Display summary of input values
        summary();

        // Energize IMS Column & ES Needle
        IMS_Energize();

        // Execute Run(s)
        Run_cycle();

        // De-energize IMS column and ES needle
        Set_HV(0,0,1);
}

/*************************************************************************/
/* Function:     void get_values(void)                                   */
/* Description:  Additional Function for the ES-IMS Mode.                */
/*      Prompts for and displays the various time & voltage values.      */
/* Parameters:   none                                                    */
/* Return:       none                                                    */
/*************************************************************************/

void get_values(void)
{   int             v_check=1;

        // Prompt for & Display # Scans per run
        printf("\r\n\nPlease enter the desired number of");
```

```
printf(" scans per run!");
printf("\r\n Default value = 1 scan per run!\r\n");
printf("\r\n   Note: a value over 255 will set N_scans");
printf(" = infinity!\r\n");
N_scans = get_long();

While(v_check == 1)
{
    // Prompt for & Display Period
    printf("\r\n\nPlease enter the desired period [us]!");
    printf("\r\n   It must be > 1 ms and <= 65500 us!!");
    printf("\r\n   Typical value is 50000 us!!\r\n");
    t_period = get_long();
    printf("\r\n  t_period = %lu us\r\n", t_period);
    if ((t_period < 1)||(t_period > 65500))
    {
        printf("\r\n\nPlease re-enter the desired");
        printf(" period [us]!\r\n\n");
        v_check = 1;
    }
    else
        break;
}

While(v_check == 1)
{
    // Prompt for & Display t_ON
    printf("\r\n\nPlease enter the desired SG Pulse Width");
    printf(" (or ON Time) [us]!");
    printf("\r\n   It must be <= t_period");
    printf(" (i.e., %lu us)!!", t_period);
    printf("\r\n   Typical value is 100 us)!\r\n");
    t_ON = get_long();
    printf("\r\n  t_ON = %lu us\r\n", t_ON);
    if ((t_ON > t_period))
    {
        printf("\r\n\nPlease re-enter the desired pulse");
        printf(" width [us]!\r\n\n");
        v_check = 1;
    }
    else
        break;
}

while(v_check == 1)
{
    // Prompt for Column Voltage
    printf("\r\n\nPlease enter the desired final voltage");
    printf(" for the IMS Column!");
    printf("\r\n   It must be >= 683 (i.e., 1 kV) &");
    printf(" <= 3413 (i.e., 5 kV)!!");
    printf("\r\n   Typical value is 2081 (i.e., 3049 V)!\r\n");
    V_IMSc = get_long();
    printf("\r\n  V_IMSc = %lu\r\n", V_IMSc);
    if ((V_IMSc > 3413)||(V_IMSc < 683))
    {
```

```
                printf("\r\n\nPlease re-enter the IMS Column");
                printf(" Voltage!\r\n\n");
                v_check = 1;
            }
            else
                break;
        }

        while(v_check == 1)
        {
            // Prompt for Needle Voltage
            printf("\r\n\nPlease enter the desired final voltage");
            printf(" for the ES needle!");
            printf("\r\n\  It must be > V_IMSc (i.e., %lu) &", V_IMSc);
            printf(" <= 4095 (i.e., 6 kV)!!\r\n");
            V_ESn = get_long();
            printf("\r\n  V_ESn = %lu\r\n", V_ESn);
            if ((V_ESn > 4095)||(V_ESn <= V_IMSc))
            {
                printf("\r\n\nPlease re-enter the ES Needle");
                printf(" Voltage!\r\n\n");
                v_check = 1;
            }
            else
                break;
        }
}

/*************************************************************************/
/* Function:     void summary(void)                                      */
/* Description:  Display Summary of Input Values.                        */
/* Parameters:   none                                                    */
/* Return:       none                                                    */
/*************************************************************************/

void summary(void)
{       // Display Summary of Input Values
        printf("\r\n\nSummary of Input Values:  ");
        printf("\r\n     N_scans = %lu cycles", N_scans);
        printf("\r\n    t_period = %lu us", t_period);
        printf("\r\n        t_ON = %lu us", t_ON);
        printf("\r\n      V_IMSc = %lu ", V_IMSc);
        printf("\r\n       V_ESn = %lu ", V_ESn);
}

/*************************************************************************/
/* Function:     void IMS_Energize(void)                                 */
/* Description:  Slowly ramps up the IMS column voltage by 200 V,        */
/*       then slowly ramps up the ES needle voltage by 1 kV.             */
/* Parameters:   none                                                    */
/* Return:       none                                                    */
/*************************************************************************/

void IMS_Energize(void)
{       int             i;
        long int        ColVolt, ESNVolt;
```

```
        // Ramp up IMS Column voltage
        delay_ms(1000);         // Delay 1 second
        printf("\r\n\nWarning!!  IMS Column Voltage is being");
        printf(" ramped up!!\r\n\n");

        ColVolt = 0;
        for(i=0;i<25;i++)       //Ramp up Column Voltage by 200 V steps
        {
            ColVolt = (long) ColVolt + 136.5;
            //printf("\r\nColVolt = %lu ", ColVolt);
            if (ColVolt > V_IMSc)
                break;
            Set_HV(0,ColVolt,1);
        }
        Set_HV(0, V_IMSc,1);  // Set Column to user-defined final value

        printf("\r\nIMS Column IS Now Energized");

        // Ramp up ES needle voltage
        ESNVolt = 0;
        for(i=0;i<6;i++)        // Ramp up Needle Voltage by 1000 V steps
        {
            ESNVolt = (long) ESNVolt + 682.5;
            //printf("\r\nESNVolt = %lu ", ESNVolt);
            if (ESNVolt > V_ESn)
                break;
            Set_HV(ESNVolt,V_IMSc,1);
        }
        // Set & leave Needle @ desired voltage
        Set_HV(V_ESn,V_IMSc,30000);
        printf("\r\nES Needle IS Now Energized");
}

/*************************************************************************/
/* Function:     void Run_cycle(int N_scans)                             */
/* Description:  Runs the desired number scans per run, where 1          */
/*      run = 1 ON / OFF state of the shutter.                           */
/* Parameters:   none                                                    */
/* Return:       none                                                    */
/*************************************************************************/

void Run_cycle(void)
{       int             j;
        long int        i;
        char            TIC_mode;

        printf("\r\n\nDo you wish to enter the Total Ion Current");
        printf(" (TIC) Mode?");
        printf("\r\n   Type 'y' or 'Y' for yes, Default is 'N'");
        printf(" or 'n'");
        TIC_mode = getch();
        printf("\r\n   TIC_mode = %c\r\n", TIC_mode);
        if ((TIC_mode == 'y')||(TIC_mode == 'Y'))
        {
            for(j=0;j<N_scans;j++)
```

```
            {
                output_low(PIN_D2);

                // Turn ON OK1
                output_high(PIN_C0);
                output_high(PIN_D1);

                if(kbhit())
                    break;
            }
        }
        else
        {
            // Run the desired number of scans per run
            for(j=0;j<N_scans;j++)
            {   i = 0;
                while(i<=t_period)
                {
                    pulse_ctrl(i);

                    delay_us(11);
                    i = i+20;   // increment counter by stepsize of 20
                }
                // Kill Switch
                if(kbhit())
                    break;
            }
        }
        Set_HV(0,0,1);          // De-energize IMS column and ES needle
}

/*************************************************************************/
/* Function:     void pulse_ctrl(long int i)                             */
/* Description:  Compares running time with desired t_ON, then           */
/*      sets the shutter to the corresponding ON/OFF state.              */
/* Parameters:   long i = running time                                   */
/* Return:       none.                                                   */
/*************************************************************************/

void pulse_ctrl(long int i)
{
        if (i<t_ON)
        {
            output_low(PIN_D2);

            // Turn ON OK1
            output_high(PIN_C0);
            output_high(PIN_D1);
        }
        else
        {
            output_low(PIN_C0);
            output_low(PIN_D1);

            // Turn ON OK2
            output_high(PIN_D2);
```

```
            delay_us(2);
        }
}



/*************************************************************************/
/* Function:     long get_long(void)                                     */
/* Description:  Function written by Loi Hua that gets a number         */
/*      from the keyboard as a string then converts to a long int.      */
/* Parameters:   none                                                    */
/* Return:       l = a long integer                                      */
/*************************************************************************/

long get_long(void)
{
        char            s[7];
        long            int l;

        str_long(s, 7);
        l=atol(s);
        return(l);
}

/*************************************************************************/
/* Function:     void str_long(char *s, int max)                         */
/* Description:  Function written by Loi Hua that converts a             */
/*      string to a number.                                              */
/* Parameters:   char *s = a string pointer                              */
/*               int max = max string length                             */
/* Return:       none                                                    */
/*************************************************************************/

void str_long(char * s,int max)
{
        int             len;
        char            c;

        max--;
        len=0;
        do
        {
            c=getc();
            if(c==8)
            {// Backspace
                if(len>0)
                {
                    len--;
                    putc(c);
                    putc(' ');
                    putc(c);
                }
            }
            else if ((c>=' ')&&(c<='~'))
                if(len<max)
```

```
                {
                    s[len++]=c;
                    putc(c);
                }
        } while(c!=13);
        s[len]=0;
}

/*************************************************************************/
/* Function:     void Set_HV(long int lDac1, long int lDac2,             */
/*      long int dur_sec)                                                */
/* Description:  Gets a desired high voltage output value [V] and        */
/*      converts to the required voltage input value.  Then this         */
/*      voltage will be converted to a longinteger to update the DAC     */
/*      (LTC1448) to setup a new high voltage for adesired duration,     */
/*      then will shut down the HV supplies. If the durationexceeds      */
/*      30000s, the high voltages will be left ON until programmed       */
/*      otherwise.                                                       */
/* Parameters:   long int lDac1 = holds the first 12-bit number to       */
/*      send to the LTC1448                                              */
/*               long int lDac2 = holds the last 12-bit number to        */
/*      send to the LTC1448                                              */
/*               long int dur_sec = duration in sec of HV step           */
/* Return:       none.                                                   */
/*************************************************************************/

void Set_HV(long int lDac1, long int lDac2, long int dur_sec)
{
        long int        lDac0 = 0, i;

        i = dur_sec;

        // Split lDac1 & lDac2 into 3 bytes and send to DAC
        if (lDac1 > 0)              // Indicate whether HV#1 is ON or OFF
            output_high(PIN_C4);
        else
            output_low(PIN_C4);

        if (lDac2 > 0)              // Indicate whether HV#2 is ON or OFF
            output_high(PIN_C3);
        else
            output_low(PIN_C3);

        Set_DACs(lDac1, lDac2);

        if (dur_sec >= 30000)
        {
            printf("\r\n\nWARNING!  High Voltages will remain ON");
            printf("\r\n until the end of the program!!\r\n");
        }
        else
        {
            // Set count down for run time (dur_sec)
            while (i>0)
            {
                delay_ms(1000);
```

```
            i--;
        }
        // Shut down (EMCO) HV power supplies
        Set_DACs(lDac0,lDac0);
        output_low(PIN_C4);         // Indicate HV#1 is OFF
        output_low(PIN_C3);         // Indicate HV#2 is OFF
    }
}

/*********************************************************************/
/* Function:     void Set_DACs(long int lDac1, long int lDac2)       */
/* Description:  This function was modified by Loi Hua from          */
/*      SetDACs(int, int) in both.c which was developed by Dr. Chris */
/*      Backhouse.  This function converts 2 long int from 0 - 4095  */
/*      to 3 bytes of hex and sends to the DAC (LTC1448) and updates */
/*      the DAC to output voltages through SPI module.               */
/* Parameters:   long int lDac1 - holds the first 12-bit number to   */
/*      send to the LTC1448                                          */
/*               long int lDac2 - holds the last 12-bit number to    */
/*      send to the LTC1448                                          */
/* Return:       none.                                               */
/*********************************************************************/

void Set_DACs(long int lDac1, long int lDac2)
{
    int             spihi, spimid, spilow;

    spihi = (lDac1 >> 4)  & 0xff;
    spimid = ((lDac1 << 4) + (lDac2 >> 8)) & 0xff;
    spilow = (lDac2) & 0xff;

    // Enable DAC
    output_low(PIN_D0);
    spi_write(spihi);
    spi_write(spimid);
    spi_write(spilow);

    // Update DAC
    output_high(PIN_D0);
    return;
}
```

PIC16F877 Memory Usage:

ROM = 62 % (of 8 kB)

RAM = 18% - 32 % (of 368 B)

A3.0.3. More on the Ripple/Ringing Phenomenon

Figure A3-6 shows the ripple response for a system without a segregated array [which was shown in Figs. 3-2, 3-3(a)]. The inset shows the response without either the segregated array or the 100 nF ceramic capacitors. Figure A3-7 shows the reduction of the ripple response, obtained when a segregated array was employed. For Fig. A3-7 the inset shows the corresponding response for the case when a few 100 nF ceramic capacitors of the capacitor-mounted side-board of the IMS column (shown in Fig. 3-2) were missing (Fig. A3-8 shows the test conditions used to obtain these responses, including the missing capacitors which are marked in a different shade than the other capacitors); note the clipped response with the missing capacitors. (The trigger signal for all four responses is represented by the 5V square-wave pulse.)

These figures show a progressive improvement of the system sensitivity, whereby adding 100 nF ceramic capacitors in parallel with the IMS column resistors allows for a slight improvement in the response (i.e., a slight change in the ripple response), while adding a segregated array (in addition to the capacitors) allows for a more significant improvement (i.e., where the ripple response is reduced in both duration and amplitude).

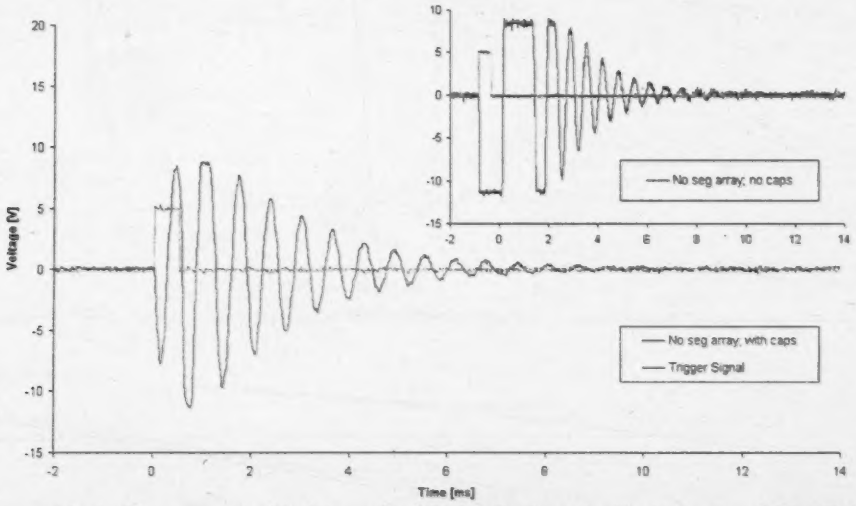

Figure A3-6. Response with (a) and without (b, inset) all sixty-one 100 nF (50 V) capacitors in place for a system without the segregated (seg) array. Note that the capacitors provide a very slight improvement. The square-wave pulse represents the trigger signal. (Figure A3-8 shows the absence of capacitors and the absence of the segregated array with dotted boxes around these components.)

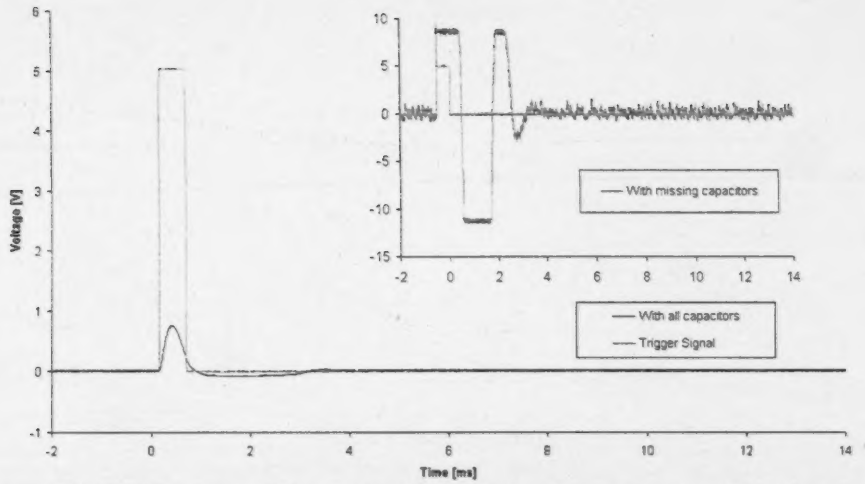

Figure A3-7. Response of the system with the segregated array with all sixty-one 100 nF (50 V) capacitors in place (a) compared with the same system with a few missing capacitors (b, inset). The missing capacitors include one between the FG and the next guard ring, and above and below the shutter gate (Fig. A3-8 depict these missing capacitors in a different shade). The square-wave pulse represents the trigger signal. (See *Section 3.2.1.2* for more details on the shutter gate controller.)

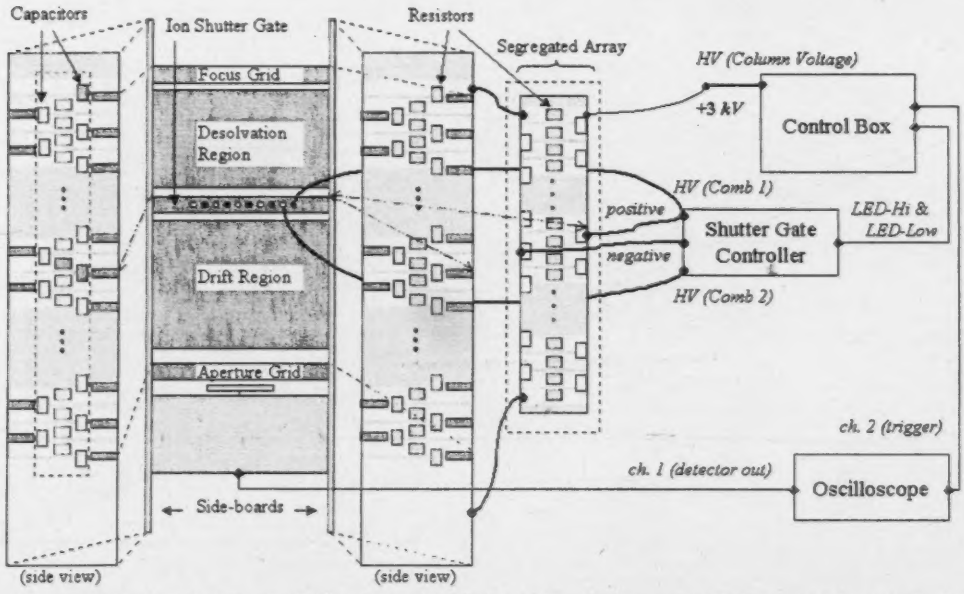

Figure A3-8. Test conditions for obtaining the responses in Figs. A3-6, A3-7. The dotted boxes indicate the components that are varied/removed (i.e., the 100 nF ceramic capacitors and the segregated array). The missing capacitors include one between the FG and the next guard ring, and above and below the shutter gate (these missing capacitors are marked in a different shade). (See *Section 3.2.1.2* for more details on the shutter gate controller. See Fig. 3-2 for more details on the components of the IMS column.)

The fact that the addition of a segregated array allows for such improved response (i.e., the significant reduction of the ripple effect) implies that a major source of the ripple is in the switching of the shutter gate. That is, the switching of the gate creates voltage pulses that propagate from the shutter gate references down the resistor array to the AG, which in-turn transmits to the antenna-like collector plate and the input of the detector.

Simulating the Ripple Response

In fact, the collector plate's ability to act as a receiving antenna was tested by placing the output (banana plug) lead of a waveform generator [the Agilent 33120A that was set to produce 0.5/49.5 ms (ON/OFF) pulses at differing amplitudes] at varying distances from the collector plate and with nothing placed between the two. Figure A3-9(A) depicts this set-up, while Figs. A3-9(B) – A3-9(D) depict the responses for varying distances [2 cm (B, C) and 7 cm (D)] and voltages [2 (B), 10 (C), and 20 V_{pp} (D)], where it is shown that the ripple signals picked-up by the collector seem to scale with the amplitude of the original signal, while the form and shape remained consistent.

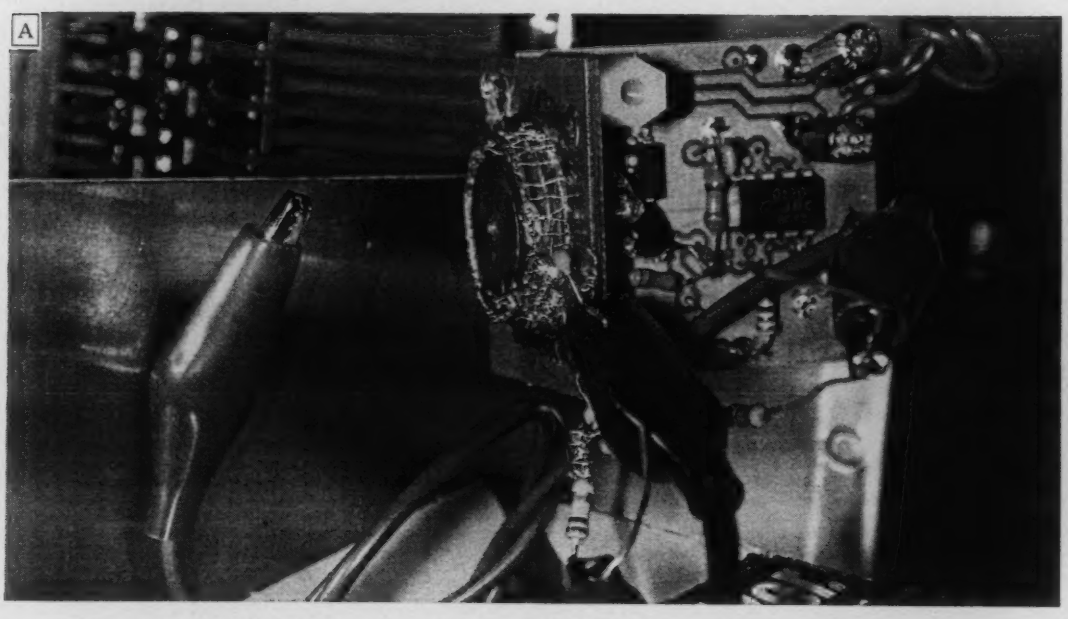

Figure A3-9(a). (A) Experimental setup for simulating the ripple effect.

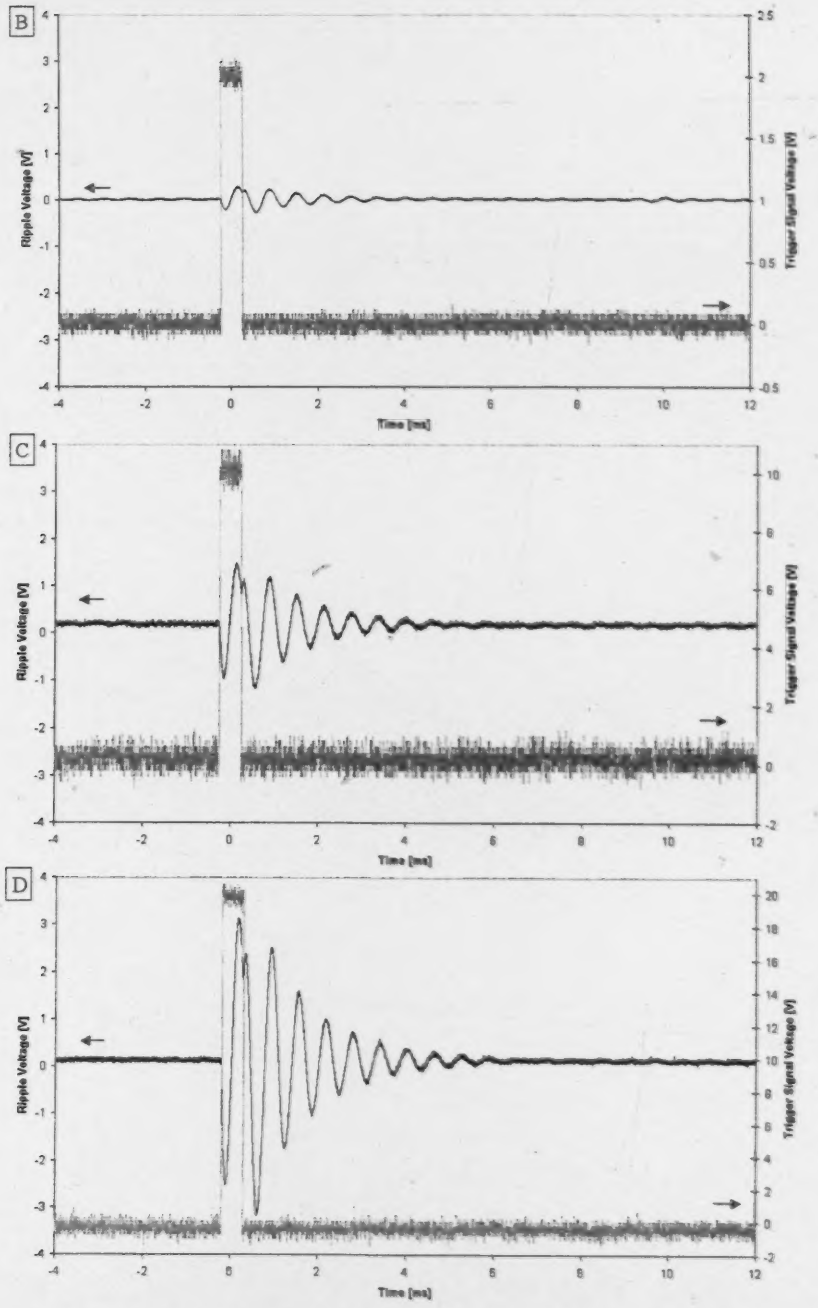

Figure A3-9(b-d). (Simulated) Ripple signals detected by the antenna-like collector for varying distances and voltages. The distances and voltages are as follows: (B) 2 cm, 2 V_{pp}; (C) 2 cm, 10 V_{pp}; and, (D) 7 cm, 20 V_{pp}. The square-wave burst signal represents the input pulse, while the ringing signal is the resultant ripple response picked-up by the detector. Note the similarity in response as the ripple effect shown in Fig. A3-6.

Testing was also done with only the distance varying (with the voltage set at 20 V_{pp}). The results are shown in Fig. A3-10, where the amplitude seems to be inversely proportional to distance.

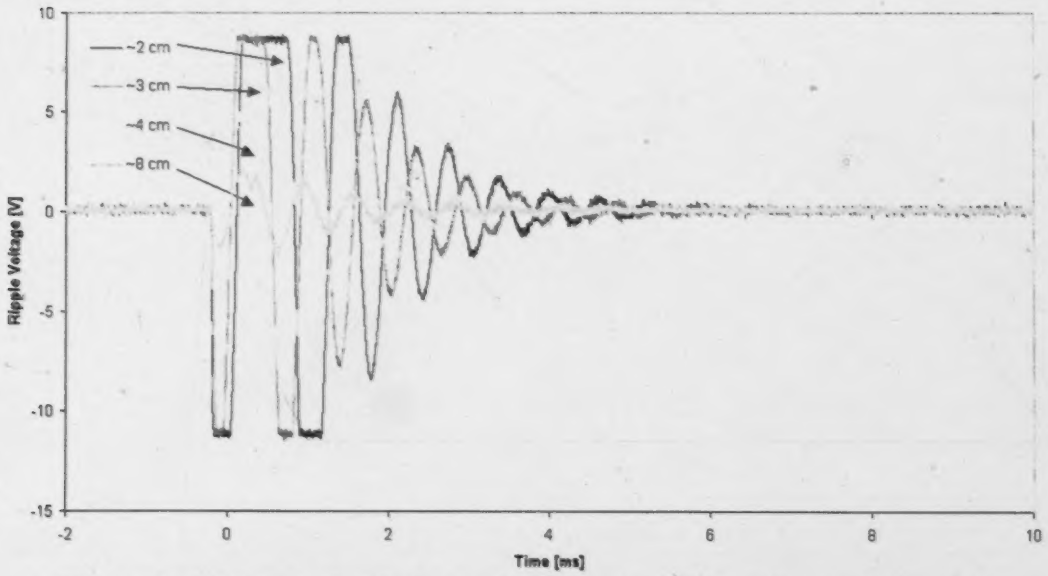

Figure A3-10. Ripple signals detected by the antenna-like collector for varying distances with a 20 V_{pp} square-wave pulse/burst. Observe that as the distance is increased, the amplitude decreases. Note the similarity in response as the ripple effect shown in Fig. A3-6.

A3.0.4. Comparison Between the Averaged and Un-averaged Control Signals

Figure A3-11 shows the control signals both averaged over 512 scans (a) and un-averaged (b) for a drift field of ~310 V cm^{-1}. Notice that the averaged signals [in Fig. A3-11(a)] are considerably smoother than the un-averaged [in Fig. A3-11(b)]. Occasionally, for the un-averaged spectra an approximately 1 kHz waveform would appear [shown as the top spectrum in Fig. A3-11(b)]; the origins of this waveform are unknown, although Juraschek and Rollgen (1998) [1] obtained spectra containing low frequency pulses (< 5 kHz) of constant amplitude and consistent peak shape that they attributed to a spray mode between spray modes SM-1 and SM-2 that were described in this dissertation (see the next section for more on spray modes).

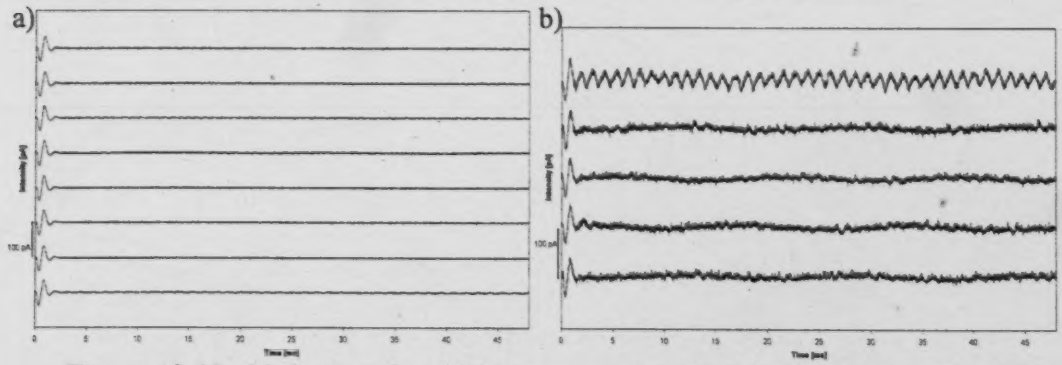

Figure A3-11. (a) Averaged and (b) un-averaged control signals obtained for a drift electric field of ~310 V cm^{-1}. The spectra in (a) were each averaged over 512 scans.

The control signals were also obtained for different drift fields (as shown in Fig. A3-12). Note that the undulations (before 5 ms) corresponding to the switching of the shutter gate is noticeably smaller in amplitude for the lower fields (i.e., lower voltages).

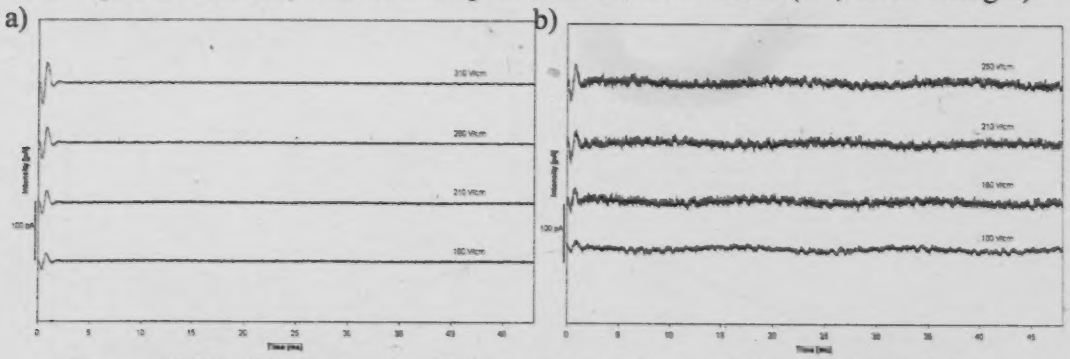

Figure A3-12. (a) Averaged and (b) un-averaged control signals obtained for varying drift electric fields.

A3.0.5. More on the Unstable, Polydisperse Spray Modes (SM-1 and SM-3)

The pulsating mode (SM-1), as described by Juraschek and Rollgen (1998),[1] occurs when there is not enough liquid to replenish the emitted liquid droplets at the tip of the Taylor cone. In other words, the flow rate of the liquid at the Taylor cone is so low that there is not enough to sustain a stable Taylor cone, which continually emits the liquid as charged droplets. This results in a collapse of the Taylor cone, which results in a cessation of spray and thus a zero-signal, until the liquid is replenished, then the cycle continues. This is the reason for the pulsating effect, where the peaks represent the heights of emission (when the Taylor cone is fully formed and emitting spray) and the troughs represent the cessation of spray (due to the collapsed liquid cone). Figure A3-13 shows the (un-averaged) spectra that captured the seemingly random occurrence of the pulse trains, where the shutter gate seems to have no effect. (Note that the under-shoot is an effect of the detector circuit.) The random nature (i.e., random placement) and the large amplitude of the peaks seem to indicate that the liquid droplets that are emitted are large compared to the efficient spray (as in SM-2), which makes sense because the instability of the liquid cone would not encourage the formation of small liquid filaments, which would result in smaller droplets being emitted (a well known occurrence in ES [2]).

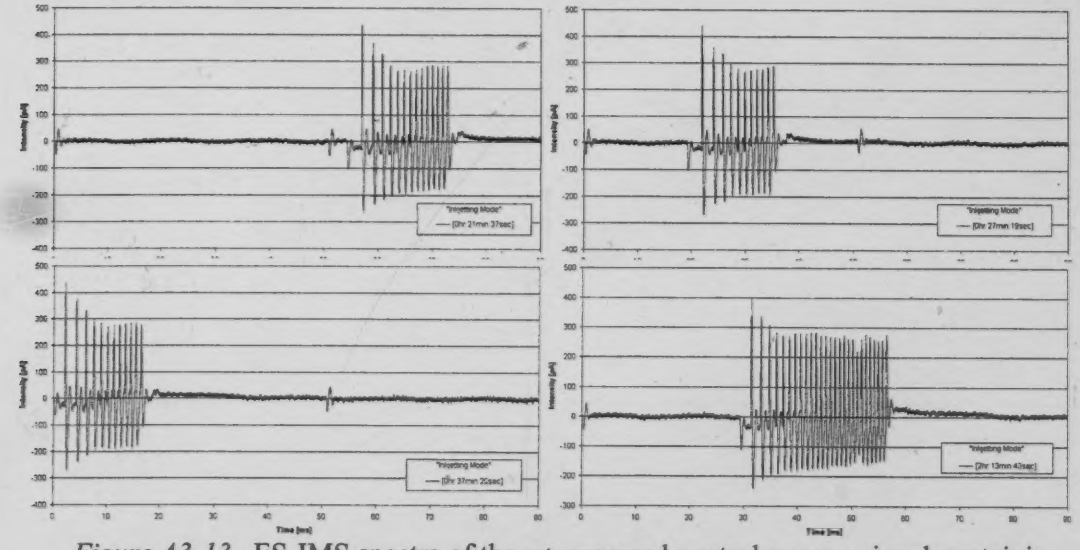

Figure A3-13. ES-IMS spectra of the un-averaged control or zero-signal containing the pulsating effect. Note the random placement of the train of peaks and their random length. Notice also the consistent initial spike, followed by one large peak then smaller ones spaced in a non-random fashion and ending in a tail peak/bump.

SM-3 can be thought of logically as the opposite of SM-1, where the high flow rates at the liquid cone exceed the rate of emission of the charged droplets, which results in an unstable Taylor cone, and thus emission of larger droplets. Where SM-1 had a pause due to the collapse of the Taylor cone, SM-3 would feature a continuous emission, represented by a blanketing spectrum (because the large droplets overwhelm the shutter gate, as with the droplets of SM-1). Due to the instability of the cone, the droplets that are emitted would be polydisperse (i.e., of different sizes), which would result in a spectrum with varying amplitudes that are at least several hundred picoamps [see Fig. 3-12(b) for an example spectrum that was averaged over a few hundred scans].

A4.0. References

(1) Juraschek, R.; and Rollgen, F. W., "Pulsation phenomena during electrospray ionization," *International Journal of Mass Spectrometry*, **177** (1998), pp. 1-15.

(2) Mutoh, M.;Kaieda, S.; and Kamimura, K., "Convergence and disintegration of liquid jets induced by an electrostatic field," *Journal of Applied Physics*, **50** (1979), pp. 3174-3179.